ATOMIC FORCE MICROSCOPY PROBING METHODS FOR SOFT VISCOELASTIC SYNTHETIC AND BIOLOGICAL MATERIALS AND STRUCTURES

A Dissertation
Presented to
The Academic Faculty

By

Seth Lawton Young

In Partial Fulfillment
Of the Requirements for the Degree
Doctor of Philosophy in the
School of Materials Science and Engineering

Georgia Institute of Technology

May 2016

ATOMIC FORCE MICROSCOPY PROBING METHODS FOR SOFT VISCOELASTIC SYNTHETIC AND BIOLOGICAL MATERIALS AND STRUCTURES

Approved by:

Dr. Vladimir V. Tsukruk, Advisor
School of Materials Science and Engineering
Georgia Institute of Technology

Dr. Jeffrey L. Streator
Woodruff School of Mechanical Engineering
Georgia Institute of Technology

Dr. Ken Gall
Department of Mechanical Engineering and Materials Science
Duke University

Dr. Jeannette Yen
School of Biology
Georgia Institute of Technology

Dr. Andrés J. García
Woodruff School of Mechanical Engineering
Georgia Institute of Technology

Date Approved: December 15, 2015

Dedicated to my family and friends for their never ending love and support, those who share my true appreciation for the ingenious complexity of biological systems, members of the SPM community who understand that SPM is more of an art than a science, and finally to those poor, poor spiders which made this work possible.

ACKNOWLEDGEMENTS

I would like to express my genuine gratitude to Professor Tsukruk for allowing me to conduct my graduate research as a member of his lab. In 2008 Prof.Tsukruk gave me the chance to work in his lab as an undergraduate researcher. This experience was a deciding factor in my choice to pursue a graduate degree in Materials Science and Engineering. Working in Prof. Tsukruk's lab has allowed me the opportunity to work on a variety of interesting projects and to have the rare chance to present my work both nationally and internationally. I would also like to sincerely thank my dissertation committee members Prof. Jeannette Yen, Prof. Jeffrey Streator, Prof. Ken Gall, and Prof. Andrés García for taking time from the incredibly busy schedules (one cannot appreciate how busy their professors are until they try to get five in the same room at the same time) to review my dissertation and to present me with helpful suggestions and feedback.

Much of this work would not have been possible without our collaboration with Prof. Friedrich Barth, Dr. Yael Politi, Dr. Igor Zlotnikov, and Dr. Maxim Erko. I can say that I have never seen a Professor so enthusiastic about being in the lab as Prof. Barth was teaching us to handle and measure the live spiders when I first met him in Golm, and also while he was at Georgia Tech. Many thanks are due to our collaborators from MPIKG. The work with the spiders afforded me the excellent opportunity to travel abroad and participate in research with Yael, Igor, and Max. They were vital in carrying out some experiments and provided excellent suggestions while preparing manuscripts.

As a member of SEMA Lab in some capacity for going on 8 years now (a "Van Wilder Fellow," if you will) I have had the opportunity to meet a lot of great people. First and foremost I would like to extend my gratitude to all members of SEMA Lab, past and present. From the old guard I would like to specifically thank Mike McConney, Srikanth Singameni, and Kyle Anderson. Mike was the first person to introduce me to AFM and teach me the intricacies of making quality measurements. The majority of my work as an undergraduate was with Srikanth, and were it not for that experience, as well as some encouragement on his part, I may have never decided to pursue my PhD. Kyle was instrumental in helping me learn more advanced imaging modes, and had to suffer scanning countless contact lenses with me. Finally I would like to thank Marius Chyasnavichyus, who helped me make many of the difficult measurements that are described throughout this dissertation.

I would also like to thank all of my friends and family. While they did not directly participate in my graduate research, they were instrumental nonetheless, especially in keeping me grounded throughout my graduate experience and providing ample opportunity

for welcome distractions from the seemingly constant looming deadlines, exams, and presentations. A very special thanks should also be extended to my loving wife, Rebecca, who has supported me wholeheartedly since the end of my undergraduate career.

Finally I would like to extend gratitude to my new employers at Georgia-Pacific Chemicals for giving me the chance to start what hopefully is a long and productive industrial career with them.

TABLE OF CONTENTS

LIST OF TABLES

LIST OF FIGURES

SUMMARY

Mechanical properties of micro- and nanoscale viscoelastic soft materials can dictate their performance and function. In this dissertation we focus on refining atomic force micrscopy (AFM) methods and data analysis routines to measure the viscoelastic mechanical properties of soft polymer and biological materials in relevant fluid environments and in-vivo using a range of relevant temperatures, applied forces, and loading rates.

These methods are directly applied here to a several interesting synthetic and biological materials. First, we probe poly(n-butyl methacrylate) (PnBMA), above, at and below its glass transition temperature in order to verify our experimental procedure. Next, we use AFM to study the viscoelastic properties of coating materials and additives of silicone-based soft contact lenses in a tear-like saline solution. Finally, a major focus in this dissertation is determining the fundamental mechanical properties that contribute to the excellent sensitivity of the strain sensing organs in a wandering spider (Cupiennius salei) by probing under in-vivo conditions. These strain-sensing organs are known to have a significant viscoelastic component. Thus, the cuticle of ***living spiders*** is directly investigated in near-natural environments (high humidity, temperatures from 15-40 °C). The main achievements of these studies can be summarized through the following findings:

- Practical experimental methods and data analysis routines were established to quantitatively characterize the viscoelastic mechanical properties of soft material surfaces. A model viscoelastic polymer, PnBMA, was found to have an elastic modulus changing from 1 GPa to 30 MPa over the temperature range from 10 °C to 55 °C. Our viscoelastic analysis allowed for calculation of key viscoelastic parameters E_0, E_∞, E', E'', $\tan\delta$, and τ. Comparing our data analysis routines which account for viscoelastic effects via the Johnson model, it was found that in the vicinity of T_g (25 °C), *elastic models overestimate the modulus by >50%*. Through the course of these efforts, a data analysis software was custom built which allows for modulus calculations with various tip geometries, elastic and viscoelastic models, as well as batch processing capabilities for simultaneous analysis of FDCs.
- These methods and analysis routines were then applied to commercially available silicone-based, soft contact lens materials immersed in saline solutions simulating in-vivo conditions. We found calculated modulus values for all lens surfaces *three times higher than those reported by the manufacturer*. Tensile testing of the bulk lens at low strains. AFM-based measurements represent the loading modes and loading rates experienced by the lens surface during patient use (e.g. blinking).
- The structure and function of a pad serving as a vibration filter and a contact between the final leg segment and a strain sensitive organ on a wandering spider was investigated. Widely varying elastic moduli were found in different regions of the pad, with the highest being the appendix structure at 8 GPa, and the lowest reported values near the dorsal and distal surfaces of ~100 MPa. The pad was observed to play a key role in transformation of mechanical stimuli from tens of micrometers at the contact point to tens of nanometers at

the organ. Furthermore the appendix was also observed to control the direction of deformation at the organ such that slits walls remained parallel during compression despite the loading direction.

- The time- and temperature-dependent mechanical properties of the outermost layer of the pad was investigated on living spiders using our AFM-based method under in-vivo conditions. It was found that this layer ranged between 20 MPa and 100 MPa over a narrow temperature range with a T_g of ~19 °C. Our viscoelastic data analysis routines allowed for visualization of the loss modulus peak as a function of temperature. At room temperature (24 °C) this peak frequency corresponded well to the 30 Hz threshold values obtained via electrophysiological experiments. As temperature decreased the loss modulus peak shifts to lower temperatures, meaning the spider is more sensitive to a wider range of stimuli frequencies. We suggested that the viscoelastic mechanical properties are tuned in a way such that the nocturnal spider is more sensitive to relevant vibrational stimuli during the cooler nighttime hours, as established by biologists.
- The viscoelastic mechanical properties of the outer membrane on the spider slit sensors responsible for eliciting action potential impulses was for the first time directly investigated with AFM. The relaxation time of this material at 24 °C was found to be ~0.4 sec, which is correlated to the time in which the rate of action potential impulses drastically decreases before leveling off. It was suggested that in addition to the properties of the neuron, the viscoelastic relaxation of the outer membrane plays a key role in in the decaying neural response of the organ. Because relaxation times of the spider epicuticle increase exponentially from 10 msec at 30 °C to > 5 sec at 19 °C, we suggest that the relaxation behavior of the outer membrane is also tuned for higher sensitivity (less impulse rate decay) at lower temperature in which the spider is active.

We suggest that full time-temperature-modulus relationships are necessary for the understanding of soft materials systems, and present a practical method for obtaining such relationships. These studies will have a direct impact on both scientists in the metrology field by developing practical experimental procedures and data analysis routines to investigate viscoelastic mechanical properties at the nanoscale, and future materials scientists and engineers by showing via spider mechanosensory systems how viscoelasticity can be applied for functional use in sensing technology.

Atomic force microscopy probing methods for soft viscoelastic synthetic and biological materials and structures

CHAPTER 1

Introduction

1.1 Background: Mechanical properties analysis techniques

Mechanical properties at the nanoscale play a critical role in the overall performance of soft nano- and micro-structured systems such as polymer blends and coatings, can significantly impact biological functions such as tissue growth or bacterial adhesion, and also serve as a key component to the functionality of biological sensory systems.[1,2,3,4] However, quantitative measurements of soft, hierarchically-structured systems such as these can be extremely challenging due to the delicate nature of the sample, complex macroscopic shape and micro- and nanoscale surface topography, and heterogeneous distribution of mechanical properties.

Common characterization techniques (discussed below) to determine materials mechanical properties, such as tensile testing, dynamic mechanical analysis (DMA), or bending tests to name a few, only account for the bulk behavior of the sample material, neglecting the potentially critical properties of contacting surfaces. Furthermore, sub-micrometer scale samples are too delicate for handling in order conduct such bulk measurements on, and can be easily damaged by high forces inducing plastic deformations. For complex soft materials, behavior in working environments may be drastically different than those observed under testing conditions. For example, polymers may swell, displaying different apparent mechanical properties in the presence of high humidity or solvent vapors. Additionally, in the case of many soft materials and biopolymers, a slight change in temperature or loading rates can drastically change material behavior due to viscoelastic

effects. Therefore, in order to adequately characterize micro- and nanoscale mechanical properties, non-destructive methods with environmental control for in-situ mapping with nanometer resolution are often desired, or even required.

Of the various characterization techniques, atomic force microscopy (AFM) is one that simultaneously allows environmental control (temperature, relative humidity, and the ability to probe in relevant fluid environments), excellent force sensitivity for measuring materials with moduli ranging from kPa to GPa in a non-destructive manner, and the ability to spatially map variances in local mechanical properties with nanoscale resolution. However, measurements in fluid and at varying temperatures can be complex and difficult to perform correctly. Furthermore, using AFM to measure the viscoelastic mechanical properties of soft materials surface is still a developing field with a variety of techniques available (discussed below). Unfortunately, these techniques have several disadvantages which include low lateral resolution, only qualitative data, elaborate characterization techniques, to name a few.

Additionally, because of the complexity of AFM-based mechanical analysis, commercially available data analysis programs are often very basic. Typically they include only one or two tip geometry models, treat the sample surface as a linearly elastic material, lack layered material analysis, and have limited adhesive model analysis and batch processing capabilities. Therefore, there is a need to develop both experimental procedures *and* data analysis routines for practical and quantitative characterization of soft viscoelastic properties at the micro- and nanoscale.

1.1.1 Stress-strain relationships. As the work presented within this dissertation is interdisciplinary, it is useful to note some basics on mechanical properties here. “Mechanical properties” is an umbrella term which describes a material’s response to

applied forces by deforming its shape (i.e. strain). In this respect, the characterization techniques described below all aim to measure strains resulting from applied stresses (i.e. forces per unit area). Strains can be either elastic or plastic, with elastic strains being completely recoverable upon removal of stresses, while plastic strains are unrecoverable permanent deformations. Knowing the stress limit separating elastic and plastic can behavior can be useful; however, within the context of this dissertation we work with live specimen, as well as delicate biopolymer and hydrogel surfaces. Therefore we are only interested in the elastic modulus of the material, which describes its resistance to strain under an applied load in the elastic regime. The higher a material's elastic modulus, the more stress is required to accomplish a given amount of elastic straining.

1.1.2 Viscoelasticity. Stress-strain relationships are relatively straight-forward for hard, crystalline materials such as metals, as they can be envisioned as ordered arrays of atoms connected by "springs" which stretch/compress under elastic loading, allowing the material to deform. However soft materials and biopolymers are composed of long-chain macromolecules which are often coiled and entangled both physically and chemically with one another.[5,6] When loaded polymers can respond by directly stretching the covalent bonds along the chain backbone. Macromolecules also possess the ability to have large segments and side chains rotate about covalent bonds, which results in large-scale segmental motion.[6] Such motion is highly time- and temperature dependent, and is the basis for viscoelastic behavior (i.e. a combination of time/temperature dependent viscous behavior and elastic behavior).[7]

For soft polymeric materials at lower temperatures (in their glassy state) the free volume is limited and large-scale macromolecular motion (segmental motion) is essentially frozen. At higher temperatures, however, the thermal energy in the system provides higher mobility to the polymer macromolecules, allowing for large-scale, reversible segmental

chain motion upon the application of a force. This results in a reduced elastic modulus (the rubbery state). The temperature at which a material transitions from the glassy to the rubbery state is known as the glass transition temperature, T_g.[6] On the other hand, at a constant temperature and sustained applied load, segmental motion can also occur given a sufficient amount of time. In this way, time and temperature are intimately related for viscoelastic materials.[6,7]

1.1.3 Mechanical characterization. Many techniques have been developed over the years to test a material's mechanical properties, with the most widely employed being the traditional tensile test.[8] Tensile testing involves loading a sample specimen (which is generally tooled specifically to fit the tensile testing machine) uniaxially, and measuring sample strain as a function of stress. From a single tensile test a wealth of information is gained including the elastic modulus, yield strength, ultimate strength, elongation to failure, as well as resilience and fracture toughness.[8,9] Alternatively, the elastic response to uniaxial compressive forces can be measured in a similar manner, and for isotropic materials, the tensile and compressive mechanical properties are known to be related.[8] While these two methods are quite useful they are only able to measure bulk mechanical properties of macro-scale specimen, and require that the sample be machined specifically to fit the testing machine.

Consequently, samples with at least one dimension in the sub-micrometer to micrometer range are too delicate to handle directly and the lack of force sensitivity for bulk measurements necessitates different mechanical characterization techniques. For example, buckling phenomena can be used as a means to probe the mechanical properties of a thin, stiff film on top of a thicker, softer, elastic substrate.[10,11] Compressional forces applied to the large elastic substrate causing stress buildup and release in the stiff thin film, resulting in periodic, out of plane buckling with a periodicity related to the film thickness (Fig. 1.1).

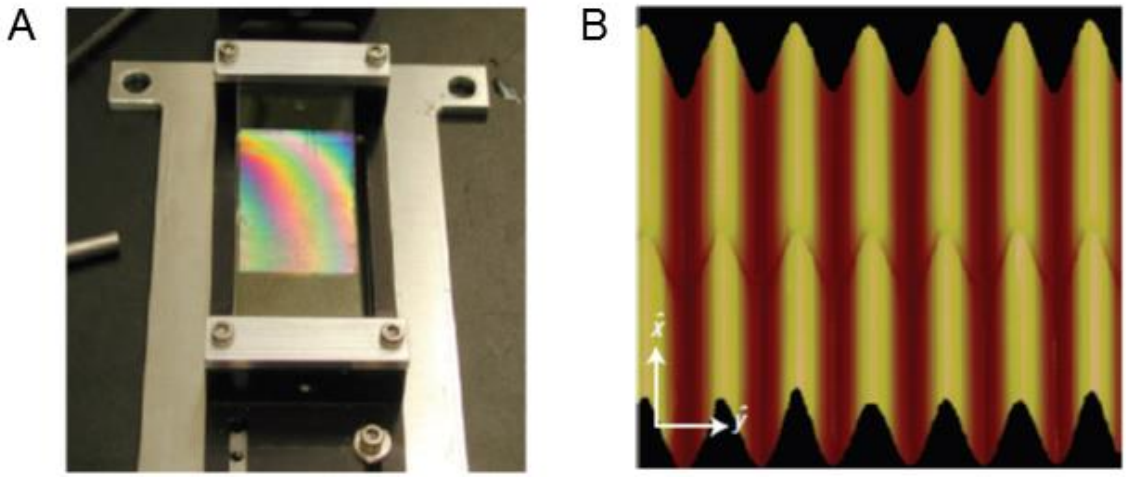

Figure 1.1: (A) Thin polymer film on a thick elastic substrate under compressional loading. Diffractional colors caused by periodic buckling. (B) AFM height image showing periodic buckling pattern.[10]

Thin film mechanics can also be probed using the so-called bulging method.[12,13,14] In bulging tests a free-standing thin film is suspended across an opening (e.g. of a TEM grid), and a external pressure is applied, causing the film to deflect upwards, with the total deflection amplitude ranging from tens of nanometers to tens of micrometers. This deflection is monitors via an interferometry setup (see Fig. 1.2). The resulting interference pattern produces concentric Newton rings. From the number and diameter of the concentric rings, as well as knowledge of the applied pressure, the elastic modulus can be back calculated.[12]

Both buckling and bulging experiments have been shown to be suitable for measuring sub-micrometer thick films with elastic modulus values ranging from several MPa to tens of GPa. However, neither has the ability to probe local mechanical properties. Furthermore preparation of freestanding thin flims and deposition onto appropriate measurement substrates is a very challenging task. In many cases, for example measuring hydrogel coatings on soft contact lenses or a thin epicuticle layer on a spider exoskeleton (both

discussed in detail below), obtaining free standing films is impossible. Additionally, methods such as these are not necessarily standardized, and require custom-built experimental setups. It should also be noted that neither of these methods are well suited for measurements of nanoscale deformation in fluid or in through a range of temperatures.

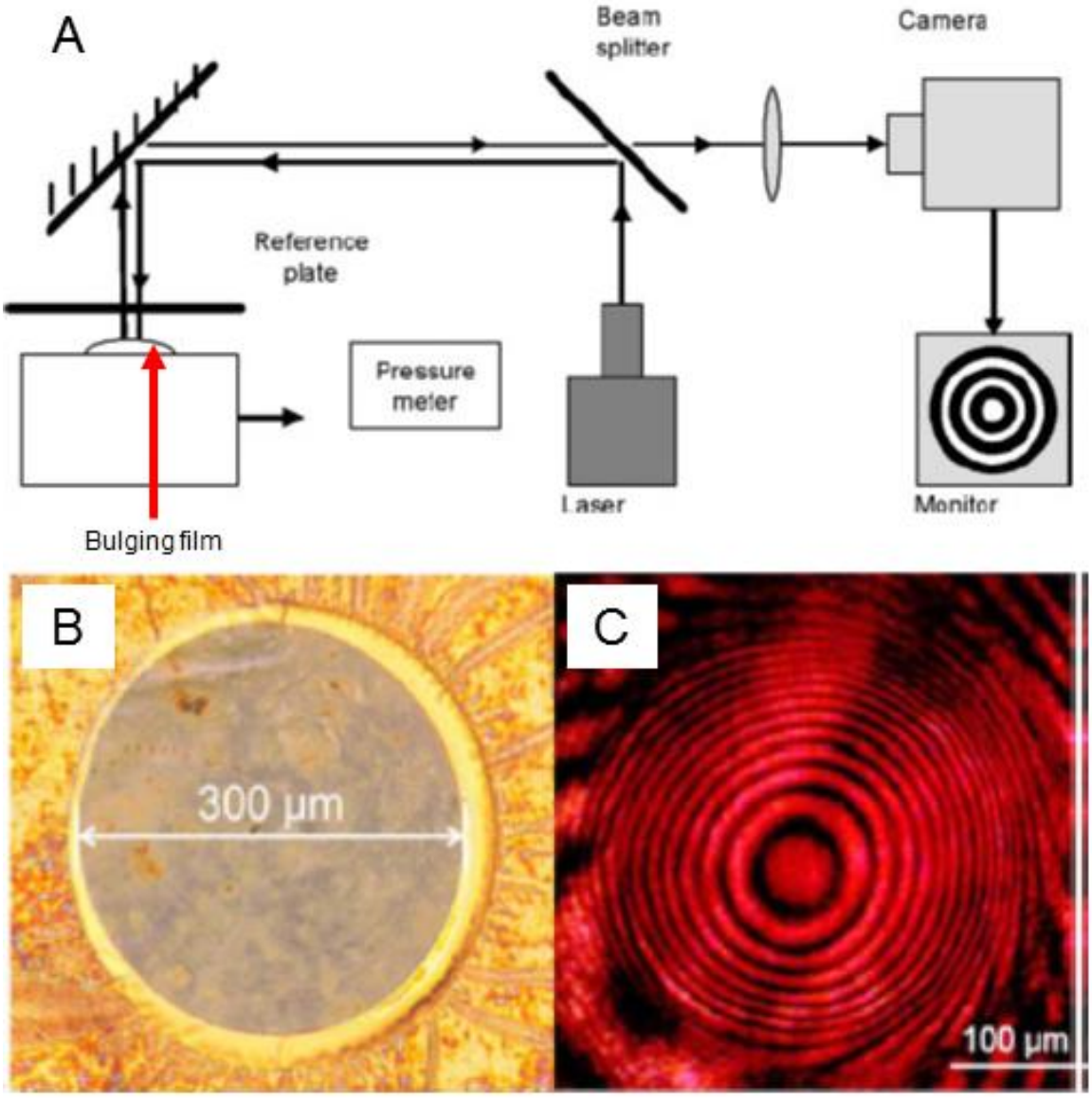

Figure 1.2: (A) Schematic showing the interferometry setup for bulging experiments.[12] (B) Optical image of a suspended thin film.[13] (C) Interference pattern on the deflected film during measurement.[13]

Nanoindentation is an extension of the indentation experiments used to determine surface hardness. During the course of these measurements a hard, typically pyramidal tip is pressed into the sample surface, causing irreversible plastic deformation. The applied force is then removed, and the slope of the initial portion of the unloading curve can be related to the projected contact area (from the residual indentations on the surface) in order to calculate the elastic modulus of the sample, as described by Oliver and Pharr:[15]

$$E = \frac{1}{\beta}\frac{(1-\upsilon^2)}{2}\frac{\sqrt{\pi}}{\sqrt{A}} \tag{1.1}$$

where A is the contact area and β is a correction shape-indenter factor which is different for different indentors.

In the case of nanoindentation, only very small penetration depths are achievable before the material yields due the sharp tips and high applied forces involved. If plastic deformation occurs, the biggest challenge is the clear separation of elastic and plastic components of the deformation. The simplest way to estimate the yielding point for the material is to use Tabor's representative strain.[16] For the case of spherical and conical indenters these limiting strains could be estimated as $\epsilon = 0.2a/R$ and $\epsilon = 0.2\cot(\alpha)$ respectively . Comparison of these values with the strain at the yield point gives a rough estimation of the transition between purely elastic and elastic-plastic regions of deformation.

This method works very well for hard materials with small elastic strains such as metals and ceramics, but has some limitations for use in soft polymeric systems with pronounced relaxations.[17] However, for soft polymeric materials, the pile-up effect significantly changes the contact geometry such that the contact area becomes unknown and cannot be

easily used in the elastic modulus calculation. Then, the model does not account for additional adhesion and frequent long neck formation, which is common in compliant and highly adhesive polymeric materials. The additional limitation is related to the time dependent properties of the polymers which can cause the appearance of an apparent negative stiffness.[18] Therefore for soft material, models which account for time dependent mechanical properties and complete loading history should be further considered.

Herein we describe the recent developments of experimental techniques and data analysis routines for the precise characterization of the viscoelastic mechanical properties of soft material surfaces.

1.2 AFM methods for mechanical properties measurements

Atomic force microscopy (AFM) methods provide variety of tools to access these properties by measuring the interactions of a sharp probe with the sample surface.[19] Precise control over the force applied to the probe allows one to study a variety of materials ranging from very compliant live cells to extremely stiff cellulose fibrils and rigid polymers.[2,3,4] At the same time, the accuracy of modern piezo actuators provides the opportunity to perform these measurements with nanoscale precision and map inhomogeneous soft materials on the length scale of a single polymer chain.[20] Furthermore, such force and spatial precision combined with current state of the art setups enabling image acquisition times on the order of seconds provides SPM-based methods with the unique ability to study changes in mechanical properties of nanostructured soft materials in real time in controlled environments. The measurements can be performed in liquid,[21] controlled atmosphere,[22] high vacuum,[23] as well as reduced or elevated temperatures.[24] In addition the probe itself can be modified to mimic the properties of specific materials or decorated with cells and molecules to study adhesive behavior of different components of nanostructured systems.[25]

Typically AFM mapping of surface mechanical properties involves considering the tip-sample interaction as purely elastic and is modeled by "spring-on-spring" Hookean behavior.[26] However, this approach gives only a snapshot of the material behavior in the time-temperature domain. It is well known that relaxation processes in soft materials delay the response to external stress. This viscoelastic behavior is especially prominent around transition temperatures, such as the glass transition temperature in polymer systems, where the storage modulus of the material can change by more than 3 orders of magnitude.[6,26] Therefore it is extremely important to take into account relaxation processes in the material as well as the rate and time dependence of these processes during mechanical AFM measurements. In this section we outline some commonly employed AFM-based methods for mechanical properties characterization, as well as discuss where their pitfalls occur, especially as it concerns to determination of materials properties through the viscoelastic regime in which apparent elastic modulus values can vary significantly.

1.2.1 Quasi-static loading. Historically the first developed mode for mechanical measurements involved quasi-static loading of the sample surface.[27] In this mode an AFM tip is brought into the contact with the sample, is pressed against it, and then withdrawn. The full approach-retract cycle is presented schematically in (Fig 1.3B) and consist of the several major regions: 1) the tip is far away from the sample with no forces exerted on it; 2) the tip first touches the sample (contact point); 3) the tip is positively deflected when pressed against the sample; 4) the tip is negatively deflected by the attractive forces during the retraction portion of the loading cycle prior to loosing contact with the surface. The forces calculated from the tip deflection can be plotted against the actuator position to achieve so called force-distance curves (FDCs). Application of various contact mechanics models to the different regions of recorded FDCs allows calculation of mechanical properties such as elastic modulus and adhesion.

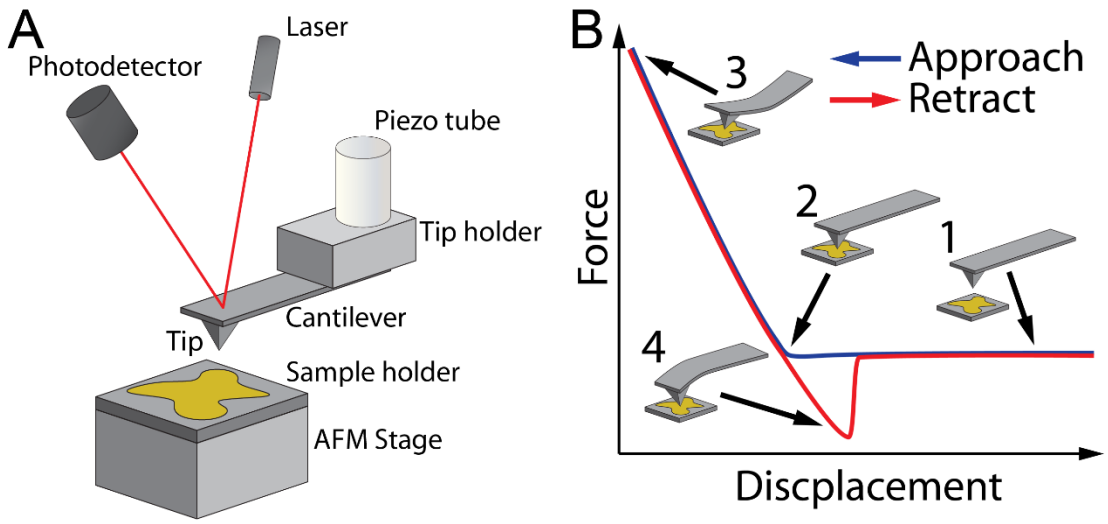

Figure 1.3: (A) Schematic of the common AFM setup. (B) Main regions of FDC – 1: approach (no contact); 2: contact point; 3: applied force to user-defined maximum; 4: retracting tip until fully off the sample (adhesive forces cause negative forces on the cantilever).

In the simplest case, Sneddon's contact model is applied to the tip-sample interaction.[28] In this model the tip is represented by the axisymmetric rigid punch indenting into the elastic half space. For common AFM tips and low indentation depths, a parabolic tip shape is usually assumed.[26] For the analysis the FDC is transformed into a force-penetration curve, where the force F is calculated from the deflection of the cantilever (d) and the spring constant of the cantilever (k) as $F = k \cdot d$, and penetration δ is calculated through the difference between the relative piezo displacement (z) and cantilever deflection (d) as $\delta = \Delta z - \Delta d$. From the slope of force-penetration curves elastic modulus can be calculated as (see Fig. 1.4):[26]

$$E = \frac{3}{4}\frac{1-\nu^2}{R^{1/2}}\frac{dF}{d(\delta^{3/2})} \tag{1.2}$$

where R is the radius of the curvature of the apex of the tip and υ is the Poisson's ratio of the sample material.

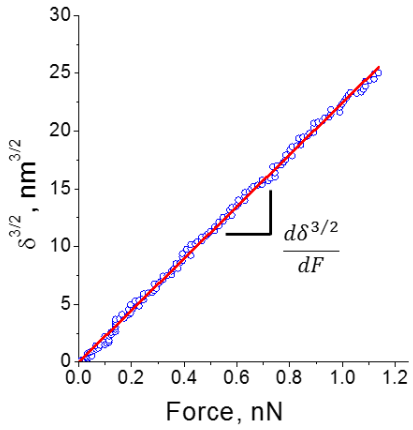

Figure 1.4: Example penetration versus force curve showing linear fitting having a slope of $\frac{d\delta^{3/2}}{dF}$.

A schematic of sample indentation due to applied force from a AFM tip is shown in Fig. 1.5. Over the years more complicated contact mechanics models were developed and currently there exists several reviews that discuss in detail the effect of tip shape, sample roughness, adhesive behavior, and electrostatic properties on the mechanical characterization of the samples with the quasi-static FDC collection.[29,30,31]

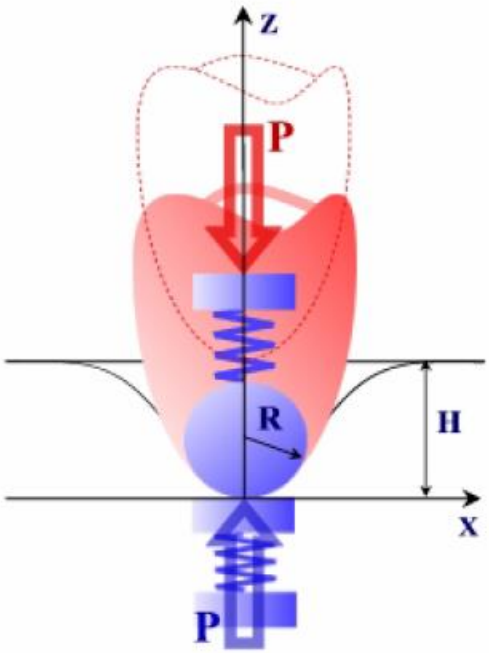

Figure 1.5: Schematic depicting sample surface indentation due to loading from an AFM tip.

Because the indentation depth can be precisely controlled using this method, the elasticity of ultrathin and multilayered thin films, which are not accessible via any other techniques, can be studied with the application of simple layered contact mechanics models.[32,33,34] Furthermore, the pull-off point of the retract curve (Point 4 in Fig. 1.3B) can be used to map adhesive properties of the surface, which was used in numerous applications.[35,36] Despite its usefulness, there are however several drawbacks to this technique. The first one is related to the assumptions of the chosen contact mechanics model. These contact models are usually applied for simple indenter shapes (such as paraboloid, sphere, cone and pyramid), and the nanoscale dimensions of AFM-based measurement can strongly influence calculated elastic properties. Thus to perform quantitative calculations, the tip shape should be precisely characterized. This characterization can be done by SEM imaging, topography reconstruction,[37] or indentation into a reference sample with a known modulus.[38] The other assumption of the simple contact mechanics models is ideally flat sample topography. Therefore sample roughness plays major role in measurements precision, as well as selection of valid regions for measurements.[39] Cantilever stiffness is another important parameter directly related to the elastic measurement precision: for high signal to noise ratios in FDCs the stiffness of cantilever should be close to that of the measured material.[40]

Another major drawback is related to the fact that a single measurement is performed at a ramp rate which limited by the nonlinearities of piezo-actuator extension,[41] therefore imaging with this technique can take a considerable amount of time and can be impractical for real time applications. Even if sample stability is not the issue, the limitation of the measurement rate brings out the problem of AFM stability over the course of the measurements. To improve these drawbacks dynamic measurement modes were developed.

1.2.2 Dynamic methods. In dynamic methods high frequency vibrations are applied to the tip-sample contact through the actuation of cantilever, the sample, or both. Cantilever response is then measured in different regions of the sample in terms of parameters of the vibrations (such as amplitude, phase or frequency changes) to create contrast maps and quantitatively calculate the elastic properties of the material. Here we will focus on several common dynamic techniques grouped by their principle of operation.

1.2.2.1 Phase imaging via tapping mode. In tapping mode vibrations are applied to the tip at a frequency close to its resonance and intermittent contact with the sample is performed. The reduction of the tip-sample contact time allows reduction of lateral forces, which appear during the tip motion across the scanned surface.[42] Typically tapping mode is performed in amplitude modulation mode: the height of the cantilever position is constantly adjusted to keep a constant ratio of the tip vibrational amplitude in contact with the sample surface to its oscillation amplitude in air, thus imaging topographical features of the sample. The phase shift of the vibrations relative to the excitation vibrations bears information about the energy dissipation by the tip into the sample. The phase imaging technique can be used to produce excellent material contrast, especially in the systems with close mechanical properties, without any additional post processing of the measurement data.[43] Due to the fact that forces between the sample and the tip are not measured directly in tapping mode, this technique does not allow precise measurement of the elastic modulus of the material. However it was shown that it can be used to perform contrast ordering in some cases of hard tapping in multi component rubbers.[44]

1.2.2.2 Force Modulation Microscopy (FMM). In contrast to tapping mode, force modulation microscopy measurements are performed in contact mode.[45] The cantilever is displaced vertically to maintain constant deflection while the tip scans across the surface

thus mapping the sample topography, while at the same time the cantilever is vibrated at a frequency which is much lower than the resonance frequency, but is still high enough to avoid distortions due to the instrument resonance. During these vibrations the tip stays in the repulsive contact regime with the sample, therefore simplifying the tip-sample interaction forces compared to tapping mode, where transitions between attractive and repulsive modes may occur.

Simple analysis can be therefore applied to the system under the assumption of elastic material behavior.[45] In this analysis the tip is assumed to be attached to the piezo-actuator with the spring with the stiffness k_c. At the same time the tip is considered connected to a spring with the stiffness k_s, which represents the elastic sample. The tip-sample vibrational amplitude u can be then described as:[46]

$$u = \frac{u_0 k_s}{k_s + k_c} \sin \omega t \tag{1.3}$$

where ω is the angular frequency of induced vibrations, and u_0 is the drive amplitude of the vibrations. Since the contact area is unknown, only tip-sample contact sample stiffness can be calculated. The relative modulus can be acquired as well by using a calibration sample with well-known elastic properties.[47,48] It is important to note that the simple elastic model presented here is not applicable in the case when nonlinear effects in the FDC are present and more complicated forms of analysis should be used.[49]

1.2.2.4 Ultrasonic AFM. Ultrasonic AFM (UAFM) technique is similar to FMM in that a tip is constantly pressed against the sample surface and vibrations are induced into the tip-sample contact. There are however two major differences in the UAFM approach: 1) the applied frequency is much higher than the natural resonance frequency of the tip vibration;

and 2) the amplitude of this frequency is constantly changing, while the average tip deflection is monitored.[50] The concept of UAFM operation is presented in Fig. 1.6. Initially, when the vibration amplitude is low, the average tip deflection stays constant. When the vibration amplitude reaches A_0 the deflection starts increasing nonlinearly, indicating that the tip has reached the attractive regime of tip-sample interaction. At an even higher amplitude, A_1, the tip fully detaches from the sample producing a noticeable increase in the average cantilever deflection (Fig. 1.6). This threshold amplitude A_1 is used in UAFM as the parameter to map the stiffness distribution of the sample surface: for more compliant material initial penetration δ_c would be higher, and therefore would require higher threshold amplitude. Due to the complexity of the tip-sample interaction only contrast imaging, which qualitatively describes stiffness of the components, can be done.

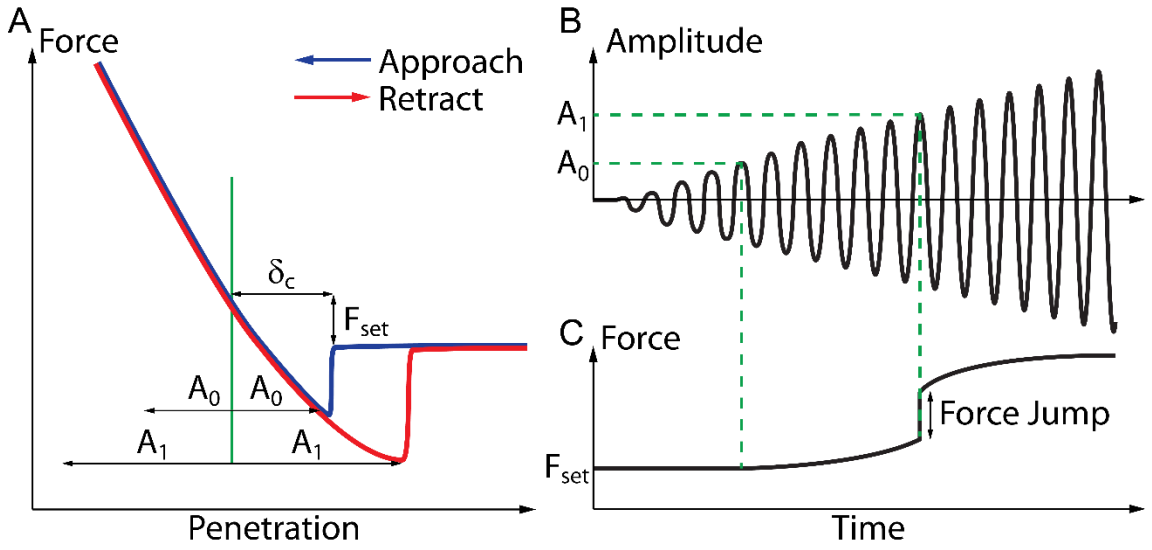

Figure 1.6: **(**A) Schematic showing typical UAFM measurements parameters on FDC. (B) Amplitude change at each point in UAFM experiment. (C) Corresponding average forces acting on the tip.

Due to the tip-sample stiffening at high vibration frequencies, UAFM can be used to study materials in the wide (1-400 GPa) modulus range. It was applied to study polymer blends, nanocomposites with high variation of component stiffness, and thin films. However, the

technique is well suited for measurements of viscoelastic samples, which change their properties at ultrasonic frequencies and materials with high variations in adhesive properties and roughness.[50]

1.2.2.5 Pulsed force Imaging. In pulsed force imaging the tip contacts the sample during the down portion of a sinusoidal vibration cycle (Fig. 1.7).[51] Each cycle starts above the surface, then the tip approaches and makes brief contact the surface resulting in a small indentation. The depth of this indentation is controlled by the maximum force excreted on the sample by the cantilever (set point). The cycle is finalized by withdrawing the tip from the surface up to the initial baseline static deflection. By limiting the set point, indentations as small as 1-2 nm can be performed, therefore achieving very soft, nondestructive measurement conditions. Approach and retract FDCs can be reconstructed from the loading data (Fig 1.7); however the analysis of these curves differs from quasi-static measurements. Because of the low calculation time requirements for real time analysis in pulsed force imaging, the set point force (F_{tip}) and adhesive force (F_{adh}) are used instead of the full curve fitting to calculate elastic modulus according to the Derjaguin-Muller-Toporov (DMT) model as:[4]

$$E = \frac{3}{4}\frac{1-\nu^2}{R^{1/2}}\frac{(F_{tip}-F_{tip})}{\delta^{3/2}} \tag{1.4}$$

Further analysis of the FDCs allows for simultaneous measurement of adhesion and energy dissipation in addition to the sample topography and elasticity.

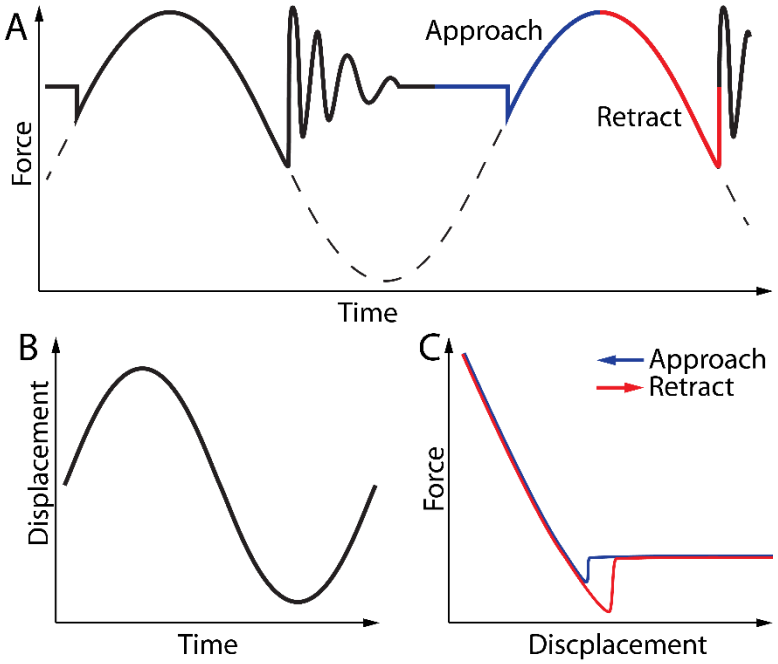

Figure 1.7: (A) Variation of the force as a function of time in a Pulsed force imaging experiment: Experimental curve (solid line) and constant tip sample contact case (dashed line). (B) Corresponding cantilever displacement. (C) FDC reconstructed from the approach and retract portions of the loading curve presented in (A).

Pulsed force imaging allows acquisition of high resolution qualitative maps of mechanical properties of the sample both for dry samples and in liquid. Thus this technique was successfully applied to multiple polymers[52,53] and biomaterials.[54,55,56] For example, we have used this method to produce a high resolution mapping of a patterned film of recombinant spider silk-like protein.[56] This mapping of the adhesive interaction of the AFM and the sample surface revealed at least two distinct regions corresponding to more hydrophobic secondary structure, and more hydrophilic secondary structure (Fig. 1.8).[56] Similar to the quasi-static measurements, to achieve quantitative mechanical properties maps one needs to fully characterize the tip.[31,57] However, even for fully characterized systems, mechanical properties acquired with pulsed force imaging can deviate significantly from quasi-static measurements due to such effects as the apparent stiffening of the sample at high loading rates, nonlinear loading effects, and for materials with

behavior strongly deviating from DMT model.[31] Recently Stan and Gates presented improvements of some of the shortcomings of the pulsed force imaging.[58] It was shown that application of overlaying independent high frequency resonant vibrations to the PeakForce tapping mode can enhance the elastic modulus calculations. This was done by resolving adhesive response of the material, which was calculated through Swartz adhesive model,[59] allowing one to pick adequate adhesive behavior in between long range (DMT) and short range (JKR) models.

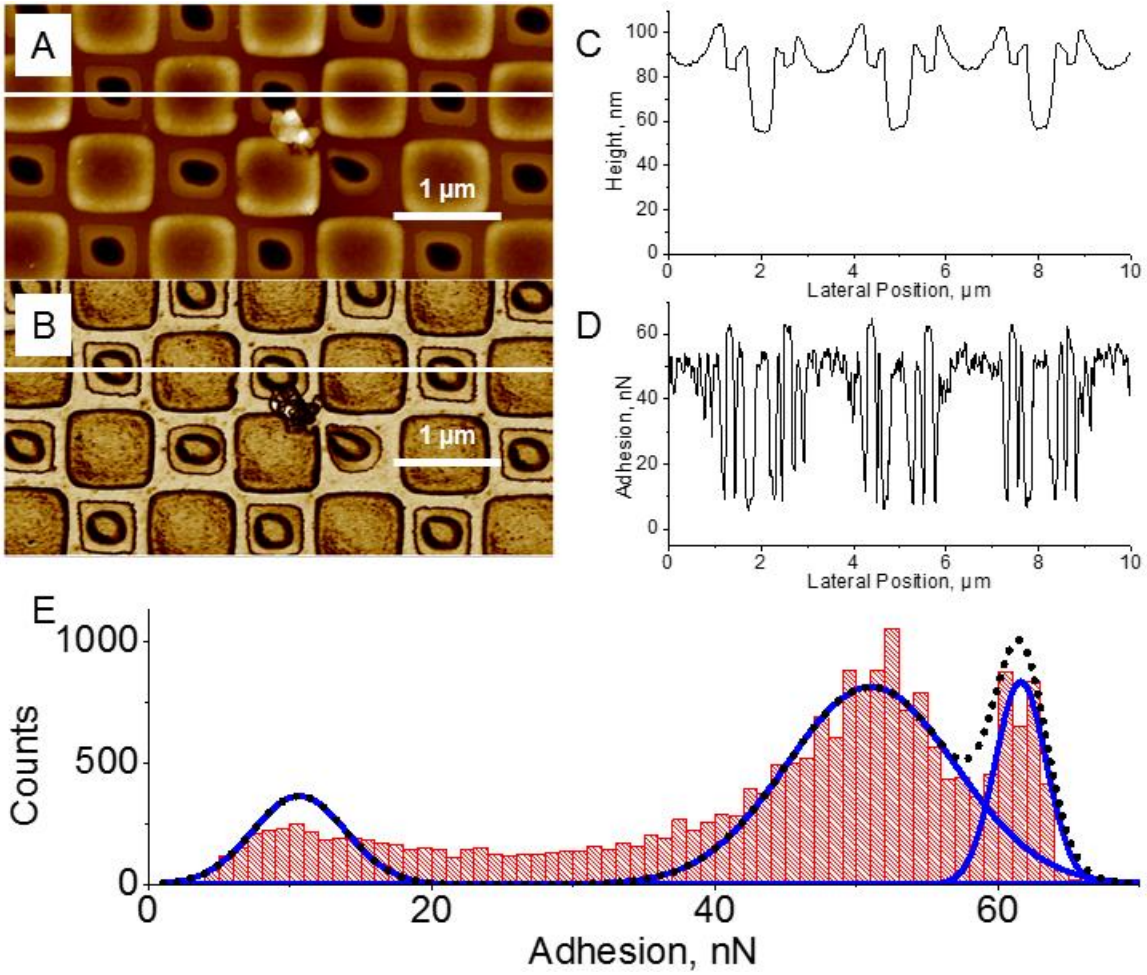

Figure 1.8: C16 cast from HFIP patterned with a square lattice. (A) Topography, (B) adhesion map, Representative cross-sections: height (C), adhesion (D). Histogram depicting the distribution of adhesion (E) overlaid with Gaussian fits. Z scales: 70 nm, 75 nN.

1.3 Viscoelastic properties measurements using AFM

As discussed above, it is well known that soft materials commonly exhibit time- and temperature-dependent mechanical properties. It is impossible to completely avoid viscoelastic contributions in polymeric and biological materials, especially in the vicinity of glass transition, where material properties become highly deformation rate and temperature dependent. Several approaches for the measurements of time-dependent viscoelastic properties of polymeric materials which use AFM-based routines are discussed below.

1.3.1 Static creep testing. The first approach is based on the direct measurements of polymer relaxation behavior in addition to the material compliance with traditional creep measurements.[60] A representative creep experiment for a viscoelastic material and corresponding deformational models are shown in Fig. 1.9.[61] During the creep experiment, at time t_0, the AFM tip is indented into the sample with force F_0 to the pre-determined depth δ_0. The force applied to the tip is then kept constant and additional, slow time-dependent tip penetration into the surface is continuously monitored. At time t', the force acting on the AFM tip is lifted and gradual recovery is monitored until equilibrium is reached at the final penetration depth, δ_f. Because plastic deformation occurs during the creep experiments, initial material deformation is not fully recovered (residual strains) and $\delta_f \neq \delta_0$ (Fig. 1.5).[62]

Collected creep data is typically analyzed using a two-element (spring (elastic) and dashpot (viscous)) Maxwell and Voigt models. However these simple models cannot describe comprehensively viscoelastic materials, since the Voigt model does not describe initial steep indentation, while the Maxwell model does not provide means for accounting strain recovery.[62]

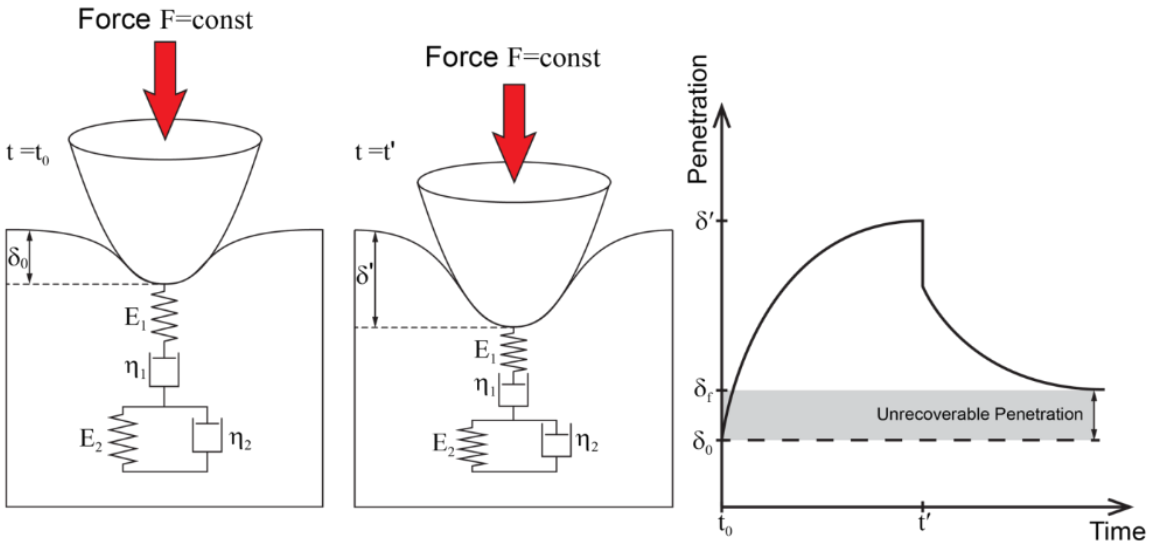

Figure 1.9: Creep experiment for the material as analyzed by a four element model and resulting penetration vs time curve.[26]

In order to reduce the piezoelement creep over the large time period of loading and improve signal to noise ratio, large indentations (hundreds of nanometers and even larger) are usually performed.[63] Unfortunately, these experimental conditions usually result in severe and unrecoverable plastic deformations. Therefore a four element model which can account for both the initial elastic response as well as unrecoverable deformations must be selected for the analysis of such experiments (Fig. 1.9). Using this model, viscoelastic components can be calculated from the experimental data using the equations:[64]

$$\delta^{3/2} = \frac{3}{4}\frac{F_0}{\sqrt{R}}\left[\frac{(1-\upsilon^2)}{E_1} + \frac{(1-\upsilon^2)}{E_1}\left(1 - e^{-tE_2/\eta_2(1-\upsilon^2)}\right) + \frac{1}{\eta_1}t\right] \quad (1.5)$$

$$\delta^{2} = \frac{\pi}{2}\frac{F_0}{\tan(\alpha)}\left[\frac{(1-\upsilon^2)}{E_1} + \frac{(1-\upsilon^2)}{E_1}\left(1 - e^{-tE_2/\eta_2(1-\upsilon^2)}\right) + \frac{1}{\eta_1}t\right] \quad (1.6)$$

which are valid for spherical and conical tip shapes, respectively.

Creep data collection possesses several challenges when performed on usual AFM devices. The initial steep increase in the surface deformation should be instantaneous, but it is in fact a ramp motion produced by the piezoelement. If the rate of this deformation is on the order of the relaxation time, material relaxation will occur during the initial engagement and, thus, will not be completely accounted for. The time-scale of this process is usually small in comparison with the full creep experiment time. However, since the experimental data is analyzed in the logarithmic timescale, the artificial deviations in calculated parameters can be significant.[61] Another challenge is related to maintaining constant tip deflection during the loading portion of the creep curve. Constant tip deflections can be achieved by the incorporation of a feedback algorithm, which monitors the tip deflection and moves the piezoelement accordingly. Unfortunately, the piezoelement creep over large timescales contributes to significant and unaccounted-for displacements, which cannot be easily controlled.[65] In addition, long experimental times make mapping of the viscoelastic properties mapping over large surface areas with even modest spatial resolution impractical. Therefore, such measurements are usually conducted for a single point with unknown topographical contributions and representation, which is especially critical for biological objects like cells and multiphase materials with complex morphologies.[65]

1.3.2 Contact resonance force microscopy. Another commonly used method for viscoelastic measurements is called Contact Resonance Force Microscopy (CRFM) that involves dynamic phase-shift measurements.[66] A vibrating AFM tip is brought into the mechanical contact with the surface and the amplitude damping and phase shift of tip vibrations are recorded (Fig. 1.10). Next, the recorded values of phase lag are analyzed by using a damped oscillator model for the tip-sample contact.[67] In order to precisely calculate the mechanical properties of a material, in addition to the tip-sample interactions a cantilever's flexural vibration mode should be considered.[68] There are several mechanical models, which describe damped cantilever vibrations, however, each of these models

contain a substantial number of unknown parameters which are difficult to quantify.[67] Instead of a parametric model description, vibrational amplitudes are usually measured relative to the "free" cantilever vibration in CRFM experiments.[69]

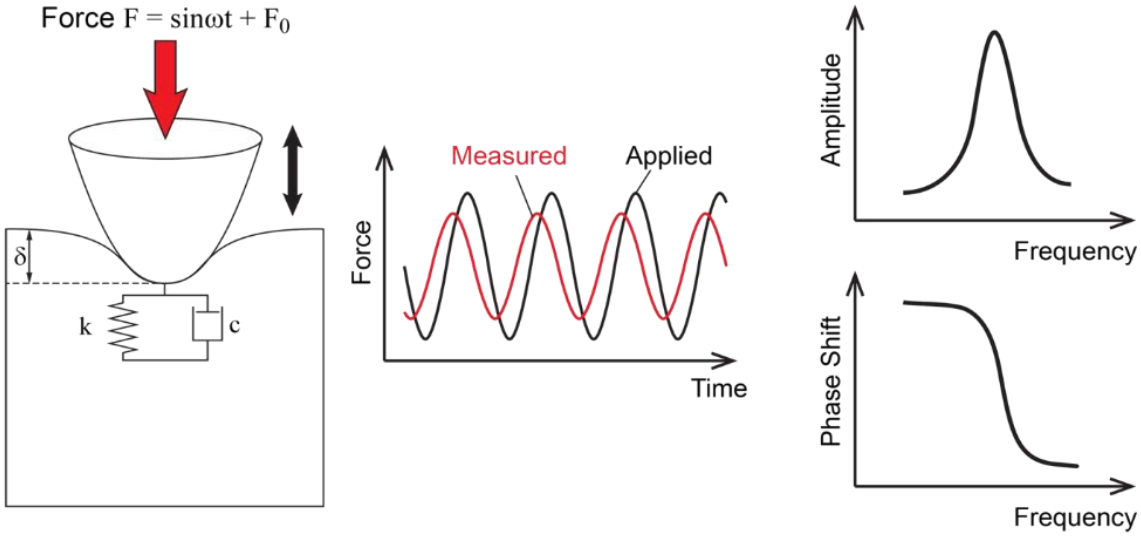

Figure 1.10: Contact force resonance measurements with dynamic indentation amplitude and phase shift plots.

In addition to the unknown tip-sample contact parameters, tip shapes are not measured directly but are indirectly determined from a reference material, which involves possible additional uncertainties.[70] CRFM is typically utilized for surface mapping with contrast caused by the difference in relative mechanical properties of the surface areas.[71] Mechanical properties of these different regions need to be relatively close in order to apply this method. An additional challenge is the inability to probe at frequencies lower than the kHz-MHz range due to resonance properties of cantilevers, which are several orders of magnitude higher than any practical frequency range used for the traditional testing of polymeric or biological materials. Moreover, even the extrapolation of mechanical values obtained with these dynamic measurements to a practical frequency range (which can be theoretically conducted with master curve construction) can become highly ambiguous due

to very limited probing frequencies (usually limited by cantilever resonance modes).

These measurements are performed at a single oscillation frequency with a fixed amplitude, and generally provide only qualitative contrast information, which can be important for mapping of composite surfaces. Therefore comparative mapping of relative surface properties with high spatial resolution can be considered as an important applicability niche for this mode of operation. To get quantitative mechanical data, more complex approaches which involve force modulation and multifrequency measurements must be employed.[72,73]

1.3.3 Multifrequency AFM. From the beginning of the development of tapping mode AFM it was noted that the phase shift of the vibrations in the amplitude modulation setup can be related to the energy loss by the cantilever through the dissipative processes in the tip-sample contact.[74] As it was discussed above, tapping mode cannot provide quantitative modulus measurements due to the complicated tip-sample interactions. To enable calculation of the elastic properties it was suggested to excite the cantilever at additional flexural modes.[75] It was shown that if the second mode is excited at much lower amplitude than the main tip vibrations, the tip interactions with the sample are strongly repulsive, which facilitates elastic properties estimations.

In bimodal AFM two flexural modes of the tip vibrations are excited at their resonant frequencies. It is important to note that both vibrations are excited and controlled by two separate feedback loops Fig. 1.7.[76] In this setup, lower frequency vibrations are performed in the amplitude modulation mode at amplitude, A_1, while the lower amplitude, A_2, additional vibrations are performed in frequency modulation mode (AM-FM configuration).[77] In this setup it is possible to extract simultaneously four parameters of both modes simultaneously: frequency shift and amplitude for both vibrations, which can be denoted as Δf_1, Δf_2, F_1, and F_2. In this case mechanical parameters of the tip-sample

contact such as reduced elastic modulus E, viscosity η and penetration δ can be calculated as:[78]

$$E = \sqrt{\frac{8}{RA_1}} \frac{k_2^2}{k_1} \frac{f_1}{f_2^2} \frac{\Delta f_2^2}{\Delta f_1} \tag{1.7}$$

$$\eta = \sqrt{\frac{2}{\pi^2 R A_1}} \frac{k_2^2}{Q_1 k_1} \frac{1}{f_2^2} \frac{\Delta f_2^2 (\Delta F_1 f_1 - \Delta f_1 F_1)}{\Delta f_1^2 F_1} \tag{1.8}$$

$$\delta = A_1 \frac{k_1 f_2}{k_2 f_1} \frac{\Delta f_1}{\Delta f_2} \tag{1.9}$$

where k_1 and k_2 are the effective spring constants of the vibration modes, Q_1 is the quality factor of larger amplitude vibrations, and R is the tip radius. This method therefore allows one to directly relate stiffness of the material to the frequency shifts of the second low amplitude mode in contrast to the simple tapping mode.[76] At the same time this method provides a way to quickly and reliably map viscoelastic properties polymer surfaces.

For example Herruzo et al. showed the possibility of reliable viscosity and modulus mapping with bimodal AFM, observing granular structures within PS in PS-b-PBMA blend samples with domain sizes as low as 10 nm and 17 nm.[78] The method has a great span of measured elastic moduli, for example it was used for mapping mechanical properties of proteins and the surface of mica, where the mapped modulus values span more than 3 orders of magnitude.[79] There exist more elaborated methods of multifrequency measurements, where more than two flexural modes of the cantilever are used simultaneously. For example Ebeling et al. used three eigenmodes to study the possibility of sub surface imaging.[80] Figure 8 shows how increases in the amplitude of the third eigenmode allows for imaging structures buried tens of nanometers under the surface with

high lateral resolution.

Multifrequency AFM methods utilize simplified tip-sample interaction models and are more instrumentally demanding than any other AFM techniques, however due to its wide applicability for wide range of materials in different environments (ultrahigh vacuum, air and liquid) it is currently emerging in variety of fields from soft materials characterization to sub-surface imaging.[81]

Overall, further developments are required to fully utilize the capability of AFM operation for continuous, high-resolution, and non-destructive monitoring of the viscoelastic behavior of compliant materials. The work outlined later in this thesis demonstrates that reliable probing of mechanical properties can be conducted in a wide range of relevant temperatures and frequencies with dramatically reduced capillary forces in order to determine the viscoelastic response of the sample surface without common distortions caused by plastic deformation, adhesive forces, supporting substrates, or high probing rates, in a wide range of frequencies, and with sufficient statistics. Such measurements can be practically done using conventional AFM setups without additional software or hardware, which is often overbearingly expensive and impractical.

1.5 Biological background: Cupiennius salei

The versatility of AFM lends itself to characterization of living biological samples for excellent, quantitative characterization of a variety of materials properties. For example, the infrared receptors of a ball python were investigated using AFM.[82] Both the thermal conductivity and the elastic modulus taken directly on the pit organ allowed for the authors to suggest the design of artificial photothermal dececters. In another example, the mechanical properties of flow sensitive fish cupulae were examined in a fluid environment,[83] which resulted in the design of a hydrogel-encapsulated MEMS haircell

flow sensor. Despite the inherent difficulty associated with making nanometer-sensitive measurements on living organisms, these two examples above highlight the quality information which can be obtained using direct in-vivo measurements on sensory organs.

Nature provides numerous examples of model mechanosensory systems exhibiting extraordinary versatility, functionality, sensitivity. Such systems are indispensable for an organism to receive, interpret, and respond to environmental stimuli.[84,85,86,87] In this respect, spiders possess well developed mechanosensory systems and heavily rely on their ability to detect biologically relevant vibratory signals when hunting and courting.[84,88,89,90,91,92,93,94,95]

Such mechanosensory systems can serve as a fundamental basis for the design of engineered strain sensors with a high degree of functionality and tenability. However, there is little known about these systems on a fundamental materials level. Because it is possible to measure mechanical properties of materials in a non-destructive manner in a variety of environments, it can be applied to *directly* study the fundamental viscoelastic mechanical properties of these mechano-sensing organs on ***living*** organisms.

A Central American wandering spider, *Cupiennius salei*, is one of the many arthropods utilized over the years as a model set of natural sensing systems to draw fundamental knowledge from in order to apply to engineered sensing systems. Practically this is due to its large size and ease in handling and breeding in a laboratory setting (Fig. 1.11), as well as for their incredibly fine-tuned mechanosensing systems discussed below.[84,96]

Figure 1.11: Adult female wandering spider, Cupiennius salei (Keyserling, 1877).

There are generally two means employed by *Cupiennius* to detect external mechanical stimuli (both of which will be discussed below), the first of which are sensitive hairs which can be divided into two classes – touch-sensitive tactile hairs and extremely sensitive air flow sensing trichobothria.[84,91,93,97,98] In contrast to the mechanosensitive hairs, *Cupiennius* is also equipped with thousands of innervated slits embedded in the stiff exoskeleton which are responsive to minute strains in the exoskeleton caused by locomotion, changes in haemolymph pressures, and substrate vibrations amongst others.[84,97,99,100]

A plethora of research to date on the mechanosensory organs of *Cupiennius* has been focused on the nervous response of the systems.[85,86] However, as it becomes more apparent that the majority of sensory filtering occurs in the periphery (especially in the case of less-complex arthropods), more emphasis is being put on understanding the relationship between the function of naturally occurring biomaterials and their structure, composition and properties.[85,86] Focus on the biomechanics of the mechanosensors of *Cupiennius* will give insight into fundamental materials properties of biological mechanosensing systems

and can be used as the basis for the design of engineered mechanosensing and actuating devices.

1.5.1 Mechanosensitive hairs. Tactile hairs represent the majority of mechanosensing hairs covering the body of *Cupiennius*, typically measuring ~20 μm in diameter at their base and tapering along their nearly 2.5 mm length (Fig. 1.12A).[86,101,102] During their lifetime, tactile hairs contact surfaces thousands of times at speeds on the order of 11 cm/s.[101] Contact forces cause the hair to deflect, resulting in strains in the structures (suspension) which couple the hair to the exoskeleton. These strains result in action potentials which give the spider information about the occurrence and velocity of exteroreceptive (between spider and external structures) and proprioreceptive (between neighboring body parts) contact.[86,101] For tactile hairs, the elastic restoring force, S, at the hair suspension was determined to be on the order of 10^{-8} Nm/rad (the hair suspension here was modeled using a two element sping and dashpot model, See Fig. 1.13 as an example), and results in the hair not only deflecting, but also bending under stimulating forces.[101] As a result the point of load to shifts towards the base of the hair with increasing loading forces.[86] Therefore the bending moments only reach approximately 20% of what is expected for a rigid rod, leading to a robust structure which can be loaded and unloaded frequently without breaking.[102]

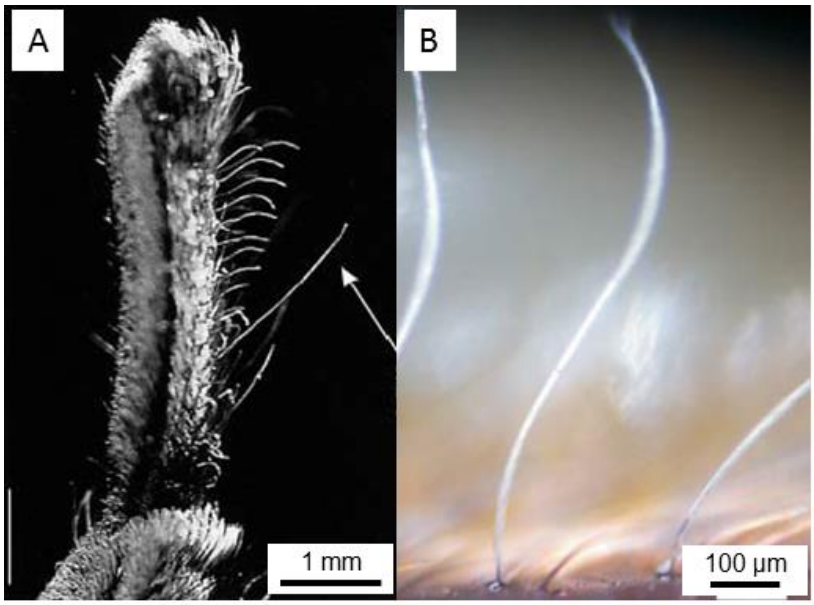

Figure 1.12: (A) SEM image of the tarsus (very last joint of the leg) on *Cupiennius* with arrow pointing to tacile hair. Smaller s-shaped hairs seen here are trichobothria. (B) Optical image of several trichobothria on the tarsus of *Cupiennius*. (C) Optical image of a representative example of a group of slit sensors embedded in the exoskeleton. This particular group is found on the tibia.[84,93]

In contrast to the tactile hairs, the tiny mass (10^{-9} g) of trichobothria in combination with their soft articulation results in the extraordinary capability of absorbing the energy of air flow with outstanding efficiency, elucidating the presence and location of nearby prey and predators (Fig. 1.12B).[91,93,94] Early studies used physical-mathematical models to describe the hair's mechanical behavior for oscillating hair flows in the biologically relevant frequency range between 10 and 950 Hz.[93,103,104] Calculations predicted the elastic restoring force at the suspension of the trichobothria are extremely low on the order of 10^{-12} N, around four orders of magnitude lower than those of the tactile hairs.[103,104] As a result the minimum mechanical energy required to elicit a nervous response was determined to be 10^{-20} J, making trichbothria among the most sensitive biological receptors.[93,105]

Direct measurement of the micromechanical behavior of trichobothria under point forces applied by AFM revealed complex, nonlinear loading curves (Fig. 1.13, Figure 1.14).[93] Hair deflection is essentially linear up to 100 nN, but becomes increasingly erratic as the hair contacts the socket and begins bending. For deflections larger than 7500 nm, the force required to deflect the hair increases sharply, indicating a change in mechanical behavior during bending of the hair. The bending stiffness of a representative hair (950 µm in length) was determined to be 0.18 N/m at a distance of 43.8 µm from the hair suspension membrane.[93] Modeling the membrane as a two parameter Kelvin solid (high angular deflection rates) and a three parameter linear solid (low angular deflection rates) resulted in elastic restoring forces of 2.9×10^{-11} Nm/rad, and 3.9×10^{-11} Nm/rad, respectively, suggesting that the viscoelastic nature of the hair suspension work to promote the phasic response of the trichobothria sensilla.[93]

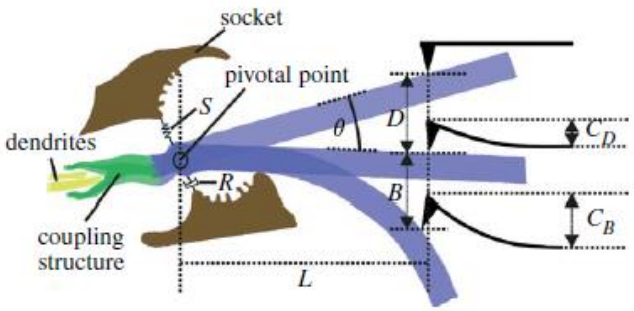

Figure 1.13: Schematic showing hair bending under an applied load (in this case an AFM tip pushing on the hair). Bending of the hair elicits an action potential. The minimum energy required to do so is determined by the viscoelastic properties of the hair suspension (elastic restoring force S, and dynamic viscosity R).[93]

These modeling experiments as well as the AFM point loading experiments described above focus on the biomechanics of the mechanosensing hair as a whole structure. There is still much work needed to determine the mechanical characteristics of each individual component of the hair sensing system. This is especially so in the case of the hair

suspension membrane, which essentially controls the overall sensitivity of the hair to mechanical stimuli.

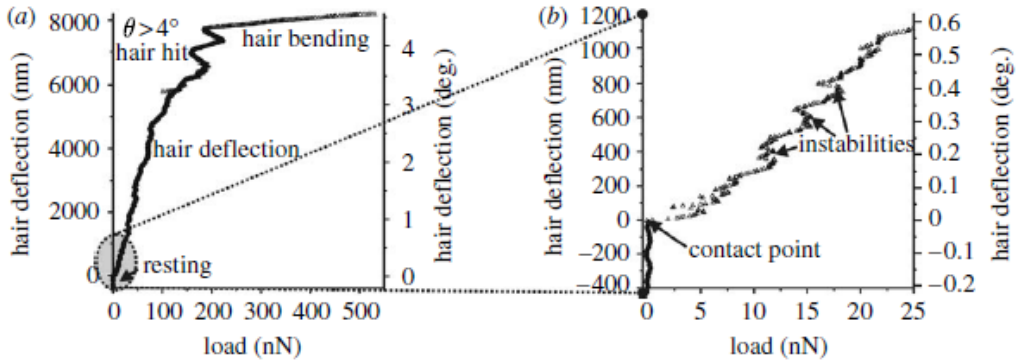

Figure 1.14: (a) Loading curve produced by an AFM tip pushing on a thrichobothrium with high forces. The deflection is linear during the initial loading while the hair is pivoting in the socket. When the hair contacts the socket (> 7000 nm deflection) the slope of the curve changes, indicating extremely high forces to cause further bending of the hair shaft (b) Zoomed in region of the initial loading showing the contact point with the hair and instabilities caused by the microstructure of the hair surface.[93]

1.5.2 Slit Sensilla

1.5.2.1 Slit Sensilla Stucture. The exoskeleton of Cupiennius has nearly 3300 strain sensing slits embedded in it, with a majority on the legs and pedipalps (appendages on the prosoma).[84,99,106] The slits are holes in the exocuticle which are generally 1-2 µm wide and anywhere from 8 µm to 200 µm long (Fig. 1.15). Figure 1.16 contains a diagram of a cross-section of a slit sensor. Connecting the two sides of the slits is a trough-shaped membrane (outer membrane) approximately 250 nm thick composed primarily of epicuticular material. Coupled to the membrane somewhere in the middle (typically centered in the middle of the width, but not necessarily in the middle of the length) is a dendrite which leads to a sensory cell located in the mesocuticle. Filling the slit is viscous, sodium-rich receptor lymph.[107] An inner membrane, composed of fibrous material, sits at the bottom of the slit. A second, smaller dendrite ends just below the inner membrane, however, the function of this dendrite is still largely unknown.[84,106]

Figure 1.15: A compound group of slit sensilla forming the lyriform organ HS-9

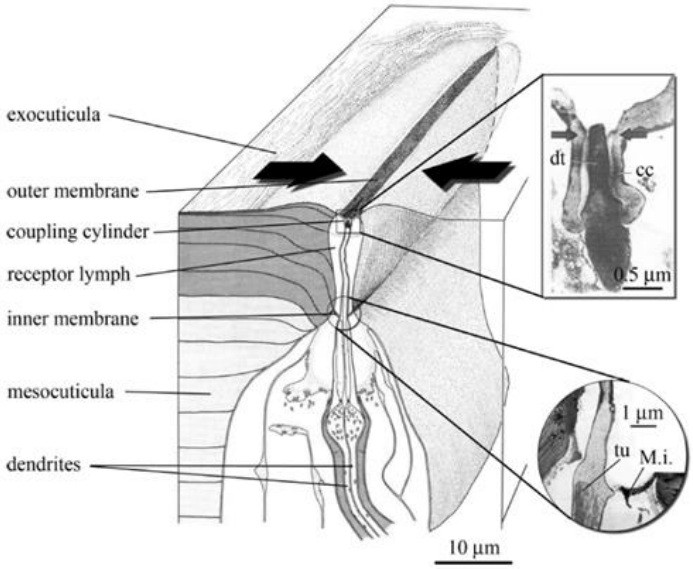

Figure 1.16: Schematic of a slit sensory organ. The slits penetrate the entirety of the stiff exocuticle. Insets show optical images of the outer membrane with the coupling cylinder (cc) and dendrite (dt) (top), and the inner membrane (M.i).[84]

1.5.2.2 Slit Sensilla Function. The fundamental function of the slits found on Cupiennius is to detect minute strains in the exoskeleton caused by muscle activity, changes in haemolymph pressure, or external loads due to substrate vibrations, for example.[84,88,108] Compression of the slit causes the outer membrane to bend and increase its curvature. As

a result, the dendrite, which is intimately coupled to the outer membrane via a coupling cylinder, becomes deformed in a direction perpendicular to the long axis of the slit causing an action potential (Fig. 1.17).[84] The slits are capable of sensing strains on the order of several nanometers.[88] It is important to note that studies by Barth have shown that only compressive forces stimulate a nervous response from the dendrite.[109,110] Therefore the slit's location and orientation on the leg determine which strains it is able to detect.[108,111]

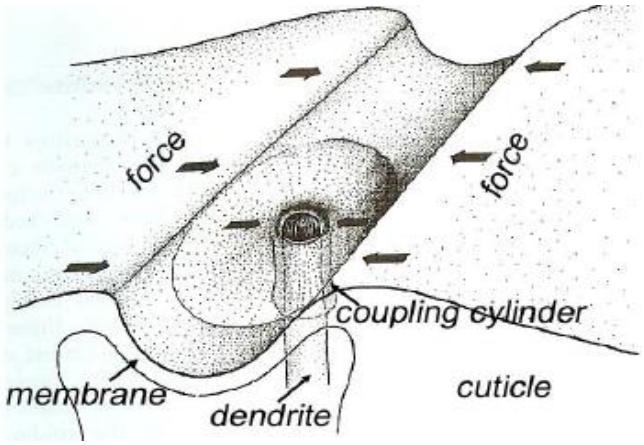

Figure 1.17: Schematic depicting the force transformation into action potential. Compression of the slits results in an increase in the bending moment of the outer membrane, which causes the compression of the dendrite.[84]

Slits sensors can be grouped according to their arrangement with respect to surrounding: isolated single slits (nearest neighbor distance greater than 1.5 times the slit length), loose grouping contain several slits (NN > 0.25 SL), and composite or lyriform (so-called because of their resemblance to the lyre) organs containing up to 30 closely packed slits, which are separated by less than 10 μm (Fig. 1.18).[110,111,112] Transmission of compressive forces to the dendrite is a rather straight-forward process in the case of isolated single slits, as the applied force and the angle with respect to the long axis of the slit determine the total amount deformation which occurs.[108,111] The maximum deformation in isolated slits always occurs in the longitudinal center of the slit.[84]

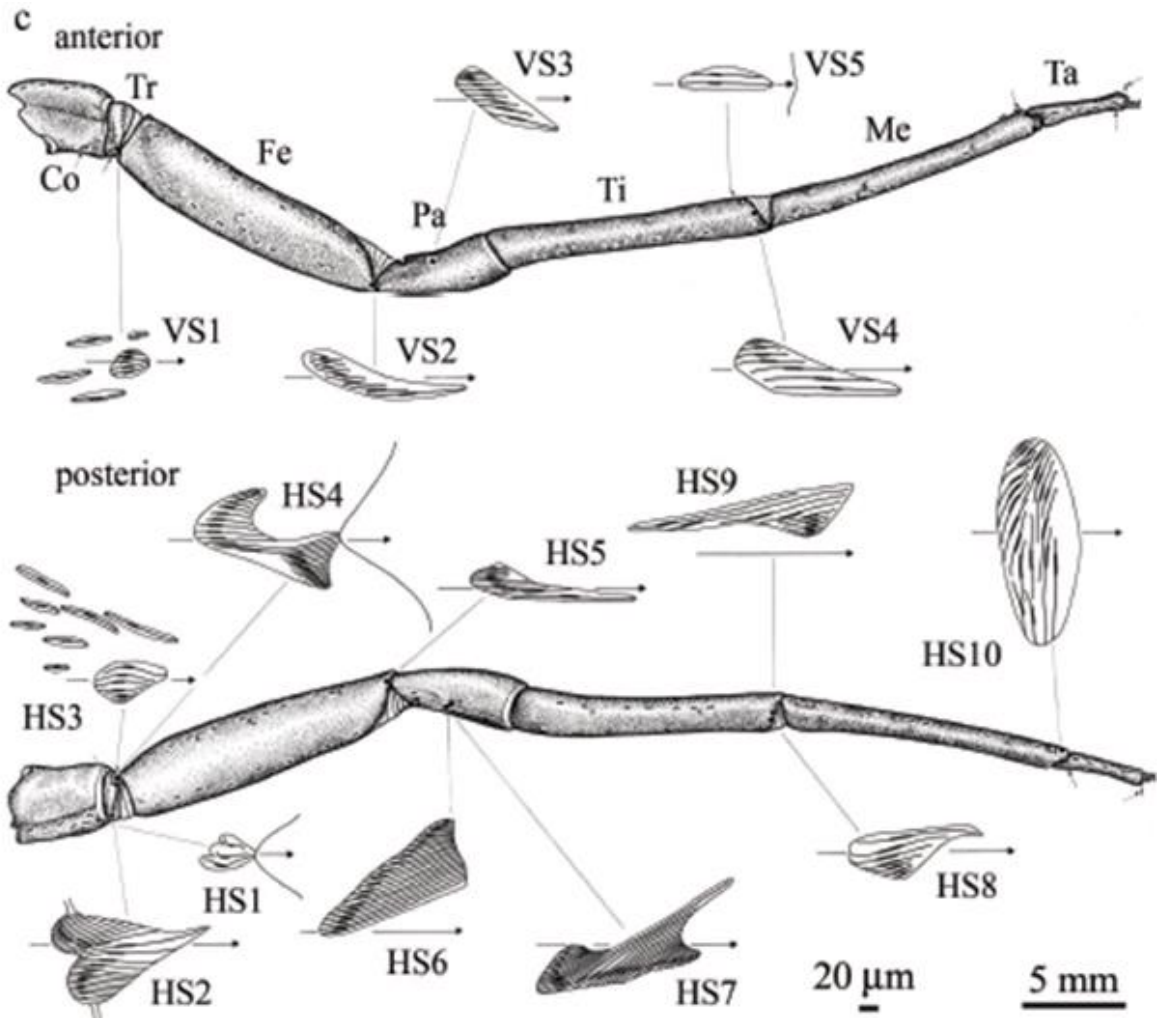

Figure 1.18: Schematic depicting the various lyriform organs and the slit orientations located on the walking legs of Cupiennius. Top: anterior half of the leg (Vorderseite (front side), "VS"). Bottom: posterior side of the leg (Hinterseite (back side), "HS"). 5 mm scale bar refers to the scale of the leg while the 20 µm scale bar refers to the enlarged lyriform organ depictions.[100]

On the other hand, the strain fields surrounding the tightly packed slits of lyriform organs interact with each other causing the location of the maximum deformation of the slit to deviate from the longitudinal center.[84,113,114] This effect was first modeled by Barth et al.[108,109,115] by monitoring the compression of a series of parallel slits cut into 6 mm thick

poly(methyl methacrylate) disks caused by static forces applied at various angles. Later, more complex slit shapes and arrangements were modeled and studied under similar conditions using finite element methods.[110,116]

Figure 1.19 shows example slit arrangements used in the model studies of the compression of spider slit sensors. The first predominant effect observed by closely spaced slits is shielding which results in the outer slits being compressed far more than inner slits.[108,110]

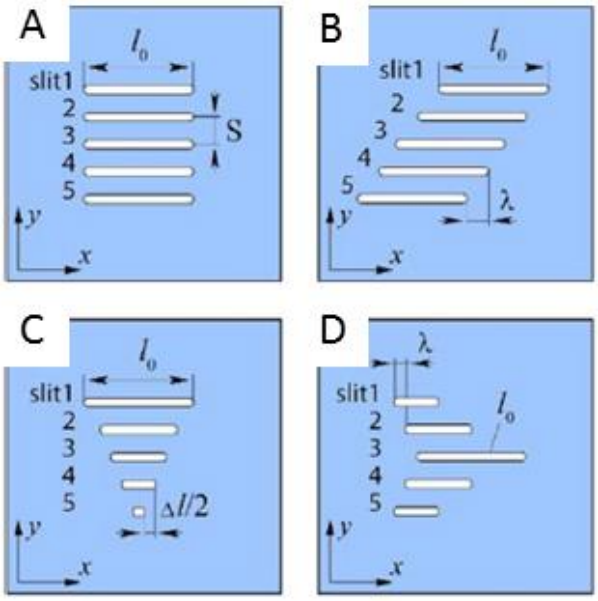

Figure 1.19: Slit arrangements used in the first model studies of slit deformation and later in FEA studies. (A) parallel, unshifted slits. (B) oblique bar. (C) triangular arrangement. (D) heart arrangement.[110]

Variations in length distribution and lateral shifts of the model slits were also found to have profound effects on their deformation behavior. In the case of the oblique bar arrangement, compressive behavior is similar for all slits and is observed over a wide range of loading angles (> 120° range), suggesting this arrangement is optimal for conditions in which a large angular working range is required.[110,111] The deformability of a triangular

arrangement of slits varies with the smaller slits being less deformed at all load angles, possibly allowing for a large spectrum of absolute sensitivities.[110,111]

More complex arrangements involving a combination of lateral shifts, length distributions, and curvature in the slits results in complex deformational behavior which can be modeled using finite element methods to determine the sensitivity of the slits to uniaxial loads applied at all angles.[117] Figure 1.20A shows an FE model slit arrangement which mimics the VS-4 organ located on the anterior side of the tibial joint of the walking leg of Cupiennius.[99,116] From this one can see that the slits are most sensitive to uniaxial loads acting at load angles between 60° and 105° (Figure 1.20D). Example deformation levels of each slit (w.r.t. a single, isolated slit) for loading angles of 90° and 60° (Fig. 1.20B,C), showing a strong increase in the deformation levels in slit 2 near the dendrite (red dot).[116]

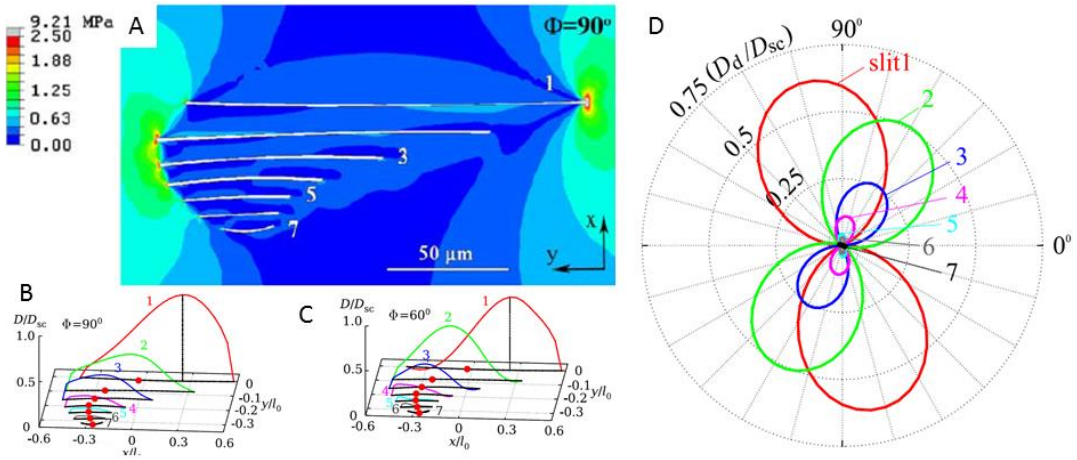

Figure 1.20: (A) FE model depicting the von Mises equivalent stresses in the lyriform organ VS-4 under a 90° load. Deformation along the length of the slits for loads applied at (B) 90° and (C) 60°. (D) Directional mechanical sensitivity of the slits under uniaxial far field loads.[116]

1.5.2.3 Vibration Filtration. Cupiennius relies heavily on its ability to detect biologically relevant vibratory signals in environments in which low frequency background noise is ever-present.[118,119,120,121] The organ responsible for the spider's highly developed vibration

sensitivity is composed of 21 strain-sensitive innervated slits embedded in the cuticular exoskeleton (rough location with respect to the spider as a whole shown in Fig. 1.21).[84,122,123]

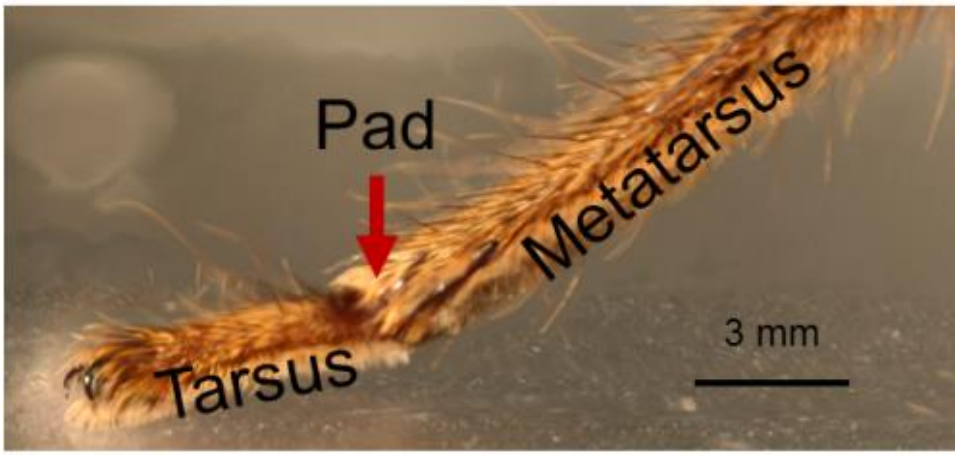

Figure 1.21: Close up image of a leg of *Cupiennius* depicting the approximate location of the metatarsal lyriform organ (red arrow).

The vibration sensitive lyriform organ is found at the distal end of the metatarsus (the second last segment of the leg) in the middle of each leg's dorsal surface (see Fig. 1.21, location is highlighted by arrow in Fig. 1.22A; arrows in Fig. 1.22B point to several of the organ's slits; Fig. 1.22C shows proximal view of the organ).[84,92,122] The slits of the metatarsal lyriform organ are oriented perpendicular to the long axis of the leg, bridging a deep furrow in the metatarsus (Fig. 1.22C), which increases the organ's sensitivity to strains in the exoskeleton.[84] External mechanical stimulating strains occur as the tarsus is deflected upwards and presses against the metatarsus as a result of substrate vibrations (Fig. 1.22A).[88,124]

Along with its extreme sensitivity to substrate vibrations, the metatarsal lyriform organ is also known to behave as a high-pass vibration filter, as suggested by electrophysiological experiments which generated tuning curves for the organ.[88] The threshold deflections

required to elicit a nervous response from the sensory cells innervating the slits are on the order of 10^{-5} to 10^{-4} m for external mechanical frequencies ranging between 0.1 and 40 Hz, while deflections can be as small as 10^{-9} to 10^{-8} m are sufficient for frequencies above 40 Hz (Fig. 1.23).

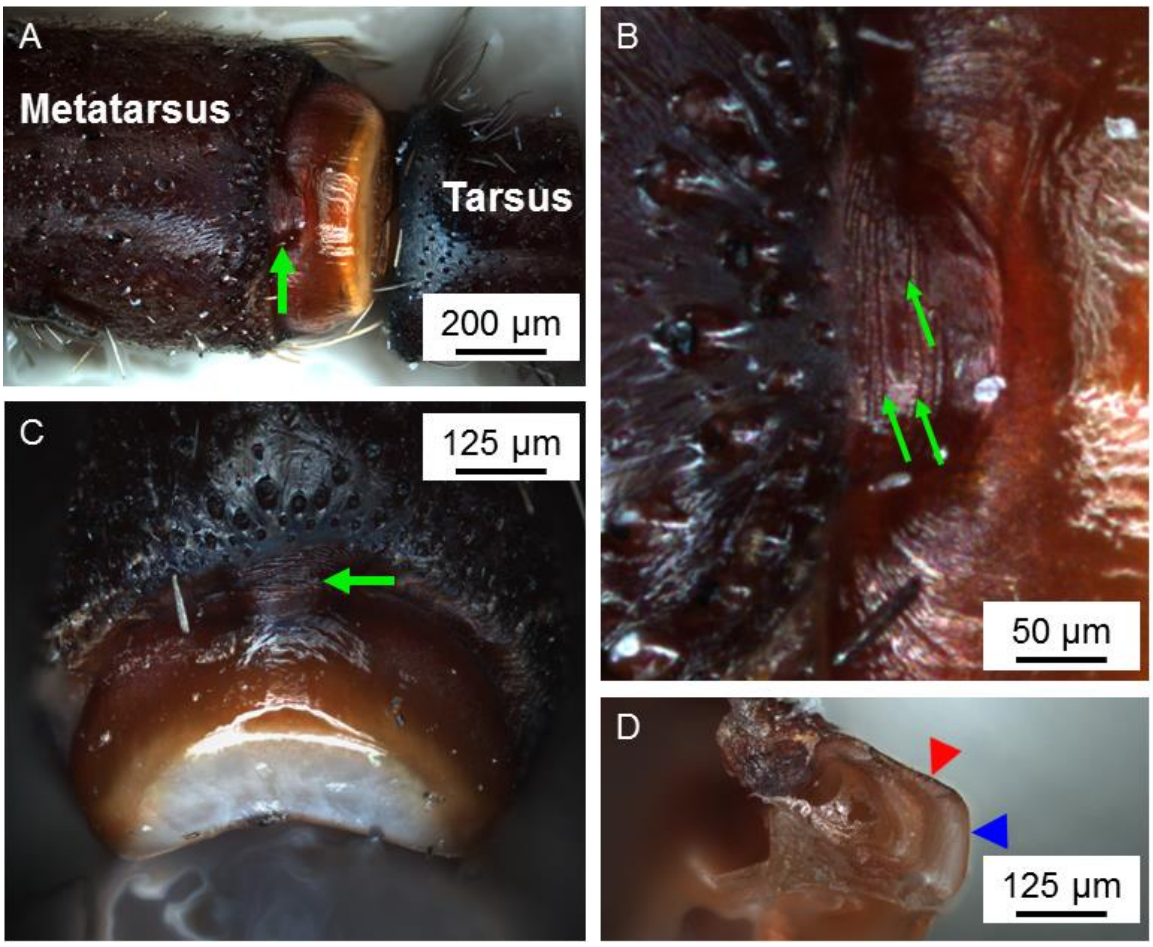

Figure 1.22: (A) Optical image of the pad with surrounding hairs removed for better viewing, with an arrow marking the location of the metatarsal lyriform organ. (B) Metatarsal lyriform organ with arrows marking the location of several slits. (C) View of the pad from the distal side (point of contact), viewing direction towards metatarsus. (D) Optical image of a pad longitudinal section with arrows demarking the "dorsal" (upper) and "distal" (left) surfaces referred to in the text.

As mentioned, the interpretation of environmental stimuli as useful information, however, is not a function of the nervous system alone.[84,85] Rather, the pre-filtering of external

stimuli for the fine tuning of sensory systems such as the spider's vibration sense is also a function of the materials properties of the organs themselves and of the surrounding cuticle in which they are embedded.[84,85] Representing one of the first studies directly measuring the biomechanical properties of the cuticle, McConney et al. found that one mechanism responsible for the high-pass behavior of the metatarsal vibration receptor is the viscoelastic behavior of the cuticular pad adjacent to the organ which is responsible for transmitting the stimulus from the tarsus to the metatarsus.[92]

Analyzing the viscoelastic mechanical response of the pad, McConney et al. used atomic force microscopy (AFM) to determine its elastic modulus at its surface as a function of loading frequency. The resultant curve showed a sharp increase of the elastic modulus from around 10-20 MPa at frequencies ranging from 0.1 to 10 Hz to larger than 70 MPa at measurement rates above 30 Hz (Fig. 1.19B). This finding mirrors the electrophysiologically determined tuning curves in a remarkably precise way. By applying the principle of time-temperature superposition and by using the Williams-Landel-Ferry (WLF)[125] equation with the universal polymer constants C_1= 17.44 and C_2 = 51.6, the glass transition temperature was estimated to be 25 ± 2 °C.

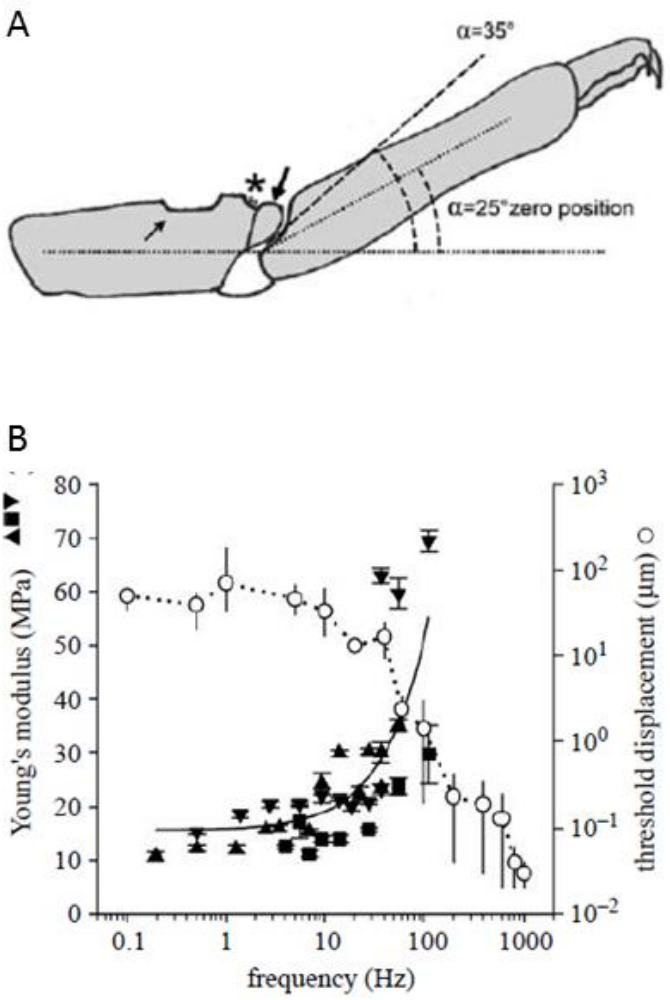

Figure 1.23: (A) Schematic depicting the upward deflection of the tarsus into the metatarsal pad (arrow) which causes compression of the HS-10 slits (*). (B) Tuning curve showing the minimum deflection of the tarsus required to elicit an action potential (open circles) superposed on a polt showing the modulus of the pad as a function of frequency.[92, 124]

1.5.3 Cuticle. The cuticle of arthropods not only serves as a means of protection, but also as an interface through which the external stimuli is received.[126,127,128] Macroscopically the cuticle of Cupiennius is arranged into distinct layers which include (working from the inside out) endocuticle, mesocuticle, exocuticle, and epicuticle (outermost exocuticle and epicuticle seen in Fig. 1.24B,C).[129,130] With the exception of the epicuticle, the cuticle of Cupiennius is a hierarchical composite composed primarily of highly oriented chitin fibers providing structural rigidity and load bearing ability embedded in an elastic protein

(presumably resilin) matrix serving to transfer load between fibers while adding flexibility and therefore toughness to the structure. [106,129]

The chitin fibers are arranged in sheets which run parallel to the cuticle surface. The interlamellar orientation has been studied extensively by Barth and is found to have five primary variations: (i) unidirectional, in which all lamellae have the same orientation; (ii) bidirectional, in which there is an abrupt change in orientation by 90° between zones of aligned lamellae; (iii) unidirectional zones alternating with zones of continuous rotation by 90°; (iv) unidirectional zones alternating with zones of continuous rotation by 180°; (v) continuously rotating Bouligand[126,131,132,133] structure (Fig. 1.24A). Of all variations, the exocuticle in which the mechanosensors of Cupiennius are embedded is dominated by continuously rotating lamellae.[130]

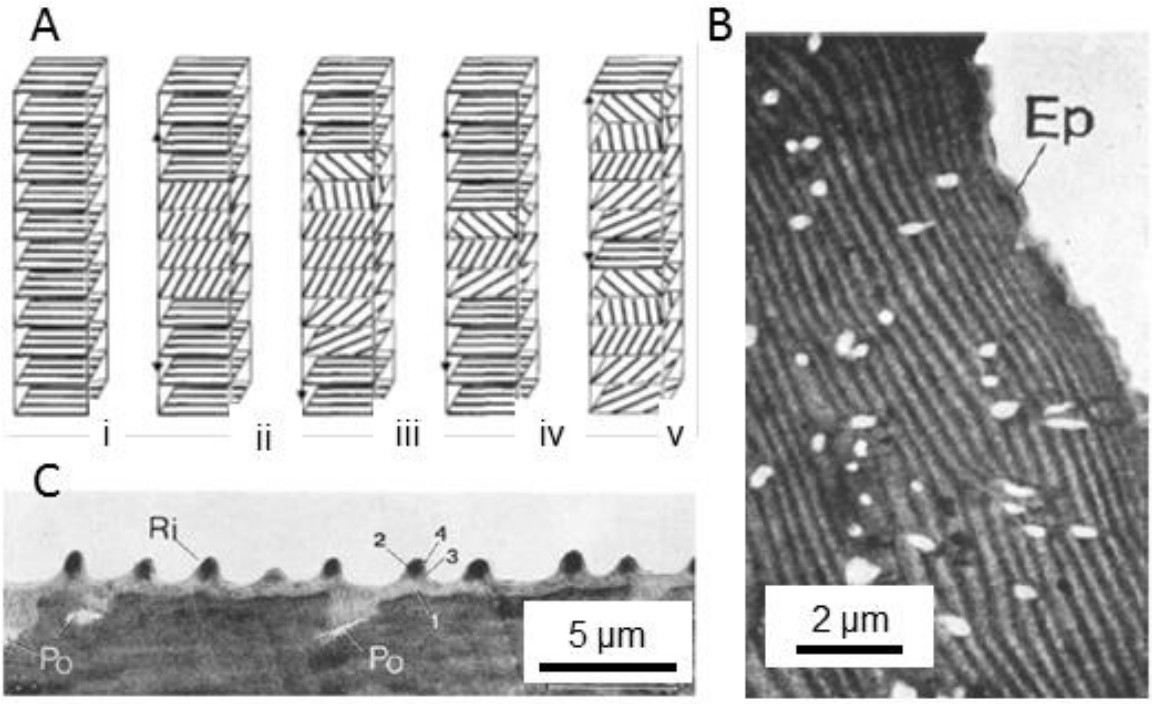

Figure 1.24: (A) Chitin fiber arrangements typically found in the cuticle of *Cupiennius* (i-v described in the text). (B) TEM image of showing the lamellar structure of the exocuticle in the tarsus. White dots seen here are pore canals (C) TEM image of a dorsal section of the metatarsus showing a chemically distinct (lighter gray) epicuticle layer.[129,130]

The composition of arthropod cuticle is highly limited, making the wide range of reported mechanical properties truly remarkable. The modulus of individual chitin fibers themselves have not been directly measured, but values ranging from 44 GPa to as high as 150 GPa have been reported.[134,135] Similarly, a wide variation in the modulus of the protein matrix has been reported from 1 kPa to 1 GPa. The modulus of the composite cuticle is governed by water content, chitin load fraction, and the degree of sclerotization (crosslinking). Typical values of the effective modulus of ranges depending on the structure and function of the cuticle. For example, the modulus of the abdominal cuticle of an assassin bug was found to be 60 MPa. Nearly three orders of magnitude higher, the tibial joint in the desert locust was found to have an elastic modulus ranging from 1.8-9.5 GPa.

1.6 Summary of critical issues and motivation

AFM based probing techniques are used extensively for the characterization of a wide variety of materials surfaces, and are well suited to determine the nano- and micro-scale mechanical properties of soft and polymeric materials. Unfortunately, data analysis routines, especially those included in standard analysis software available through AFM manufacturing companies, are often rudimentary. These typically treat the material as a linearly elastic solid, and provide only two possible contact geometries to use for analysis: spherical and conical. However viscoelasticity is a prominent behavior exhibited by soft materials composed of long chain macromolecules, which can cause dramatic shifts in the apparent stiffness of a material over a narrow temperature or strain rate range in the vicinity of the glass transition temperature. As a result, careful attention needs to be paid to these viscoelastic effects to avoid significant errors during characterization.

Currently there is limited AFM-based method to practically account for the time- and temperature dependent behavior of viscoelastic materials surfaces which is quantitative,

non-destructive, and can be performed in any environment. Methods such as static creep testing necessitate sample surface or tip damage during the measurement process. Furthermore the time required for each single measurement substantially reduces the practicality of mapping different regions of the sample surface. Dynamic methods such as CRFM and phase imaging are non-destructive and able to produce high resolution maps, however their data is often only qualitative. Quantitative extraction of materials properties from dynamic methods require cumbersome modeling and additional calibration procedures. Additional complexity with these dynamic methods involve the impractical frequency range (on the order of MHz) for many polymers, and cantilever damping wile measuring materials in fluid environments. *Therefore significant efforts were put forth in the work presented in this dissertation to create an experimental procedure and data analysis routine for practical characterization of viscoelastic synthetic and biological materials and structures.*

These methods for careful examination of the mechanical properties of soft, viscoelastic materials are directly applied to a range of interesting synthetic and biological materials. First and foremost, a well characterized polymer, poly(n-butyl methacrylate), is used as a control material to examine the validity of our probing methods. Next, the advantage that careful AFM measurements such as these have over standard mechanical properties measurement techniques is exploited to probe multiphase, silicone-based soft contact lenses, and explore the possible role viscoelasticity plays during practical use of such lenses. Finally, a main focus in this dissertation is determining the fundamental mechanical properties that contribute to the excellent sensitivity of the strain sensing organs in a wandering spider (Cupiennius salei). These extremely sensitive strain-sensing organs embedded in the exoskeleton are known to have a significant viscoelastic component. Thus the cuticle of living spiders is directly investigated in near-natural environments (high humidity). This exploration gives a better fundamental understanding of the key

mechanical properties that contribute to the functionality and sensitivity of the organs, and helps to paint a broader picture of how exactly the relevant temperature ranges which the spider experiences can affect the organs sensing abilities.

Mechanosensing in arachnids, in general and in spiders in particular, is well recognized for its high sensitivity and specificity.[84,85,98] The spiders' strain detectors, the so-called slit-sensilla, are elongated openings within the exoskeleton, innervated by sensory cells and often located in the vicinity of joints in the leg or elsewhere.[109,115,136,137] They are widespread among spiders and share some similarity to the campaniform strain sensors of insects. The metatarsal lyriform organ of the Central American wandering spider *Cupiennius salei* forms a close and roughly parallel array of 21 slits. It is the spider's main vibration detector.[88,138,139] It is responsible for sensing vibration signals originating from predators, prey, or courting partners with extraordinary sensitivity.[140,141]

To date, there have been few direct measurements to determine the mechanical properties of the cuticle of *Cupiennius.* Specifically, the tibia was estimated by Blickhan and Barth to have an in-plane modulus of approximately 18 GPa.[135] The cuticular pad discussed above was measured to have a dynamic modulus ranging from approximately 15 MPa to greater than 70 MPa depending on the loading conditions. In the most recent investigation of the biomechanics of the cuticle of *Cupiennius,* nanoindenation and scanning accoustic microscopy were used to determine the modulus of the fang, yeilding values of approximately 20 GPa nearest the tip.[142] *Therefore, a fundamental issue to be examined her is the direct measurement of the biomaterials properties of mechanosensors in* ***live spiders****, with a primary focus on the strain-sensing slits.* Through direct examination of the biomechanics of slit sensors (including time- and temperature-dependent effects) a more thorough understanding of the slit sensor time- and temperature-dependent deformational behavior can be obtained. Knowledge of this behavior will serve to enhance

our understanding of mechanical stimuli detection in compound lyriform organs from a fundamental materials perspective, and as a result serve as a foundation for the future bio-inspired design of functional, viscoelastic engineered mechanosensors.

CHAPTER 2

Research goals, objectives, and overview

2.1 Goals

The research outlined within this dissertation has two overall goals. The first, and farthest reaching to the broadest audiences, is to *develop practical, and quantitative AFM-based probing methods for investigating the viscoelastic mechanical properties of polymeric and biological surfaces*. Currently there are several AFM-based techniques available for characterization of viscoelastic mechanical properties of complex surfaces; however, each suffers from critical disadvantages (see Chapter 1). In the case of static creep measurements, these include with low spatial resolution, piezo-element drift-induced error, and necessary surface damage in the case of static creep measurements. Dynamic methods such as CRFM and multifrequency AFM provide means to map the viscoelastic properties of material surfaces with high resolution; however because of the complexity of these methods, specialized equipment is required. Furthermore, these methods often produce only qualitative results, with precise characterization of cantilever dynamics, additional calibration methods, and cumbersome modeling needed for quantitative calculations of mechanical properties using these methods. Finally, these dynamic methods often work at frequencies near, or higher than, the cantilever resonance frequencies which can be on the order of several hundreds of kHz to a few MHz – a regime often impractical for many viscoelastic polymeric and biomaterial surfaces. Therefore critical to the work presented herein is the use of readily available scanning modes as well as practical temperature ranges and loading rates, and the development of data analysis routines which enable the extraction of relevant viscoelastic parameters.

We use these methods to study the viscoelastic mechanical properties for a model viscoelastic polymer surface (PnBMA), which has a glass transition temperature near room

temperature. Furthermore, analysis considering appropriate geometrical conditions of tip-sample contact are outlined. In these cases we measured a variety of relevant materials such as silk fibroin ionomers, polystyrene, and soft hydrogels to investigate the errors in elastic modulus calculation induced by applying wrong tip-shape geometry equations. An underlying theme within this goal was also the *careful measurement of materials with complex geometries* ***under practical environmental conditions***. Here practical environmental conditions refers to scanning not only at ambient conditions, but also in fluid environments including biological saline solutions, through relevant temperature ranges, and using a wide range of loading rates. As mentioned, these measurements add significant difficulty to collecting reliable, useful data with AFM. However, it is vitally important to measure many sample in such environments because their properties may drastically change with temperature or dehydration. Additionally, measuring under fluid conditions inhibits capillary bridge formation, and facilitates collection of FDCs without large snap-in instabilities. As an example, we measure the surfaces and cross sections of silicone-based soft contact lens materials (highly curved surfaces which are incredibly difficult to see in fluid environment). In this case AFM has the unique ability to measure these samples in a relevant environment (submerged in saline solution). AFM was also able to measure nanometer-sized inclusions and micrometer-seized phase-separated regions, which traditional tensile testing cannot measure.

The second goal of this dissertation is to establish and refine AFM-probing methods to *probe* ***live spiders*** *in order to gain a deeper understanding of the fundamental materials properties which dictate mechanical signal detection, transmission, and signal filtration in their strain-sensitive slit sensilla organs*. The microscale viscoelastic mechanical properties of the cuticle making up the biological strain-sensing systems were explored and the findings were related to the function of those organs as sensitive and efficient transmitters of external mechanical stimuli, as well as their role in discerning dynamic

applied loads. We suggest that the mechanical properties of the cuticle measured here are key parameters for the time-dependent mechanical response during slit compression and the efficient transmittance, transformation, and filtering of external mechanical stimuli. Thus, the sensitivity and specificity of the slit sensors studied earlier with relation to their functional morphology, physiological response, and arrangement in a compound organ, were related to the biomaterial's mechanical properties as described in subsequent chapters. Such knowledge of the fundamental principles, *found from measurements on* ***living spiders***, in these natural mechanoreceptors can be exploited for the future design of functional mechano-responsive and adaptive nanostructured materials.

2.2 Objectives

In this comprehensive study, the overall goals described above will be accomplished through the following ***technical objectives:***

- *Development of an experimental procedure for scanning soft, viscoelastic surfaces in both ambient conditions and under relevant fluid environments (e.g. saline buffers), also including varying temperatures and loading rates. This procedure will be utilized for the practical and quantitative measurements of time- and temperature-dependent mechanical properties on soft material surfaces using widely available scanning probe microscopy equipment and scanning modes.*

- *Establish data analysis routines of such that the information collected in the form of FDCs can be manipulated to return useful viscoelastic parameters as functions of temperature and loading frequency, such as storage modulus, loss modulus, and tangent delta.*

- *Further experimental methods and data analysis will focus on ensuring appropriate scanning conditions, which are often challenging for AFM-based measurement setups, as well as selecting correct that tip-sample contact geometry models, which are critical to calculated results.*

- *Expansion of our data analysis capabilities via a custom-built software, "MicroMechanical Analysis of Soft Polymeric Materials (MMA-SPM)", specifically for analyzing FDCs with different contact mechanics models. Batch processing will be include to facilitate simultaneous calculations of many curves.*

- *Analysis of a model viscoelastic surface, PnBMA below, at, and above the glass transition temperature to validate our experimental and data analysis routines. Further analysis of complex surfaces including hydrogel materials and biopolymers to explore the different contact mechanics models and tip shape reconstruction functionalities of our home-built software.*

- *Testing these measurements on soft contact lenses, which are viscoelastic hydrogel materials with highly irregularly shape, in a saline solution simulating natural biofluids they encounter during use to exemplify the practicality and usefulness of these procedures.*

- *Creating a suitable storage facility for live spiders as well as cleaning and maintenance plans, and establishing safe handling guidelines, general care and feeding schedules.*

- *Establishing routines for spider handling, preparation, and mounting procedures including hair removal, sectioning, and rehydrating, that involve minimal sample manipulation. These will ensure our ability to make measurements on* ***living***

samples *when available, as well as samples that are in as near natural state as possible when required.*

- *Characterization of overall pad structure and function using various optical fluorescence and scattering techniques, as well as 3-dimensional observation of pad deformation behavior using µCT imaging.*

- *Investigation of time- and temperature-dependent properties of the cuticular pad surface adjacent to the major vibration-sensitive lyriform organ implementing newly established data analysis procedures.*

- *Mechanical characterization of the subsurface features of the vibration-sensitive lyriform organ as well as the cuticular pad, relation to the surface characterization performed prior, combination of the results for a clear picture of how the sensory system transmits stimuli as a whole.*

- *High resolution, AFM-based investigation of the nanoscale details of the surface topography of slit sensory systems and comparison amongst several lyriform organs of interest. Structural details observed include slit membranes topography and curvature, epicuticular ridges, and dendritic surfaces.*

- *High-resolution micromapping and determination of the local mechanical properties of slit sensory organs, with an emphasis on the suspended outer membrane. Quantitative characterization of layer-like structure of slit membrane using a wide range of applied force. Establishment of a relationship between these mechanical properties and the observed time-dependent neuron response.*

Micro- and nanoscale mechanical properties of soft viscoelastic materials serve critical roles in many areas of science and technology. This study will provide experimental methods and data analysis routines which are widely applicable to a variety of material surfaces exhibiting strong viscoelastic behavior in order to quantitatively characterize their mechanical properties through practical temperature ranges in both ambient conditions as well as submerged in relevant fluid environments. Such characterization will aid in the understanding of the mechanical behavior of many complex soft materials systems such as nanophase separated polymer blends, biopolymer coatings, living cells, or micro- and macro-scale sensory systems such as the one studied here.

2.3 Organization and composition of dissertation

Chapter 1 provides a critical review of current AFM methods used for probing the elastic as well as viscoelastic mechanical properties of soft materials. Also critical to a large portion of this work is the measurements we performed on a live wandering spider, therefore this chapter also includes fundamental introductory information concerning sensory systems in biology, with an emphasis on the strain-detecting lyriform organs studied in this dissertation.

Chapter 2 includes a concise description of the goals and technical objectives of the work presented in this dissertation. Furthermore, it provides a brief overview of the organization of the dissertation, with brief descriptions of the contents of each chapter.

Chapter 3 outlines the experimental techniques utilized throughout the work presented in this dissertation. It includes storage, feeding, handling and general care procedures required to work with living spiders over the course of a long-term project. Also included are sample preparation techniques for both live spiders and model materials, as well as descriptions of the characterization techniques which were critical to the experiments

presented below. Model material sample preparation includes thick film casting of well-established and extensively characterized polymers. Other preparation methods such as spin-casting and patterning via soft lithography are also discussed. Characterization techniques include AFM for measuring topography, mechanical properties, X-ray scattering and μCT to understand the chemical composition and structural features of the lyriform organs investigated here, as well as several optical microscopy techniques used for imaging complex samples. In several subsequent chapters the experimental techniques are supplemented with specific protocols used for the particular studies presented.

Chapter 4 describes in detail the development of a practical AFM-based measurement method which can be utilized for the quantitative characterization of the viscoelastic mechanical properties of soft material surface. In this context a combination Johnson-Sneddon models are used on a widely characterized polymer (PnBMA) with glass transition temperature close to room temperature. Also discussed thoroughly in this chapter is the application of different tip geometries to the relevant contact problems encountered throughout the dissertation.

Chapter 5 discusses the application of careful measurement procedures to commercially available soft contact lenses. Within this chapter it is shown that more common techniques used to determine elastic modulus suffer from lack of spatial resolution, which results in reported values being an average of the whole lens. This is an inadequate description of lens mechanical properties as new generation lenses are multiphase materials often having some type of surface treatment. Additionally, tensile tests are commonly undertaken at slow strain rates. Here it is shown that the surface materials of these lenses have a viscoelastic component which have apparent modulus values nearly 3 times higher than reported in literature, when subjected to higher strain rates.

Chapter 6 describes the overall structural functionality of a viscoelastic pad which serves as a transducer of vibratory stimuli onto the metatarsal lyriform organ of Cupiennius salei. It was shown that the different structural features of this pad exhibit a wide variety of apparent elastic moduli, spanning nearly two orders of magnitude. It was also seen that this pad can serve to transform large, micro-scale tarsal deflections from the distal contact point of the pad to nanoscale deformations on the lyriform organ slits. Furthermore a very rigid object was seen to be responsible for maintaining deformation of the slits perfectly perpendicular to their long-axis.

Chapter 7 delves into the time- and temperature-dependent mechanical properties of the thick epicuticular coating of the pad. Here the mechanical properties dependence on temperature was directly measured via a custom built heating/cooling bath. By collecting FDCs not only at different temperatures, but also at different ramping rates, a master curve was constructed which describes the epicuticle time-temperature-modulus relationship. Further data analysis extracted temperature-dependent relaxation times. From these values, loss and storage modulus could be determined and their dependence on temperature was explored. It was found that changes in temperature that the spider would likely see in its natural environment shift the peak of the loss modulus curve, indicating that it is tuned to be more sensitive during the cool nighttime hours in which it is most active.

Chapter 8 explores the mechanical properties of the strain-sensitive organs by directly collecting FDCs on them. During this investigation we focused our attention on the outer membrane which is directly coupled to the sensory cell responsible for firing action potentials. It was apparent that the outer membrane was a layered-like structure composed of an upper, soft viscoelastic layer on top of a stiff supporting layer. From this the relaxation times of the upper layer were determined and compared to the time in which the impulse rate of action potentials dramatically decreases. Because these were on the same

order of time it was suggested that this decay in impulse rate is at least partially related to the viscoelastic nature of the outer membrane, in combination with the properties of the sensory cell itself.

Finally, **Chapter 9** provides general discussion and conclusions drawn from the overall body of work presented within this dissertation with an emphasis on broader impacts and future directions

CHAPTER 3

Experimental details

Chapter 3 serves to provide a brief overview of the experimental details and characterization techniques utilized throughout this work. More detailed descriptions of the experimental details are also available within each chapter.

3.1 Materials and sample preparation

3.1.1 Model materials. Several model materials which have well characterized properties were frequently used as controls such that our micromechanical analysis routines could be verified. Commercially available polystyrene (PS, 250 kDa, Sigma Aldrich), poly(n-butyl methacrylate) (PnBMA, 340 kDa, Sigma Aldrich), and polydimethylsiloxane (PDMS, Sylgard 184 silicone elastomer), representing a range of mechanical properties from several MPa (PDMS) to approximately 3 GPa (PS), were acquired and thick cast films of each were fabricated as described below. According to literature data the glass transition temperature, T_g, of PnBMA is around 25 °C and thus AFM measurements made on this polymer at temperatures from 10 to 55 °C will display a highly viscoelastic nature with its elastic modulus varying from ~50 MPa to ~1 GPa.

3.1.2 Silcone-based contact lenses as viscoelastic substrates. In this work, four different commercially available silicone-hydrogel contact lens brands were selected for comparative studies: Balafilcon A (Purevision, Bausch & Lomb Inc.), Senofilcon A, (Acuvue Oasis, Johnson & Johnson Vision Care Inc.), Lotrafilcon B (AirOptix Aqua, CIBA Vision Corp.) and (Biofinity, CooperVision Inc.) purchased through Contactlenses Ltd (see Table 2.1). Lenses were used to scan both the front curve surface (i.e. the portion in contact with the eyelid), and cross sectional areas along the edge of the lens. Fresh contact lenses were removed from their original blister packaging and sectioned with a

fresh razorblade in a droplet of contact lens saline solution. Surfaces were attached to metal sample disks, and AFM scans were collected in a droplet of saline solution. Sections were aligned in a custom metal clamp such that only a small portion of the sectional surface was above the top of the clamp walls (i.e. easily reached by AFM, but not so high that the lens wobbled during measurements). The entire lens/clamp setup was submerged into saline solution for scanning. Schematic representations of the lens scanning setup are shown in Fig. 3.1. After removal from the blister packs all lenses were discarded after one day of scanning and new lenses were used for further measurements.

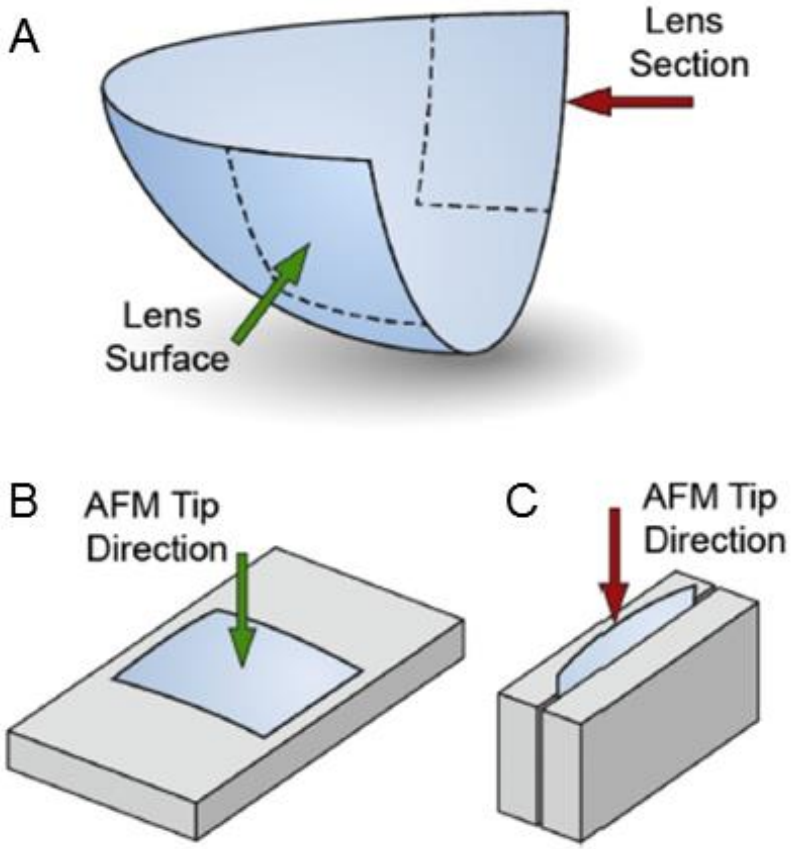

Figure 3.1: (A) Schematic of contact lens sectioning procedure. (B) Setup for lens front curve surface scanning. (C) Cross-section analysis experimental setup in custom clamps. In the case of (B) scanning was performed in a small droplet of saline solution applied to the lens surface. For section images, the entire clamp/lens was submerged in a saline bath.

Table 3.1. The characteristics of contact lenses used in this study.

Name	Manufacturer	Material	Water Content,[a] %	Surface Treatment	Modulus, MPa [a]
Air Optix	Ciba Vision	Lotrafilcon B	33	Plasma coating	1.0
PureVision	Bausch and Lomb	Balafilcon A	36	Plasma oxidation	1.1
Acuvue Oasys	Johnson and Johnson	Senofilcon A	38	NA	0.72
Biofinity	CooperVision	Comfilcon A	48	NA	0.75

[a] Manufacturer reported values.[143]

3.1.3 Silk and silk derivative materials.

Regenerated silk fibroin: In accordance to well-established procedures in our group[144] *B. Mori* pupae will be removed from the cocoons, and the cocoons will be degummed (removal of the glue- like sericin coating) by boiling for 20 minutes in a 0.02 M Na_2CO_3. The degummed silk fibroin will then be rinsed thoroughly in 18.2 MΩ·cm Nanopure water and allowed to air dry overnight. The extracted fibroin will then be dissolved in a 9.3 M LiBr solution. Aqueous solutions of fibroin will be made by removal of LiBr ions via dialysis against distilled water for three days, and then diluted to the desired weight percentage. The solution will then be centrifuged and the supernatant collected to ensure no large contaminants remain.

Silk Fibroin Ionomers: Regenerated silk fibroin protein was modified with poly-l-lysine (PLL) and poly-l-glutamic acid (PLA) with different molecular weight and grafting densities in order to obtain amino acids functionalized silk polyelectrolytes (ionomers) with high and low charge densities.[145] A high degree of derivation of silk ionomers, namely SF(Y,S)-PLL and SF(Y,S)-PGA, was achieved by grafting highly dispersed in M_w ($M_w \leq$

15 kDa) long chains of polyamino acids to tyrosine (Y) and serine (S) residues of carboxylate-modified SF (SF(Y,S)-COOH), which accounted for ~18 mol % modification of the available amino acids in SF. The increase in charge density allowed efficient charge–charge interactions during electrostatic LbL assembling of modified silk proteins. Low charge density silk ionomers were obtained by grafting PLL or PGA chains of low molecular weight (M_w = 3 kDa) to serine residues only of SF(S)-COOH intermediate. The degree of derivation for SF(S)-PLL and SF(S)-PGA was calculated to be 0.1 and 0.9 mol % in terms of moles of amino acids in SF macromolecule modified with PLL or PGA, respectively.[146,147]

Recombinant spider silk-like protein: The recombinant spider silk protein eADF4 (C16) was produced and purified as described in greater detail in a recent publication.[56] Transformed cells (*E. coli* strain HMS174[DE3]) were grown at 37 °C in LB medium to an OD_{600} = 0.5. Before induction with 1 mM IPTG (Isopropyl-ß-D-thiogalactosid), cells were shifted to 25 °C. Cells were harvested after 3-4 hours of induction. After cell disruption and removal of cell debris, the supernatant was incubated at 70 °C to precipitate bacterial proteins, followed by an ammonium sulfate precipitation to precipitate eADF4 (C16) which was stored after lyophilisation. C16 thin films were prepared dissolution in either formic acid (FA) or hexafluoroisopropanol (HFIP) at a concentration of 2% w/v. Film thickness was checked via ellipsometry and the so-called scratch test using AFM. C16 films were patterned using capillary transfer lithography and solvent-assisted micromolding techniques.

3.1.4 Model material film fabrication. Thick films of PS and PnBMA (thickness > 1 mm) are formed by casting saturated solutions (~150 mg/mL) in toluene into a glass Petri dish and annealing at 40 °C under vacuum for a week to remove residual solvent.

A 10:1 mixture of Sylgard 184 elastomer base to curing agent is mixed thoroughly and cast into a petri dish. Vacuum is applied for 30-60 minutes to ensure all air bubbles are removed, then the PDMS is cured at 70 °C for overnight resulting in a ~5 mm thick film.

Thin films of silk materials were created by spin-assisted layer-by-layer (LbL) assembly on clean silicon wafers. Silicon wafers were cleaned in piranha solution (3:1 mixture H_2SO_4:H_2O_2) for one hour and subsequently rinsed thoroughly with 18.2 Ω·cm resistivity Nanopure water, obtained from a Barnstead Nanopure system. Sub-micrometer thin films (thickness typically on the order of 50-150 nm) of these materials were then spin-cast onto the clean silicon substrates at 3000 rpm.

3.1.5 Cupiennius salei. For these studies, live adult females of the spider *Cupiennius salei* (Ctenidae) received from the University of Vienna breeding stock were used.[84] Because the goal of these experiments were to measure the properties of the spider cuticle in as close to natural state as possible, live spiders were measured when possible. As a result special handling and care routines needed to be established prior to any experimentation, as described in detail below.

3.1.5.1 Live spider facilities and care. A bench-top hood space was cleared for use as a spider storage facility (Fig. 3.2). Two UV lamps were installed and connected to a circuit timer which cycled at 12 hours on and 12 hours off, generally coinciding with natural light cycles. For storage large glass jars were obtained and filled with a fluid retaining substance (e.g. bark, mulch, and frequently sphagnum moss). These substances were allowed to absorb a significant amount of water prior to placing the spiders within the jar. To allow for sufficient airflow as well as UV light passage, the solid tops of the jars were discarded and replaced with a flange which had a screen mesh spanning the flange opening (mesh

attached with super glue). A humidifier was used in order to keep the RH as high as possible, and frequent measurements with a hygrometer confirmed that RH of the open space in the hood was generally > 80%, with a small increase inside each of the jars. Spiders were fed crickets at ~1 week intervals and the jars were inspected for molding frequently and completely cleaned and replaced monthly.

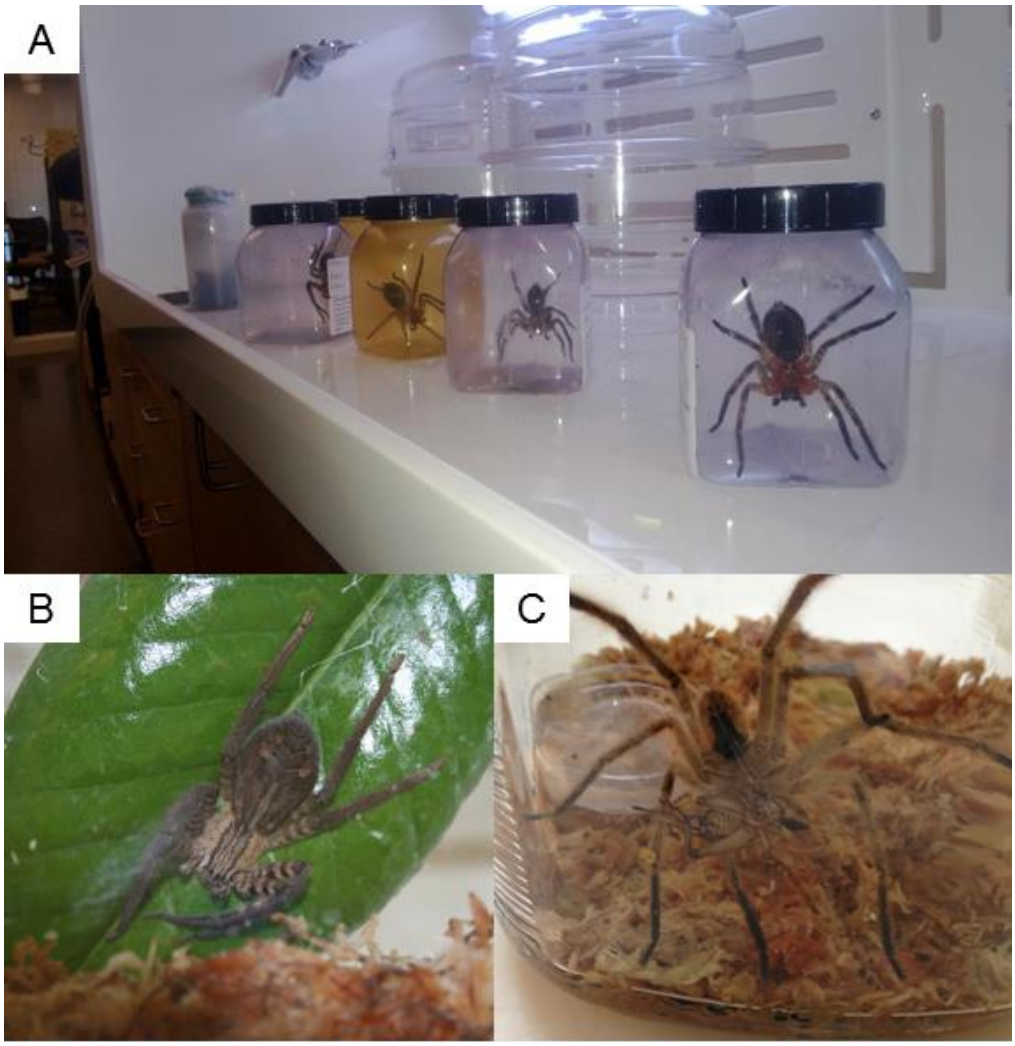

Figure 3.2: (A) Benchtop spider facilities, with spiders in their shipment containers. (B) Female Cupiennius after placement in permanent storage jar. (C) Male Cupiennius in permanent storage jar. In these images, the tan substance is sphagnum moss soaked in water. Leaf in (B) is from one of the many magnolia trees located on Georgia Tech's Atlanta campus.

3.1.5.2 Spider mounting. Live spiders were sedated under carbon dioxide gas enabling several minutes of facile handling. The spiders were gently taped down and subsequently point-glued (dorsal surface up) using a 1:1 weight mixture of beeswax (Sigma Aldrich) and rosin (colophony, Alpha Aesar) to a removable AFM chuck (Fig. 3.3).

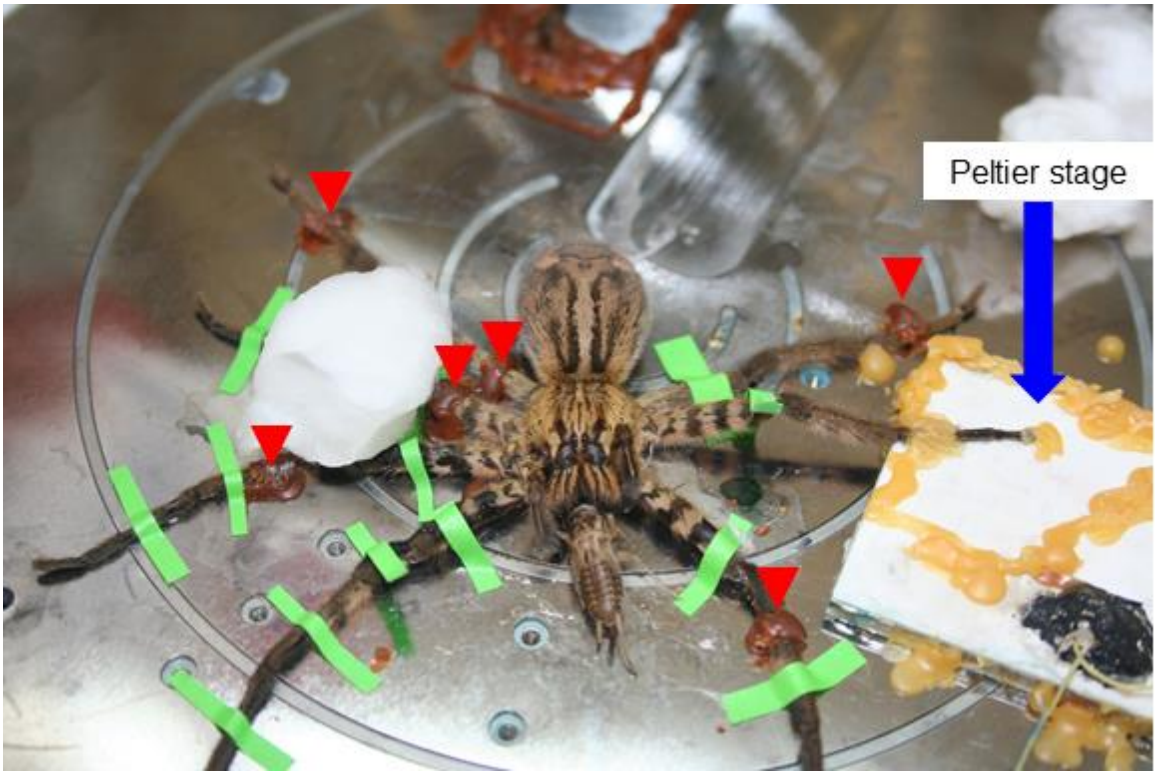

Figure 3.3: Image showing a live spider which has been mounted to an AFM chuck for measurement. One leg here is attached to a Peltier stage for heating/cooling experiments. Red arrowheads demark locations of beeswax/rosin mixture used for point gluing leg segments. Cotton balls here were soaked in water and used to keep local RH elevated.

In order to expose the areas of interest sufficiently for AFM measurements, the hairs in the surrounding region of the leg were removed by gently rubbing against the grain with a KimWipe, the remaining hairs nearest the organs were carefully plucked with fine-point tweezers under a stereomicroscope (4X magnification) in order to minimize any

unnecessary damage to the cuticle. Wet cotton balls were kept around the spider to elevate the local RH, and after a round of measurements the entire chuck could be placed in the high RH hood. If possible, after all measurements the small dots of rosin/beeswax mixture were removed and the spider released back into its jar.

3.1.5.3 Leg autotomization and rehydration. In the case of slits which are not easily accessible by AFM, freshly autotomized legs were also used for mechanical measurements. Leg autotomization consisted of squeezing the femur joint of the spider leg near the cephalothorax, resulting in a self-defense mechanism in which the entire leg is self-amputated via muscle contraction and drastic haemolymph pressure increase. Consequently fresh cuticle could then be positioned optimally within the AFM. The limited supply of live spiders also necessitated the use of some rehydrated cuticle samples (preserved in 70% EtOH solution). Rehydration of a leg segment was achieved by placing the leg into a saline solution with an ion content closely matching that found naturally in *Cupiennius*. Spider saline solution was made according to the recipe outlined by Maier et al.[148] and Höger et al.:[149] 223 mM NaCl, 6.8 mM KCl, 8.0 mM $CaCl_2$, and 5.1 mM $MgCl_2$ were dissolved in Tris-HCl buffer, pH 7.8. It was found that the rehydration process was nearly completely reversible, and there were no indications of drastic changes in mechanical properties between the live/autotomized legs and rehydrated legs.

3.1.5.4 Sample sectioning. Sections of cuticle were made by slicing downward from the center of the dorsal surface using a Bard-Parker #10 carbon steel surgical blade (sagittal section). The beeswax/rosin mixture was used to secure sections onto a glass substrate, and optical microscopy was employed to confirm that the sectioned surfaces were oriented roughly parallel to the glass surface such that artifacts were not be produced by scanning on a large angle.

3.1.6 Sample heating/cooling. In several cases our samples required heating and cooling control. This was achieved via a custom made heating bath consisting of a Peltier heating source and moderately (~1-2 cm) deep sidewalls to allow for submersion into fluid (water or saline in all cases). The temperature of the fluid system (and thus our samples after sufficient equilibration time) was measured and constant temperature will maintained during the experiment using a thermocouple feedback loop (ILX Lightwave LDT-5948 Precision Temperature Controller). The accuracy of the thermocouple was frequently verified independently using a volume expansion thermometer.

3.2 Characterization techniques

The research presented within this dissertation utilized a wide range of characterization techniques to assess various surface and bulk properties including surface topography, micromechanics, compositional profile and structure orientation, to name a few. Many of the more common and well established techniques will only be briefly discussed here. Because a main technical goal of this dissertation was the development of experimental procedures and data analysis routines for precise measurement of the nano- to microscale viscoelastic mechanical properties using available AFM-based technology, only a very brief description of AFM is discussed here, with Chapter 4 devoted to a very in-depth discussion of our methodology development.

3.2.1 Optical microscopy. While optical microscopy is one of the most established procedures, our additional data processing steps are not as well known, and therefore will be discussed briefly below. Because of the highly non-planar nature of our samples and the inherent lack of any significant depth of field associated with optical microscopy, the clarity of each optical image was digitally enhanced using the method of focus stacking (see Figure 3.4). Optical imaging was undertaken via a BX-51 microscope with a Dage-MTI XLM high-resolution cooled digital camera at 10X magnification under dark field

illumination. Many images (>100) are recorded at different focal planes and the in-focus portions of each image are superimposed. Helicon Focus version 5.3.14 was utilized for the optical image focus-stacking.

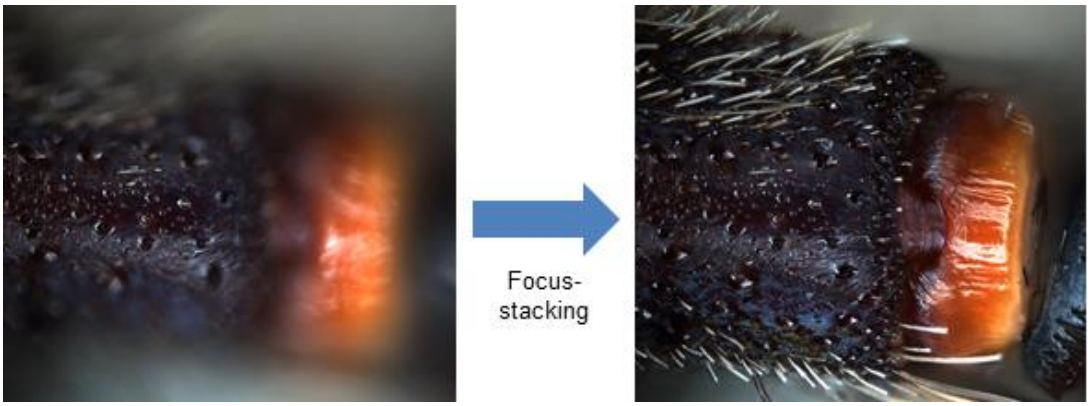

Figure 3.4: Example of one out of ~100 images of the metatarsal-tarsal joint (left) showing only a small portion in focus. After the focus-stacking procedure the entire dorsal surface can be seen in focus (right) despite its highly non-planar shape.

3.2.2 Scanning electron microscopy. Scanning Electron Microscopy (SEM) images presented within this research were taken using two machines: (i) JSM-7500F field emission SEM (JEOL, Tokyo, Japan); and (ii) S-3400N thermal emission SEM (Hitachi, Tokyo, Japan). The measurements are performed in high vacuum (10^{-7} mBar) in low-magnification mode, with a working distance of ~8-12 mm and electron beam accelerating voltage of 5.0-10.0 kV.

3.2.3 Atomic force microscopy. AFM allows for the direct measurement and spatial mapping of surface topography, chemical, mechanical, and electrical properties with high resolution (down to tens of nanometers, depending on the method employed). Therefore, AFM was chosen as a primary technique due its suitability for measuring the micromechanical properties of soft polymeric and biological materials in a non-damaging manner.[19,30,31,56] Furthermore, the versatility of AFM facilitates measurement of surface

forces at various temperatures and in a variety of environments, allowing for viscoelastic characterization of soft material surfaces. [40,150,151,152,153,154] All AFM measurements were performed using a Dimension Icon microscope (Bruker) equipped with a Nanoscope V controller.

3.2.3.1 Tapping mode. General topographical imaging was performed in one of several common scanning modes. Tapping mode relies on a cantilever which is vibrated near its resonance frequency. A laser reflected off the backside of the cantilever monitors vibration amplitude via a four quadrant photodiode. Vibrational damping is used as a feedback mechanism to closely track the sample surface. Additional surface information can be obtained by monitoring the phase shift between the piezo-element driving the cantilever and the cantilever's response detected by the photo-detector. So-called phase imaging can be used as a qualitative method to discern different materials on a sample surface.

3.2.3.2 PeakForce Quantitative Nanomechanical Mapping (QNM). PeakForce QNM operates in what is known as pulsed-force imaging mode. During QNM measurements the tip contacts the sample during the down portion of a sinusoidal vibration cycle.[51] Each cycle starts above the surface, then the tip approaches and makes brief contact the surface resulting in a small indentation. The depth of this indentation is controlled by the maximum force excreted on the sample by the cantilever (set point). The cycle is finalized by withdrawing the tip from the surface up to the initial baseline static deflection. By limiting the set point, indentations as small as 1-2 nm can be performed, therefore achieving very soft, nondestructive measurement conditions. Approach and retract FDCs can be reconstructed from the loading data (see Fig. 1.7); however the analysis of these curves differs from quasi-static measurements. Because of the low calculation time requirements for real time analysis in pulsed force imaging, the set point force (F_{tip}) and adhesive force (F_{adh}) are used instead of the full curve fitting to calculate elastic modulus according to

various contact mechanics models. Further analysis of the FDCs allows for simultaneous measurement of adhesion and energy dissipation in addition to the sample topography and elasticity.

3.2.3.3 Surface force spectroscopy. For mechanical properties characterization a version of atomic force microscopy, usually called surface force spectroscopy (SFS), was exploited since it allows high-resolution measurements in forces, position, and deformation.[155] During the SFS measurements, an AFM tip is brought into an intimate contact with the surface under investigation and is pressed into the material. The corresponding applied force versus tip displacement is measured in the form FDCs.[156] From these direct measurements, surface deformation (δ) can be evaluated and the elastic properties of materials can be calculated and mapped by assuming certain contact mechanics models of elastic deformation and avoiding plastic deformation.[28,157,158]

Further development of this method is discussed thoroughly in Chapter 4.

3.2.3.4 Data post-processing. The analysis capabilities of collected FDCs was expanded through custom-made data processing software (MicroMechanical Analysis of Soft Polymeric Materials, MMA-SPM, License Pending). This program was built using MatLab R2012b, and was compiled using MatLab Compiler Runtime (MCR), which allows users to run MMA-SPM without having to download MatLab software. MMA-SPM expands processing FDC data beyond what is available from manufacturer analysis software, and includes simple elastic models considering different tip shapers, JKR and DMT adhesive models, viscoelastic modeling, layer modeling, as well as a tip radius estimation modulus. Also included is a batch processing function which allows the user to automatically analyze many curves simultaneously. All data can be exported as text files or image files.

3.2.4 Confocal laser scanning microscopy (CLSM). CLSM was utilized here not only for its ability to collect high resolution optical images with excellent depth profiles, but also for its ability to collect sample auto-fluorescence data. Specimen of spider cuticle were imaged on a Leica TCS SP5 (Leica Microsystems GmbH, Wetzlar, Germany) equipped with an inverted microscope (Leica DM IRBE) and two visible light lasers (wavelengths 488 nm, Argon, 100 mW; 561 nm, diode pumped solid state DPSS, 10 mW). For each sample the most appropriate lens was chosen depending on sample size. The excitation wavelengths and the wavelengths of the emitted fluorescence were chosen according to previous studies of arthropod cuticle.[159] The power of each laser was reduced to 2 mW to avoid damage of the sample. The signal detection gain was optimized for each sample individually. The lenses and settings used for the visualization of each sample are given within the respective figure caption. Image data processing was performed using ImageJ software.[160] The auto-fluorescence images represent superimposed emission signals resulting from 488 nm and 561 nm excitation wavelengths assigned to the green and the red software channel, respectively.

3.2.5 Micro-computer tomography (µCT). µCT provides a means to non-destructively create a 3-dimensional virtual model of a sample with micrometer-scale resolution via cross-sectioning using an x-ray beam. µCT experiments were performed at the European Synchrotron Radiation Facility (ESRF) in Grenoble, France, utilizing the imaging setup at beamline ID19. In order to find a compromise between high imaging sensitivity and low radiation damage the samples were measured at 25 keV photon energy.[161] A so-called single-harmonic undulator (u13, gap 11 mm) with a narrow bandwidth was used as radiation source with a diamond filter and a Be window as the only mandatory optical elements in the beam path, leading to a homogeneous wave front at the position of the experiment and therefore excellently suited for X-ray phase contrast imaging in parallel-

beam geometry. Approximately 35 mm downstream of the specimen a high-resolution indirect imaging detector was placed. It was equipped with a 8.8 µm thin single-crystal scintillator (Tb-doped Lu2SiO5), a 10x objective (0.3 numerical aperture), a 2x eye-piece and the ESRF custom made CCD camera FReLoN (type: A7899), operating with a nominal effective pixel size of 0.7 µm.[162] The exposure time was set to 0.2 s for each of 1000 projection images while rotating the sample over 180°. Pad morphology data were reconstructed using the ESRF software package PyHST_2,[163] which includes a phase-retrieval using Paganin's approach.[164] For data visualization and segmentation ZIBAmira software (Zuse Institute, Berlin, Germany; FEI Visualization Science Group, Burlington MA, USA) was used.

3.2.6 X-ray scattering. X-ray scattering experiments were performed at the µ-spot beamline at the BESSY II synchrotron radiation facility in Berlin, Germany. The wavelength of 0.826 Å (energy 15 keV) was selected using a multilayer monochromator. The beam was focused by a toroidal mirror and the scattering patterns were collected on the area detector (MarCCD 225, MarUSA, Evanston) with 3072 x 3072 pixels placed behind the sample. The sample-detector distance was 0.408 m and the beam diameter at the sample position was 10 µm. This gives a covered range of scattering vectors of 0.4 $nm^{-1} < q < 25\ nm^{-1}$, defined by $q = 4\pi \sin(\theta) / \lambda$, where 2θ is the scattering angle and λ the wavelength of the incident beam. All measurements were calibrated using a quartz powder placed at the sample position. For the analysis of the two-dimensional scattering data the software Fit2D[165] was used.

3.2.7 Scanning acoustic microscopy (SAM). SAM measurements were performed using KSISAM2000 by Krämer Scientific Instruments (Herborn, Germany) and data was collected using software MATSAM custom made by the Q-BAM Laboratory (University of Halle-Wittenberg, Germany). Temperature in the room was maintained at 21° C. Two

spider leg samples had been previously embedded in MMA. After polishing (removing one half of the metatarsus) the sample surface represented the sagittal plane of the pad. The SAM analysis of this surface was performed under deionized water using 400 Hz and 820 Hz, respectively.

3.2.8 Nanoindentation. Nanoindentation measurements were performed using Ubi1 Nano Indenter (Hysitron, Minneapolis, MN, USA). The same samples were used as for SAM. After choosing regions for measurements using a built-in light microscope, the samples were immersed in water and allowed to equilibrate for 30 min. In this time the samples swelled considerably. The measurements were performed under water with the Berkovich tip immersed in deionized water. The following load function was applied: loading/unloading rates: 100 μN s^{-1}, holding time 60 s at a peak load of 500 μN. Each measurement included 64 indents at the respective pad region. The values for the reduced elastic modulus E_r and for hardness H were obtained from the load–displacement curves according to the Oliver and Pharr method.[166] They represent mean values ± standard deviation of 60 indents per region.

3.3 Collaborative efforts

Much of the work presented within this dissertation was made possible through collaboration with excellent scientists both in the United States and Europe. Live spiders were received through Professor Friedrich G. Barth's group in the Department of Neurobiology at University of Vienna in Vienna, Austria. Maxim Erko, Yael Politi, and Igor Zlotnikov from the Max Planck Institute of Colloids and Interfaces, located in Golm, Germany, assisted in CLSM, scattering, SAM, and nanoindentation experiments. Professor Thomas Scheibel from the University of Bayreuth in Bayreuth, Germany, provided recombinant spider silk-like protein (C16). Finally, silk fibroin ionomer samples

were made available to us through Professor David Kaplan's laboratory at Tufts University in Medford, MA, USA.

CHAPTER 4

Development for micromechanical probing of complex soft material surfaces.

The quantitative characterization of surface microstructure, morphology, and properties of biomacromolecules and soft nanomaterials such as proteins, peptides, DNA, synthetic gels, and corresponding bionanocomposites is critical for many technical fields. As discussed, AFM methods provide variety of tools to access these properties by measuring the interactions of a sharp probe with a specimen surface, and can often produce topographical images with near atomic resolution.[19] Furthermore, unmatched force sensitivity (10^{-12}-10^{-10} N) allows one to non-destructively investigate a variety of materials.[2,3,4,167] However, precise measurements of the micromechanical properties of soft material surfaces is often a challenging task, and data analysis procedures can become non-trivial in the case of increasing sample complexity. Chapter 4 thoroughly describes the experimental procedures and data analysis routines developed through the course of this thesis work, which played vital roles in describing the true micromechanical properties of soft, viscoelastic surfaces.

4.1 Experimental and data analysis refinement for quantitative probing of micromechanical properties in the viscoelastic regime

In this section, we describe our experimental methods for precise determination of micro- and nanoscale viscoelastic mechanical properties of soft polymeric and biological surfaces. In order to facilitate such measurements with minimized ambiguities, in this study we present a combined method to evaluate the viscoelastic properties of compliant polymeric materials. We collected force-distance data in the "static regime" for a benchmark polymer material (poly(n-butyl methacrylate)) with easily an accessible glass transition temperature (about 30 °C) at different loading rates and different temperatures across the glassy state, glass transition region, and rubbery state. For this analysis, we exploited Johnson-modified

Sneddon's approach in a combination with the standard linear solid model. Critical experimental steps suggested for robust probing are: (i) the use of a tip with a well-characterized parabolic shape, (ii) probing in a liquid environment in order to reduce jump-in phenomenon, and (iii) minute indentations to ensure the absence of plastic deformation. While standard Sneddon's model generates quantitatively adequate elastic modulus values below and above glass transition, this traditional approach can significantly underestimate actual modulus values in the vicinity of the glass transition region (15 °C above/below T_g), with major deviations occurring at the loss tangent peak. The analysis of the experimental data with Sneddon's model for the elastic region (glassy and rubbery states) and Johnson's-modified model for the viscoelastic region allowed for the restoration of the universal master curve and the evaluation of storage modulus, loss modulus, loss tangent, relaxation times, and activation energies of polymer surface across glass transition region and at relevant loading rates.

4.1.1 Introduction. Measurements of micromechanical properties on thin polymer films, organic coatings, biological materials, and polymer surfaces with traditional tools such as dynamic mechanical analysis, nanoindentation, bulging, and buckling is a challenging task due to a range of unfavorable circumstances including modest strain and stress sensitivities, substrate contributions, insufficient local deformation, and poor control of minute deformations and forces.[168] Therefore, a version of AFM, usually called surface force spectroscopy (SFS, collection of an array of FDCs), is widely exploited since it allows high-resolution measurements in force, position, and deformation even if precise contact mechanics behavior frequently remains debatable.[19] As described in Chapter 1, during the collection of FDCs, an AFM tip is brought into an intimate contact with the surface under investigation and is pressed into the material. From these direct measurements, surface deformation can be evaluated and the elastic properties of materials can be calculated and

mapped by assuming certain contact mechanics models of elastic deformation and avoiding plastic deformation.[169]

SFS probing has been successfully used for micromechanical measurements with high spatial resolution of ultrathin soft materials such as homopolymers, polymer blends, polymer brushes, block copolymers, hydrogels, or individual molecules on various substrates, in liquid, and at various temperatures.[19,170,171] The AFM is capable of applying and detecting forces which are orders of magnitude lower than that of covalent bonds and comparable to weak interactions, making it a unique tool for probing intermolecular interactions.[172,173] The limitation of SFS is that it can only probe surfaces (or topmost sub-layers and sub-surfaces), as opposed to other approaches, such as micro-/nano-indentation, which are capable of probing sub-micron to micrometer-sized depths. The "pull-off" forces acting on the tip during SFS measurements are widely employed in the studies of synthetic and protein macromolecular unfolding, brush layer stretching, and other tensile-related mechanical properties of individual molecules and usually requires modification of the tip surface with selective binding groups.[174,175,176]

Initial developments in SFS methods were devoted to the verification of the mathematical contact models of tip-sample interactions.[177] Various methods of data analysis were introduced to account for the tip shape (Sneddon's model),[28] tip-sample interactions (Derjaguin-Muller-Toporov (DMT), Johnson-Kendall-Roberts (JKR), Maugis-Dugdale, MD),[158,178,179] and plastic deformations (Oliver-Pharr, OP).[166] These developments exploited contact mechanics to study complex deformational, elastic and plastic, tensile and compressive, and static and dynamic behavior of various compliant and hard surfaces.

However, even if plastic deformation, strong adhesive forces, and substrate contributions can be avoided or reduced during experimental routines, the major assumption of purely

elastic deformation cannot necessarily be considered valid for inherently viscoelastic polymeric and biological materials. Indeed, at temperatures near the glassy-to-rubbery transition, T_g, the time-dependent behavior becomes dominant and viscoelastic materials can exhibit a dramatic decrease in storage modulus by as much as three orders of magnitude, which is accompanied by dramatic increase in loss modulus at temperatures slightly above the formal glass transition, at maximum loss tangent. [5,6,150,151] To analyze this complex phenomenon, significant efforts have been undertaken to develop AFM-based probing modes and corresponding data analysis approaches to determine the viscoelastic properties of materials with significant mechanical energy losses under various assumptions.[72,180]

In this experimental study, FDCs are analyzed by combining standard Sneddon's contact mechanics model with Standard Linear Solid (SLS) viscoelastic model in Johnson's interpretation for indentation experiments to extract the critical materials parameters such as the sample's instantaneous modulus (E_0), which represents the elastic modulus of the material at very fast loading rates, infinite modulus (E_∞), which represents the elastic modulus of the material at substantially slow loading rates, and, finally, relaxation time (τ), the time scale of polymer chain rearrangement upon applied stress.[62] Furthermore, the micromechanical properties of the amorphous polymeric material selected here with a glass transition temperature close to room temperature (see §4.1.3) is analyzed by employing the time-temperature correspondence principle.[62] Such an approach allows for the reproduction of generalized time-dependent mechanical properties of viscoelastic polymeric materials such as global master curves, relaxation times, and activation energies in a wide temperature and frequency range around the glass transition.

4.1.2 Basic SFS probing concepts.

4.1.2.1 FDC collection. As described in detail in § 1.1.1, SFS experiment are usually

analyzed in terms of the continuous penetration of the AFM tip into the material as induced by a near-normal load. These loading curves are derived from experimental FDCs in which cantilever deflection d and position z are directly measured while the tip moves toward (approaching curve) or away from (retracting curve) the surface. [29,181] For simplicity, here we define the contact point as the point where the AFM tip first touches the surface, with the actual definition of the contact point varying for different approaching conditions (e.g., with significant repulsive or attractive forces). Assuming purely elastic cantilever behavior (very low damping in air with Q of several hundreds) with a spring constant k, the force exerted by the AFM tip on the surface, F, can be calculated from the measured cantilever deflection, and this deformational behavior can be simply treated with a spring-against-spring model (Figure 4.1).[155]

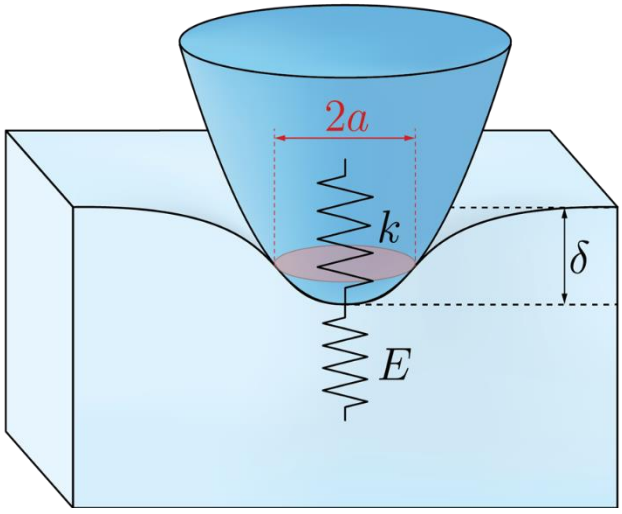

Figure 4.1: Schematics of Sneddon's model for axisymmetric punch pressed against purely elastic material with modulus ***E***.

4.1.2.2 Tip-surface interactions. The spring-against-spring model includes the classical Hertzian model that describes small reversible deformations of compliant elastic semi-spheres pressed against each other.[157] However, in the most practical cases, the indenter is

much harder than the studied material, thereby limiting the use of this classical model in indentation experiments, especially in cases which involve significant penetration depths. Therefore, Sneddon's model extended the contact mechanics theory by solving the problem of the indentation of an axisymmetric hard punch into an elastic half space with Young's modulus E (Fig. 4.2).[28]

In this model, an indentor shape is described by the function $f(x)$ (to describe different shapes) and the hard punch makes a contact area with a circular plane projection of radius a with the elastic material. His analysis led to the analytical equations for the penetration δ and force F exerted by the hard punch in the form:[28]

$$\delta = \int_0^1 \frac{f'(x)}{\sqrt{1-x^2}} dx \tag{4.1}$$

$$F = 2\left(\frac{E}{1-\nu^2}\right) a \int_0^1 \frac{x^2 f'(x)}{\sqrt{1-x^2}} dx \tag{4.2}$$

where ν is the sample Poisson's ratio (usually assumed to be close to 0.5 for elastic deformation of polymeric materials). Here, and in the following discussion of indentation contact models, the punch is assumed to be rigid and not deformable.

Analytical solutions and deformational relationships for common indenter geometries are summarized in Fig. 4.2. It can be seen that for the case of the spherical indenter, there is no simple relation between the force and penetration. However for the indenter of a parabolic shape, there is a simple equation, which relates the penetration $\delta^{3/2}$ with the applied load in a linear manner. Since in the vicinity of the apex, a spherical indenter can be approximated with a parabolic shape, the same linear relationship $\delta^{3/2}(F)$ can be used in the case of spherical indenters for penetrations, which are much smaller than the radius

of the sphere.

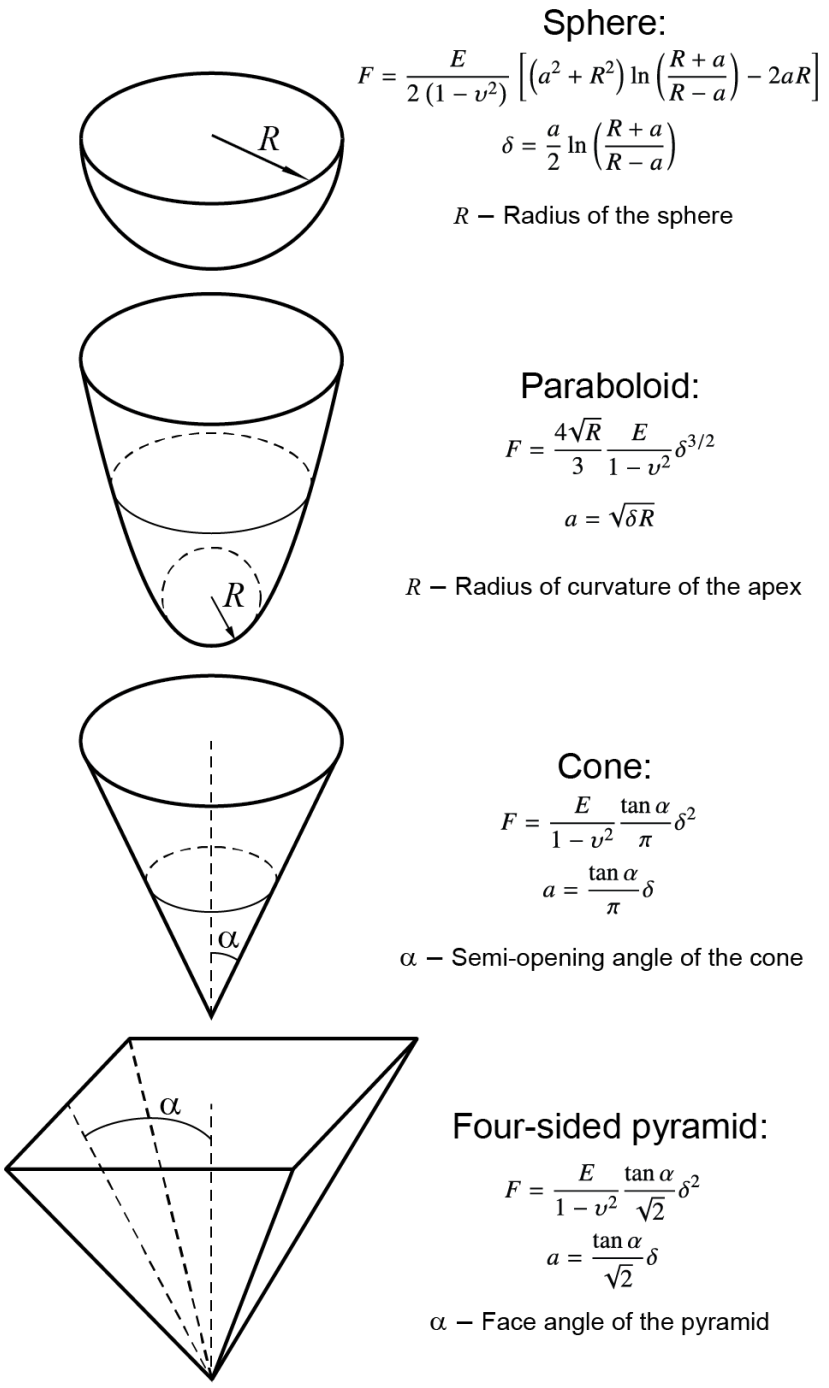

Figure 4.2: Sneddon's model equations for applied force ***F*** and contact area with effective radius of contact ***a*** for several common indenter shapes.

In the case of very soft surfaces such as that for living cells or very compliant hydrogels where during the indentation the tip penetrates deep into the sample, the tip shape should be approximated by a cone as the area under the apex of the tip becomes small compared to the total contact area. Other relations are utilized as well, for example in the case of AFM tips of well-defined pyramidal shape with square base, which is important for large deformations.[182] Therefore, the Sneddon model presents a universal solution for the indentation problem, which is not limited to spherical shapes and small indentations while providing analytical expressions for the penetration and load in the case of the hard indenter and the elastic sample.

4.1.2.3 Surface forces and elastic deformations. One of the main limitations of the Sneddon approach is the fact that it does not account for the presence of surface forces (van der Waals or Coulomb) acting on the tip during mechanical contact and in the vicinity of the surfaces. These forces are evident from the appearance of jump-to-contact and jump-off-contact instabilities observed in FDCs in common SFS experiments.[181] The jump-to-contact phenomenon appears on the approaching part of the FDC as an instantaneous snap of the tip onto the sample surface when the rate of increase of attractive forces exerted by the sample onto the tip with decreasing separation exceed the cantilever spring constant. These surface forces exert additional load on the tip-sample interface at the contact point and in the vicinity, therefore changing initial force distribution, definition of the contact point, and the penetration profile (Fig. 4.3). Over the years different models were established to account for this important effect.[73]

The first model describing the adhesive behavior was introduced by Bradley.[183] This model describes the contact between the two rigid spheres with no elastic deformation. The adhesive force, F_{ad}, acting between two spheres was estimated as $F_{ad} = 2\pi R\gamma$, where γ is the work of adhesion – the energy which is needed to separate two surfaces. Following

this simplistic approach, two more complex models describing the deformable contact with the inclusion of adhesive forces were introduced: Derjaguin-Muller-Toporov (DMT) model[178] and Johnson-Kendall-Roberts (JKR)[158] model (Fig. 4.3A). In the DMT model, which was initially developed for the case of a soft sphere indented into a rigid half space, the deformed state of the tip-sample interface is not influenced by the presence of the attractive force. There, the only deviations from simplistic Hertzian behavior are additional long range attractive surface forces acting outside of the contact region:

$$F_{ad} = 2\pi R\gamma \tag{4.3}$$

$$a = \sqrt[3]{\frac{3R(1-\upsilon^2)}{4E}(F + F_{ad})} \tag{4.4}$$

$$\delta = \frac{a^2}{R} \tag{4.5}$$

The alternative JKR model accounts for an additional deformation of the tip-sample interface, which is caused by the adhesive forces (Fig. 4.3A). These forces act only at a short range within the contact area, which is increased in comparison to simple Sneddon's model and results in the following relationships:

$$F_{ad} = \frac{3}{2}\pi R\gamma \tag{4.6}$$

$$a = \sqrt[3]{\frac{3R(1-\upsilon^2)}{4E}(F + 2F_{ad} + 2\sqrt{F_{ad}(F + F_{ad})})} \tag{4.7}$$

$$\delta = \frac{a^2}{R} - \sqrt{\frac{4}{3}\frac{F_{ad}}{R}\frac{(1-\upsilon^2)}{E}a} \tag{4.8}$$

It should be noted that the penetration calculated with the JKR model can have negative values due to the adhesion of the sample surface to the tip, whereby upon the tip retraction a physical neck can be formed between the indenter and the sample.[184] Since the JKR model completely neglects the long range interactions and the DMT model does not account for the influence of the adhesive forces in the contact region, it is evident that neither model can fully describe the complete deformational behavior of the highly adhesive elastic materials.

Maugis presented the next model (Maugis-Dugdale model, MD), which describes the limiting cases of the adhesive behavior of tip-sample interactions in the form of potential curves (Fig. 4.3B).[179] Maugis introduced the potential as a step function, known as the Dugdale potential. To describe the shape of this step function the dimensionless parameter λ (elasticity parameter) was introduced:

$$\lambda = \frac{2.06}{z_0}\sqrt[3]{\frac{R\gamma^2}{\pi}\left(\frac{3}{4}\frac{(1-\upsilon^2)}{E}\right)^2} \tag{4.9}$$

where z_0 is the effective range of surface forces.

The parameter λ can be shown to represent the ratio of the elastic displacement of the surface at the jump-off-contact point, δ_a, to the effective range of adhesive forces, h_0. Therefore, for large spherical indenters and compliant materials, $\lambda \to \infty$, whereas for small indenters and stiff materials, $\lambda \to 0$. By introducing an additional parameter, which corresponds to the ratio of applied load to the effective adhesive energy, $\bar{F} = F/\pi\gamma R$, Johnson and Greenwood constructed a full adhesive map depicting the ranges of the applicability of various contact mechanics models for a particular experimental setup (Fig.

3C).[185] For example, this map suggests that if the adhesive force at the jump-off-contact point is less than 5% of the applied mechanical load, the simple Hertzian model describes the deformations at the contact region well. Several additional models presented simplified approximations for the range of λ parameters.[59,186]

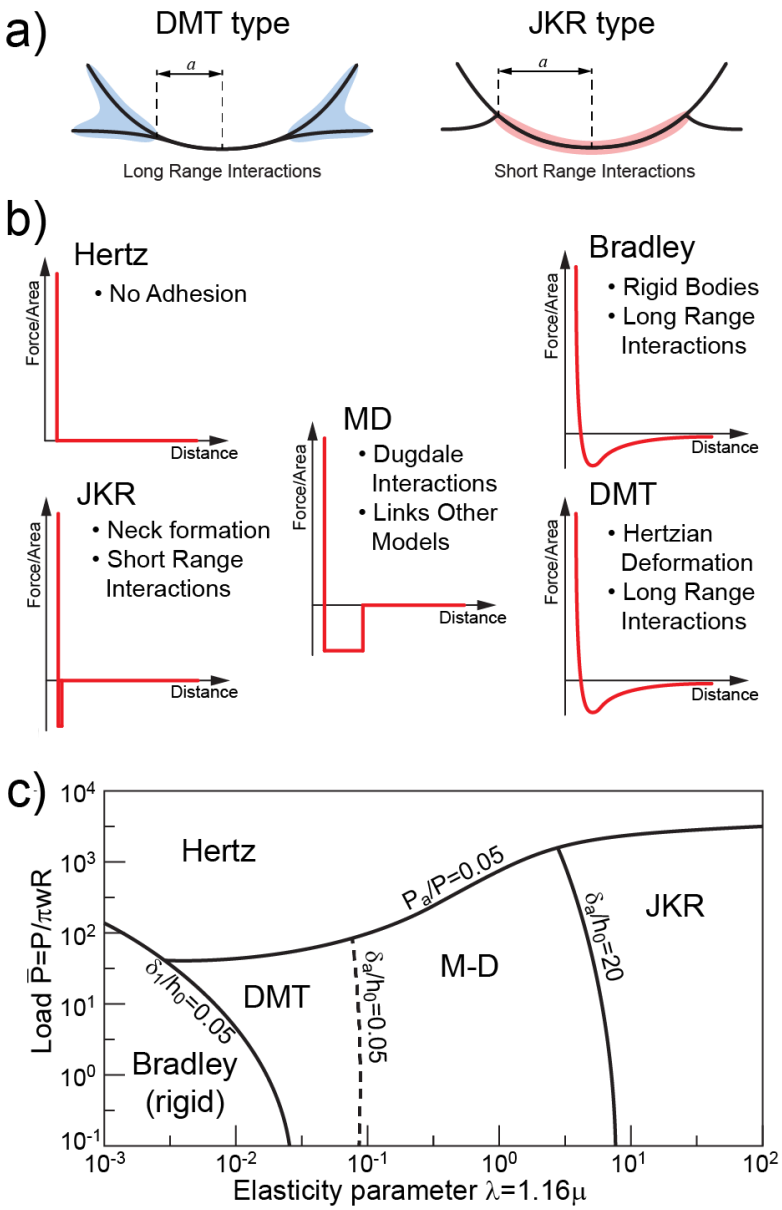

Figure 4.3: (A) Tip-sample interactions as presented by DMT and JKR models. (B) The interaction forces used in various contact mechanics models. (C) Adhesion map depicting the ranges of applicability of various contact mechanics models, adapted from 185.

4.1.2.5 Viscoelastic behavior considerations. In order to simplify the mechanical analysis for viscoelastic materials, the selection of appropriate AFM probes and environment (dry or liquid) should be considered to minimize the influence of adhesion on indentation experiments. Several approaches for the measurements of time-dependent viscoelastic properties of polymeric materials which use AFM-based routines were discussed in § 1.2 of this dissertation.

The goal of this study is to present a practical approach for the nanomechanical analysis of viscoelastic polymeric materials in glassy and rubbery states as well as in immediate the glass transition region. The "static" SFS probing method presented in this work involves viscoelastic parameters extraction from FDCs collected at a variable loading rates and different temperatures. We demonstrate that combining Sneddon's model with the common SLS model allows for the evaluation of storage and loss moduli and relaxation times in a wide range of temperatures and practical low frequencies. It also allows more precise control over cantilever motion than dynamic measurements, reducing the number of unknown parameters of the model in a frequency range relevant to practical dynamic conditions. Additionally, in contrast to creep experiments, the present probing technique does not require a feedback loop and enables precise force control (outside of initial mechanical contact), since the timescale of the practical measurements is much faster than that of the piezoelement creep.

Finally, it is worth noting that we also verified that the traditional SFS probing conducted under the assumption of elastic deformation is applicable for quantitative analysis of polymeric materials in glassy and rubbery states and still adequate for qualitative analysis in the glassy transition range. This study can be considered as natural development of the continuous efforts in the our lab devoted to the micromechanical probing of various polymer materials such as polymer blends, block-copolymers, elastomers, and

hydrogels,[187,188,189,190,191] polymer and organic coatings such as polymer brushes, self-assembled monolayers, layer-by-layer films, porous polymers, and multilayered coatings,[31,192,193,194,195,196] or individual macromolecules, microcapsules, and biological materials,[197,198,199] as summarized in a recent book.[19] Below, we discuss probing results with experimental detail summarized in the Experimental section.

4.1.3 Experimental

4.1.3.1 Materials. For this study, we selected poly(n-butyl methacrylate) (PnBMA, weight-average molecular weight 337,000, Sigma Aldrich), which is a well-known amorphous polymeric material with low glass transition temperature . Saturated PnBMA solution (150 mg/mL) in toluene was cast into a glass Petri dish and held at 40 °C under vacuum for a week to remove residual solvent and to anneal this polymer film with the thickness of about 1 mm. According to literature data, T_g of PnBMA is around 25 °C[150,200] and thus all AFM measurements have been conducted at temperatures from 10 to 55 °C.

4.1.3.2 AFM measurements. AFM and SFS measurements were performed on a Dimension Icon AFM instrument (Bruker) equipped with a Nanoscope V controller. Rectangular n-type Si cantilever probes (HQ:XSC11/ Al BS) are obtained from MikroMasch. Spring constants of the cantilevers varied from 1.8 N/m to 2.3 N/m and were measured via the thermal tuning method and selected to maximize the signal to noise ratio.[40,201] For each measurement, actual tip shape was estimated independently by scanning 10-20 nm gold nanoparticles and performing tip shape deconvolution.[202] Apex curvatures varied in the 10-50 nm range during FDC collection procedure. Tip shape measurements were repeated after probing of the polymer materials if substantial changes in forces or irreproducible jumps have been observed (e.g., due to tip contaminations). Scanner sensitivity was determined by using a sapphire crystal.

Considering that liquid bridges between the AFM tip and the sample surface can produce significant forces to distort the information provided by the AFM,[203] all SFS measurements were conducted in Ultrapure water (Millipore Corp) (18 MΩ cm). This approach abates capillary bridge formation and reduces snap-to-contact forces, thus, simplifying the data analysis dramatically. In addition, because Ultrapure water is a bad solvent for PnBMA, artifacts in the FDCs due to surface swelling are avoided and the chance for surface contamination from ambient air is significantly reduced.

A small tip deflection of 4 nm was used in the experiments as verified to be the regime with no plastic deformation. Such measurements produced deflections with high signal to noise ratio while keeping indentations in the elastic regime and forces below 5-10 nN. For the consistency of SFS measurements, the displacement ramps for all experiments were kept constant, at 150 nm. Cantilever z position was monitored via piezosensors for increased precision. Before and after the force measurements, AFM scans in light tapping mode were performed in the probing surface area to confirm the smoothness of the surface and absence of non-recovered plastic deformations after the measurements (indentation marks).

To visualize modulus variations in a full scale of times and temperatures, a set of force-volume measurements was performed at several probing frequencies. Frequency of the measurement was calculated as the reciprocal value of the time of a single FDC acquisition. Indentations at several different frequencies of 10Hz, 5Hz, 2.5Hz, 1Hz, 0.5Hz, 0.25Hz, 0.125Hz (corresponding loading rates of 3000nm/s, 1500nm/s, 750nm/s, 300nm/s, 150nm/s, 75 nm/s, 37.5 nm/s for 150 nm ramps) were performed at different temperatures in the 10-55 °C range with 5 °C intervals. For each experiment, about 30 FDC curves were collected, averaged, and further analyzed. To account for possible piezoelement creep and AFM tip contaminations, SFS measurements with deviations in non-contact part of the

curve higher than the 25% of maximum deflection observed after the contact with the surface were excluded from the further analysis. For each experiment, less than 20% of individual measurements were excluded from further averaging. At each temperature and frequency no significant deflections due to the liquid drag force were observed (e.g., see examples below). Collected FDC curves were converted to loading curves in a conventional manner and multiple runs have been averaged for further analysis.

For temperature variation experiments, samples were placed on a custom-made Peltier element/heating bath using silver conductive coating 18DB70X obtained from Electron Microscopy Sciences. Constant temperature was maintained during the experiment using a thermocouple feedback loop (ILX Lightwave LDT-5948 Precision Temperature Controller) with temperature stability better than 0.01 °C.

4.1.3.3 Evaluation of mechanical rates of deformation. To analyze acquired experimental data in the time-temperature domain, two approaches have been employed in the present study for the estimation of the timescale of the deformations. The first approach used full time of one FDC acquisition cycle as a timescale of a single experiment. The second approach used only the portion of the curve when the tip and the sample are in the contact. For the clarity the term "*apparent frequency"* will be used to characterize timescale in the first approach, while the term "*loading frequency"* will characterize the timescale related to the second approach. Because the change of the direction of the tip is controlled by the force threshold rather than by actual indentation depth, the second approach gives much more precise evaluation of the time of tip-sample interaction. As known, the contact portion of the FDC presents a varying fraction of total curve acquisition time as polymer softens during polymer transition from the glassy state to the rubbery state. Therefore, two measurements performed at the same frequency below and above glass transition will have a different tip-sample interaction times and thus different deformation rates. This time

difference presents a significant factor for the viscoelastic calculations and should be accounted for by considering actual deformation rates from FDC data.

While not precise, the first approach of the timescale calculations gives the ability to compare FDC curves collected at different frequencies and does not require precise knowledge of the contact fraction of the FDC. Therefore, it is widely utilized in the AFM community, especially in the case of simple elastic material behavior analysis, where only contact portion of the FDC can be fitted for the elastic modulus calculation. Therefore, in the part of the present work where fitting of the experimental data is performed under the assumption of simple elastic material behavior, apparent frequency is used as the timescale of the experiment. For the calculations of relaxation time (τ), and loss and storage moduli (E' and E''), actual loading frequency should be employed that represents a reciprocal value of the calculated time of tip-sample interaction.

4.1.4 Measurements of viscoelastic polymer behavior

4.1.4.1 FDC collection with low impact. In this study, FDC data was collected for PnBMA in a liquid cell at temperatures below, around, and above nominal T_g (about 25 °C).[150,200] Only the approaching curves were used for viscoelastic properties estimation to avoid large hysteresis in the course of retracting due to adhesive contributions and piezoelement creep. High capillary forces usually observed at ambient conditions for polymer surfaces (peak jump of 10-15 nN as demonstrated in Fig. 4.4B) result in high, uncontrolled initial surface deformation that compromises micromechanical probing and thus SFS measurements in ambient air were excluded. To reduce the initial deformation due to strong capillary forces, all measurements in this study were performed in liquid, where modest snap-to jumps were observed (force variation below 20 pN, Fig. 4.4A) that indeed facilitates the fine SFS probing with high accuracy and minor uncertainties after initial mechanical contact. Indentation analysis performed in this study was based on the contact portion of the force-

distance curve therefore determination of the contact point is a critical issue. Here we define the contact point as a point where the cantilever deflection deviates from the deflection baseline for more than a standard deviation of the baseline noise. For some setups, presence of adhesive forces and high noises during the measurement can mask the contact point. In the case of simple elastic behavior this can be accounted for by fitting only well-defined part of the contact curve[204]. However, in the case of PnBMA the initial contact point was well defined, as it can be judged from the behavior of the first derivative of deflection[204].

Low probing frequencies in this study were not affected by damping in liquid. The polymer surface was very smooth (microroughnesses of 0.3 nm within 500 nm x 500 nm surface areas), essentially eliminating data scattering related to topographical contributions at different probing locations (Figure 4.4C).

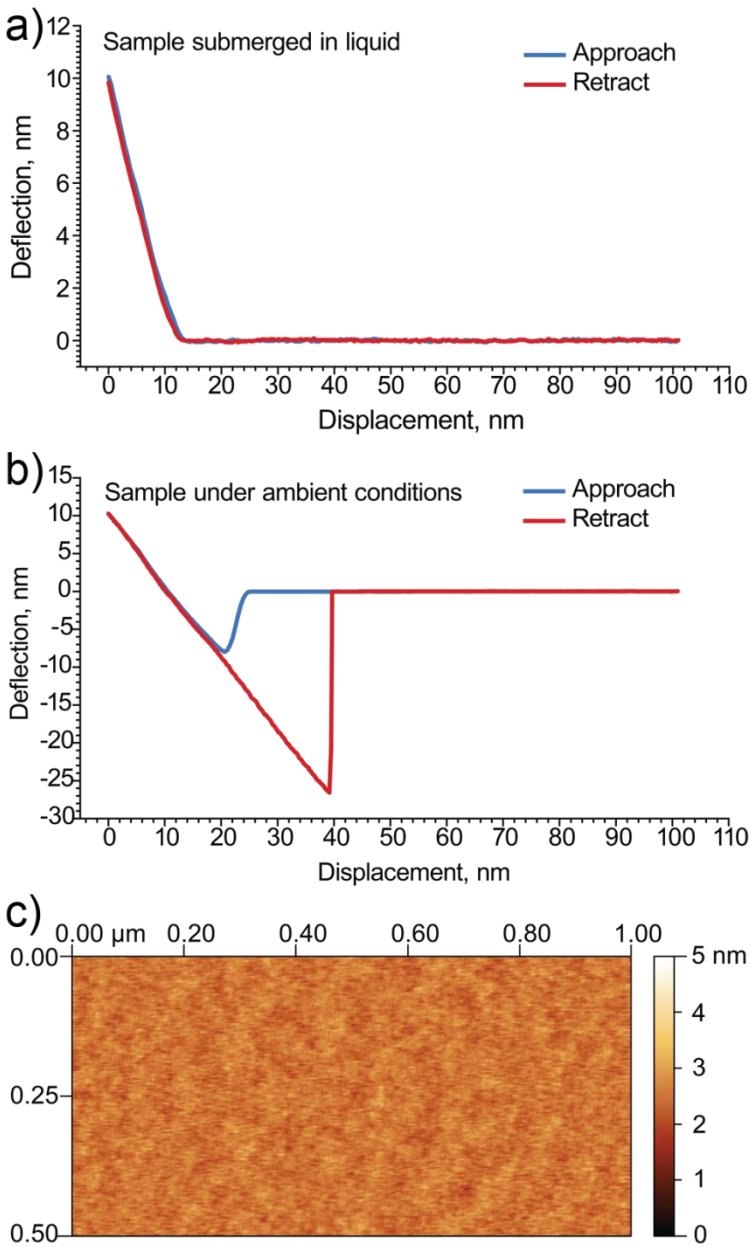

Figure 4.4: (A) Approaching and retracting curves for the in-liquid measurements of PnBMA at 25ºC and (B) same measurements in ambient humid environment. (C) AFM image of the PnBMA surface acquired in liquid at 25°C.

Examples of representative loading curves for PnBMA surface collected at an intermediate apparent frequency of 2.5 Hz (a cantilever displacement rate of 750 nm/s), averaged over at least 20 different locations, at temperatures below, near, and above the glass transition (from 10 °C to 45 °C) are presented in Fig. 4.5A. Overall, very modest indentations are

exploited in this study which are limited to 2-3 nm in the glassy state and to 10-30 nm in the rubbery state to avoid plastic deformation and long relaxation processes (see examples in Figure 4.5). The scattering of the experimental data points is very modest as well. Apparently, the polymer surface becomes more complaint as the temperature rises to above the glass transition, as indicated by the doubling of the indentation depth up to 10 nm under the same mechanical load (Fig. 4.5A). Additional heating well above the glass transition not only increases the compliance much further up to 30 nm but also completely changes the shape of the loading curve due to increasing viscous contributions with curvature of deflection vs. displacement plot varying significantly in the 30 °C – 45 °C range (Fig. 4.5A).

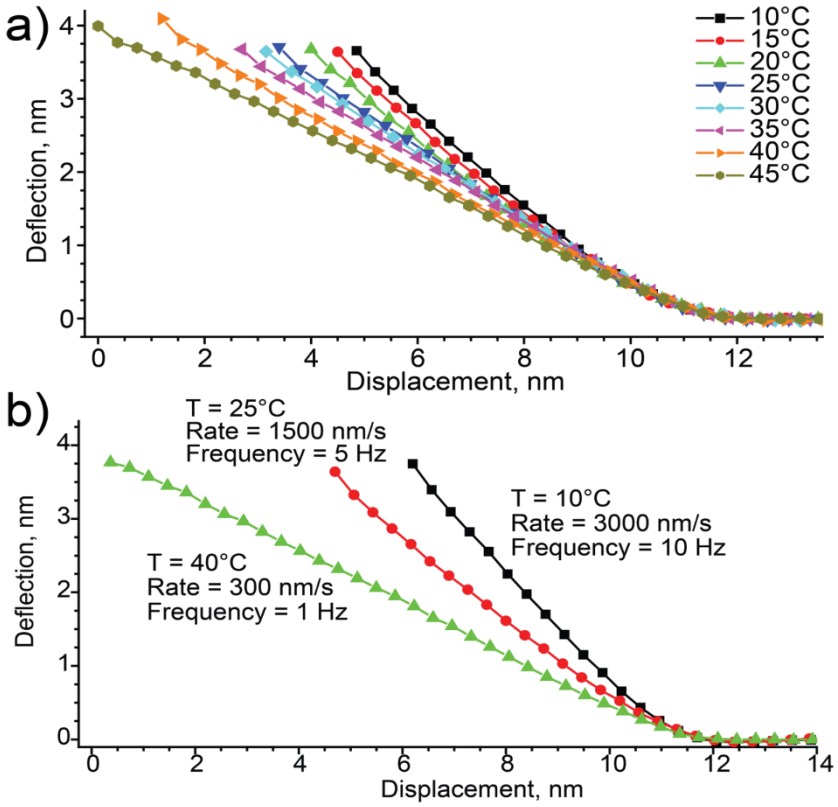

Figure 4.5: (A) Force-displacement curves for indentation experiments of PnBMA at different temperatures and at the same loading rate (750 nm/s). (B) Examples of representative force distance curves at three characteristic temperatures: below, around, and above T_g.

Several representative loading curves with different apparent frequencies for the fast (10 Hz or 3000 nm/s) measurements below T_g, slower measurements (1 Hz or 300 nm/s) at the onset of T_g and slowest measurements (0.1 Hz or 30 nm/s) above T_g are selected to show the combined role of temperature and deformation rate (Fig. 4.5B). It is apparent that, in these coordinates, the rate variation results in the difference in the deformation behavior presented in Fig. 4.5A even more pronounced. This time-temperature complex behavior can be analyzed in terms of purely elastic and viscoelastic processes within the polymeric material, as will be discussed in detail below.

4.1.4.2 Elastic deformational case. Before going into the complex viscoelastic behavior discussion, the traditional simple elastic model based upon Sneddon's analysis will be summarized below.[28] As was discussed above, assuming the AFM tip to be in the form of rigid parabolic punch (Fig. 4.2), the force applied to the elastic surface by the indenter is related to elastic modulus, *E*, as:

$$F = \frac{4}{3}\frac{a^3}{R}\frac{E}{1-\upsilon^2} \tag{4.13}$$

where $a = \sqrt{\delta R}$ is the radius of contact between the tip and the sample and $R = 2f$ is the radius of curvature of the apex of parabolic tip and f is the focal distance (Fig. 4.2). If the tip is described by the function $y = bx^2$, this effective radius can be evaluated as $R = 1/(2b)$.

Knowledge of the force applied to the indenter as a function of penetration $F(\delta)$ acquired during the loading experiment allows for the calculation of the Young modulus using simple linear slope approximation:

$$E = \frac{3}{4}\frac{1-\nu^2}{R^{1/2}}\frac{dF}{d(\delta^{3/2})} \quad (4.14)$$

It can be seen from Eqn. 4.14 that, along with other independently determined experimental parameters, the simple elastic modulus (E) is simply a proportionality coefficient between the applied force and the elastic deformation of the sample.[150] It is important to note that unlike the Hertzian contact mechanics model, Sneddon's model with a parabolic tip, which is exploited here, does not have "built-in" limitation on very small deformation depths. Although this is not critical for current studies where the radius of contact is always well below the tip radius of curvature and minute adhesive forces for under-liquid probing virtually eliminates the initial jump-in event which compromise further analysis.

4.1.4.3 Modulus variation with time and temperature space. To calculate elastic modulus in Sneddon's approximation form the data collected in the form of FDCs, the penetration values should be considered (Fig. 4.6A). Here, several representative FDC curves are shown to cover most of the range of observed material behavior from the glassy state at high loading rates and low temperatues to the rubbery state at low loading rates and high temperatures. Next, by using Eqn. 4.14, the tip penetration as $\delta^{3/2}$ is plotted versus F and linearly fitted with using a zero intercept condition (see a solid line in Fig. 4.6B). It can be seen that for SFS measurements at 10 °C and 20 °C (the glassy region for our polymer), the loading curves are perfectly described by a linear relationship as represented by Eqn. 4.14 (coefficients of determination, R^2, are 0.995 and 0.993 for 10 °C and 20 °C respectively). However, around 30 °C (close to glass transition), the loading curves start to strongly deviate from simple linear behavior (see a solid line at Fig. 4.6B) ($R^2 = 0.95$ for 45 °C). This progressing deviation indicates that at these measurement conditions the polymer surface shows temperature- and loading rate-dependent properties. Such deviations affect the evaluation of the elastic modulus accuracy which drops dramatically

at elevated temperatures and non-linear responses. Although it is apparent that under these experimental conditions, simple Sneddon's model cannot describe the material behavior adequately, it provides important insight into the overall material behavior, represents a practical elastic approximation, and thus is frequently utilized in current AFM measurements of presumably elastic solids even in the vicinity of the glass transition.[205]

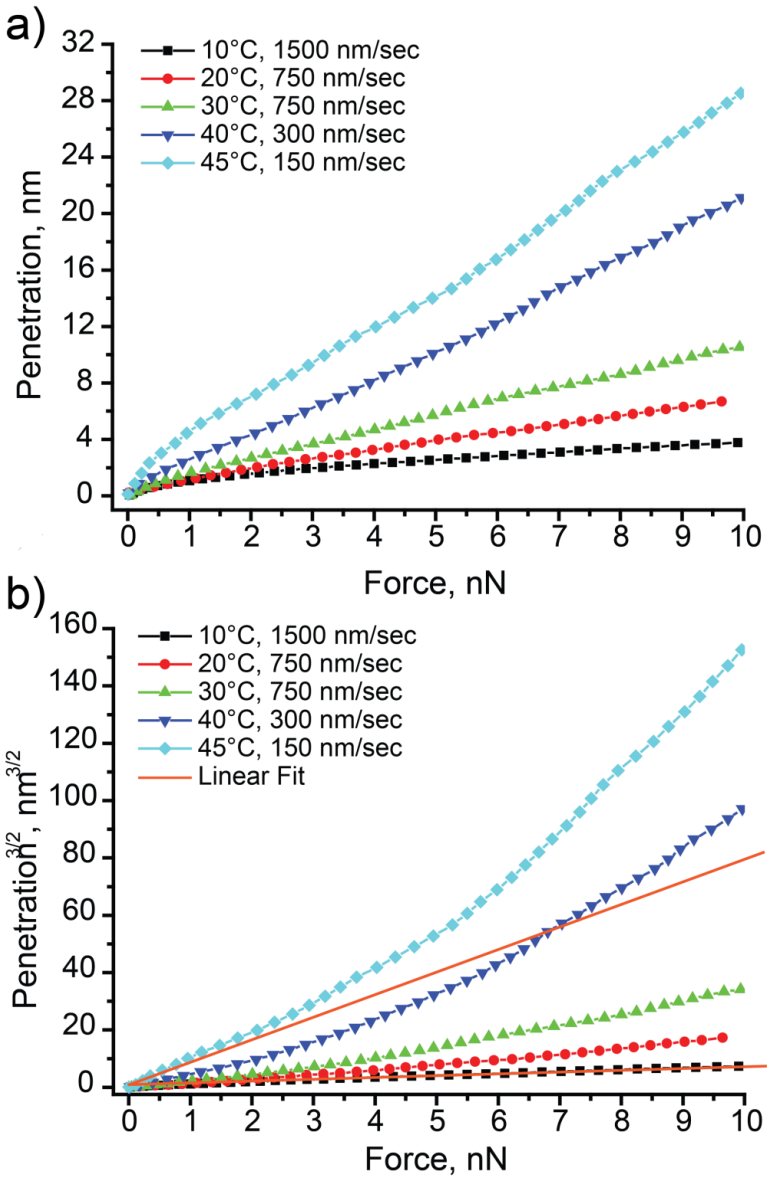

Figure 4.6: (A) Representative loading curves depicting the evolution of data with temperature increase. (B) Corresponding (penetration)$^{3/2}$ data used for the Sneddon's model and examples of linear fit of the data in elastic and viscoelastic regimes (solid lines).

Corresponding "apparent" elastic modulus values calculated from these linear fits (Fig. 4.6B) for different temperatures and probing frequencies for our model polymer, PnBMA, are summarized in Fig. 4.7A. Error bars in the plots, which are modest in different physical states, represent the calculated standard deviation from a set of about 20 individual SFS measurements. As is apparent from the analysis of this data set, at temperatures below 25 °C (below nominal glass transition of the PnBMA material) the elastic modulus remains mostly unchanged at different loading rates and approaches the absolute value of around 1 GPa, which is a common value reported for PnBMA in the glassy state.[200] As expected, at elevated temperatures, a gradual decrease in the elastic modulus values from 1 GPa to 30-50 MPa for the highest temperatures (the rubbery state) and the slowest probing frequencies were observed (Fig. 4.7A). These values are close to that reported in the literature for the rubbery state of PnBMA material.[150]

The experimental data collected here can be further converted to the universal modulus-time-temperature relationship (so-called "master curve") by using the time-temperature superposition principle.[62] Indeed, the Williams–Landel–Ferry (WLF) equation provides the relationship between relaxation processes and temperature shifts at temperature T and selected reference temperature T_{REF}:[125]

$$\log(a_T) = \frac{-C_1(T-T_{REF})}{C_2+(T-T_{REF})} \tag{4.15}$$

where $a_T = f/f_{REF}$ is the shift factor, f is the current apparent frequency and f_{REF} is the reference apparent frequency, C_1 and C_2 are constants for the material. If the reference temperature is selected to be the glass transition temperature of the material, the universal constants $C_1 = 17.44$ and $C_2 = 51.6$ can be used for amorphous rubbery materials.[5] Using these universal constants and the glass transition as a reference temperature $T_{REF} = T_g =$

25 °C for PnBMA, shift factors can be calculated and utilized to generate a universal master curve (Fig. 4.7B). Such a universal master curve presents the values of the elastic moduli as projected to a much wider apparent frequency range (10^{-3}–10^{4} Hz) and to a wider temperature interval with conversion between time and temperature scales presented on a double-horizontal axis in Fig. 4.7B.

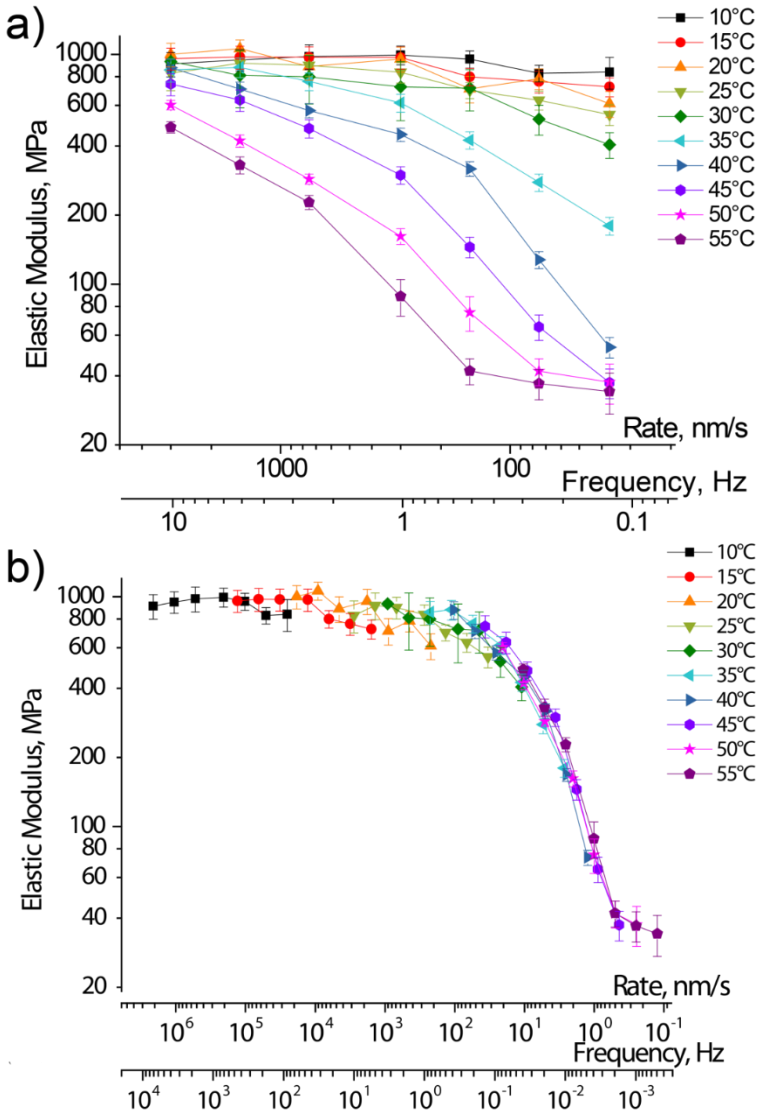

Figure 4.7: (A) The elastic moduli for the PnBMA at different experimental conditions grouped by temperatures. (B) Master curve constructed with elastic Sneddon's model through WLF equation with reference temperature of 25°C.

On the other hand, a similar analysis can be performed for the elastic modulus measurements grouped by apparent frequencies (Fig. 4.8). At higher frequencies (higher loading rates) temperature-dependent elastic modulus is small over the full temperature range. In contrast, at lower frequencies, dramatic softening of the polymer surface can be observed at elevated temperatures (Fig. 4.8A). This data can be further converted to the universal master curve as discussed above (Fig. 4.8B). By shifting the frequency curves using the same universal constants C_1 and C_2 in the relation to 1 Hz (300 nm/s), one can obtain a full master curve, which fully relates time and temperature for the elastic modulus measurements of PnBMA (Fig. 4.8B). The result of this approach is fully consistent with that generated above (Fig. 4.7B and 4.8B). Comparison of the master curves generated with two different conversion approaches shows that the temperature change is more versatile than the frequency variation in the sense that it allows for a broader range of the mechanical properties variation to be projected. Such a high sensitivity of the measured modulus to the temperature in comparison to the loading rates arises from the power dependence of the shift factor on the temperature change (Eqn. 4.15). This temperature sensitivity is important in the discussion of limitations of the time and temperature conversion procedures for the viscoelastic properties analysis.

Overall, master curves generated here from SFS measurements under an assumption of the elastic deformation closely resemble those expected from literature data for polymer material with the glass transition about 25 °C. The values of the elastic modulus in glassy (below 25 °C) and rubbery (above 50 °C) states are in good correspondence with the known literature values.[150] However, the shape of the master curves in the temperature range around the glass transition temperature with maximum mechanical energy dissipation (25-40 °C) is apparently compromised by the purely elastic deformation assumptions and, thus, the polymer material behavior in this range requires refined consideration by accounting for the dissipative behavior.

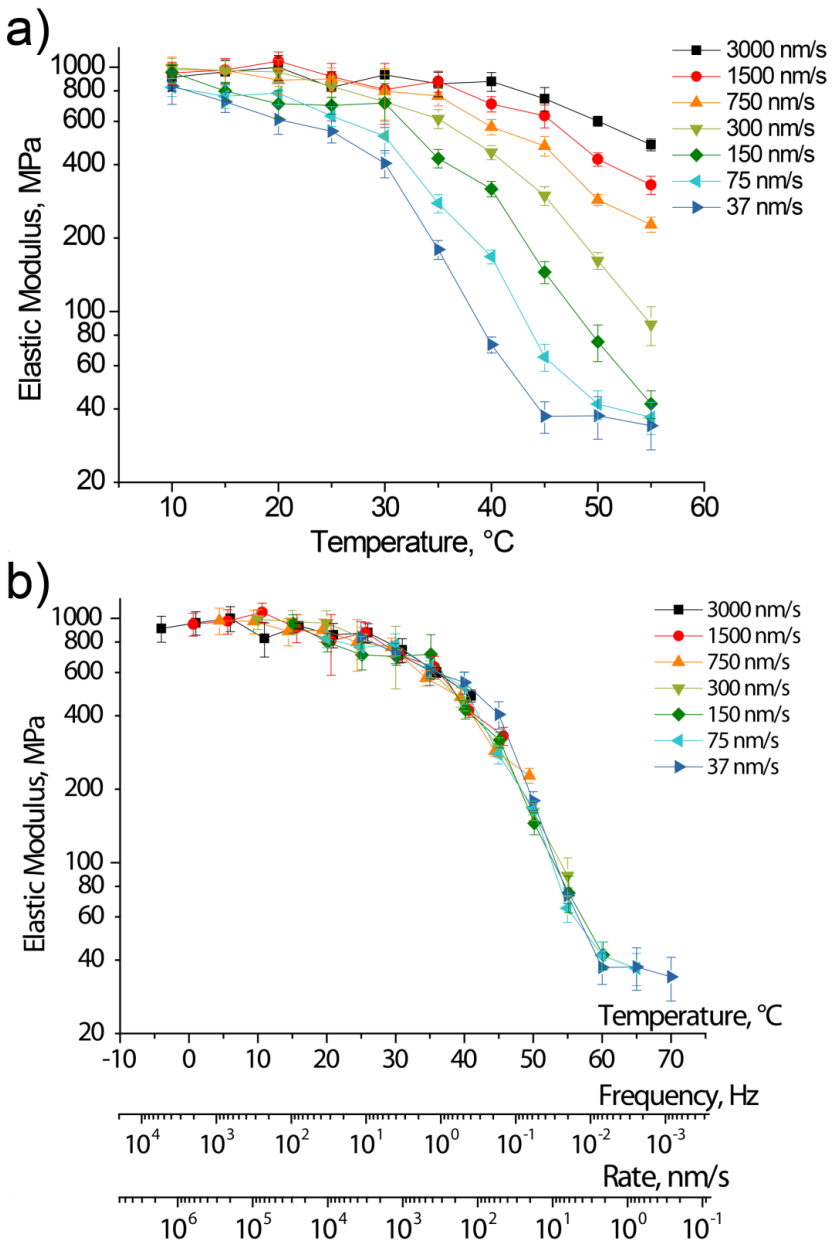

Figure 4.8: (A) Elastic moduli for the PnBMA at different experimental conditions grouped by frequencies. (B) Master curve constructed with elastic Sneddon's model through WLF equation with reference frequency at 1 Hz.

4.1.4.4 Micromechanical viscoelastic analysis. Here, we present the refined analysis of the experimental data in the glass transition region with viscoelastic SLS model, which deals with this limitation and allows for the evaluation of a full mechanical properties

profile. This traditional SLS model is represented by a spring element attached in series to spring and dashpot elements connected in parallel (Fig. 4.9A). The SLS model is well known to accurately represent the time-dependent behavior of viscoelastic materials without residual strains and has already been applied to SFS analysis.[206,207]

We do not use a more complex four element model since we concentrate on the region of the stress-deformation curve where no unrecoverable deformations are present. In contrast to SLS model, the more complex four-element model will never equilibrate due to the presence of plastic flow which is next to impossible to account for. For higher loads, which leads to unrecoverable deformation (plastic deformation), an additional viscous element should be added to adequately describe the system behavior. Such change, however, significantly complicates the data analysis and makes overall data processing extremely cumbersome, ambiguous, and unstable.[64]

The traditional SLS model possesses a very well-known time-dependent behavior, which can be represented by time-dependent modulus variation (compliances, $J \sim 1/E$, are presented in Fig. 4.9B). This general schematic shows that after an instantaneous step loading, the SLS system will immediately respond as a perfectly elastic material with an instantaneous modulus, E_0. Next, due to the presence of the dashpot with the dynamic viscosity, η, a second spring will undertake the load partially and gradually over time, until, eventually, the SLS system will equilibrate with the initial load distributed between two springs exhibiting effective infinite modulus, E_∞ (Fig. 4.9B). In the SLS viscoelastic material, at any given time t the coefficient of proportionality between the stress and the strain can be described by the creep-compliance function, $\varphi(t)$, in accordance with the relationship:[208]

$$\varphi(t) = \frac{1-\upsilon^2}{E_\infty}\left(1 - \left(1 - \frac{E_\infty}{E_0}\right)e^{-t/\tau}\right) \tag{4.16}$$

where $\tau = \frac{E_0 - E_\infty}{E_0 E_\infty}\eta$ is the relaxation time of the viscoelastic material. Thus, the creep-compliance function, $\varphi(t)$, is a representation of a single rate dependent elastic modulus of the material (Fig. 4.9B).

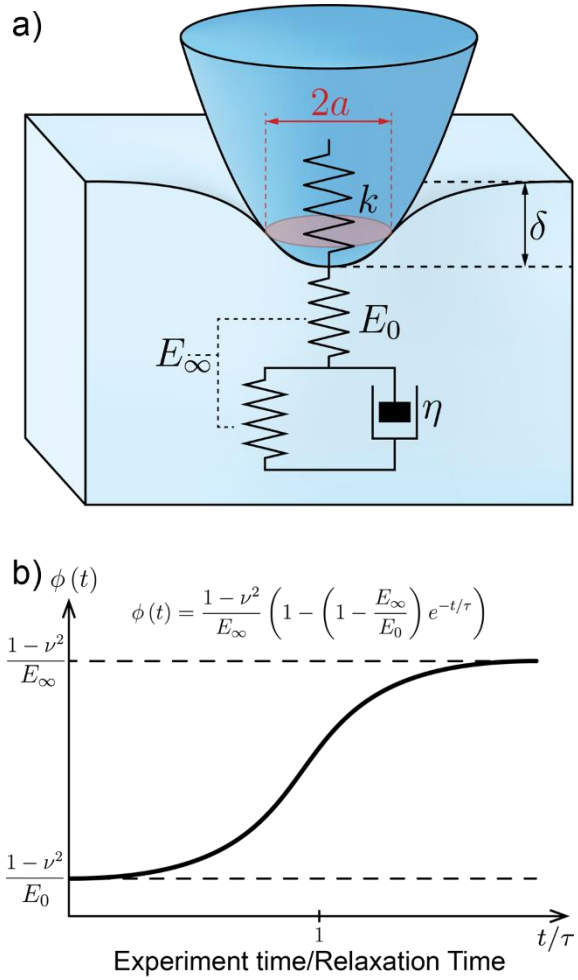

Figure 4.9: (A) Sneddon's model applied to the case of viscoelastic SLS material. (B) Creep-compliance function for SLS material.

To describe the loading behavior for a SLS material during an indentation experiment, Johnson[208] suggested the application of the viscoelastic correspondence principle to

Sneddon's elastic model. He has derived the modified relationship for the variation of the contact area a of the axisymmetric indenter represented by a complex function:[208]

$$a^3(t) = \frac{3R}{4}\int_0^t \varphi(t-t')\frac{d}{dt'}F(t')dt' \tag{4.17}$$

and the penetration depth to be calculated as:

$$\delta^{\frac{3}{2}}(t) = \frac{3}{4\sqrt{R}}\int_0^t \varphi(t-t')\frac{d}{dt'}F(t')dt' \tag{4.18}$$

It is important to note that in contrast to the case of a simple linear elastic material, Eqn. 4.18 for SLS viscoelastic material represents the loading rate-dependent relationship. As suggested by Johnson,[208] in the case of a constant loading rate $U = \frac{d}{dt}F(t)$ (common mode of operation during the SFS data collection procedure) Eqn. 4.18 can be simplified to:

$$\delta^{\frac{3}{2}}(t) = \frac{3UT}{4\sqrt{R}}\frac{1-\upsilon^2}{E_\infty}\left(\frac{t}{\tau} - \left(1-\frac{E_\infty}{E_0}\right)\left(1-e^{-t/\tau}\right)\right) \tag{4.19}$$

The three unknown parameters E_0, E_∞ and τ in Eqn. 4.19 can be found by fitting the experimental time-dependent loading data as well as independent measurements of E_∞ and E_0 under limiting conditions as discussed below. In all of the following calculations, a timescale was derived from the loading frequency as discussed in the Experimental section. It is worth noting that this analysis must only be used on the approaching part of the indentation curve, since it only accounts for the compressive load.[208]

For extremely long and short experimental times the creep compliance function presents two limiting cases of the material behavior represented by two different values of elastic moduli (Fig. 4.9B). Johnson's model inherits this feature, therefore these special cases can be explored for independent measurements of the limiting elastic moduli values, E_0 and E_∞. To analyze these extreme cases, it is useful to plot penetration in dimensionless coordinates as normalized to penetration at a selected reference time (Fig. 4.10A). Such an aproach allows for the reduction of the difference in deformation of glassy and rubbery states, therefore, facilitating the observation of overall model behavior in a broad range of loading ratesand temperatures.

Following the approach introduced by Johnson,[208] the normalized penetration is plotted against dimensionless time for several values of the reduced measurement time, T (Fig. 4.11A). In this plot, the x-axis is normalized by the loading time T (time of the tip sample contact during the approach part of FDC). The y-axis is normalized by the penetration δ_0 calculated under the assumption of infinite relaxation time, as if the material would have perfectly elastic behavior with infinite elastic modulus E_∞. With such normalization of y-axis, relative penetration at the time t/T will vary from E_∞/E_0 to 1 depending on the rate of the experiment. Using such approach one can examine the relaxation behavior at different timescales relative to relaxation time τ without knowledge of the absolute values of τ. Hovewer, one should still make assumptions about the ratio E_∞/E_0 of elastic properties of the model in the extreme cases of short and long measurement times. As an example here, we use the values $E_0 = 958\,MPa$ and $E_\infty = 30\,MPa$ obtained experimentally for our PnBMA materials at extremely high and low probing frequencies.

The two limiting cases where relative penetration changes linearly with time stand out immediately from this reconstruction (Fig. 4.10A). Under fast loading times, $t \ll \tau$,

Eqn. 4.19 is reduced to the simple elastic relationship (Eqn. 4.14) with $E = E_0$. On the other hand, at very slow measurements for the points where $t \gg \tau$, the behavior is again elastic with $E = E_\infty$. For the second case, however, it is important to note that linearity does not hold for a limited probing time range, where $t \sim \tau$, as can be seen in Fig. 4.11A for case $T = 1 - 10\tau$. Therefore, under these conditions, one should use the latest stages of the loading curve for the linear fitting in order to analyze the quasi-elastic behavior. For the relaxation times in between those two extreme cases, nonlinear behavior is observed with continuous slope variation during the loading cycle (Fig. 4.10A).

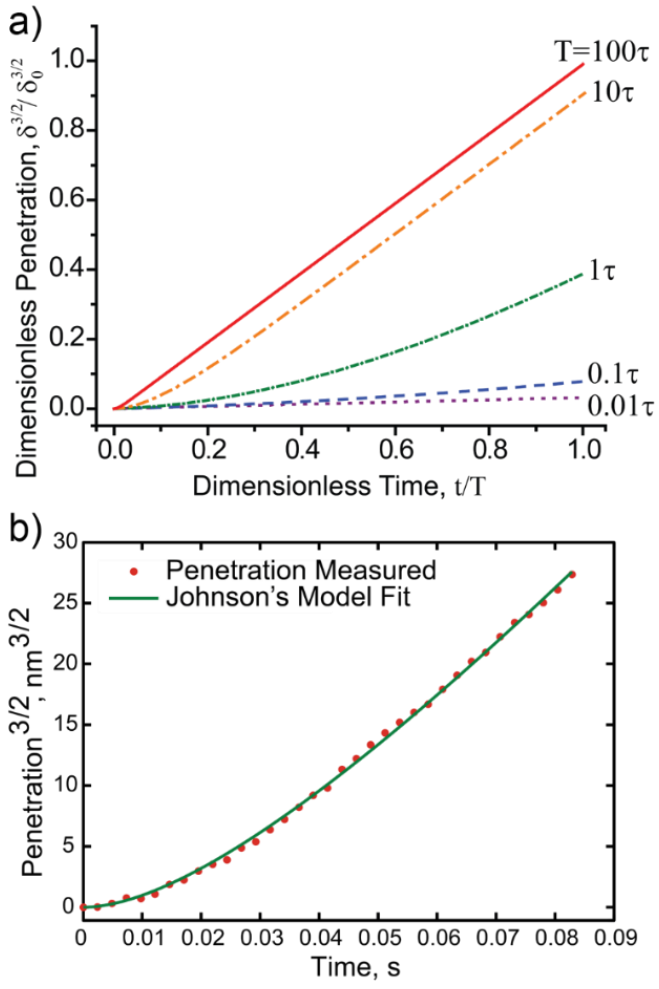

Figure 4.10: (A) Theoretical penetration curves for SLS materials with different relaxation times plotted in dimensionless coordinates. (B) Example of fitting of the actual experimental data with Johnson's model.

An important practical observation can be further made from the dynamic penetration reconstruction presented in Fig. 4.10A. Since in the extreme cases of slow and fast measurements described above the SLS model follows the standard elastic behavior, the parameters E_∞ and E_0 can be estimated from the experimental measurements at these very different loading time conditions using Eqn. 4.14. SLS model assumes no variation in the infinite and instantaneous moduli with the changes of the timescale of the measurement. Therefore, the limiting parameters E_∞ and E_0 can be used for the calculations outside of the linear deformation regions. According to this consideration, values of relaxation time can be found by fitting the experimental penetration data using Eqn. 4.19 with the known values of E_∞ and E_0 with τ as the single fitting parameter.

Taking into account aforementioned behavior of the SLS model, the following analysis procedure was adapted in this study and can be recommended as a standard procedure. Firstly, the values of E_0 and E_∞ must be experimentally found by fitting the loading data for the limiting regions of the perfect elastic behavior at low temperatures and high frequencies for E_0 and, inversely, at high temperatures and low frequencies for E_∞. The loading curve was assumed to be linear if the standard error of the linear fit was less than 5%.[209] Notably larger deformational stages were used for E_∞ calculations to meet $t \gg \tau$ condition (for example, the curve collected at 45 °C, Fig. 4.6B). Therefore, from the experimental data for PnBMA material, these values were calculated to be $E_0 = 958\ MPa$ and $E_\infty = 30\ MPa$. Both values correspond well to limiting values derived from the master curve (Fig. 4.7B) and are indeed close to that reported for PnBMA material in glassy and rubbery states.[150] Thus, these values were used for further analysis in the viscoelastic regime.

Before going into the analysis of the deformation in the viscoelastic region the load application should be discussed. The piezoelement does not apply pressure to the tip-sample contact region directly. Instead, a base of the compliant cantilever is displaced, therefore, the actual applied force depends on the force balance between the deflected cantilever and displaced sample surface. In the case of fast loading in the elastic regime, the equilibrium between the tip and the sample is instantaneous, and therefore the tip of the cantilever moves with the same rate as its base. However, in the viscoelastic regime, the presence of a dashpot in the system does not allow for the instantaneous deformation of the material, resulting in a lag between the motion of the base of the cantilever and its tip.

Examples of this behavior are presented in Fig. 4.11 as actual time-dependent deflection data sets for the extreme cases of fast and slow measurements (apparent frequencies 10 Hz and 0.1 Hz) and two temperatures (10 °C and 45 °C). It is apparent from these examples, that at 10 °C motion of the cantilever is linear with time and the approach and retract portions of the curve are symmetrical. When the PnBMA is heated to 45 °C the viscoelastic behavior becomes prominent as the loading becomes non-linear and asymmetric against the point of the maximum deflection, which is especially notable for the 0.1 Hz case (Fig. 4.11).

Therefore, although the base of piezoelement extends at a constant rate in all experiments, Eqn. 4.19 derived for a constant loading rate is limited to fitting data collected at high rates and low temperatures. However, since E_0 and E_∞ were determined from the elastic conditions, the relaxation time τ is the only unknown parameter and Eqn. 4.18 can be used to fit the loading data with the $dF(t')/dt$ calculated from the smoothened deflection data. Fitting was also done with Eqn. 4.19 calculated under the assumption of a constant loading rate. Experimental data was analyzed by using unconstrained nonlinear optimization with MATLAB software.

It is worth noting that comparison of the fitting errors and calculated relaxation times showed less than 5% difference between analytical (linear) and digital (actual) forms of the Johnson's model in the cases of the highest nonlinearity of the loading rates (around 45 °C, Fig. 4.11). However, since the computational time for fitting with Eqn. 4.18 is greater than 10-fold more time consuming, all calculations were performed under the constant loading rate assumption (Eqn. 4.19). An example of such fitting is presented in Fig. 4.10B for the indentation measurements performed at 40 °C at 2.5 Hz apparent frequency (750 nm/s loading rate). In this particular case, the relaxation time was found to be $\tau = 0.7s$.

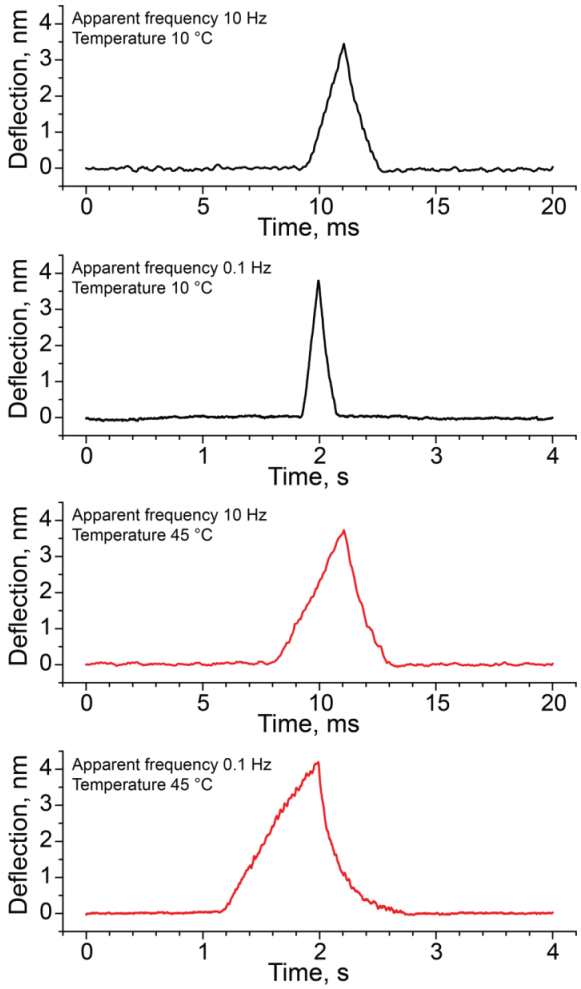

Figure 4.11: Examples of the deflection vs. time data collected for PnBMA at 10 °C and 45 °C with apparent frequencies 10 Hz and 0.1 Hz.

Similar SLS analysis was performed at different temperatures and resulted in the evaluation of the temperature dependency of the relaxation times at several different temperatures above T_g (within 35-55 °C, Fig. 4.12). For temperatures below 35 °C, loading curves showed very small deviations from the linear elastic behavior and, therefore, the relaxation time estimation could not be performed properly because of the relaxation times being much faster than the measurement times. Assuming Arrhenius-type behavior in this temperature range and plotting $\ln(\tau)$ versus inverse temperature, $1/T$, the apparent activation energy associated with relaxation processes involved in the material deformation can be estimated from the slope of the experimental data (Fig. 4.12A). This way, the apparent activation energy was found to be around 230 kJ/mol, which is close to the values found in the literature for the relaxation processes related to unfreezing of segmental mobility of macromolecular chains of PnBMA during the glass transition.[210,211]

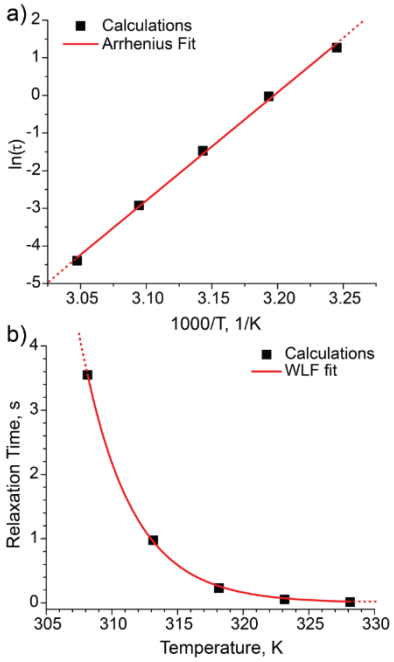

Figure 4.12: (A) Arrhenius plot for the temperature dependence of relaxation time and its linear fit (left). (B) Absolute values of relaxation time calculated through Johnson's viscoelastic model and WLF equation fit of relaxation time data.

Next, the temperature variation of the relaxation time for a wider temperature range was evaluated by using the extrapolation from the WLF equation. In this approach, the dependence of relaxation time on temperature is analyzed by employing a WLF-type relationship in the form:[7]

$$\tau = \tau_{REF} \cdot 10^{\frac{-C_1(T-T_{REF})}{C_2+(T-T_{REF})}} \tag{4.20}$$

The corresponding fitting of the experimental data resulted in a wide spectrum of relaxation times (Fig. 4.12B). Fast relaxation times of about 10 msec were evaluated in the rubbery state at the highest temperatures probed here (around 55 °C). However, the relaxation process slows dramatically to about 4 sec at lower temperatures close to the glass transition. It is important to note that these values of the relaxation time are close to the independent literature values obtained by photon correlation studies for the same polymer in a similar temperature range.[211]

Finally, by using the values of relaxation times measured above, it is possible to fully characterize mechanical properties of PnBMA in a wide temperature range by using the classical relationships derived from SLS model for viscoelastic materials. In this model (see above discussion and Fig. 4.9), the values of the storage modulus E', loss modulus E'' and loss tangent E''/E' can be calculated by using the relaxation times τ and limiting values E_0 and E_∞, which have been measured independently:[212]

$$E' = E_\infty \frac{1+\omega^2\tau^2(E_\infty/E_0)}{1+\omega^2\tau^2(E_\infty/E_0)^2} \tag{4.21}$$

$$E'' = E_\infty \frac{\omega\tau(1-(E_\infty/E_0))}{1+\omega^2\tau^2(E_\infty/E_0)^2} \quad (4.22)$$

where ω is the angular frequency and can be calculated from loading temporal frequency f through the relation $\omega = 2\pi f$. It is important to note the difference between tip-sample interaction time and an apparent measurement time as discussed in the experimental section.

The final evaluation of the viscoelastic mechanical properties from the SLS viscoelastic model by using Eqns. 4.21 and 4.22 for PnBMA is presented in Fig. 4.14. Relaxation times outside the 35-55 °C region were extrapolated from the experimental data using Eqn. 4.20. For the following calculations, the reference tip-sample interaction time was selected to correspond to a standard loading frequency of 1 Hz. The temperature variations of E', E'' and E''/E' in the temperature range of 10-70°C derived from this analysis and experimental data show characteristic features of empirical dynamic measurements of polymeric materials with characteristic features of a glass transition (Fig. 4.13).[5] Since the relaxation values were extrapolated using the 35-55 °C temperature region, β-relaxation below T_g is not included in the reconstructed plot and thus loss modulus shows a symmetrical shape and reaches zero from both sides.

It is important to note the difference of this plot and bulk dynamic mechanical analysis (DMA) measurements.[213] During conventional DMA measurements the presence of additional group relaxation in the glassy state causes the left shoulder of loss modulus to raise by 5% of its maximum value. The storage modulus shows the transition region at 25-50 °C with a dramatic drop in the modulus value during the transition from the glassy state to the elastic rubbery state. An onset of sharp modulus change lies around 27 °C, which corresponds to the glass transition of PnBMA.[150,200]

The maximum value of the loss tangent, calculated from the SLS model, is shifted to an elevated temperature (around 40 °C), which is consistent with the common dynamic mechanical measurement trends for polymeric materials in the viscoelastic regime.[62] It is important to point out that Eqns. 4.21 and 4.22 exhibit dependence on measurement rate ω and therefore plots for E', E'' and E''/E' will be shifted along the temperature axis if different loading frequencies other that 1 Hz are selected. Another important feature, which should be noted here is the fact that Eqn. 4.20 is not valid below T_g, where a special form of the Arrhenius dependence should be used[62] and, therefore, the relaxation times cannot be accurately estimated from the proposed extrapolation in this temperature range. However, glassy materials show purely elastic behavior under small deformations and thus the mechanical response under these conditions can be described by the elastic model.

It is useful to compare the results for storage modulus variation reconstructed in Fig. 4.13 with the linear penetration data fitting (elastic approximation) to evaluate the applicability of simple Sneddon's model for the viscoelastic regime. To compare two sets of evaluations the following procedure was used. Penetration versus force data was reconstructed for 1 Hz measurements in the 10-70 °C temperature range using measured relaxation times τ along with the independently measured limiting cases of modulus values E_0 and E_∞ using Eqn. 4.19. Next, these curves were fitted using traditional Sneddon's approach to obtain "integrated" elastic modulus value, E, for each temperature under the elastic approximation (Fig. 4.13, dashed line). Reconstructed penetration versus force data was used instead of the experimental data in order to compare only the mathematical models and neglect the possible contribution of the measurement noise introduced by the SFS measurements.

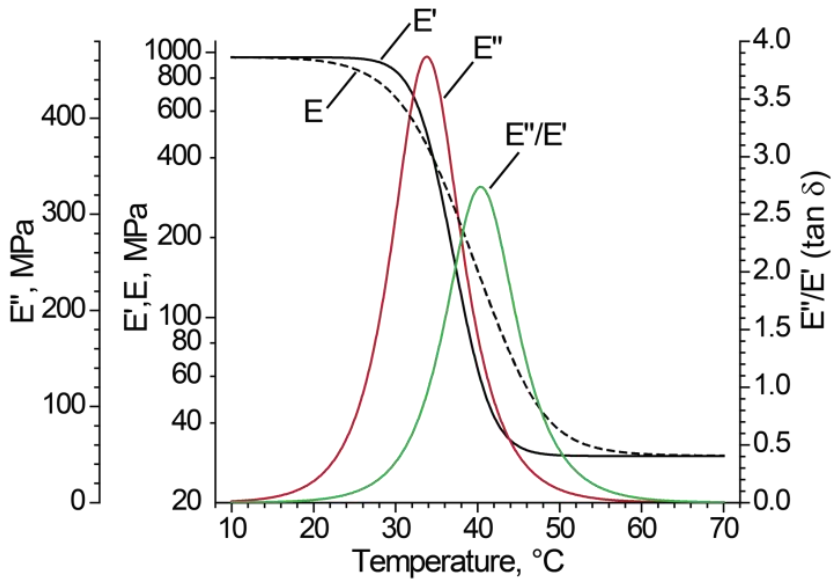

Figure 4.13: Storage (E') and loss (E'') moduli and $\tan\delta$ plots for PnBMA under SLS behavior assumption (solid lines). Master curve for "apparent" elastic modulus for PnBMA calculated from elastic Sneddon's model fit of the penetration data acquired from SLS model (dashed line).

From the temperature variations for the elastic modulus values restored under purely elastic conditions assumption, we can conclude that Sneddon's elastic model accurately predicts the behavior of storage modulus E' in both glassy and rubbery regions with deviations less than 5% (Fig. 4.13). However, in the glass transition region of the polymer material (from 25 to 55 °C), the differences between E' values calculated with the viscoelastic model and that derived from purely elastic model can be substantial. For example, at 10 °C below glass transition temperature, the apparent elastic modulus is 20% below true storage modulus. Moreover, the most pronounced difference (more than three-fold) is observed within a narrow temperature range (around 43 °C) with the highest loss of mechanical energy where the loss tangent E''/E' reaches its maximum value (Fig. 4.13). Such high differences are caused by the fundamental fact that in this highly viscoelastic region the $\delta^{3/2}$ versus F plot is highly nonlinear and cannot be even remotely approximated with linear relationship correctly (Fig. 4.6). Such a large deviation renders simple elastic analysis incorrect and irrelevant by overestimating the true storage modulus manifold by

not considering sharply increased contributions from the dominating loss modulus. In this region of active unfreezing of segmental chain motion and steep increases in mechanical energy dissipation, the traditional Sneddon-based elastic probing measures only initial fast deformational response and time-dependent resistance is essentually interpreted as rising elastic modulus rather than increasing contribution of the loss modulus component.

Again, after full transition to the elastic rubbery state at elevated temperatures (above 50 °C for PnBMA), the apparent values of the elastic modulus evaluated with the purely elastic model becomes close to the true value due to dramatic reduction of the loss modulus and again returns to the elastic deformation regime (but with higher deformation, Fig. 4.13). Overall, this analysis shows that outside of a temperature region which can be defined as T_g ± 15 °C, the Sneddon's elastic model can be applied for the accurate quantitative determination of the true elastic modulus with a high accuracy (within ± 10-15%). However, in a close proximity to T_g (approximately 30°C transition range for this material), the "apparent" value of the elastic modulus derived under the assumption of elastic deformation deviates manifold from the true storage modulus due to dominating energy dissipation which is unaccounted for by the elastic model. In this temperature range, the SLS viscoelastic model must be used in conjunction with the Johnson-Sneddon treatment to restore true values of both storage and loss moduli at low deformational rates relevant to practical applications of polymeric materials.

4.2 Data analysis for different tip geometries

The data obtained from AFM-based mechanical properties probing methods must be subjected to specific models for deconvolution of the effect of the probe's tip size and shape. While analytical models have been developed to assist in this endeavor, a thorough understanding of the limits of these models is essential to fitting data accurately. In this section, we explore the relationship between three different analytical tip shape models for

the AFM tip (spherical, parabolic, and conical indenters) and present an analysis of mechanical testing on selected materials. Along with this, we present a simple numerical method for computing the contact radius for true spherical contact. The role of tip size (large vs small radius) on the limitations of data analysis and the benefits and drawbacks inherent to different tip sizes is discussed. Our analysis demonstrates the ability to accurately apply multiple models to a given data set, while also showing the limitations of simple analytical models to accurately describe tip-sample interactions outside of certain indentation regimes.

4.2.1 Introduction. Surface micromechanical properties calculations involve specific contact mechanics models which closely resemble actual tip-sample contact geometry. It is known that even for the simplest cases of semi-infinite elastic half-spaces and axisymmetric punch indentations, the calculated elastic modulus will strongly vary with the size of the probe and punch profile shape. Often this geometry is not precisely known, and as a result the standard Sneddon's model for a paraboloidal indenter on a flat half space may be improperly applied as opposed to say a conical, or spherical indenter. Furthermore, it is vitally important to precisely monitor and control sample deformation. This is especially true for very soft material surfaces where the nature of the tip-sample contact geometry can change due to increasing penetration, or in the case of a thin film on top of a the stiff substrate which could increase apparent modulus. In the case of compliant cells, or other soft materials with irregular shapes, increased forces may lead to structural deformations instead of the local ones, which will yield structural rigidity instead of the localized mechanical properties the investigator may be seeking.

In this section several aspects of measurements of elastic properties of materials with AFM are discussed. The effects of tip shape variation on FDC fitting and elastic modulus extraction as well as importance of characterization of actual tip shape for elastic modulus

measurements are examined. In particular, we will discuss parabolic, spherical, and conical models and will examine specific cases where these models should be used. In addition we will introduce improved algorithm for fast fitting of FDCs for spherical tip shape approximation, as spherical model is the only model, where there is no analytical equation for tip-surface contact area dependence on penetration. Therefore, some discussion is devoted to describing our algorithm for numerically solving the parametric equation for determining the relationship between force and contact radius in the case of a truly spherical indenter shape. Additionally, we will show how to properly characterize radius of curvature of the probing tip radius, and the potential errors associated with fitting a spherically-shaped tip with a parabolic equation. Furthermore, all of these analysis procedures have been incorporated into a next generation of analysis program, *Micromechanical Analysis (MMA) Software* introduced in our lab.

In addition we discuss how probe size affects results of FDC fitting by using as example soft synthetic and biological materials in dried and swollen states. For that purpose we used silicon probes annealed at high temperature to achieve higher tip curvature.

4.2.2 Experimental

4.2.2.1 Materials. Regenerated silk fibroin was obtained via extraction from Bombyx mori cocoons, as described in Chapter 3.

In this study we also use examples from a commercially available soft polymeric contact lens, Balafilcon A (Purevision, Bausch & Lomb Inc.). The lenses were measured immediately after removal from their original blister pack containing saline solution and discarded after one day of measurements. The lenses were mounted according to procedures outlines in § 3.1.2.

In one example, we use the polystyrene (PS, weight-average molecular weight ~250000 g/mol, Sigma-Aldrich), which is a well-known amorphous polymeric material with values of elastic modulus frequently reported in the literature to be around 3 GPa. A saturated PS solution (150 mg/mL) in chloroform was cast in a glass Petri dish and held under vacuum for several days to remove solvent. The final thickness of this substrate was on the order of 1-2 mm. AFM measurements were made directly on the top surface of the PS substrate without removing from the glass Petri dish.

4.2.2.2 Atomic force microscopy. All AFM measurements were performed using a Dimension Icon microscope (discussed in § 3.2).

In some cases we used moderately-sized probes, obtained via annealing a fresh tip in air at 1100 °C. In these cases in addition to standard methods, tip shape was also independently investigated by using by collecting SEM images on a Hitachi S-3400N thermal emission SEM. AFM tips were placed in a spring loaded clamp and scanned in ultra-high vacuum at magnifications of ~25k and ~100k with an accelerating voltage of 5 kV.

Scanner deflection sensitivity was determined by collecting force distance curves (FDCs) on a sapphire crystal. The cantilever spring constant, *K*, was measured using the thermal tune method.[214,215] Topography images were collected on the sample surface prior to taking FDCs (to check for surface uniformity) in peak force tapping mode using the established procedure[56] where the AFM tip is moved sinusoidally in the z-direction (normal to the surface which is being measured) and a user defined force (typically a few nN) is used as a feedback in order to track the surface topography. Scan areas ranged from 500 nm x 500 nm to 20 µm x 20 µm using resolutions of either 512 x 512 pixels or 1024 x 1024 pixels. Scan rates were chosen within 0.5 - 1 Hz.

4.2.3 Discussion

4.2.3.1 Spherical versus parabolic tip shape. For the case of truly spherical contact, the contact equations become much more complicated as there is no analytical solution which relates applied force to penetration depth. In this case the applied force is related to the contact area radius via Eqn. (4.23):

$$F = \frac{E}{1-\upsilon^2}\left[(a^2 + R^2)ln\left(\frac{R+a}{R-a}\right) - 2aR\right] \tag{4.23}$$

while the penetration depth is separately related to the contact area radius Eqn. (4.24):

$$\delta = \frac{a}{2} ln\left(\frac{R+a}{R-a}\right) \tag{4.24}$$

This difference in the contact behavior applicability is related to the fact that the contact area for the spherical indenter is finite and cannot exceed the radius of the indenter, which can be the case for many probes tips (for example, see Fig. 4.14A, B), whereas for the parabolic indenter this area increases indefinitely and is proportional to the square root of penetration (see Fig. 4.2). Although for a wide variety of hard materials large penetrations will cause plastic deformations and cannot be fitted with the elastic model.[26] However, for many soft polymeric materials large penetrations (δ on the order of several R) are easily achieved in the elastic regime above glass transition.[26]

Fig. 4.14C shows penetration depth versus contact area radius both normalized to indenter radius, which allows for the examination of the difference in the contact area between the two models. For simplicity, in the following discussion, we assume the radius of the spherical punch, R, to be the same as the radius of curvature of the apex of a paraboloidal punch.

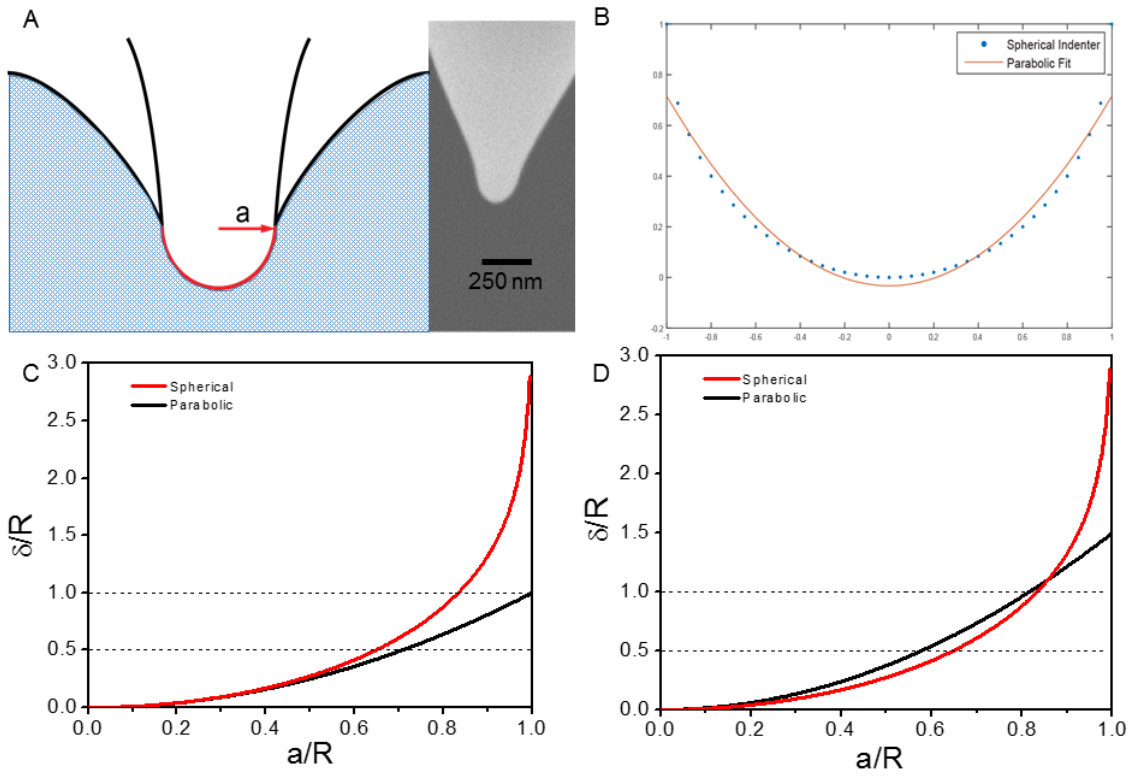

Figure 4.14: (A) Graphical schematic showing an example of how the end of an AFM tip could behave as a spherical indenter wherein the maximum contact radius does not exceed the radius of the spherical cap. Also shown is an SEM of an annealed AFM tip which displays a similar shape to the schematic. (B) Example of fitting of the spherical indenter with the parabolic models. (C) Differences between the contact area changes with penetration for the spherical indenter with radius R and parabolic indenter with the apex curvature 1/R. (D) Comparison between parabolic and spherical models with radius of curvature for the apex of parabola equals to 0.6675R.

Under these conditions, the initial regions of the penetration curve for both models show the same δ/R versus a/R. This is a consequence of Eqn. 4.24 being the limiting case of Eqn. 4.5 for small a (or for small δ). However, there is a large discrepancy between parabolic and spherical model in the terms of contact area for larger penetrations. It is ~9% for $\delta = 0.5R$ and grows to ~20% at $\delta = 1.0R$ (See Fig. 4.14C, and Fig. 4.14A for visualization of physical reason for such deviation). Therefore under relatively large indentation depths incorrect selection of the fitting model can result in substantial errors in

the calculated elastic modulus value. This is especially true for the case for some annealed tips with larger radius and used AFM tips, which each have a unique shape (Fig. 4.14A).

In general, if one would try to approximate a spherical indenter with a parabolic profile under conditions of moderate to high penetration depth, the radius of curvature at the apex of the parabola would be smaller than R, thus increasing discrepancy between the two models even more than discussed above. As an example, we have assumed a dimensionless perfect sphere with a radius of $R = 1$ (Fig. 4.14B). Fitting this profile using points up to $0.7R$ with the general formula for a parabolic profile, $y = ax^2 + b$ gives the values $a = 0.7491$ and $b = -0.0334$, which gives $R_{parabolic} = \frac{1}{2a} = 0.6675$. In this case the curves of δ/R versus a/R are different than those shown previously (see Fig. 4.14D), with 22% discrepancy at $\delta = 0.5R$ and just 2% at $\delta = 1R$. But in both cases error dramatically grows beyond the threshold: $\delta \cong 1.5R$.

In terms of elastic modulus calculation the main difference between the parabolic and spherical model is absence of an analytical equation which directly relates force and penetration for semi-spherical shape (i.e. the experimental values that are easily acquired from FDCs). This is in contrast to the parabolic and conical models (discussed below), where force is proportional to the penetration through the power law and the elastic modulus is calculated through the constant of proportionality. In order to calculate modulus using a truly spherical indenter, it is thus required to first calculate contact area corresponding to each penetration in the experiment through the Eqn. 4.24 and then use Eqn. 4.23 to calculate the modulus. Since Eqn. 4.23 is nonlinear and does not have an analytical solution, solving for a can take considerable amounts of time using simple minimization algorithms, especially for gathering statistics for multiple curves with high numbers of data points which is not very practical solution.

Another problem of the simple minimization algorithm is the precision in the contact area calculation for high penetration values (see Fig. 4.14C, D), since large changes in penetration produce only minute changes in the contact area.

In order to get around this complication, we have developed fast calculation algorithm, which allows for real-time calculations of elastic modulus. The algorithm exploits the monotonic behavior of Eqn. 4.23 as well as the fact that the function $a(\delta)$ has limit at $a = R$. Values of penetration δ are known, so a can be calculated from Eqn. 4.25 to get the parameter in the brackets in Eqn. 4.23 and this value should be calculated for each a. In order to easily perform this calculation we propose Newton's method for developing values of a from δ. Given an initial guess on a_0, the value of $a(\delta)$ can be calculated iteratively:

$$a_1 = 1 + \frac{\delta(a_0)}{\delta'(a_0)} \tag{4.25}$$

…

$$a_n = 1 + \frac{\delta(a_{n-1})}{\delta\prime(a_{n-1})} \tag{4.26}$$

The formula for the first iteration of finding of the contact radius becomes:

$$a_1 = a_0 + \frac{a_0 ln\left(\frac{R+a_0}{R-a_0}\right) - 2\delta}{ln\left(\frac{R+a_0}{R-a_0}\right) + 2\frac{Ra_0}{(a_0^2+R^2)}} \tag{4.27}$$

However the method requires values of a_0 as an initial guess. The nature of the Eqn. 4.24 ($\delta(a)$ is monotonically increasing function and contact area a has the limit $a = R$) necessitates that the initial guess, a_0, should always be bigger than the precise value of

$a(\delta)$, but smaller than the tip radius R. We propose the following algorithm to find a vector of initial guess values (Fig. 4.15).

The general formula for such a guess will be:

$$a_0(n) = -\frac{1}{n^2} + R \tag{4.28}$$

where n changes from $k_1 = \sqrt{R/2}$ to $k_2 = \sqrt{\frac{1}{R-a'R}}$ with the step $s = (k_2 - k_1)/N$, where N is the total number of points in the vector. As mentioned, the values of a' should then lie somewhere between the true solution (see Fig. 4.15, true solution for the biggest penetration value δ_{max}), but remain smaller than R. The value of the last point depends on penetration: the bigger the penetration is – the closer this point will be to the value of R. Therefore, the values of a' can be pre-calculated for preset ratios of δ_{max}/R and stored for future use. This pre-calculation step requires a high precision true solution for $a(\delta_{max})$ and requires considerable amount of time but needs to be performed only once.

Thus for each penetration experiment the following procedure is applied in our fitting routine:

1. The ratio δ_{max}/R is calculated for maximum penetration and depending on this value, a' is selected from the preset data array.
2. Values of the initial guess $a_0(n)$ are calculated using Eqn. 4.28.
3. Newton's method is applied for 7 iterations using Eqn. 4.27 and a high precision true solution $a(\delta)$ is found.

4. The elastic modulus of the sample surface is then calculated from the slope of the F vs $\left[(a^2 + R^2)ln\left(\frac{R+a}{R-a}\right) - 2aR\right]$ plot.

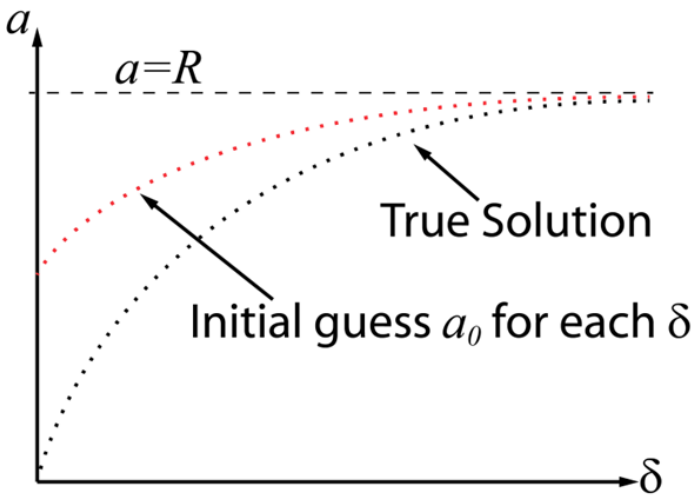

Figure 4.15: True solution to be found via Newton's method (black dots) and initial guess $\boldsymbol{a_0}$ for each value of $\boldsymbol{\delta}$, which will give values close to the true solution after several iterations (red dots).

As a practical example, Fig. 4.16 shows FDCs taken on swollen soft polymer contact lens. Figure 4.16A shows $\delta^{3/2}$ versus F fit with Sneddon's model for a rigid parabolic punch. From this, one can see that instead of a linear dependence of $\delta^{3/2}$ on F, there is significant observable curvature. Back calculating and superimposing onto the original FDC shows different characteristic FDC shape (Fig. 4.16B). As mentioned, in the initial stages of indentation the parabolic and spherical models correspond quite closely. Inset in Fig. 4.16A and Fig. 4.16B is the initial portion of the FDC also fitted with Sneddon's model for a rigid parabolic punch. From this it can be seen that the parabolic model fits very closely with the experimental data with minimal deviation. Figure 4.16C shows a plot of $(a^2 + R^2)ln\left(\frac{R+a}{R-a}\right) - 2aR$ (denoted as δ-a, with units of nm^2) versus F, which has significantly lower fitting error than the parabolic model.

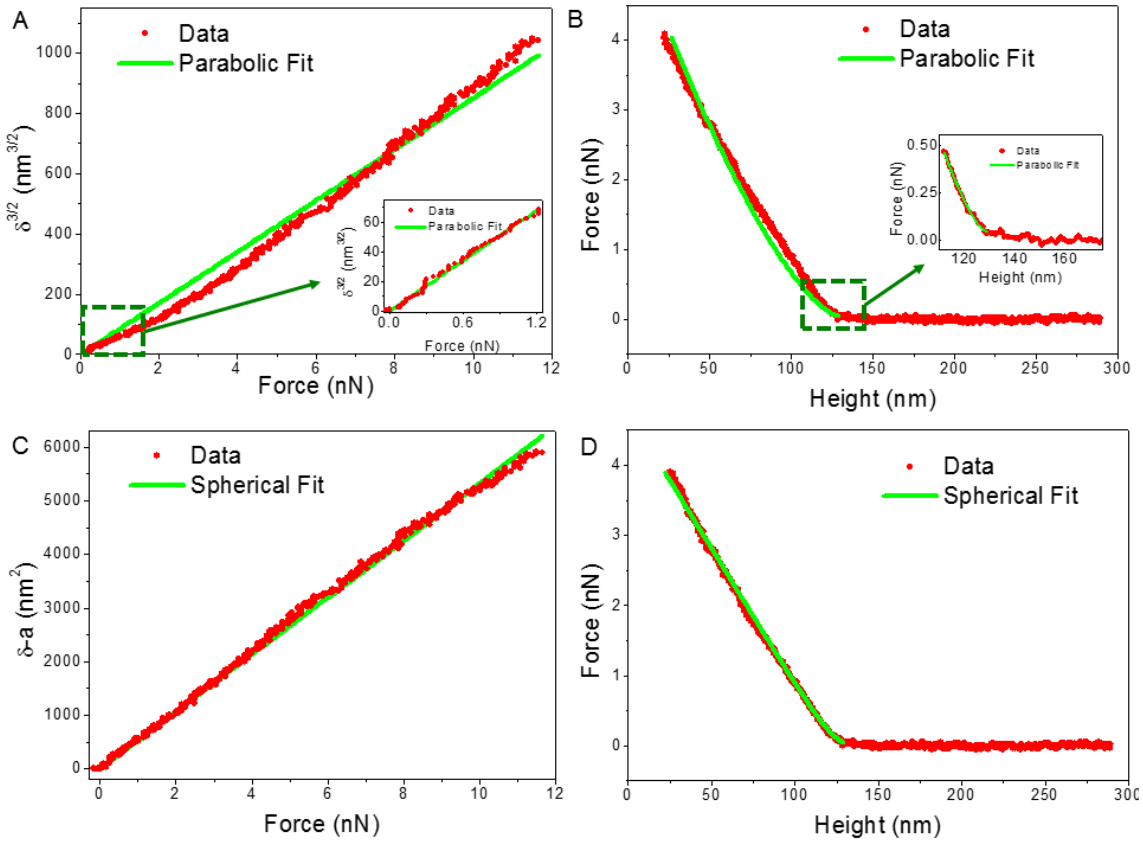

Figure 4.16: Force distance curves taken on Balafilcon A contact lens surfaces in fluid and fit with either Sneddon's model for a rigid paraboloidal punch (A and B) or for a rigid spherical punch (C and D). Inset in A and B are initial regions of the FDC which have been fitted separately with the parabolic model, exhibiting how well only the very first portion of indentation in this case can be considered parabolic.

As can be seen in Fig. 4.16D, the same back calculation and superimposition results in a much closer fit over the entire FDC. To summarize, Sneddon's model for a rigid parabolic punch and spherical punch gives very similar results for small indentation depths, with the calculation for the parabolic tip shape being much less cumbersome. As a result, for many users the parabolic model is employed (either knowingly or unknowingly) in preference to the truly spherical model. However, as can be seen in Fig. 4.14A and Fig. 4.16C, the shape of AFM tips is not always exactly parabolic, and can be actually more close to a more cylindrical punch capped with a hemispherical shape. For such cases we have developed a simple algorithm for numerically fitting our data with the spherical equations, and have

demonstrated a case in which it is preferential to use this model for precise values of elastic modulus.

3.2 Conical versus parabolic tip shape.

For very compliant soft polymeric and biological materials, especially in the case when they are in the highly swollen state, very high deformations can be achieved without inducing plastic deformation. Such large indentations require fitting with contact mechanics model which considers a rigid conical indenter on a semi-infinite half-space. During measurements involving large penetration depths, the initial parabolic shape of the tip makes very small contribution to the overall contact area increase, thus the tip can be considered conical in shape. Figure 4.17 shows an indentation experiment performed on silk ionomer layers. The parabolic model can be used only for the small initial portion (<20 nm) where contact force changes as $\delta^{3/2}$, after which the penetration changes as δ^2, signifying a different indentation regime.

This view is something of a simplification, as the real tip shape is generally more complex than the simple geometric shapes used in the general approaches. This can be particularly troublesome in the case of surfaces with complex morphologies: establishing a suitable model for the tip-sample interaction is daunting for sharp tips.[216] Various attempts[217] have been made to correct for the tip modelling errors when testing on homogeneous materials. The analytical approaches to these corrections have focused on the inclusion of a small parabolic region at the base of a tip and a smooth transition to a conical or pyramidal region. Numerical methods have also been utilized[218,219] which can be used to obtain a very detailed picture of the effect of tip shape. While exceptionally accurate, the solutions to these methods can be quite cumbersome and do not lend themselves well to a rapid solution algorithm for practical measurements.

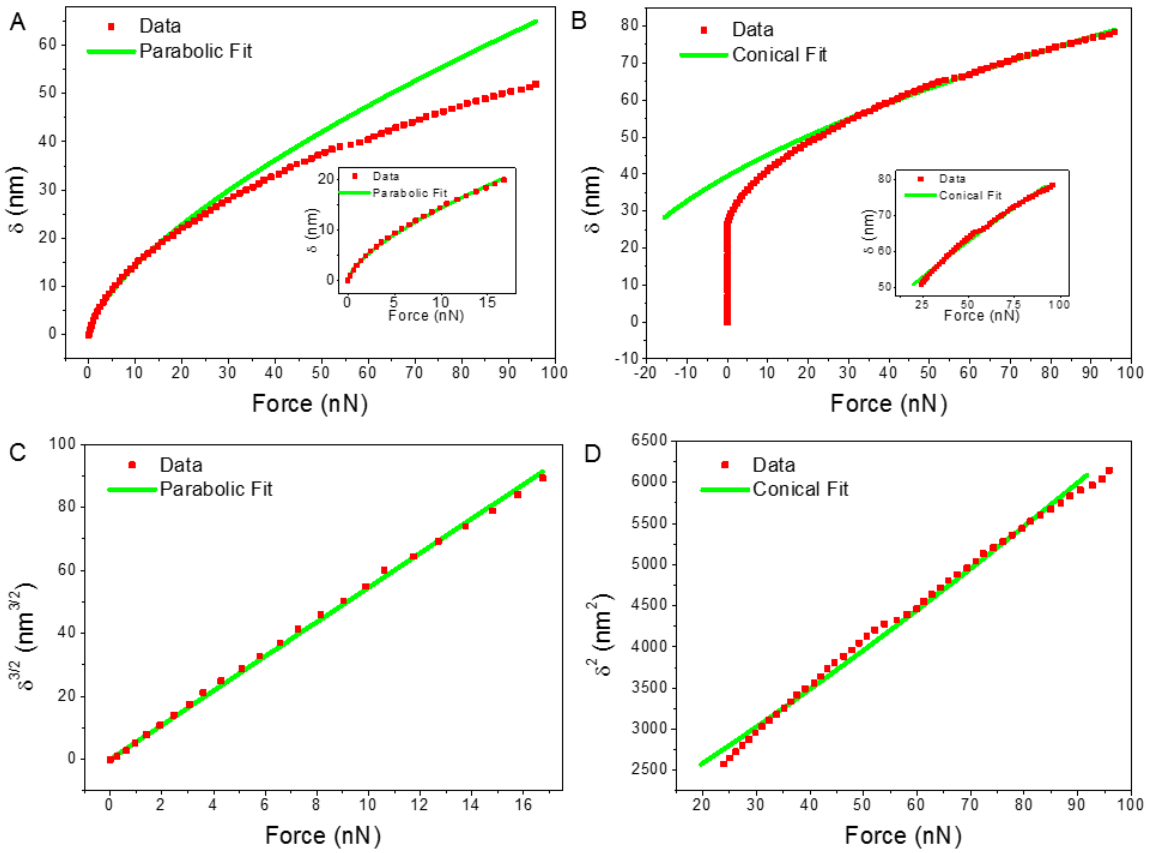

Figure 4.17: A comparison of FDC fitting using the equations for a parabolic punch (A & C) and the equations for a conical punch in our silk ionomer system (B & D). The top row shows the fit of our model function to the whole dataset, while the inset shows the fit in a smaller region more appropriately suited for the specific model (i.e. early in the FDC for parabolic model, and later in the FDC for conical model). Note that the second row is the fitted region plotted as $\boldsymbol{\delta^{3/2}}$ or $\boldsymbol{\delta^{2}}$ to show linearity.

An intriguing compromise between a naïve conical model (that is, one which uses the snap-in point for the penetration starting point) and a more complex tip shape consideration can be used. In general, the determination of tip shape is performed through either electron microscopy[220] or blind estimation.[221] While possible to obtain an accurate reconstruction down to a few nm, obtaining an accurate estimate of tip opening angle generally requires less resolution than determining the tip radius at the apex, which allows for better determination of the tip-sample interaction. Additionally, tip damage or contamination of the tip apex does not generally impact the behavior of a conical tip at sufficiently deep

penetrations (since the defect might contribute to only a fraction of the penetration behavior). In the geometric analysis performed by Berla et al.[222] a real tip can be modeled as a combination of a conical tip with a parabolic terminus defect (often called a "blunted tip"). The projected conical tip will overshoot the real end of the tip by an amount found to be $h = kRm^2$, where k is a constant specific to this equation determined by Berla et al., R is the radius of curvature of the AFM probe, m is the slope of the line parallel to the side angle of the AFM tip.

By fitting the profile of the tip apex with a parabolic function, we determined that our probe tip had a radius of about 7 nm, which corresponds well with the manufacturer's stated estimate. The conical profile of the tip was obtained by taking a linear fit of the reconstructed tip profile further away from the tip apex (roughly 15-20 nm away) and lead to a cone semi-angle of 25.3°. In our case, this leads to projected cone height which extends roughly 26 nm past the real tip. In our analysis, we compare the results for a parabolic tip, which is fit to small penetrations (0-20 nm), and a conical tip, which is fit to deeper penetrations (15-50 nm) and has its starting point adjusted to account for the 26 nm of the "phantom" tip height.

Because we do not correct for the effects of the blunted tip, the region of small penetration is not accurately fit by this model. As a result, a significant number of points past this initial region is required to obtain a suitable fit for our conical model. In some materials, this constraint coupled with the sharp tips used in this study can be problematic because the large indentations can lead to a significant degree of plastic deformation in the sample.[223] With a swollen thin film of modified silk fibroin, we were able to achieve relatively large penetrations (50 nm) with a negligible amount of plastic deformation as indicated by a lack of hysteresis in the approach and retract curves, and no changes in sample topography after indentation experiments.

For these films, we fit a parabolic indenter with radius of curvature of 7.09 nm and a conical indenter with an opening semiangle of 25.3°. In Fig. 4.17, the fitting results are displayed. As can be seen in the two graphs, the obtained fitting is quite good for both models and the results obtained for the modulus calculation is comparable. By analyzing 25 of such force distance curves, we found that a modelling of the data based on a paraboloid geometry gave an elastic modulus of 47.1 ± 9.3 MPa, whereas modelling a conical geometry led to an elastic modulus of 52.7 ± 5.2 MPa, with errors reported as 1 standard deviation. Given the observed similarity of these values (within the experimental error), the approach used in this study seems to be valid. Of note, the conical model appear to exceed the parabolic model by an average of 15%, though such a deviation is not statistically significant. Considering the relatively high degree of uncertainty in the parabolic fits, we suggest that our model suffers from a degree of uncertainty in the tip-sample interaction within the first few nanometers (particularly, a precise tip profile and starting point location). This can complicate the choice of the starting point adjustment needed to accommodate the conical model, and thus further investigation is warranted.

3.3 Tip size variation.

In many cases, the use of probes with large tip radius or colloidal beads can be advantageous over sharp probes. Foremost, it is known that larger tip radii reduce the maximum stress on the material in the area just blow the tip-sample contact point, and thus the use of probes with larger tip radii significantly reduces the possibility of inducing plastic deformation during FDC collection. Quick examination of the simple Sneddon model of a rigid paraboloidal punch shown in Eqn. 4.14 reveals that, for a given applied force F, penetration depth (as $\delta^{3/2}$) and tip radius of curvature (as $\sqrt{R}$) are inversely proportional. As a result, one can see that for extremely soft samples such as loosely networked hydrogels or other compliant biomaterials, increasing tip size can significantly

reduce the penetration depth for a given applied force, thus diminishing the probability of inducing plastic deformation on the sample surface. Furthermore, because of this inverse proportionality, in cases where high lateral resolution is not required (e.g. thick, homogeneous material surface), much higher force resolution can be achieved with large radii probes because larger much larger forces can be applied to the surface while maintaining low penetration depths. This can serve to significantly reduce data analysis errors associated with few data points, and can also be used to overcome the snap-in instabilities associated with large probes as the snap-in forces becomes negligible compared to the overall applied force.

However, for many SFS experimental setups, the use of very sharp probes (~10s of nm radius of curvature) is advantageous as it provides higher lateral resolution in surface mapping of properties facilitating the discernment of different phases of a heterogeneous material surface, or it can allow for the measurement of the micromechanical properties of small structures such as fibrils. We present two examples in which higher resolution is needed in Fig. 4.18. In Fig. 4.18A-C the surface of regenerated silk fibroin macromolecules deposited on a silicon wafer is shown with the corresponding adhesion image taken in Bruker's PeakForce QNM mode. As can be seen, the silk fibroin macromolecules interact with the AFM tip differently than the silicon surface, resulting in distinctly different surface adhesion behavior. An AFM tip with a large radius would be far less discriminant between the two materials at the surface. Furthermore, larger radii tips are more prone to capillary forces due to the presence of a thin water layer at the surface, which would make crisp adhesion mapping shown in Fig. 4.18B nearly impossible.

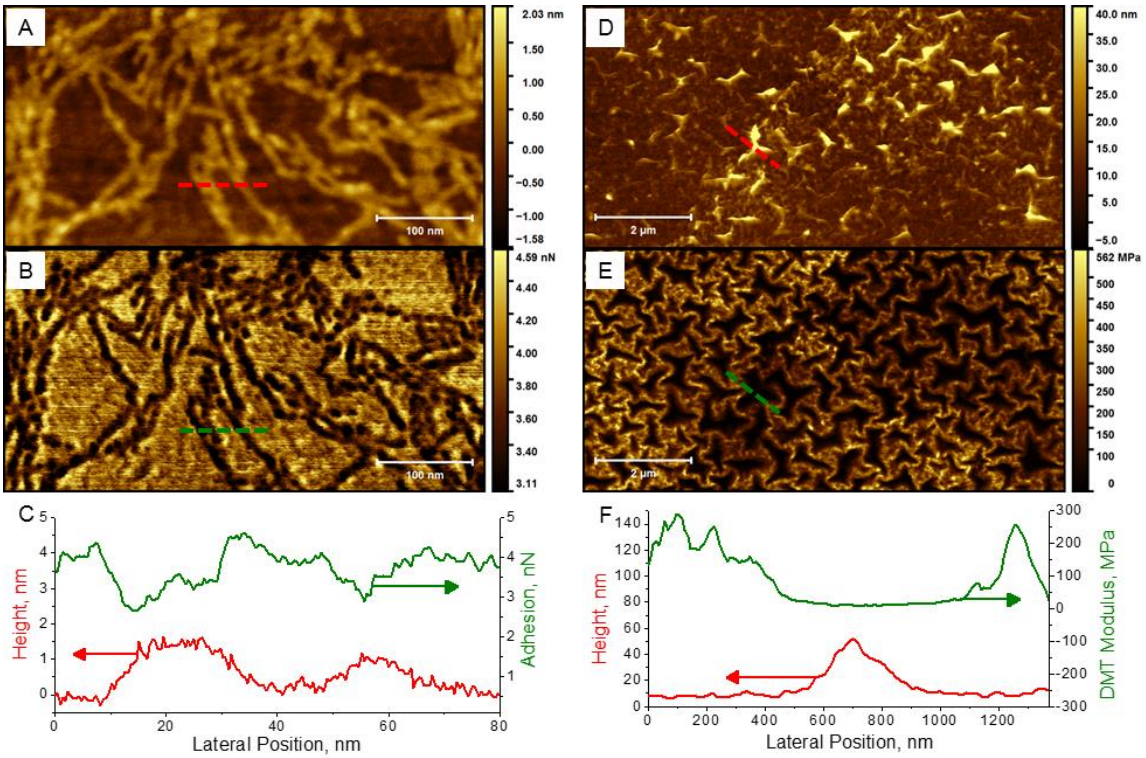

Figure 4.18: (A) Height image of nanofibrils of regenerated silk fibroin biomacromolecules cast on a clean silicon wafer. (B) Surface adhesion collected simultaneously, showing a distinct difference between the silk and the silicon ssurface. (C) Sectional profiles of height and adhesion data taken from the locations in A and C denoted by dashed lines. (D) Topography of silk ionomer surface with raised regions occuring as the result of buckling. (E) DMT modulus image acquired simultaneously which highlights the need for a sharp probe as the unsupported buckled regions give unrealisticly low values of modulus while the supported regions can be used for accurate estimation of mechanical properties. (F) Sectional profiles of height and adhesion data taken from the locations in D and E denoted by dashed lines.

As another example, Fig. 4.18D-F show a buckled silk ionomer surface with the corresponding DMT Modulus (taken using PF QNM). In this case the raised buckled regions are generally between 45 and 90 nm (Fig. 4.18F shows sectional profile) and are not supported by the underlying substrate. Consequently these structures are extremely compliant when force is applied by an approaching AFM tip. Because a large radius probe would contact many of these high features first it would be extremely cumbersome to determine true contact area, resulting in high error in calculating the sample elastic modulus. Furthermore any calculated modulus for FDCs taken with a large radius probe

on these samples would be a composite value of the extremely complaint buckles and the stiffer material. Scanning with a sharp probe allows for access to substrate-supported regions of the silk ionomer surface, and more accurate measurement of the surface mechanical properties (here the apparent DMT Modulus shows 100-300 MPa for supported regions and ~0 MPa for buckled regions).

In some cases, even with well-known polymeric materials, processing conditions can create the possibility for high surface roughness, or perhaps a more mobile surface layer which can affect measurements taken with exceedingly sharp probes. We present here several micromechanical measurements taken on a thick glassy PS film made by casting a highly concentrated solution dissolved in chloroform. FDCs were taken in fluid for both as received AFM tips (R = ~20 nm, Fig. 4.19), and for thermally annealed tips (R = ~330 nm, Fig. 4.20). However in this specific case an abnormally low surface elastic modulus was observed. Figure 4.19 shows a representative FDC collected using a sharp probe (spring constant = 6.9 N/m), with a total maximum penetration depth of approximately 8 nm. Fitting the $\delta^{3/2}$ versus applied force data obtained from the FDC in Fig. 4.19A resulted in a calculated elastic modulus of 569 MPa. Examination of >20 FDCs from different locations along the surface resulted in an average modulus of 479 ± 111 MPa.

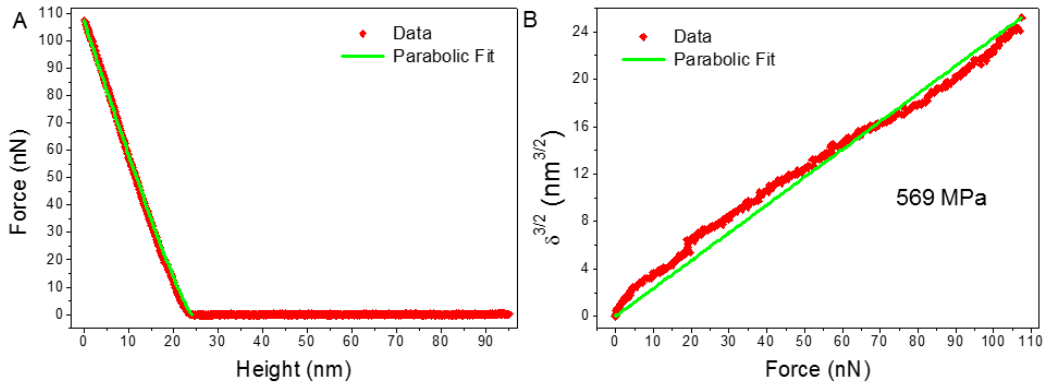

Figure 4.19: (A) Force-distance curve taken with a sharp probe (radius of curvature ~20 nm) on a cast polystyrene substrate. (B) $\boldsymbol{\delta^{3/2}}$ versus applied force. The elastic modulus was calculated to be 569 MPa.

When this same surface is probed using an annealed AFM tip with a large radius of curvature (~330 nm tip radius) the FDC behavior is different. Figure 4.20A,B show a representative FDC and $\delta^{3/2}$ versus applied force plots. In this case the applied force was adjusted by using a stiffer cantilever (spring constant = 65.8 N/m) such that a similar penetration depth could be reached as compared to the FDCs taken with the small radius probe. In this case the maximum penetration depth was ~7.5 nm (Fig. 20D has raw penetration depths determined from the experiment). As can be seen in Fig. 20B, there is some significant fitting error associated with using the parabolic model for these curves. This is a result of the apparent "layered" behavior seen in the plot of $\delta^{3/2}$ vs. F (Fig. 20B), as one linear slope transitions gradually to another, representing a change from a lower modulus to a higher modulus. Fitting the overall curve, therefore, represents a composite value of the two separate moduli, giving a calculated modulus of 1.3 GPa in this example. However, this curve was also analyzed in at different penetration depths. For low penetration depths (e.g. ~4 nm seen in Fig. 20C) the sample surface appears much more compliant with a modulus of approximately 650 MPa, which is much more closely associated with the value determined from FDC analysis with a sharp probe. If the region of the FDC corresponding to higher penetration depths is fit the calculated elastic modulus is determined to be 2.8 GPa, which corresponds well with standard values of PS elastic modulus. The primary stress from the applied force from the tip onto the surface extends farther into the subsurface as the tip radius increases for a given penetration depth.[169] Therefore in this case the large tip radius probe is able to better probe the bulk material away from the compliant surface. Facilitated by a simple fitting algorithm, this routine could perhaps be very useful in exploring different mechanical responses with penetration depth. It should be noted here that the explanation of this soft outermost layer for our PS substrate was not examined, however we suggest that it is still useful and relevant to the type of analysis described about.

Further examples of the usefulness of varying tip size when making micromechanical measurements of soft materials is the ability to switch between strictly surface modulus (with a depth of 10s of nm) while using small radii probes, to examining the structural rigidity of a sample of with a large tip radii. There are several examples in the literature in which the structural rigidity of small cells is measured by examining their mechanical properties with large colloidal probes.[216]

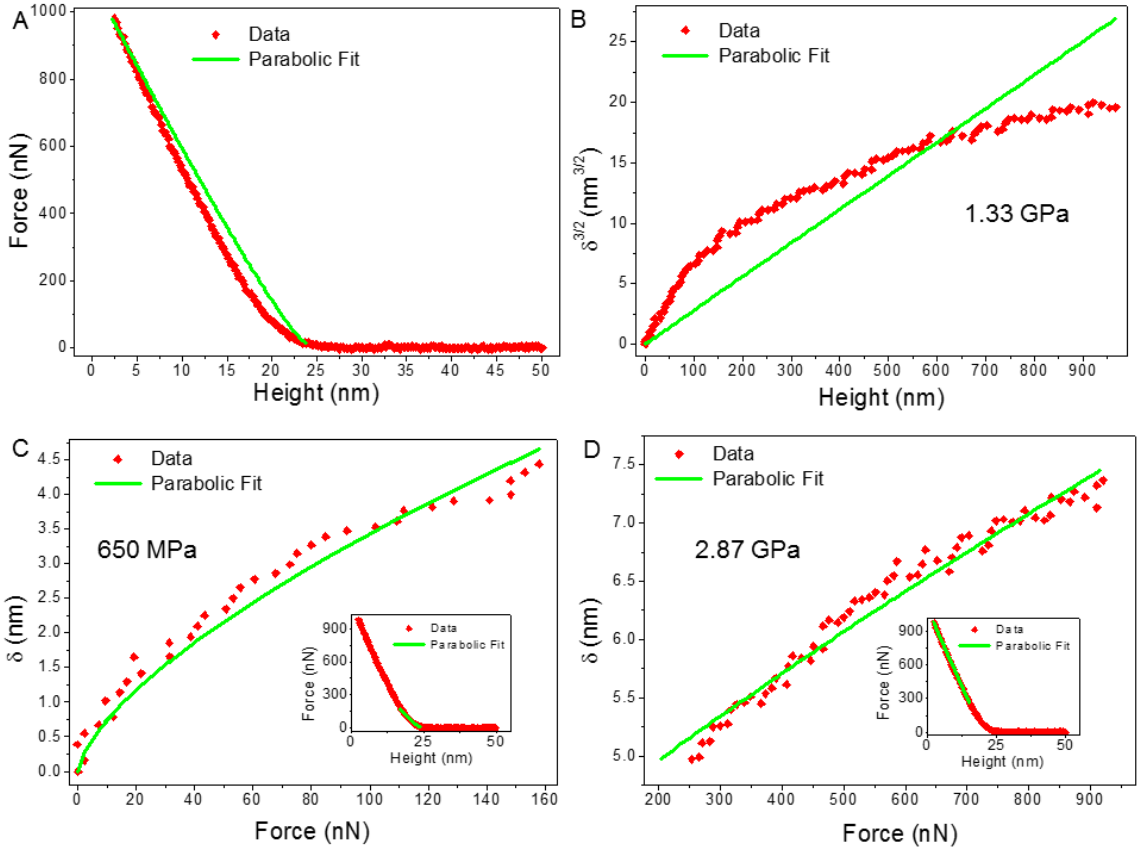

Figure 4.20: (A) Force-distance curve taken with a large, annealed probe (radius of curvature ~330 nm) on the same cast polystyrene substrate as the measurements in Fig. 6. In this measurement the maximum sample penetration depth is 8 nm. (B) $\boldsymbol{\delta^{3/2}}$ versus applied force used for fitting with Sneddon's model for a rigid parabolic punch with the calculated elastic modulus of approximately 1.3 GPa. The bottom two panels show the fitting of $\boldsymbol{\delta}$ (used here to show actual deformation levels) versus applied force for initial penetration (C) and final penetration depths (D). Inset is the original FDC and fitting for the corresponding portion of the curve.

4.3 MicroMechanical Analysis of Soft Polymeric Materials

The **M**icro**m**echanical **A**nalysis of **S**oft **P**olymeric **M**aterials measurements (*MMA-SPM*, developed by Dr. Marius Chyasnavichyus throughout the course of this work, see Fig. 4.21) program was designed to expand the capabilities of the Bruker Nanoscope Program in the processing of so-called Force-Distance Curves (FDCs) collected during indentation experiments performed with Bruker Dimension Icon AFMs (also compatible with other Bruker AFMs using the Nanoscope V controller).

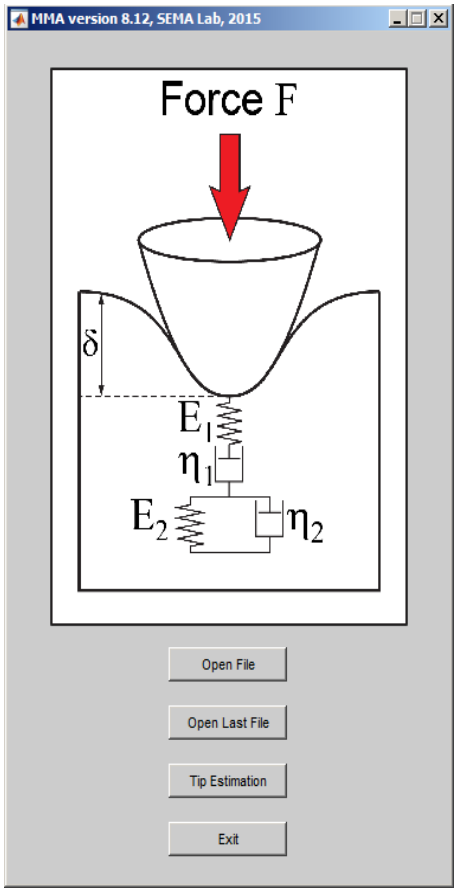

Figure 4.21: Main window of MMA Software.

Force-Distance indentation curves contain data which can be used to study in detail the mechanical behavior of the materials and allows for quantitative determination of such properties as elastic modulus, adhesive forces, and relaxation time of the material. *MMA-*

SPM is capable of running analysis for simple elastic materials, materials with viscoelastic properties, and layered materials. In addition it allows acquiring of the tip shape and radius of curvature to use appropriate model of tip-sample contact geometry. It is also capable of analyzing large amounts of data by performing automated detection of the tip-sample contact point and helps pinpoint statistical outliers for large volumes of data.

MMA-SPM was created through MatLab, but comes packaged with MatLab Runtime Compiler (MCR). MCR is a freeware standalone set of shared libraries that enables the execution of compiled MatLab applications on computers that do not have MatLab installed. Therefore, after completion of the licensing process, this software will be available for use to both academic and industrial labs interested in AFM-based mechanical properties characterization.

As mentioned, MMA-SPM includes several, useful functions. The first of which is tip shape calculation (Fig. 4.22). This function to loads tip profiles in the form of X-Y data and calculates the radius of curvature of the tip apex. Often reconstructed tip profiles have some slight offset angle due to the angle of the cantilever in the AFM tip holder. Therefore, we also included the ability to rotate the profile for better fitting.

Elastic modulus fitting in MMA-SPM includes the ability to quickly switch between tip geometries, select various regions of the FDC to fit, include adhesion models, change parameters on the fly, and to export both text data and high quality images (Fig. 4.23). After all settings are finalized for fitting, the user is able to move into a batch processing mode which fits many curves using the same properties set in the elastic modulus fitting

window. This greatly increases the analysis speed when taking arrays of FDCs in small areas on the sample surface.

Finally, as discussed previously, no commercially available analysis software includes viscoelastic modeling capabilities. Consequently, we can included the ability to fit FDCs as a function of time in order to extract viscoelastic parameters using the combination of Johnson and Sneddon models described in § 4.1 of this chapter (Fig. 4.24).

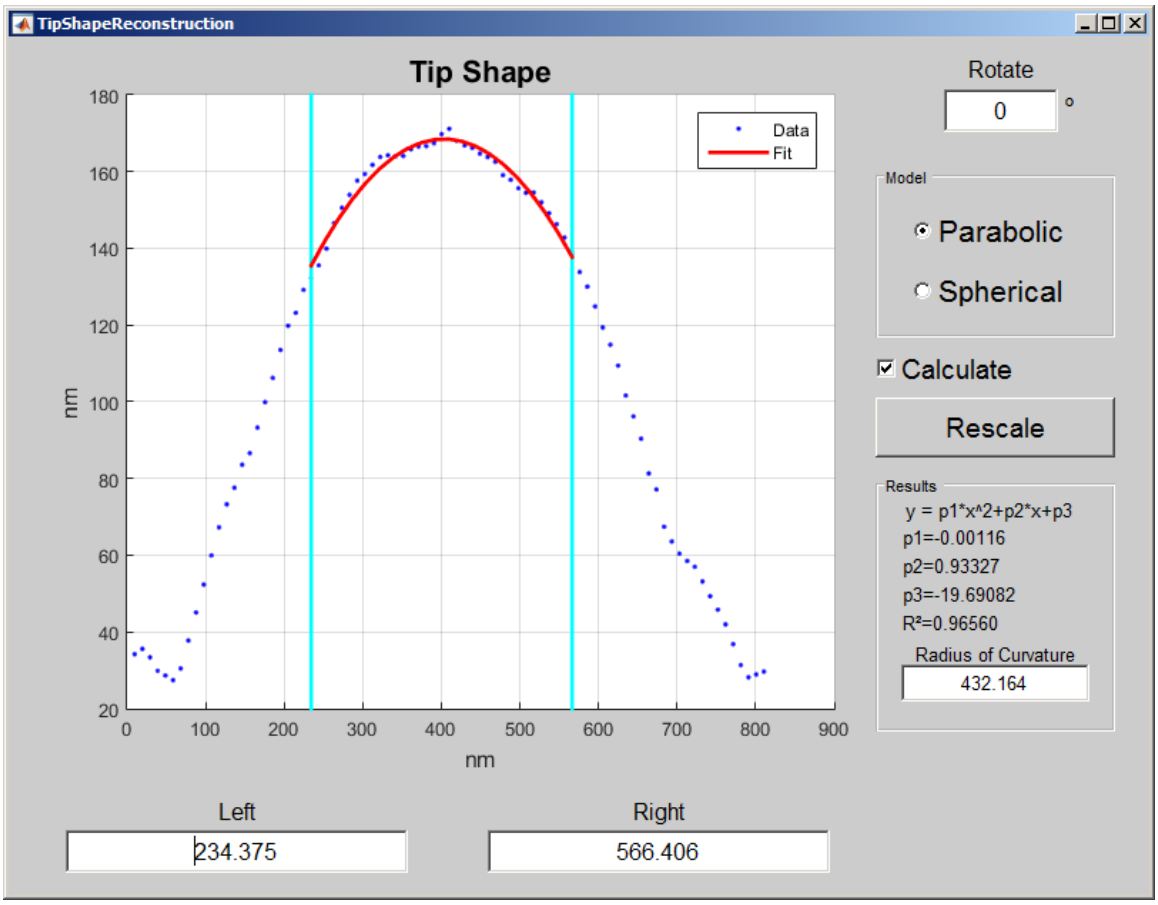

Figure 4.22: Tip curvature estimation window.

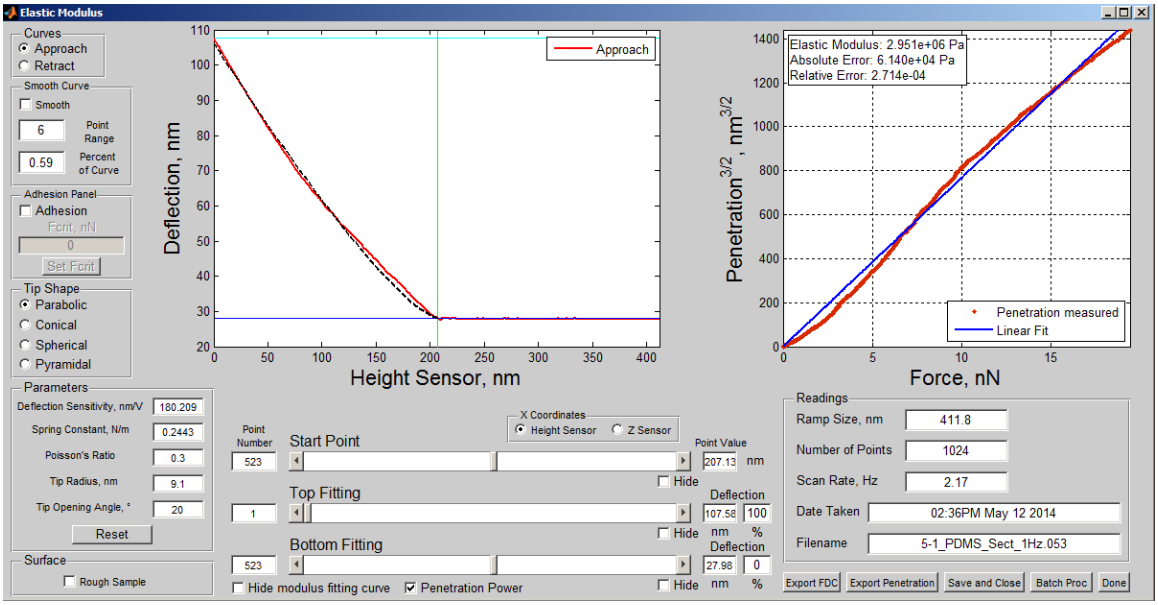

Figure 4.23: Elastic modulus fitting window of MMA-SPM.

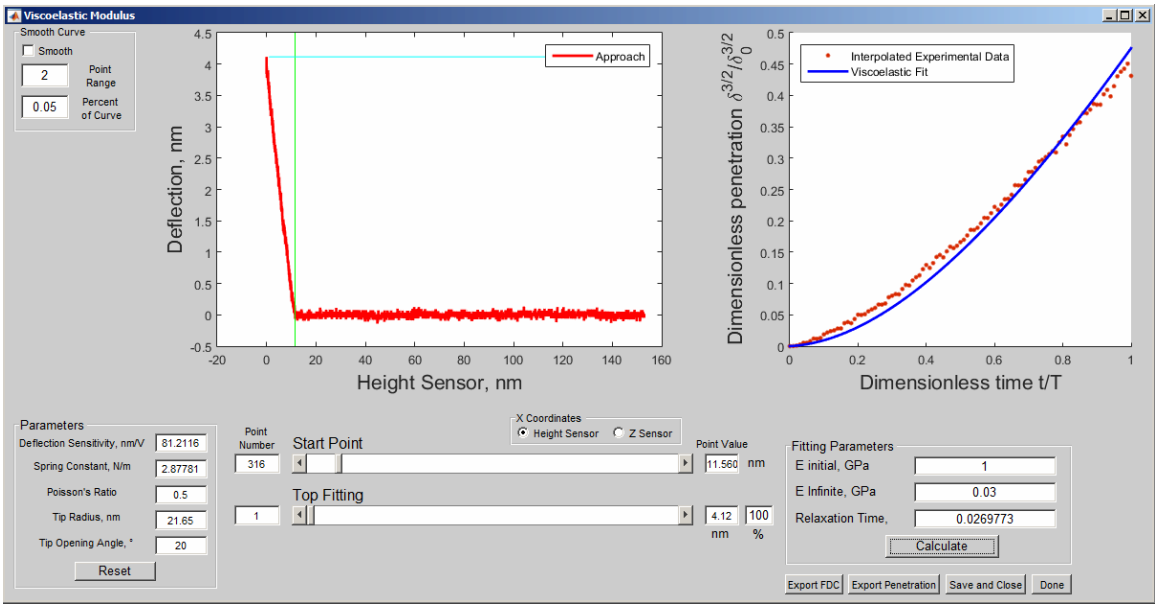

Figure 4.24: Viscoelastic fitting window in MMA-SPM.

4.4 Conclusions

In conclusion, we summarized the methods of the SFS probing of nanomechanical properties of polymeric and biological materials with time-dependent behavior. We discussed the traditional application of shape-dependent Sneddon's model for different experimental conditions and the limitations of the common indentation methods used for hard materials for the studies of soft matter. More importantly, we have evaluated several current approaches for probing of the viscoelastic properties using special loading methods such as creep and dynamic loading. We suggested that creep measurements can be used to quantitatively characterize mechanical properties of the viscoelastic materials, but require high precision control over the piezoelement displacement, relatively long timescales of the measurement, and a constant deflection retention feedback loop. Dynamic loading methods with high scan rates are not subjected by the piezoelement creep and thus can be readily applied to mapping of differential surface mechanical properties including storage and loss properties with high spatial resolution. However, these methods require complete theoretical description of the tip motion and, therefore, are the best fit to high rate qualitative characterization and contrast imaging of multiphase materials. They have limited use for the measurement of very soft materials with small differences in elastic response.

An example of the experimental and analysis routine for the evaluation of the viscoelastic properties of a model polymeric material using "static" force-distance data collected at a variety of loading rates and different temperatures across glassy, glass transition, and rubbery regions by using combined Johnson-Sneddon's model for the quantitative analysis of the time-dependent polymer materials properties was given.

The analysis of the experimental data with appropriate models (Sneddon's model for elastic regions (glassy and rubbery) and SLS-based Johnson's model for the viscoelastic region)

allowed for the restoration of the universal master curve for the polymer materials under investigation with full temperature-time dependent behavior restored for storage modulus, loss modulus, loss tangent, relaxation times, and activation energies. Standard elastic Sneddon's model generates adequate modulus values below and above glass transition but can significantly underestimate actual modulus values within the glass transition region ($T_g \pm 15$ °C) with major deviations occurring at the peak of the loss tangent. Comparison of the master curves obtained with the viscoelastic Johnson-Sneddon model from the experimental data showed that standard viscoelastic SLS model adequately describes the viscoelastic materials behavior in the temperature region of the glass transition.

We have also described in detail several contact mechanics models for commonly encountered tip geometries: paraboloidal, conical, and spherical, and used a variety of soft materials to exemplify situations in which each model should be employed. Additionally we have demonstrated the usefulness of our home-built analysis program, *MMA Software* (available from authors), in calculating micromechanical properties of soft materials from FDC data.

In § 4.2 , we showed how quickly results could deviate after simple incorrect assumption of tip geometry, and use of the equations of a paraboloidal punch rather than those for a spherical punch for FDC analysis. FDCs collected on the soft elastic surface of a commercial contact lens were observed to exhibit behavior that is not fitted very well with the parabolic model. As a result, we suggest that in some cases the sharp tip of a brand new probe could actually resemble more a hemispherically-capped cylindrical punch with a finite limit to contact radius than a paraboloidal punch which has a contact radius that can continuously increase. Unfortunately there is no analytical solution to the spherical equations and numerical analysis can be very cumbersome. However we have described

our simple algorithm for working with spherical equations, which will be practical for real-life applications.

Analysis routines for utilizing the conical model here showed that the initial portions of FDCs could be used with the parabolic model, but as indentation depth grows, the blunt tip apex plays a decreasing role in the overall contact area. Thus calculations using the initial indentation with the parabolic model and the latter stages of indentation with the conical model gave results within on standard deviation. However, the caveat to this approach is that a significant amount of data points need to be collected (i.e. high enough indentation depths need to be achieved) in order to reduce the effect of the blunted tip apex for the conical model to fit well.

The effect of tip radius can be briefly discussed. In general, it is well known that larger probes facilitate mechanical properties determination while reducing the probability of plastic deformation. We have also shown some specific examples when a sharp probe could be preferential to a dull probe, especially in the case where precise positioning is required for the determination of the properties of extremely fine surface features. In the case of a large radius probe, the stress distribution immediately below the tip-sample contact point extends farther into the subsurface. As a result, the FDC behavior observed on the same material surface may be different when probed with different radii probes. Here we used an example of a PS surface in which the very top layers were abnormally compliant. By probing farther into the bulk using a large radius probe, we could detect a modulus which more closely matched literature values.

Finally, we briefly discussed the data analysis software which was developed throughout the course of this dissertation. This program greatly facilitated our efforts calculating the micro- and nanoscale mechanical properties of soft, viscoelastic surfaces.

CHAPTER 5

Silicone-based soft contact lenses as viscoelastic substrates

We present comparative micromechanical characterization of surface and cross-sections of several commercially available soft silicone hydrogel contact lenses. Such data allows for the examination of the spatial distribution of different regions with local mechanical properties variation within the subsurface lens regions. More importantly, this study highlights the advantages that AFM-based probing techniques have over traditional mechanical characterization methods. First, all studies were conducted with minimal sample preparation saline solution such that the swelling behavior of each lens is close to practical usage. We analyze force-distance curves collected with high-resolution within elastic deformation limits at different loading rates. These indentation experiments were used to determine quantitative values of micromechanical properties from different regions within the lens structure and were ultimately compared to conventional lens-averaged macroscopic measurements available in the literature. It was found that the lens-averaged modulus previously reported in literature frequently misrepresented the values by a factor of 2-3, due to low strain rate tensile testing. We suggest that higher strain rate compressive testing employed at the surface of the lens by AFM more accurately represents in-situ conditions of blinking and can be better correlated with patient comfort. In addition, we have studied topography and mechanical properties of the lens surfaces, which come to the direct contact with the surface of the eye and eyelid. AFM images show high contrast distribution maps for the adhesive and mechanical properties of the microstructured regions such as pores, lamellae and different material inclusions within the lenses.

5.1 Introduction

Mechanical properties which critically depend upon lens water content, porosity, and oxygen permittivity are the most important parameters affecting the ultimate performance of soft contact lenses.[224] State of the art contact lens materials should be soft and flexible enough to provide comfort to the wearer and reduce complications associated with constant stress within the eye such as papillary conjunctivitis and changes in corneal curvature.[225,226] At the same time the lens material should maintain overall shape for the best optical performance and for preserving long-term integrity and clarity during extended wear, interactions with salty fluidic environment, and multiple stress cycles.[227] Recent materials solutions have resulted in dramatic increase in lens performance.

In fact, introduction of silicone hydrogel materials for lens fabrication allowed for design of new, high performance lenses. This development brought even more attention to the mechanical properties of soft contact lenses, since silicone hydrogel materials generally have much higher elastic modulus than the first generation of hydrogel materials used in soft contact lenses.[228,229] Thus, since introduction of silicone hydrogel materials much effort was put into the reduction of the rigidity of the lens structure, design of their soft surfaces and improvement of oxygen permittivity and water content within the material.[230] Most popular current designs involve additional physical and chemical surface treatments to address these issues and modify lens-eye interactions including adhesion and lubrication.[231] Therefore, it becomes even more important to precisely characterize global and local mechanical properties of these multiphase materials under relevant practical conditions.

Most current mechanical measurement methods involve conventional tensile testing to evaluate elastic modulus of the lens materials.[232,233] However these tensile methods have several drawbacks. First, it is hard to compare the stiffness of different contact lenses as

the measurements strongly depend on the sample preparation: such factors as small cracks and differences in thickness between lenses with different optical power dramatically reduce the precision. Second, complex sample shape makes measured values vary greatly and thus frequently simple slab shape is used instead of actual lenses for these measurements.[234] Finally, these measurements do not provide local modulus, but provide overall averaged mechanical properties disregarding specific contributions from materials components. Therefore, this technique cannot reveal micromechanical properties of different structural components of modern silicone hydrogel lenses such as bulk material, interfaces, and surfaces. For example, to reduce differences in surface chemistry between the material and ocular surface and to prevent tear film breakup, contact lenses can have various surface coatings and wetting agents incorporated into the bulk of the lens structure. In the case of surface modification the mechanical properties of the coating will dominate in the eye-lens contact interface although the overall rigidity is controlled by the bulk properties of lens matrices[235] Thus high resolution, spatially capable techniques should be employed to evaluate distributed mechanical properties of multiphase lens materials.

As known, AFM-based surface force spectroscopy (SFS) technique is well known approach for the characterization of micromechanical properties of multiphase polymeric materials.[19,31] SFS is known to be versatile technique for characterization of mechanical properties of soft materials with nanoscale resolution. This technique was successfully used for micromechanical characterization of complex polymeric materials such as polymer composite materials, grafted polymers, natural polymers, nanoscale polymer films, soft biomaterials and individual molecules[40,123,155,176,189,236,237,238,239,240,241,242,243] AFM based techniques are widely used in vision science to study surface topography,[244] friction,[245] and protein absorption[246] for contact lens materials and eye tissue[237,247] however they are rarely used for the mechanical measurements.

Several successful examples of measuring micromechanical properties of the surface layers of hydrogel contact lens have been published by Somorjai et al.[248,249] It was found that elastic modulus of the lens surface depends strongly on the loading rate and water content within the lens. However only the thin surface regions were studied and spatial distribution of the mechanical properties was not examined in this study. Up to this date to the best of our knowledge, no studies on the distributions of the variations in mechanical properties of different structural regions within the soft contact lenses were performed.

From experimental prospective, such measurements can be performed in two modes: fast high frequency mode (different common names such as Quantitative Nanomechanical Property Mapping (QNM)) and Force-Volume (FV) mode.[69] Both modes rely on the collection of Force-Distance curves (FDCs), which contain tip sample interaction information and can be used to calculate sample mechanical properties using known tip parameters and different models of contact mechanics.[30,169] In the high frequency mode, an AFM tip oscillates sinusoidally (usually at several kHz frequency) and briefly interacts with the sample surface in the middle of each cycle.[56] This measurement mode allows for the determination of various mechanical properties of the sample surface, such as elastic modulus and adhesion, as well as surface topography with nanoscale resolution. However, as a result of the short interaction time, the mechanical measurements performed in this mode lack precision and usually only provide qualitative contrast maps of surface mechanical properties distribution.[31] In FV mode AFM tip moves in saw tooth-like motion indenting into the sample during each cycle. Due to the piezoelement mobility limitations, the frequency of these indentations are limited to several tens of Hz,[41] however the well-defined FDCs enables determination of quantitative data for the material with high precision.[19]

In present study we develop a methodology to characterize spatial distribution of regions with different mechanical properties within the soft microstructured materials. Using soft silicone hydrogel contact lens materials as an example we demonstrate that high frequency measurements to acquire high resolution maps of topography and mechanical properties can be combined with FV nanoindentations to provide reliable micromechanical measurements to such complex composite materials under wet conditions. We mapped the micromechanical properties of the lens surface as well as lens cross-sections to reveal complex sub-surface structure with greatly different elastic responses that cannot be obtained with conventional macroscopic mechanical testing.

5.2 Experimental

5.2.1 Contact Lens Preparation. In this work, four different commercially available silicone-hydrogel contact lens brands were selected for comparative studies: Balafilcon A (Purevision, Bausch & Lomb Inc.), Senofilcon A, (Acuvue Oasis, Johnson & Johnson Vision Care Inc.), Lotrafilcon B (AirOptix Aqua, CIBA Vision Corp.) and (Biofinity, CooperVision Inc.) purchased through Contactlenses Ltd. Lenses were mounted and measured according to the procedure described in Chapter 3.

Poly(dimethyl siloxane) (PDMS) sample was used as a control model substrate for elastic modulus measurements. Centimeter thick PDMS substrates were prepared using a Sylgard 184 Silicone Elastomer Kit (Dow Corning, USA). The elastomer base was vigorously mixed with curing agent in a 5:1 ratio (w:w) for 10 minutes, then placed under vacuum at room temperature for 30 minutes in order to remove all remaining air bubbles. The mixture was cured overnight at 70 °C and allowed to cool before use in AFM measurements.

5.2.2 AFM measurements. AFM measurements were performed with a Dimension Icon AFM microscope (Bruker), using PeakForce Quantitative Nanomechanical Mapping

(QNM) mode at 1kHz tip vibration, as discussed in Chapter 3. High resolution (1024x1024 pixels) images were acquired in this mode. In addition to surface topography, these measurements provide simultaneous contrast variation for regions with differences in stiffness and adhesive properties.[250]

From the topographic images root mean squared (rms) roughness values were calculated for randomly selected 1x1 μm^2 and 10x10 μm^2 surface areas. Of all three channels, only the topography channel presents quantitative data; DMT modulus channel and adhesion channel show qualitative contrast images and z-scale for these measurements was not scaled to show real physical quantities. For the actual quantitative mechanical measurements FDCs were collected from the selected regions of the lens surface. All curves for mapping were collected at 4 Hz indentation rate with applied force in the 3-12 nN range. For frequency variation experiments, the frequency was varied in 0.01-10Hz range.

5.2.3 FDC analysis. FDC data was analyzed using Sneddon's model for a rigid axisymmetric punch[28] as described in details elsewhere.[26] Briefly, tip deflection, d was measured as the tip was displaced by distance z towards the sample (Fig. 5.1A). After the tip-sample contact, the cantilever penetrates into the surface by the distance $\delta = z - d$. The force F exerted onto the tip during indentation can be calculated from the cantilever deflection as $F = kd$, where k is the spring constant of the tip. According to this model, this force can be related to the penetration assuming the elastic material behavior. The following equation is used for axisymmetric tip with parabolic cross-section:[28]

$$F = \frac{4}{3}\sqrt{R}E'\delta^{3/2} \tag{5.1}$$

where R is the radius of curvature of the apex of paraboloid, determined from the parabolic fitting of the reconstructed tip profile, and $E' = E/(1-\upsilon^2)$ is the reduced modulus of the material with Poisson's ratio, υ, and Young's modulus, E, of the material. Poisson's ratio $\upsilon = 0.5$ was used in the present study under the usual assumption of incompressive elastic behavior of the lens materials. Curvature of the apex of the tip was calculated by fitting the tip shape (Fig. 5.1C) with a parabolic function.

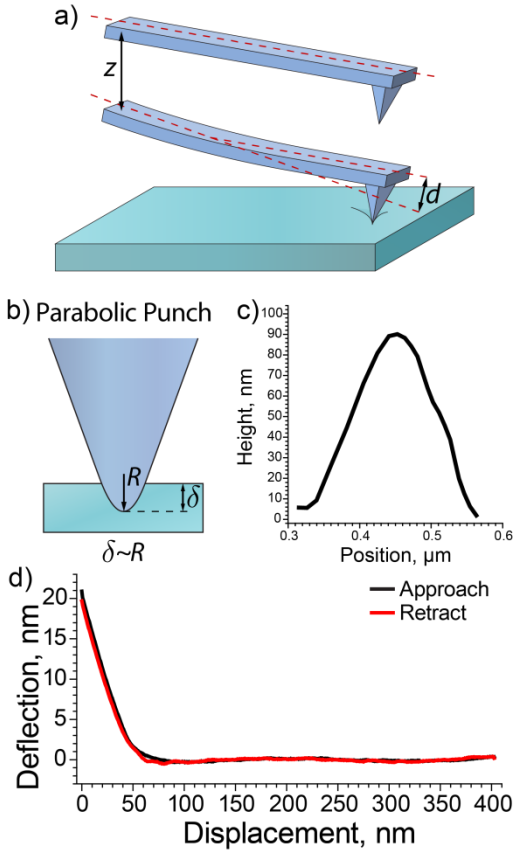

Figure 5.1: (A) AFM cantilever motion during indentation experiment. (B) The AFM tip surface penetration for parabolic punch. (C) Tip profile from tip shape reconstruction. (D) Example of approach and retract curves for typical indentation experiment (bulk indentation into Comficon A).

Fitting of the penetration versus force data with Eqn. 5.1 allows calculation of the elastic modulus of the material. It is important to note that Sneddon's analysis cannot be performed in the presence of substantial adhesion between the surface and the tip.[30]

However in all cases in the present study under fluid, the adhesive force was at least 20 times lower than the maximum tip deflection, allowing for the assumption of zero adhesion, see example in Fig. 5.1D. At least 36 force-distance curves were collected for each investigated region. For each curve elastic modulus value was calculated and mean value was determined from the set of the curves. All values are reported in this study as mean ± standard deviation.

5.3 Results and discussion

5.3.1 AFM tip selection. For this study sharp 10-30 nm AFM tips were preferred to colloidal probes. Such choice was governed by two factors. First, sharp tips allow nanosacle resolution due to the small tip-sample contact area. Second, sharper tips have advantage for targeting regions of the sample with lower roughness. Since Sneddon's model describes interaction of the punch with elastic half space, only indentations into the flat regions of the sample can be described by the model.

In addition, colloidal probes are much less sensitive, than sharper tips for the studies of layered structures with the layer thickness much smaller than the size of the probe.[251] It is important to note, that colloidal probes have advantage over sharp tips for measurements of the structural rigidity of composite materials[252] and polymer brush studies.[253]

5.3.2 Surface Topography and Mechanical properties. For this study outer (convex) surface of the contact lens was chosen for the topography examination. Figure 5.2 shows general topography of the lens surface. Topography images clearly show residual structural lines for all lens materials except Comfilcon A. These lines are usually attributed to the defects of the mold, which are transferred to the lens surface during cast molding.[254] Despite the fact that all four lens types were manufacturing by cast molding, Comfilcon A material does not show a web-like structure of linear defects. Instead, the surface of

Comfilcon A lens is covered by a series of fine lines with less than 6 nm elevation. In addition to these features surface of Balafilcon A (Fig. 5.2B) shows deeper grooves, which are small fractures of outer layer appearing, likely, during plasma oxidation process,[235] as well as elongated surface depressions of about 60 nm deep. The roughness values within 2-20 nm are characteristics of very smooth surfaces and are close to the those reported in the literature for similar lenses.[255] For some lenses such as Balafilcon A and Lotrafilcon B at larger scale size (10 μm^2) (Tab. 5.1) the roughness is higher but at smaller scale (1 μm^2) all lenses show similar low roughness, therefore, in the indentation experiments these surfaces were considered to be flat.

All indentation experiments were performed in the flat regions between the linear grooves away of any surface irregularities. Typical FDCs for the surface indentation experiments and penetration vs. force data are presented in the Fig. 5.3. Elastic moduli for the surfaces of all lens materials were calculated according to the Eqn. 5.1 by fitting penetration versus force data with Sneddon's model. Results are summarized in Tab. 5.2.

Table 5.1. Microroughness of the lens surfaces

Material	**Roughness (rms) 10x10 µm, nm**	**Roughness (rms) 1x1 µm, nm**
Lotrafilcon B	7.1 ± 1.6	2.1 ± 0.4
Balafilcon A	15.8 ± 2.0	3.2 ± 0.4
Senofilcon A	3.2 ± 0.3	1.9 ± 0.3
Comfilcon A	2.4 ± 0.1	2.0 ± 0.1

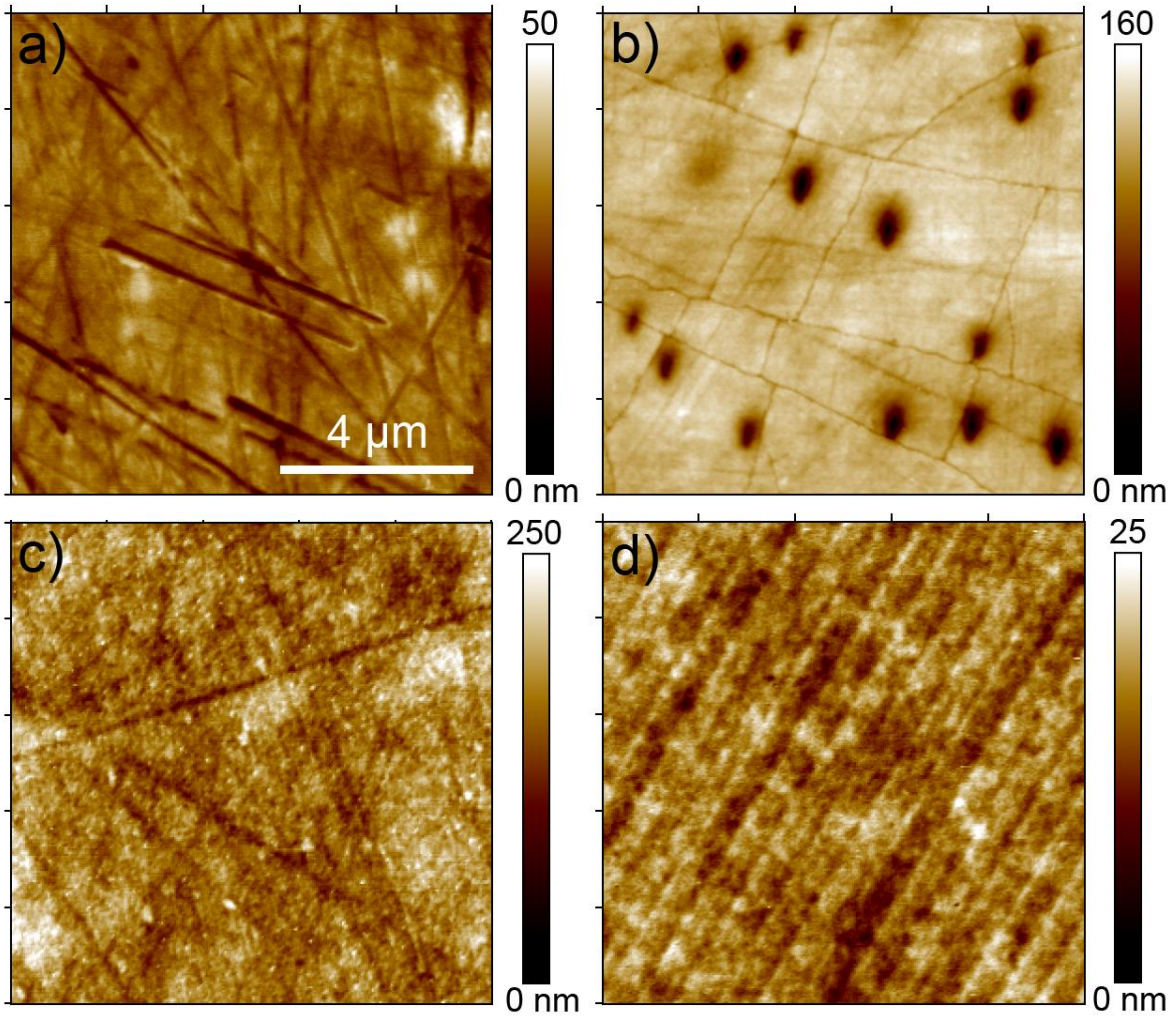

Figure 5.2: . Surface topography of submerged soft contact lenses used in this study. (A) Lotrafilcon B, (B) Balafilcon A, (C) Senofilcon A, (D) Comfilcon A.

Figure 5.3A and 5.3B show typical surface indentation experiments for Lotrafilcon B and Balafilcon A lenses, respectively. From the Sneddon's model reconstruction Fig. 5.4A and 5.4B one can see, that in both cases penetration data shows two distinct linear regions, with the first region having higher slope than the second. Such behavior is characteristic for indentations into the soft thin film supported by stiffer substrate.[32] Indeed, as known, Lotrafilcon B and Balafilcon A lens materials are inherently hydrophobic.[231] Thus, to provide wettability to the lens surface, both materials are plasma treated. In the case of Lotrafilcon B it is plasma polymerization, which results in ~25 nm hydrophilic layer on the

lens surface and for Balafilcon A its plasma oxidation, which provides hydrophilic groups to the lens surface.[256]

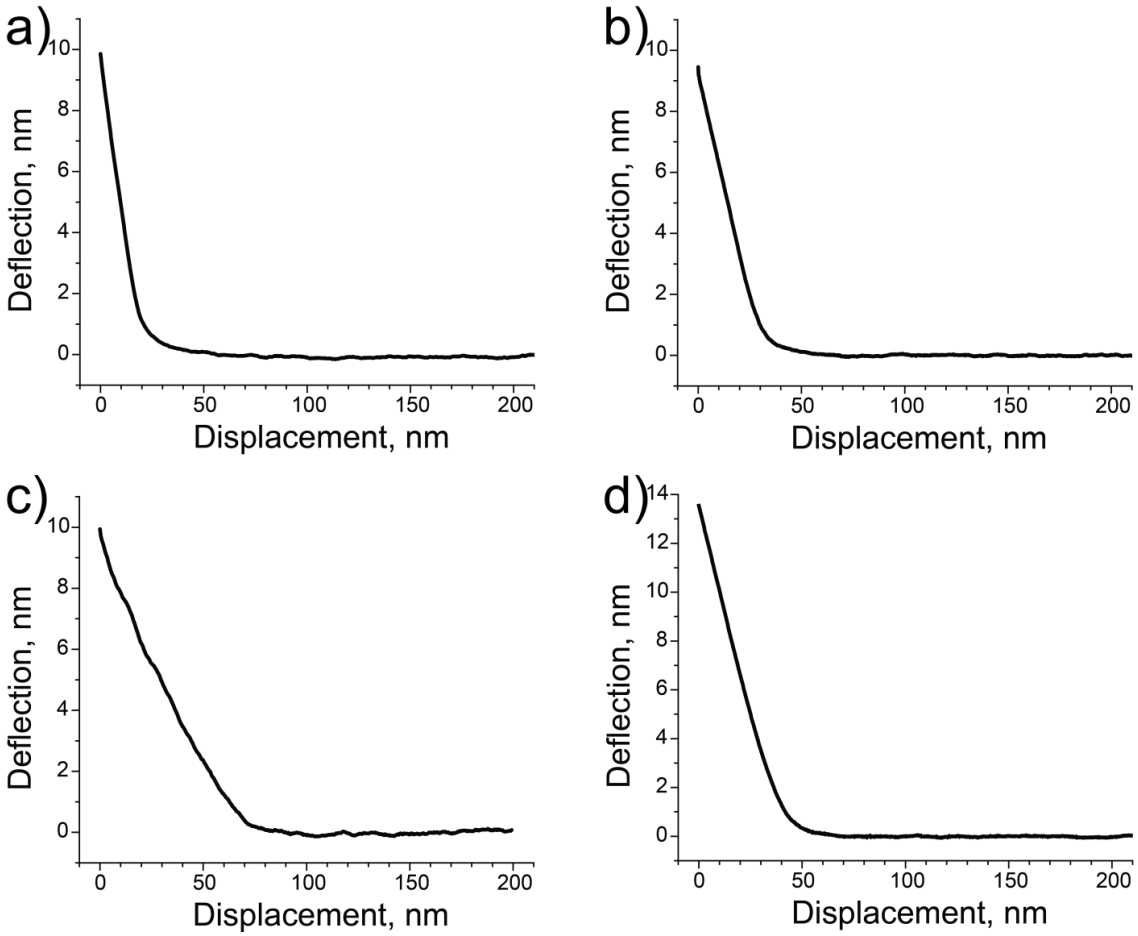

Figure 5.3: Typical FDCs for indentation experiments with ~10 nN setpoint performed on the surface of: (A) Lotrafilcon B, (B) Balafilcon A, (C) Senofilcon A, (D) Comfilcon A.

We suggest that the presence of these plasma treated surface layers is reflected in penetration data. In the case of Lotrafilcon B lens slope starts to change at ~28 nm penetration, which is close to thickness of the reported value of outer polymer layer[256] (Fig. 5.4A). Resulting calculated moduli are 0.45 ± 0.07 MPa and 3.69 ± 0.36 MPa for the coating and lens surface respectively. For Balafilcon A lens, the thickness of the coating

is lower, on the order of 15 nm and both coating and surface moduli are lower (0.21 ± 0.06 MPA and 1.35 ± 0.12MPa respectively).

Fig. 5.3C shows typical indentation curve for the surface of the Senofilcon A lens. Senofilcon A belongs to the second generation of lens materials, where hydrophilic properties were introduced through the internal wetting agent, poly(vinyl pirrolidone) (PVP).[230] Therefore this material does not have to be treated to provide wettability to the surface. Penetration vs force data (Fig. 5.4C, inset) exhibits constant slope through the indentation experiment with calculated modulus of 1.49 ± 0.28 MPa.

Finally, Comfilcon A represents the third generation of silicone-hydrogel materials, which contains hydrophilic chain segments within its structure and therefore this lens is inherently wettable material.[257] From penetration versus force data one can observe slope variation with increased indentation depth (Fig. 5.4D). However, unlike the case of Lotrafilcon B and Balafilcon A lenses, the initial region does not have linear part; the slope of the penetration data starts to decrease immediately after the contact point. Eventually the slope reaches constant value, which corresponds to 1.59 ± 0.17 MPa elastic modulus at deeper penetrations.

It is important to note, that all indentations performed in this study were nondestructive to the lens surfaces. Extremely low forces were applied to the cantilever to avoid irreversible changes of the lens surface. Imaging of the surface of the lens after the indentation experiments showed no indentation marks. In addition linear penetration vs. force plots suggest pure elastic deformations, which support full surface recovery.

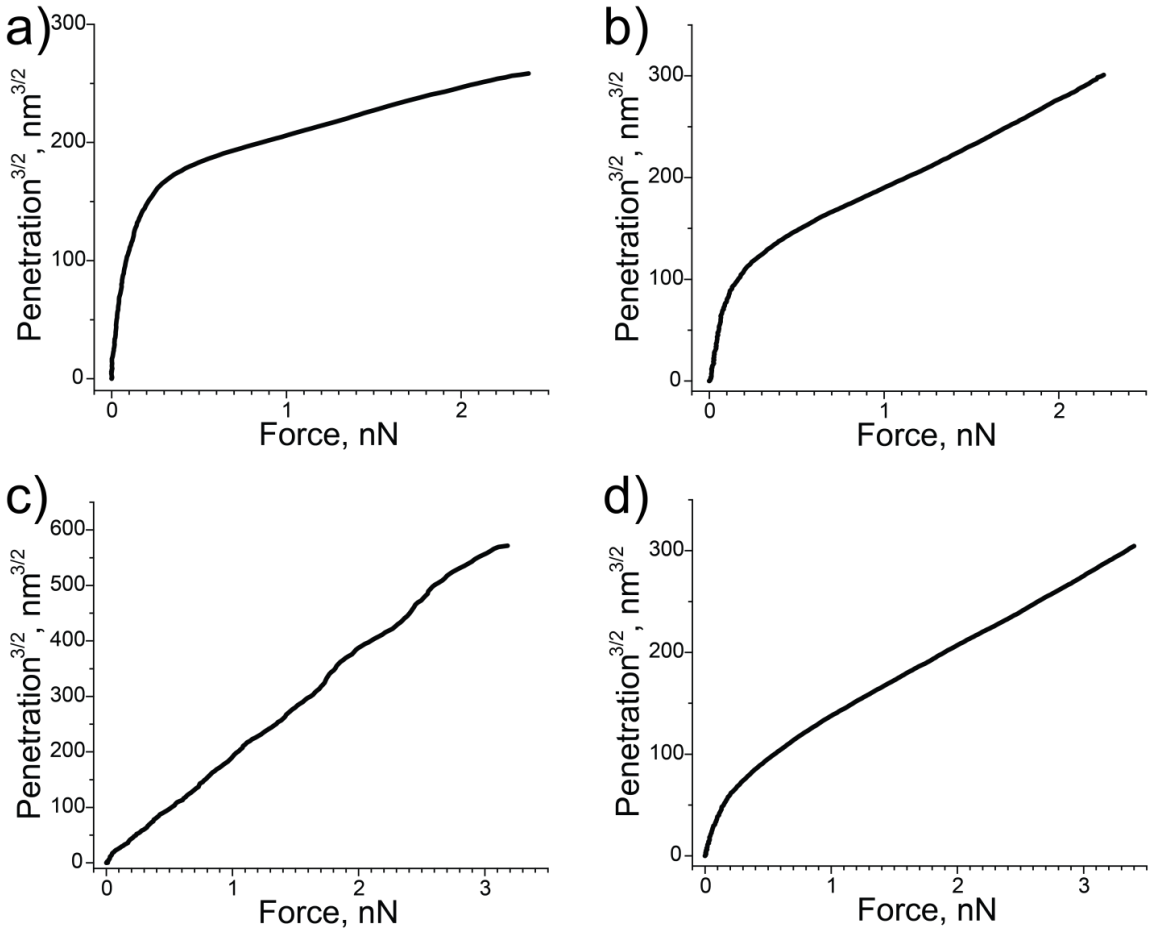

Figure 5.4: Penetration vs force plots derived from FDCs shown in Fig.3 assuming Sneddon's model for parabolic punch for: (A) Lotrafilcon B, (B) Balafilcon A, (C) Senofilcon A, (D) Comfilcon A.

5.3.3 Lens cross sections. In surface probing, the probing depth of the SFS indentation experiments is negligible as compared to the thickness of the lens. Maximum penetration depth reached in the present study is 100 nm, while thickness of the lens is in 50-100 µm range.[234] Therefore, to study the mechanical properties of the sub-surface and bulk regions of the lens material it is necessary to make a cross section of the lens and perform indentations within the bulk of the lens. The QNM images were used as a contrast map to locate regions with different mechanical properties. Next, indentation experiments were performed in these regions, with the same fitting procedure discussed in the surface analysis section. Despite the fact that fast rate QNM scans show presence of adhesive forces on the lens materials, all indentation curves collected during FV scans showed no

adhesion. The sections of the lens profiles from each of the channels were performed along the lines going across regions with property variation. Unlike some surface indentation curves, all indentation curves acquired from the cross section displayed constant elastic modulus for each indentation depth. Results of these measurements are summarized in Tab. 5.2. Detailed results of the cross section measurements for all lens materials under fluid are presented below.

Table 5.2. Summary of elastic moduli calculated from indentation experiments on the lens surface, lens cross sections and literature values of manufacturer reported elastic modulus.[258]

Material	Surface Indentations, MPa		Cross Section Indentations, MPa		Manufacturer Reported, Bulk, MPa
	First Layer	Second Layer	Outer Layer	Bulk	
Lotrafilcon B	3.69±0.36	0.45 ± 0.07	2.92±0.52	2.77±0.15	1.0
Balafilcon A	1.35±0.12	0.21 ± 0.06	N/A [a]	3.11±0.43[a]	1.1
Senofilcon A	0.52±0.07	N/A	0.66±0.18 / 4.38±0.78	1.49±0.28	0.72
Comfilcon A	1.59±0.17	N/A	1.59±0.26	1.75±0.26	0.75

[a]Both bulk and outer layer of Balafilcon A contain inclusions with modulus of 1.74±0.29 MPa

5.3.3.1 Lotrafilcon B. In Fig. 5.5 the results of QNM imaging of Lotrafilcon B lens are presented. The edge of the cross section is located on the left side. Each of the channels shows two distinct regions: the bulk of the lens and an approximately 14 µm thick outer layer. The outer layer appears to be swollen and has an increased height as compared to the bulk of the lens. The portion of the outer layer which is closest to the edge bears a resemblance to an additional coating of ~200 nm thick (green rectangle outline, Fig. 5.5). This coating however is mostly torn away by the razor blade during lens cutting procedure.

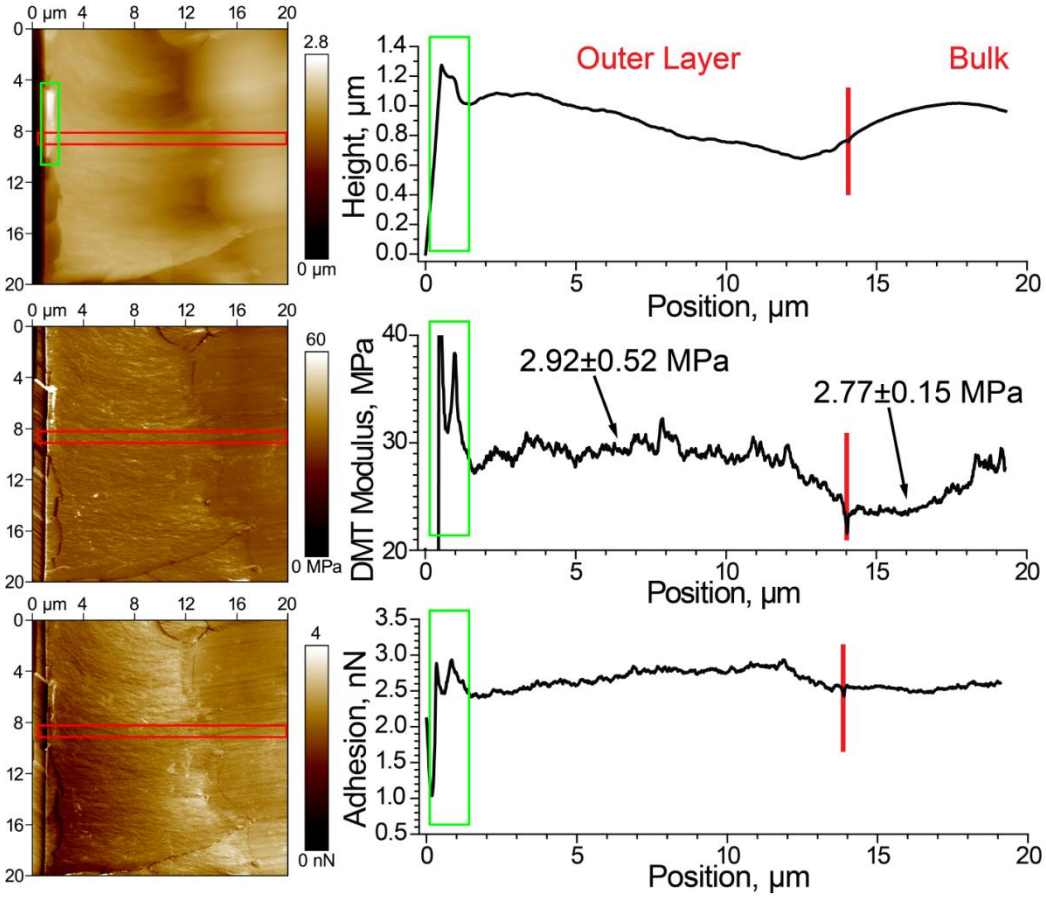

Figure 5.5: QNM mapping of Lotrafilcon B section in topography, DMT modulus and adhesion channels. Red rectangle shows position of the profile section. Green rectangle shows outer coating position.

FV measurements of the bulk of the lens and the outer layer show elastic modulus of 2.77 ± 0.15 MPa and 2.92 ± 0.52 MPa respectively. The additional outer coating was too thin and tilted to perform quantitative FV measurements on, however the DMT modulus channel of QNM measurements show slightly increased modulus for this coating (green rectangle outline, Fig. 5.5). This result is consistent with the surface measurements, where the modulus in this region was found to be 3.69 ± 0.36 MPa. Due to the low thickness and the edge effects, the 25 nm thick plasma coating cannot be imaged reliably from the cross section measurements.

5.3.3.2 Balafilcon A. Figure 5.6 shows the surface of the cross section of Balafilcon A lens material. All channels show two distinct regions. The bulk of the lens is flat and smooth and the outer region is ~10 µm thick, with a region of lamellar morphology within this region.

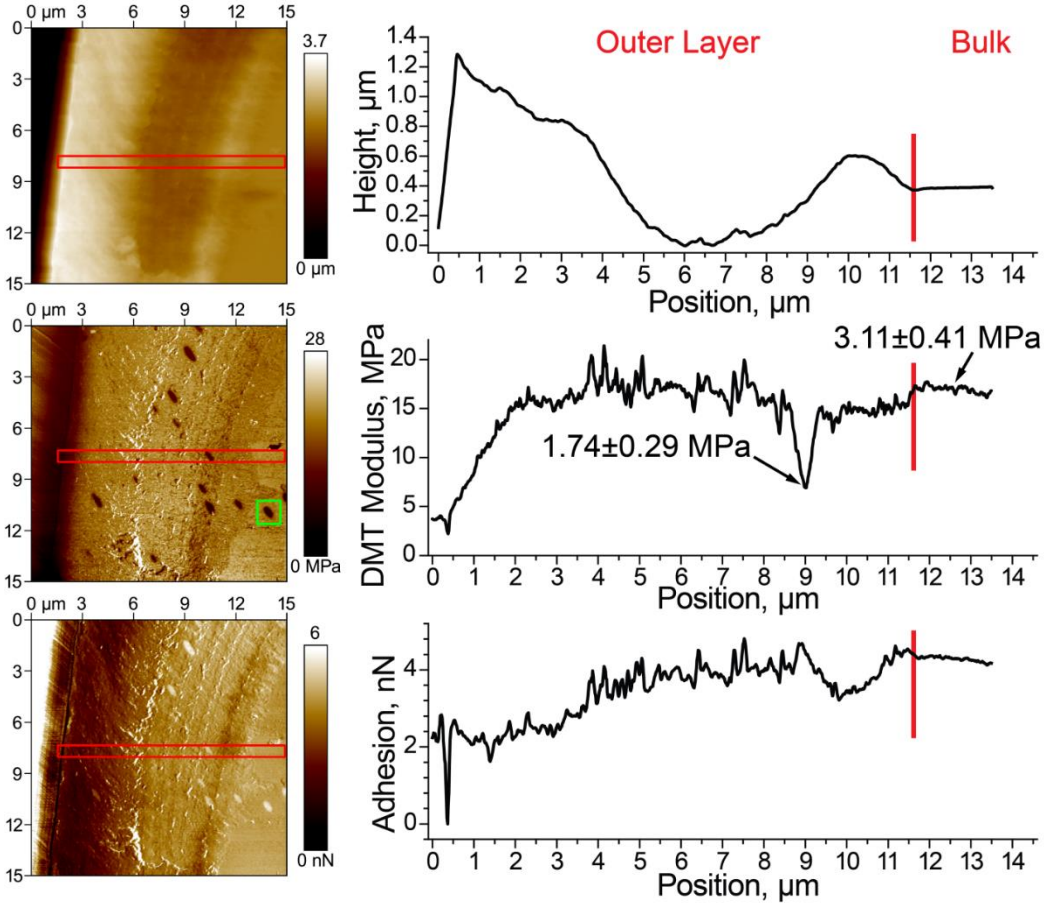

Figure 5.6: QNM mapping of Balafilcon A section in topography, DMT modulus and adhesion channels. Red rectangle shows position of the profile section. Green square shows the position of zoom in shown in Fig. 4.18.

Mechanical and adhesive properties of both regions were found to be very similar, with the bulk modulus value found to be 3.11 ± 0.41 MPa. Quantitative measurements of the modulus near the edge of the lens cross section could not be performed due to the high roughness of the sections at that location. Both regions have elongated inclusions with

lower modulus (1.74 ± 0.29 MPa) distributed within them. Since the measured modulus depends strongly on the topography of the surface at the point where the indentation is performed,[19] care should be taken in assigning the value to the selected features.

Fig. 5.7 shows 1 μm^2 offline zoom in of one of these elongated inclusions (green box in Fig. 5.6B). One can clearly see, that the AFM tip can reach the bottom of the inclusion, which is 40-50 nm deep and 200 nm wide.

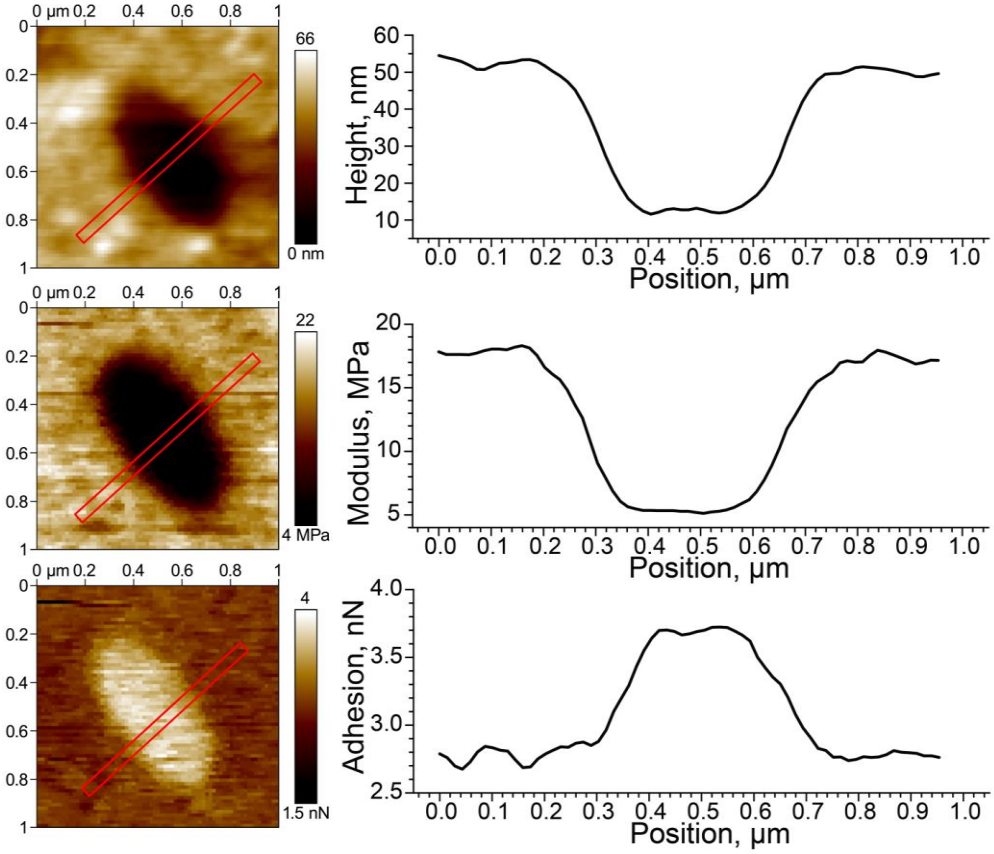

Figure 5.7: QNM mapping of Balafilcon A section in topography, DMT modulus and adhesion channels (zoom in from Fig. 6). Red rectangle shows the profile section.

This height variation in the lens cross section was likely caused by cutting due to the mechanical properties difference between bulk of the lens and the inclusions. Since the bottom of the inclusion is relatively flat and is much bigger that the radius of the curvature

of the tip (see Fig. 5.1C), one can reliably perform indentation experiments to calculate the modulus of the inclusion in the wet state. It is interesting to note that SEM studies of the same material performed in vacuum showed porous structure instead of compliant inclusions under wet conditions revealed here.[259]

5.3.3.3 Senofilcon A. The Senofilcon A lens shows distinct boundary between the bulk of the lens and and outer layer of ~4 μm thickness in all three channels (Fig. 5.8). The outer layer has higher roughness and lower modulus and adhesive properties than the bulk of the lens. Calculated modulus was found to be 1.49 ± 0.28 MPa for the bulk and 0.66 ± 0.18 MPa for the outer layer (Tab. 5.2). The modulus for the outer layer is close to the modulus calculated from the surface indentation (0.52 ± 0.07 MPa). The case of Senofilcon A lenses demonstrates that in order to study the stiffness of soft contact lenses using SFS with a sharp tip, surface indentations alone are insufficient. Despite the fact that surface indentation curves exhibited constant slope and constant modulus during indentation, only ~60 nm of the surface material is probed (Fig. 5.3C). To fully characterize mechanical properties of the material we also studied the lens cross sections.

In this study, we observed that the outer layer of Senofilcon A has multiple inclusions of higher modulus (Figs. 5.8, 5.9). From the adhesion mapping one can clearly see the effect of topography on the measurements: the adhesion has a spike on the right side of the inclusion, suggesting higher area of contact between the tip and the material when, in addition to the tip apex, the side of the tip comes into the contact with the material. Nevertheless there are flat regions within the inclusions, where the accurate measurements could be performed. The resulting modulus for the inclusions was calculated to be 4.38 ± 0.78 MPa. This value has high standard deviation due to the topographical irregularities of the inclusions

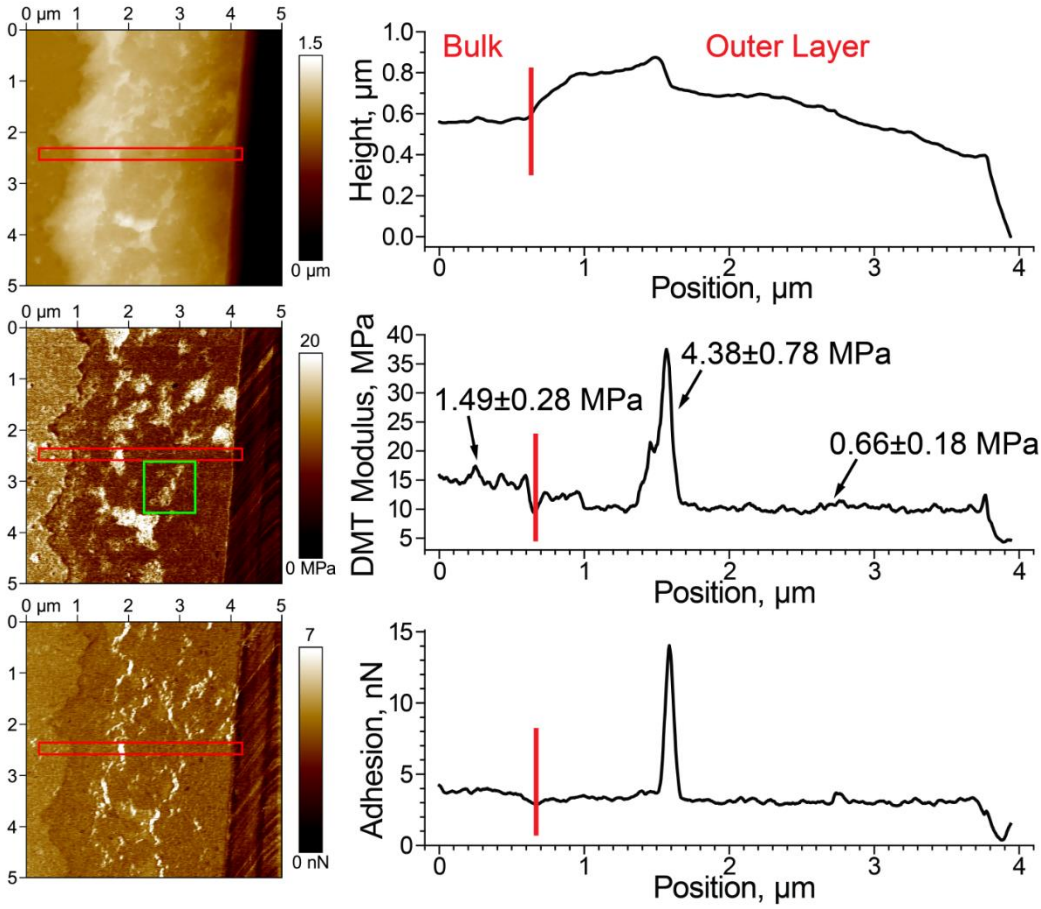

Figure 5.8: QNM mapping of Senofilcon A section in topography, DMT modulus and adhesion channels. Red rectangle shows position of the profile section. Green square shows the position of zoom in, shown in Fig. 4.34

.

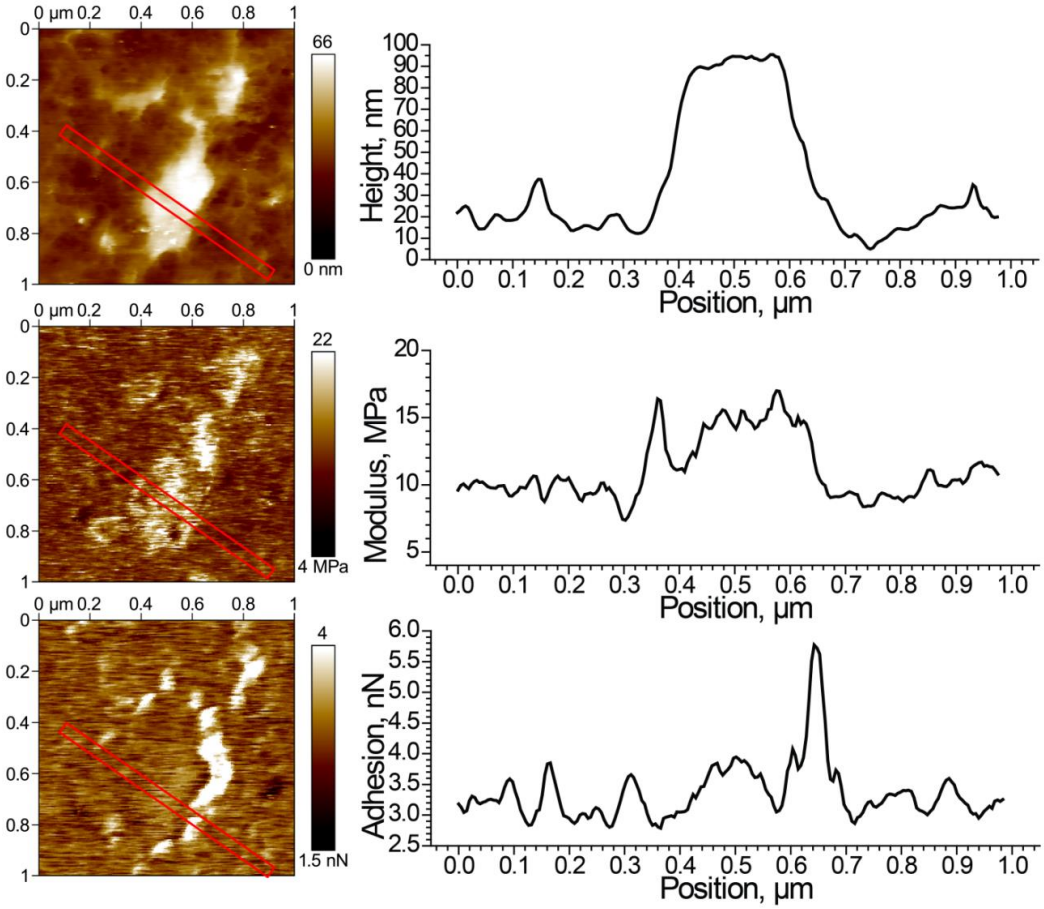

Figure 5.9: QNM mapping of Senofilcon A section in topography, DMT modulus and adhesion channels, zoom in from Fig. 4.33. Red rectangle shows position of the profile section.

5.3.3.4. Comfilcon A. The Comfilcon A lens section shows ~5 µm coating with modulus of 1.59 ± 0.26 MPa, which is slightly lower than the modulus of the bulk, 1.75 ± 0.26 MPa (Fig. 5.10). The outer layer appears to be swollen as compared to the bulk. Irregularities in the modulus and adhesion mappings are caused by fluctuations in the topography. However, for modulus measurements the flattest regions were selected. As with the Senofilcon A lens, the modulus of the coating closely matches the modulus measured with surface indentation. However, since the thickest portion of the lens can reach ~100 µm, the bulk portion will mostly contribute to the structural modulus of the whole lens.

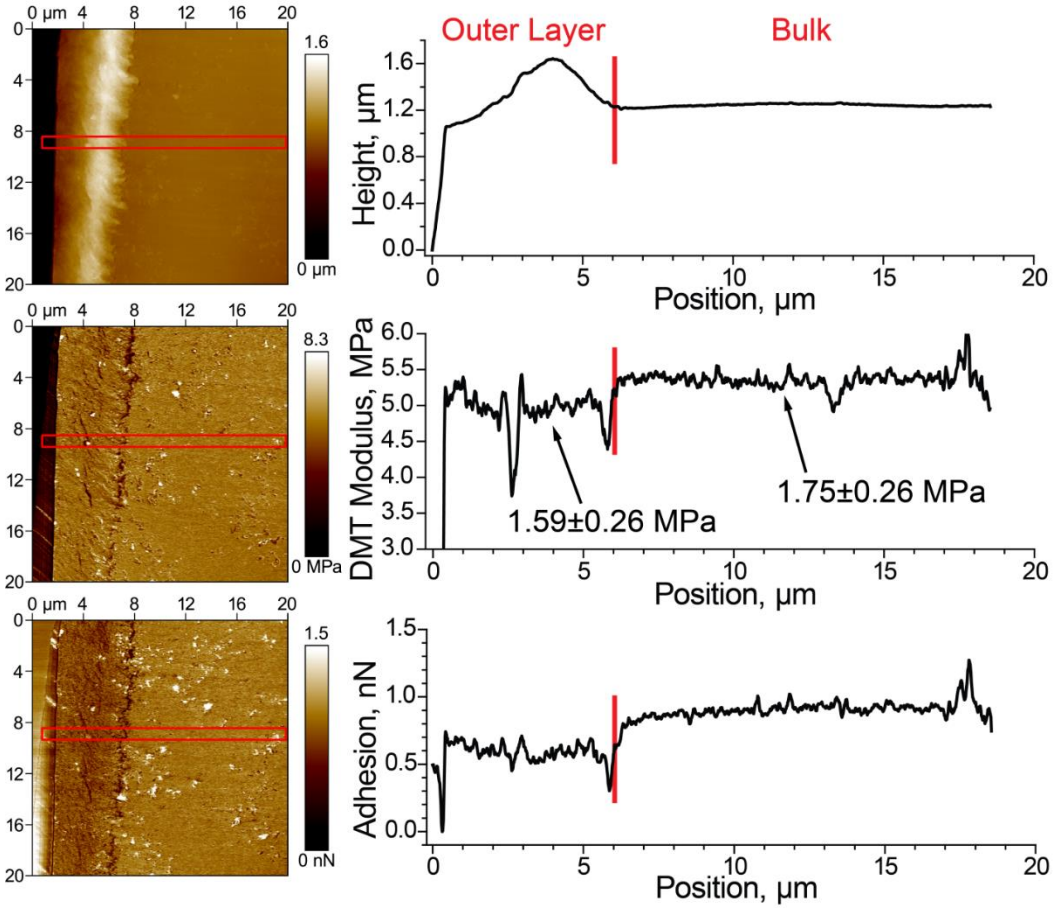

Figure 5.10: Peakforece QNM characterization of Comfilcon A section in topography, DMT modulus and adhesion channels. Red rectangle shows position of the profile section.

5.3.4 Comparative analysis of measured moduli. Table 5.2 shows accumulative data for the measured bulk modulus of all four studied materials along with the values reported in the literature. It is worth noting that for all the lens materials the elastic modulus from FV measurements is consistently 2-2.5 times higher than the value reported by the manufacturer. For Balafilcon A lenses, the trend is different, with measured values being ~3 times higher. However, since lens manufacturers employ conventional tensile testing,[234] the presence of compliant inclusions would lower the overall modulus of the material (Fig. 5.7).

We can associate above-mentioned difference in modulus values with the viscoelastic effects in the measured materials. These effects are known to manifest themselves in the rate dependence of elastic properties in soft polymer materials in the swollen state and in the vicinity of glass transition.[26] In the work of Horst et al.,[234] where the values of elastic modulus were found to be similar to the ones reported by manufacturers for Balafilcon A and Senofilcon A (1.1 MPa and 0.7 MPa respectively), a strain rate of 1% per second was used. For the AFM indentation experiments the strain induced within the material can be estimated as $\varepsilon = a/R$, where a is the radius of contact between the surface and the indenter, and R is the radius of curvature of the indenter.[16] Since under Sneddon's assumptions for parabolic indenter $a = \sqrt{\delta R}$,[28] one can estimate strain for low indentation depths as:

$$\varepsilon = \sqrt{\delta/R} \tag{5.2}$$

From Eqn. 5.2 it follows that at the constant loading rate penetration δ changes nonlinearly with time, however here for the comparative study we will estimate the strain rate as strain at maximum penetration divided by the time of indentation experiment.

Taking the indentation into the bulk of Lotrafilcon B as an example such estimation results in extremely high strain rate of 6200% per second for 4 Hz experiment frequency (this frequency was used in FV measurements in this study). According to the general theory of polymer elasticity, a material becomes stiffer at higher loading rates,[206] therefore indentation measurements would produce higher values of the elastic moduli for the lens materials than the literature values of conventional tensile measurements. To prove this concept, frequency dependent measurements were performed on the bulk region of Lotrafilcon B lens as an example. In addition, similar measurements were performed on a purely elastic PDMS sample with well-known elastic properties. As it was mentioned

before, due to the nonlinearity in the penetration rate, a single constant value of strain rate cannot be assigned to each indentation experiment. Therefore here we will use indentation time (period when tip and the sample are in contact during the approach portion of the indentation cycle) as variable to show changes in elastic modulus (Fig. 5.11).

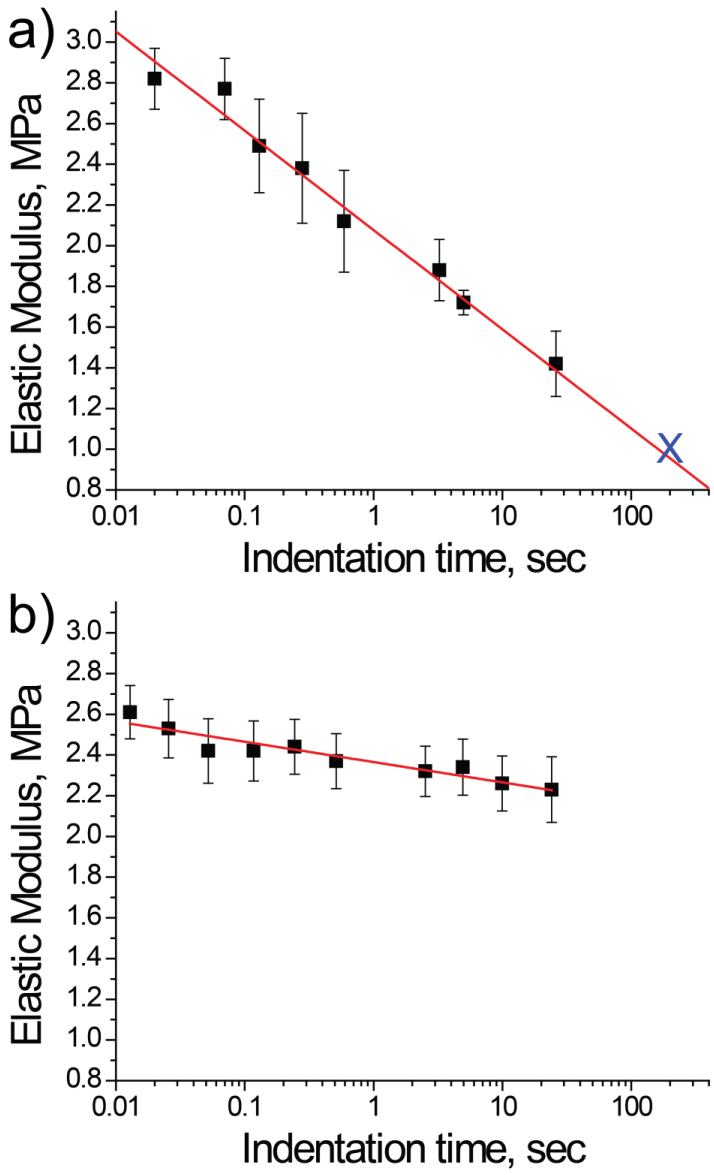

Figure 5.11: QNM characterization of Comfilcon A section in height, DMT modulus and adhesion channels. X mark shows approximate time of indentation, which corresponds to 1% per second strain rate.

The standard measurements performed in this work for Lotrafilcon B lens at the 4 Hz frequency corresponds to an indentation time of 0.07 sec and the apparent modulus value decreases with the increase in the indentation time as expected for viscoelastic materials. The values exhibit linear decrease with time when plotted in logarithmic scale, which suggests well known Williams-Landel-Ferry (WLF) dependence, common for polymer materials.[125] Calculated virtual indentation time, which corresponds to the 1% strain rate of conventional tensile measurements, is indicated by 'X' mark in Fig. 5.11A. The literature value of the modulus at this point for Lotrafilcon B lens is 1 MPa, and as one can see the fitting line for the experimental data tends close to this value. However reliable AFM measurements with such long indentation times cannot be reliably performed due to piezo-creep effects. In contrast, similar indentation experiments for PDMS samples (Fig. 5.11B) shows very little variation with indentation time and elastic modulus values close to literature.[260]

5.4 Conclusions

Experimental protocol for measurements of the soft composite materials is suggested here with soft silicone hydrogel contact lens materials used as an example. Results from the fast scans and slow force-volume measurements of the surfaces and cross section of four contact lenses are presented. Measurements of the surface topography of the lenses revealed smooth areas suitable for indentation measurements. Surface indentations curves exhibited Sneddon's model behavior, which allowed elastic modulus calculation. In addition surface indentation experiments in the case of Lotrafilcon B and Balafilcon A revealed the presence of the thin coating resulting from the plasma treatment of these materials. Cross sectional measurements of the lens materials showed the capability of the SFS to resolve surface features with high special resolution and revealed the presence of the composite subsurface regions with variation of adhesive and mechanical properties

within the lens volume. Force-volume measurements in these regions allowed to acquire quantitative mechanical properties for these regions.

Values of the measured elastic moduli for the bulk portion of the studied lens materials were found to be higher than the literature data, however if examined in relation to each other present a similar trend and attributed to the differences in the strain rate between Instron and indentation measurements. Frequency variation experiments with Lotrafilcon B sample showed the elastic modulus variation with frequency, with the modulus value for Lotrailcon B tending to the literature value for measurement rates close to the literature data. The experimental values acquired for all lens materials at 4 Hz present physically relevant quantities, which can be used for the lens comparison and the proposed method can be employed for comparable measurements of mechanical properties of soft contact lenses under practical conditions.

CHAPTER 6

Micro- and nano-structural features of a spider's filter for substrate vibrations. Relevance for low frequency signal transmission.

The metatarsal lyriform organ of the Central American wandering spider *Cupiennius salei* is its most sensitive vibration detector. It is able to sense a wide range of vibration stimuli over four orders of magnitude in frequency between at least as low as 0.1 Hz and several kHz. Transmission of the vibrations to the slit organ is controlled by a cuticular pad in front of it. While the mechanism of high frequency stimulus transfer (above ca. 40 Hz) is well understood and related to the viscoelastic properties of the pad's epicuticle, it is not yet clear how low frequency stimuli (<40 Hz) are transmitted. Here we study how the pad material affects the pad's mechanical properties and thus its role in the transfer of the stimulus, using a variety of experimental techniques, such as, x-ray micro-computer tomography (μCT) for 3D imaging, x-ray scattering for structural analysis, and atomic force microscopy (AFM) and scanning electron microscopy (SEM) for surface imaging. The mechanical properties were investigated using scanning acoustic microscopy (SAM) and nanoindentation. We show that large tarsal deflections cause large deformation in the distal highly hydrated part of the pad. Beyond this region, a sclerotized region serves as a supporting frame which resists the deformation and is displaced to push against the slits, with displacement values considerably scaled down to only few micrometers. Unraveling the structural arrangement in such specialized structures may provide conceptual ideas for the design of new materials capable of controlling a technical sensor's specificity and selectivity, which is so typical of biological sensors.

6.1 Introduction

The metatarsal lyriform organ is situated at the distal end of the second last segment of each leg, i.e. their metatarsus (Fig. 6.1). Substrate vibrations deflect the most distal leg segment, the tarsus, which transmits the signal to the vibration sensitive slit sensilla by pressing against the metatarsus. A cuticular pad (Figure 6.1B-D) is situated just in front of the metatarsal lyriform organ, at the contact area with the tarsus. The pad plays a major role in the mechanical filtering of vibrational stimuli and represents an effective high-pass filter.[93] This latter function was recently mapped to the external most layer of the pad, a layer of epicuticle.[123] This layer is unusually thick and behaves visco-elastically. Its glass transition temperature is around 19 °C, corresponding to a frequency of 100 Hz according to the time-temperature-modulus relationship in viscoelastic materials.

In its natural habitat and during its time of activity the spider sits on a leaf in its characteristic "hunting position", with the proximal end of the tarsus just in contact with the pad. From this point of contact onwards, further deflection of the tarsus will elicit action potentials in the sensory cells of the metatarsal lyriform organ - if its amplitude is above threshold (depending on frequency) and overcomes the filtering restrictions of the pad. Electrophysiological studies have shown that for high frequencies only minute deflections of the tarsus beyond the "first contact" with the pad are needed in order to elicit action potentials. In particular, for frequencies of several hundred Hz vertical threshold displacements of the substrate down to the order of nanometers and corresponding to deflection angles of around 0.01° from the "first contact" angle elicit physiological responses in the receptor cell.[124] Below stimulus frequencies of about 40Hz, however, threshold deflections of the tarsus by tens of microns or up to 10° from the "first contact" position are needed in order to elicit a nervous response.

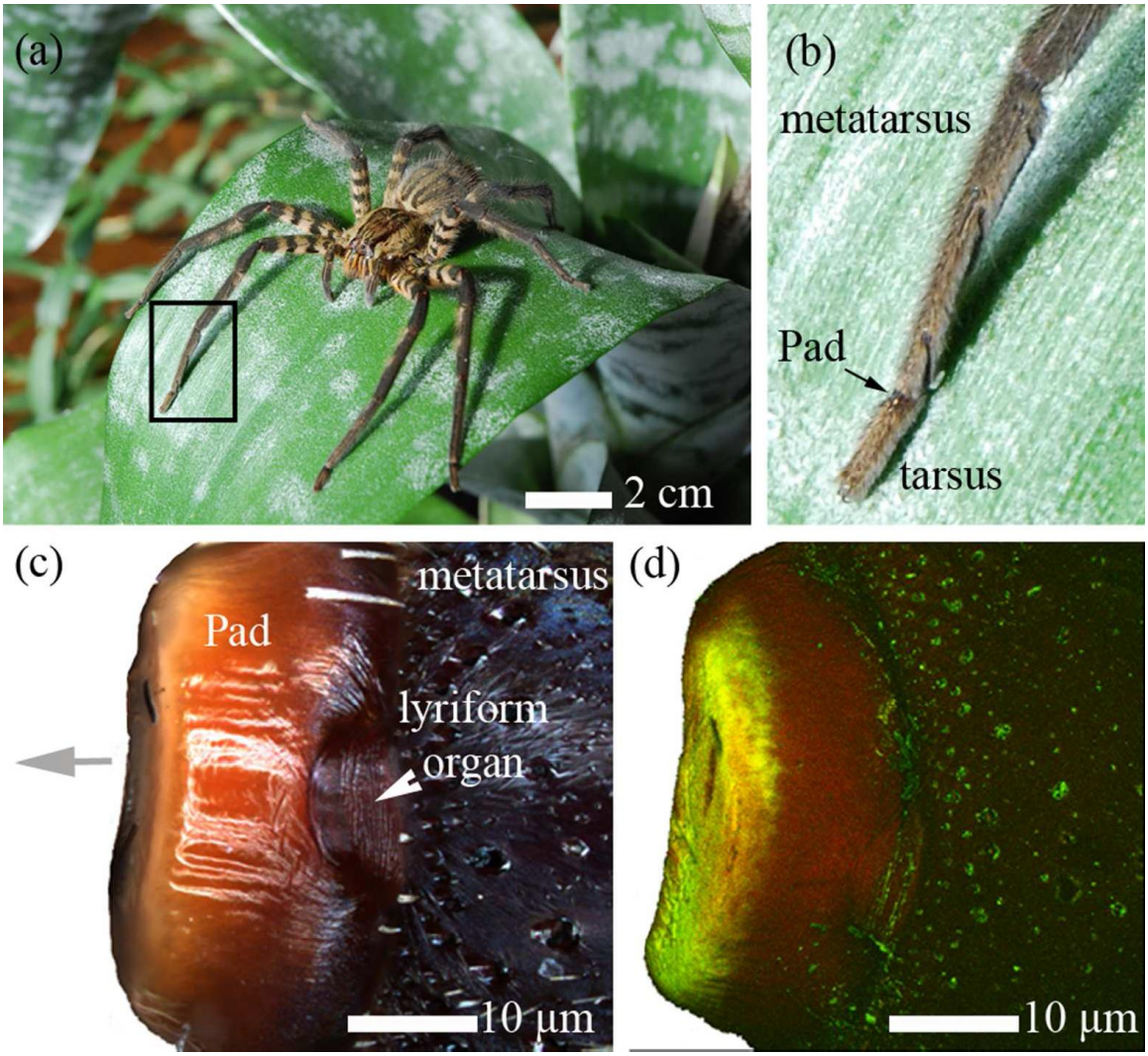

Figure 6.1: (A) Adult female spider Cupiennius salei. (B) TMagnification of the two last (distal) leg segments; the metatarsus and the tarsus. The cuticular pad is situated at joint between the two segments (arrow). (C) Optical light microscope image of the cuticular pad and the vibration receptor of the spider. Top view on the dorsal side of the pad. The distal direction is marked by a gray arrow. White arrowhead indicates vibration sensitive metatarsal lyriform organ. (D) Confocal laser scanning microscopy (CLSM) view of the pad in (C). The image is constructed by a superposition of the auto-fluorescence signals (as maximum intensity projection) of excitation / detected emission wavelengths: 488 nm / 499 - 555 nm (green channel); 561 nm / 578 - 678 nm (red channel).

The remarkably high sensitivity of the slits at high frequencies is owed first to the properties of the epicuticular layer of the pad, which assumes a glassy state at these frequencies, thus efficiently transmitting the signal.[123] Other mechanical factors affecting the mechanical sensitivity of the slits at a subsequent stage of stimulus transmission are slit length, aspect ratio and specific location within the array of slits as previously documented

in detail. [110,117,137] The question remains, how low frequency stimuli are transmitted to the slits considering that the epicuticle then assumes a rubbery state, strongly damping the incoming vibrations. In addition, since large deflection amplitudes are involved, what protects the delicate slit system from damage?

Here we address these questions by studying the structure and composition of the pad and relating them to the material's mechanical properties. We also monitor the three-dimensional deformation behavior of the pad upon the static application of mechanical load similar to the natural load application at low frequencies. Thus the tarsus was deflected against the pad during X-ray micro-computer tomography (µCT) measurements in wet state. We show that the three-dimensional morphology and specifically sub-structure of the pad allows large tarsal deflections to be converted into small displacements at the pad-slit contact region, thus allowing transmission of low frequencies stimuli while providing mechanical robustness and damage protection at high loads.

6.2 Materials and methods

6.2.1 Sample preparation. Adult females of the Central American wandering spider *Cupiennius salei* were received as described previously. In all experiments, except in those applying micro-computer tomography (µCT), we used spider legs taken from shock frozen (at -196 °C) specimens initially anaesthetized and kept at around -18° C until use. For µCT experiments fresh autotomized spider legs were prepared. For a better view the hairs covering the metatarsus were removed by gently wiping the surface with a cotton tissue.

6.2.2 Sectioning. For X-ray scattering experiments and Confocal Laser Scanning Microscopy (CLSM) the pad was dissected from the tarsus and sectioned into 30 µm thick slices using a vibratome (Leica VT1000S; Leica Microsystems GmbH, Wetzlar, Germany) at 80 Hz steel blade frequency and 0.025 mm/s blade velocity. For sectioning, the

metatarsus was glued to a plastic substrate using a tiny superglue droplet (Roti coll 1, Carl Roth, Karlsruhe, Germany). Contamination of the pad region with the superglue was avoided by fixing the metatarsus sufficiently away from its dorsal side where the pad and the slits are situated. The slices were cut in high-purity water at 20 °C and kept wet until the time of the experiment. The entire sample preparation process took only few minutes and was performed shortly before each measurement.

6.2.3 Embedding and polishing. For Scanning Acoustic Microscopy (SAM) measurements and for Nanoindentation the metatarsus containing the pad was immersed in methylmetacrylate (MMA) for 8 h followed by polymerization in an oven at 60 °C. The embedded samples were gently polished (in their sagittal plane) until the cuticular pad region of interest was exposed to the surface. Although incubation in MMA and heating to 60 °C cause drying of the samples, after sectioning and polishing the samples were rehydrated (considerable swelling was observed) in order to measure the properties of the sample as close as possible to their natural state. We expect limited influence of the embedding material (reduced mechanical modulus of 4 GPa) on the measured mechanical properties of the cuticle since, we do not observe significant infiltration of MMA into the sample as judged from the fact that the sample can be easily detached from the embedding material and that the swelling behavior is not affected.

6.2.4 Optical microscope imaging. Optical images were taken using a light microscope and digitally enhanced as described in Chapter 3.

Polarized light images (1388 x 1038 pixel; 0.37 µm/pixel) were recorded on an upright microscope (Axio Imager A2, Zeiss, Jena, Germany) equipped with a 20x objective (LD A-Plan 20x/0.35 Ph2) (Zeiss, Jena, Germany) using a polarizer and an analyzer with a

relative orientation of 90°. The images were analyzed using the software package Zen 2012 (Zeiss, Jena, Germany).

6.2.5 Electron Microscopy. Scanning electron microscopy (SEM) images were taken as described in § 3.2.2.

6.2.6 Confocal laser scanning microscopy (CLSM). Free standing pad sections (30 µm thick) were imaged on a Leica TCS SP5 (Leica Microsystems GmbH, Wetzlar, Germany), as described in § 3.2.4.

6.2.7 Micro-computer tomography (µCT). The experiments were performed at the European Synchrotron Radiation Facility (ESRF) in Grenoble, France, utilizing the imaging setup at beamline ID19. These measurements were elaborated on in § 3.2.5.

In order to prepare fresh samples for µCT measurements, the most distal two leg segments of freshly autotomized spider legs were separated from the rest of the leg using a scalpel. In order to avoid drying, the fresh cut was instantly sealed with a droplet of candle wax. The samples, now containing only metatarsus and tarsus, were mounted in a micro tomography fatigue press (Tomo-press) developed at ESRF.[261] The metatarsus was fixed horizontally on one side of the Tomo-press while the free-hanging tarsus was pointing towards the opposite side, where a rectangular aluminum wedge was mounted. Using a remote control the wedge was brought closer towards the tarsus thus pushing it against the pad as in natural stimulation. The desired deflection angle between the tarsus and the metatarsus (between 0° and 45°) was adjusted by horizontally changing the distance between the two fixed parts. The corresponding vertical displacement of the tarsus distal side (substrate displacement) was calculated by measuring the angle between the two leg-segments from digital images of the camera connected via a C-mount to a microscope with

long working distance. A series of rotation angles was used to avoid perspective errors. The maximum angle value of 45° was defined by the geometry of the aluminum wedge. The angular deflection values were chosen according to previously reported values well within the physiological working range of the slits.[124] The tarsus was thus deflected against the metatarsus in a stepwise manner, and µCT data sets were obtained at each stationary position after one hour relaxation time for each step. For tomography measurements the sample was rotated around the horizontal axis while keeping the distance between the leg sample and the wedge constant. The Tomo-press chamber was sealed with Kapton foil and was kept humid by a continuous stream of fully hydrated air during the entire course of the measurements. Two tarsus-metatarsus joints were measured, at six and at three angular positions, respectively. The temperature inside the hutch was maintained at 20 °C, which is above the glass transition temperature of the epicuticle.[123]

6.2.8 X-ray scattering. X-ray scattering experiments were performed at the µ-spot beamline at the BESSY II synchrotron radiation facility in Berlin, Germany, as described in § 3.2.6.

6.2.9 Scanning acoustic microscopy (SAM). SAM measurements were performed using KSISAM2000 by Krämer Scientific Instruments (Herborn, Germany, § 3.2.7).

6.2.10 Nanoindentation. Nanoindentation measurements were performed according to § 3.2.8.

6.3 Results and Discussion

6.3.1 Pad morphology and deformation during load. The three-dimensional shape of the pad is rather complex (Fig. 6.2): it has a crescent-like shape and a lumen filled with cellular materials showing slightly lighter contrast in the µCT data. Just below the lyriform organ

a small cuticular “ridge” extends along a plane perpendicular to the leg long axis, which is roughly parallel to that of the slits. We refer to this ridge as “appendix”. Figure 6.2A shows the pad surface according to µCT data (green) with three sub-regions marked in different colors. These regions specify the location and orientation of 3 types of sections used in our compositional and structural analyses. The outlines of each section are also depicted schematically in Fig. 6.2B. In Fig. 6.2C-H six sagittal virtual sections of the reconstructed three-dimensional pad structure (extending laterally from the center of the pad) illustrate its structure.

In order to better visualize and quantify the deformation of the pad under loads relevant to the transmission of low frequency stimuli to the slits we performed X-ray micro-tomography measurements (under hydrated conditions) of the pad in compressed state, stimulated by deflecting the tarsus against the pad. The angle formed by the long axes of tarsus and metatarsus at which the tarsus first touches the pad is defined as the “mechanical threshold angle” and measures 28° ± 1°. From now on we refer to this angle as 0° when deflecting the tarsus against the metatarsus. We measured six different angular positions between -4° and 9° (±1°). For angles above 0° the tarsus pushes into the pad, significantly deforming its distal part. We quantified this deformation my measuring the distance of the distal surface of the pad at each degree from its resting position at 0°.

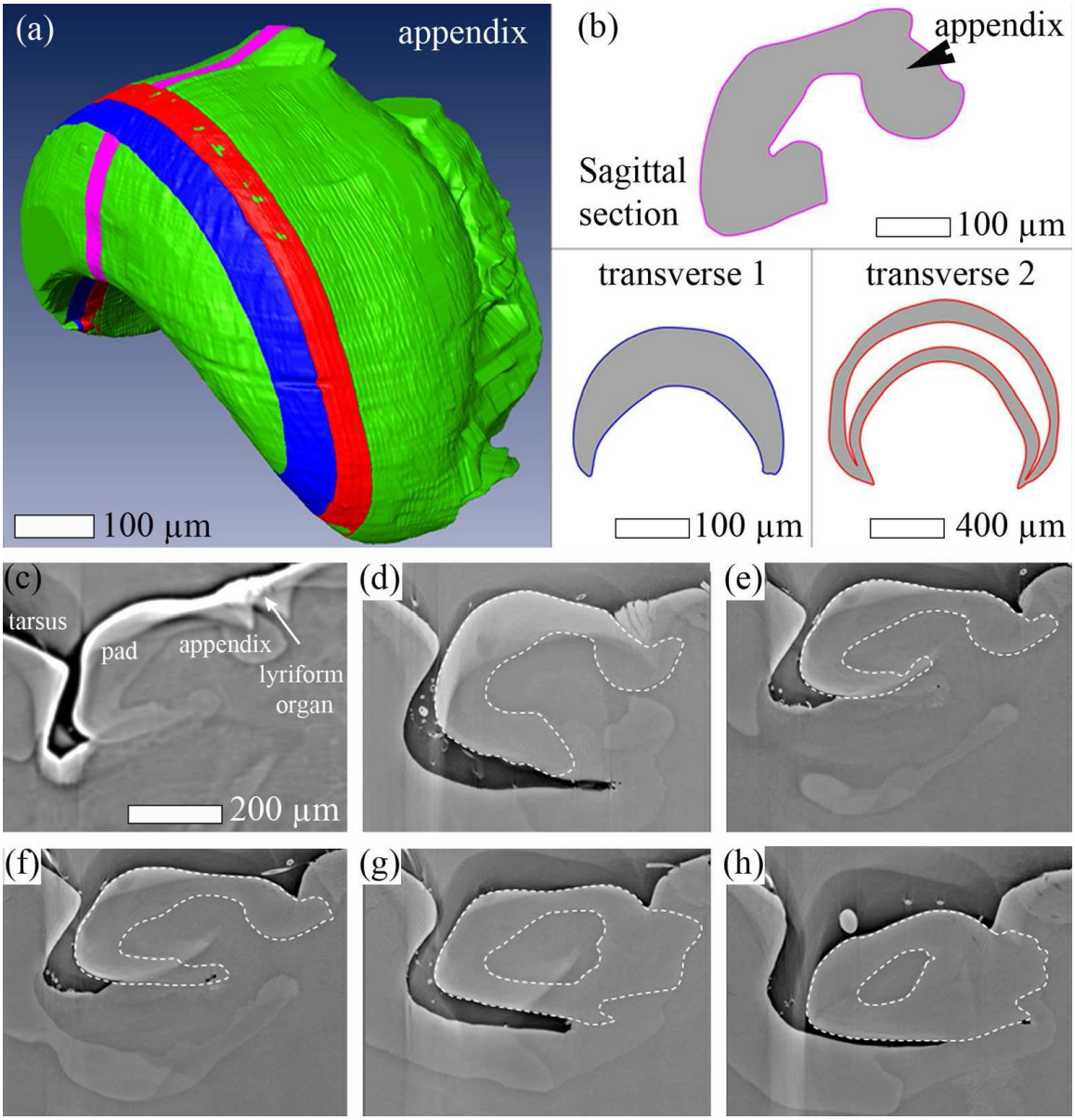

Figure 6.2: (a) Surface rendering of the reconstructed µCT data of the pad. Virtual sections representing sample sections used in this study are indicated by three differently colored slices: pink, blue, and red (b) Schematic representation of the shape for the slices shown in (a). (c-h) µCT virtual slices along the long- axis of the leg (sagittal plane) laterally extending from the pad center (c) to the pad lateral edge (h). The dashed lines show the outline of the pad traced along the organ. The line was determined using a number of successive images.

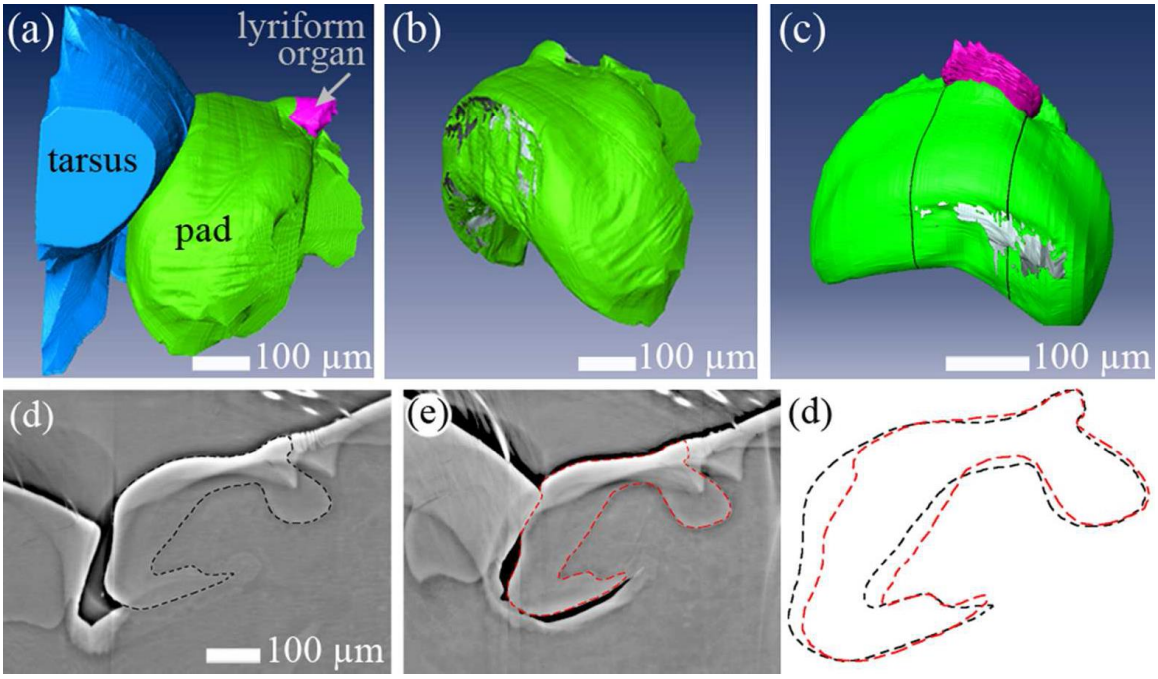

Figure 6.3: (A) Surface rendering of reconstructed µCT data showing three selected components of the metatarsal vibration receptor including the tarsus (blue), the pad (green), and the slit-sensilla lyriform organ (pink) measured during contact. The deflection angle between the tarsus and metatarsus was 9°. (B) 3D shape of the cuticular pad extracted from (A). Grey regions at the distal side of the pad indicate the contact area with the tarsus. (C) 3D shape of the cuticular pad under load with a slight lateral component. The tarsus-metatarsus angle was 8°. Grey regions at the distal side of the pad indicate the contact area with the tarsus. (D-F) µCT virtual slices of the sample in A-B sectioned in the sagittal plane in the center of the pad in relaxed (D) state (< 0°), and deflected by 9° (E). The dashed lines indicate the outline of the cuticular material of the pad. The white arrows indicate one slit of the metatarsal lyriform organ. Darker region below the ventral side of the pad is caused due to reduction in vapor pressure; the pad itself however is still moist. (F) An overlay of the pad shape from D and E.

For example, at 9° ± 1°, the pad surface is pushed in 29.4 ± 0.7 µm. Figure 6.3D-E show that other parts of the pad hardly change their shape. However, small displacements of a few micrometers (3.5 ± 0.7 µm at 9° ± 1°) at the contact region with the slits can be seen. In addition, the slits themselves are also compressed up to 50-60% of their initial width (width of the most distal slit at 9° ± 1° in Fig. 6.3D-E) in agreement with a previous white light interferometry study.[117] Importantly, the slits are compressed evenly throughout their length and depth. Another interesting observation from Fig. 6.3B is that the contact area of the tarsus and the pad, is limited to a rather small region. When the pad is loaded by a lateral deflection, the lateral regions of the pad assume the maximum deformation

(Fig. 6.3C). Such deflections do occur during natural stimulations and are also known to elicit action potentials.[84]

6.3.2 Pad sclerotization pattern. Figure 6.1C shows the dorsal view of an intact pad. The different colors of the distal and dorsal sides of the pad suggest different degrees of sclerotization, the darker color often being associated with higher sclerotization.[262] While the surface is bright creamy-colored distally (blue arrow in Fig. 6.1C), it is darker dorsally (red arrow). Auto-fluorescence measurements performed with a confocal laser-scanning microscope (CLSM) and two different excitation wavelengths support the assumption regarding the different degrees of sclerotization. In Fig. 6.1D the emission signal images collected at 499-555 nm (green channel) and 578-678 nm (red channel) for excitation at 488 and 561 nm, respectively, are overlaid to form one composite image. Whereas the distal surface of the pad shows a predominantly green channel auto-fluorescence signal, usually attributed to cuticles with low sclerotization levels, the dorsal surface shows a strong auto-fluorescence signal in the red channel, indicative of cuticle sclerotization.[263]

CLSM was also applied to a pad section cut along the sagittal plane. The section was first measured hydrated and again after allowing it to dry for 30 min at room temperature (Fig. 6.4).

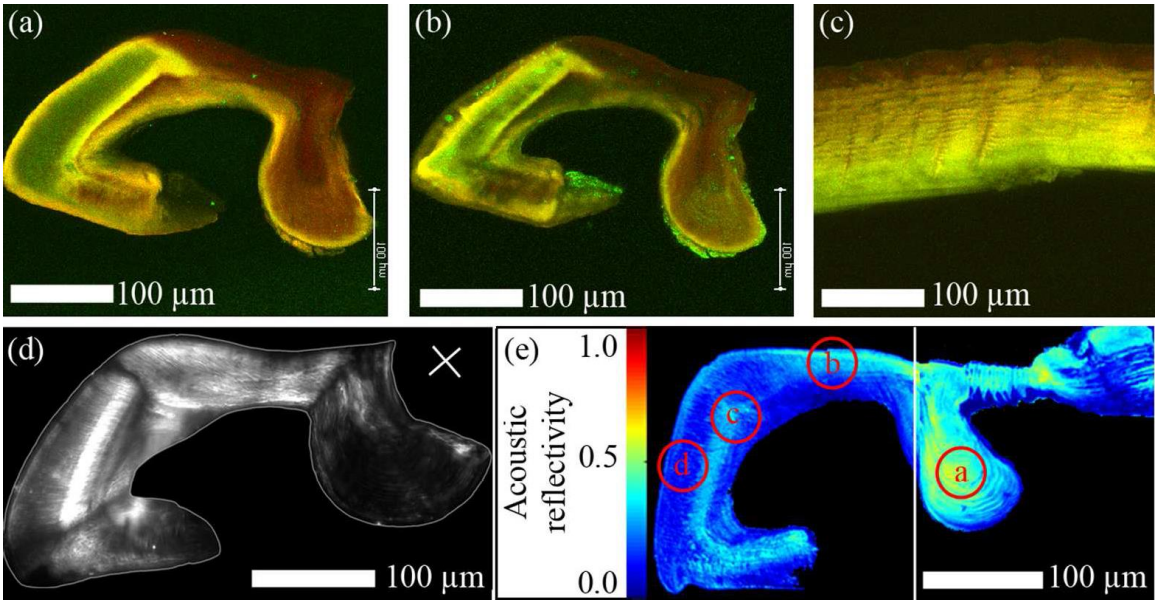

Figure 6.4: (a,b) Autofluorescence signal (maximum intensity projection) of a longitudinal section (thickness 30 µm) of the pad in (a) wet and (b) dry states. Excitation / detection emission wavelengths: 488 nm / 499-555 nm (green channel); 561 nm / 578-678 nm (red channel). (c) Maximum intensity projection of a longitudinal section of the metatarsal exoskeleton (thickness 30 µm) in wet state. (d) Polarized light microscopy image of the pad in wet state. The white line indicates the outline of the the pad. The orientation of the polarizer- analyzer is indicated by the white cross. (e) Scanning Acoustic Microscopy (SAM) image of the pad sagittal section. The picture consists of two merged images (dotted line) obtained from two samples measured at the same experimental conditions. The color code indicates the reflectivity distribution for acoustic waves. Regions a-d indicate the positions chosen for Nanoindentation measurements on the same samples.

The auto-fluorescence pattern of the pad section is rather complex compared to what is commonly found in the spider's exoskeleton, e.g. along the metatarsus (Figure 6.4C). While the distal part of the pad is dominated by green-channel fluorescence and contains an internal inner region with only weak fluorescence the dorsal part and the "appendix" are predominantly showing auto-fluorescence in the red channel. Interestingly, a pronounced dark-red region in the inner part of the distal pad region is observed. Such strongly sclerotized internal cuticle is not common in arthropods, except in structures like muscle attachment sites or clerites.[84] The level of sclerotization in the metatarsus away from the pad region decreases from exocuticle inwards to meso- and endocuticle following a well-known pattern common in arthropods (Fig. 6.4C). [129,262] After dehydration, CLSM images show large shrinkage in less sclerotized cuticle regions (Fig. 6.4B) while highly sclerotized

cuticle regions retain similar shape regardless of the water content. The largest effect is seen in the distal part of the pad, which shrinks to about half of its original size.

6.3.3 Chitin and protein distribution and alignment. X-ray scattering measurements were performed with 30 µm thick pad slices in hydrated and dry states, using a focused beam measuring 10 µm in diameter. Structural parameters as well as an estimate of the relative content of chitin and protein in the pad material were obtained from analyzing both, Small- (SAXS) and Wide-Angle X-ray Scattering (WAXS) regions (Fig. 6.5).

The signal in the WAXS region (Fig. 6.5A), nominally referred to the scattering region above q = 4 nm^{-1}, is dominated by diffraction signal from the crystalline chitin-protein fibrils (Fig. 6.5A). Although crystallite orientation strongly affects WAXS intensity, integration over the scattering intensity of Bragg reflections with close to orthogonal orientation, (110) and (013) were used in order to gain qualitative information on the relative distribution of chitin in the pad (yellow scale in Fig. 6.5B).

Scattering signal from chitin crystals is observed throughout the entire pad cross-section, however with significantly lower intensity at the distal end of the pad. In this region the intensity of both (110) and (013) reflections are low, indicating that chitin density is low. In other regions-with low WAXS intensity, within the "appendix" and in the ventral wall of the pad, the (013) reflection is completely missing in the WAXS signal, indicating that the crystallites here are oriented mainly out of the section plane.

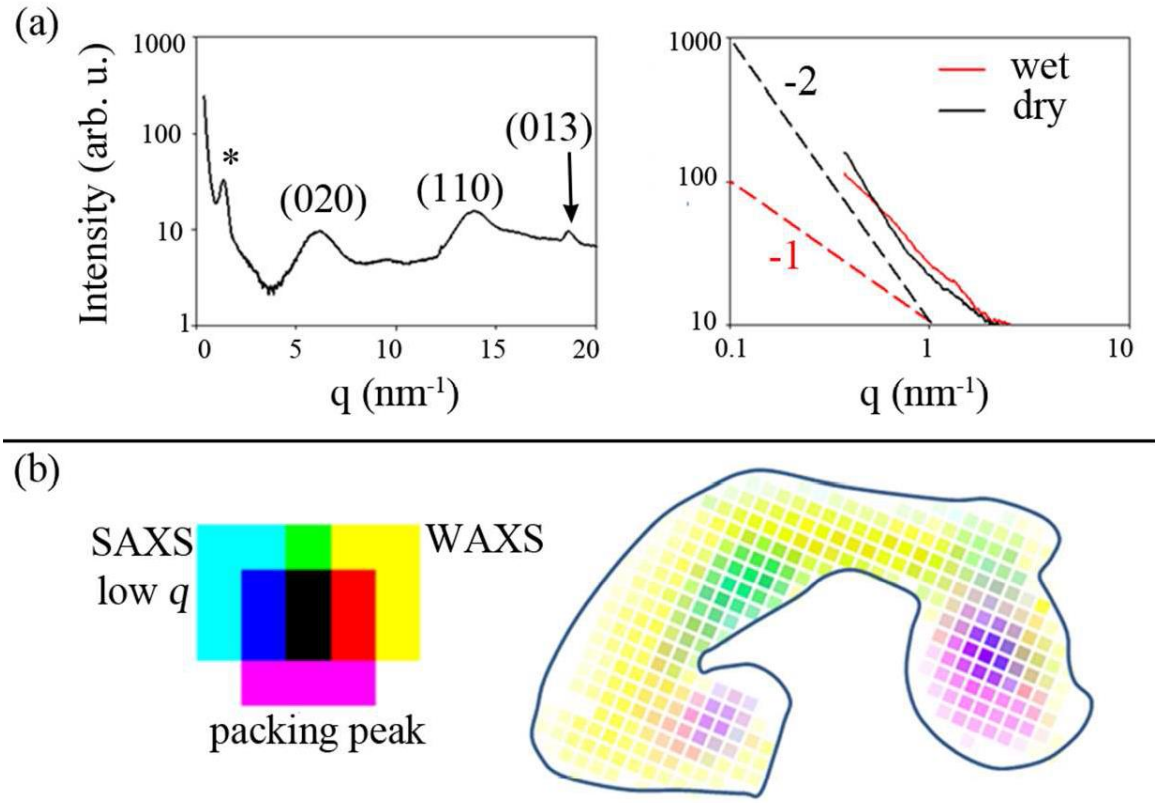

Figure 6.5: X-ray scattering analysis of the pad slice cut in sagittal plane. (A) Left: characteristic pattern of radially integrated X-ray scattering measured at the dorsal part of the pad in its wet state. The pattern contains both SAXS and WAXS scattering regions. The SAXS peak around q = 1.3 nm-1 is assigned as the packing peak from chitin fibrils (marked with *). The main chitin diffraction peaks in the WAXS region are indicated. Right: SAXS region radially integrated X-ray scattering pattern plotted in a double log scale, extracted from the distal region of the pad in wet and dry states. The dashed lines represent slopes of -1 (red), and of -2 (black). (B) Intensity map assigning different components contributing to the X-ray scattering patterns as shown by example in (A). Cyan color intensity: diffuse scattering intensity at lowest measured scattering vectors (q = 0.37 – 0.45 nm-1) and representing scattering from nanometer-sized cuticle components. Yellow color intensity: integrated scattering intensity from (110) and (013) chitin diffractions (fitted peak areas), representing the distribution of chitin. Magenta intensity: the packing peak intensity (fitted peak area) in the SAXS region, representing the in-lattice ordering degree of chitin fibrils.

In the SAXS region the inter-fibrillar packing peak can be used to determine the packing degree of chitin-protein fibrils and their spacing.[264] The intensity of the packing peak, related to the degree of chitin-protein fibril alignment and their orientation, is mapped in Fig. 6.5B (magenta scale). The packing peak intensity is largest in the ventral part of the pad, and in the central part of the "appendix" (violet regions in Fig. 6.5B). The *q*-position of the packing peak relates to the distance *d* between the fibrils by $q = 2\pi/d$. *d* is largest

(4.82 ± 0.02 nm) in the center of "appendix", and smallest (4.59 ± 0.04 nm) at the outer cuticle layers. Sample dehydration results in a slight reduction of the inter-fibrillar distance, now ranging between 4.76 ± 0.03 nm and 4.52 ± 0.04 nm, respectively. Note that these values are exemplarily for one studied specimen only. An independent measurement of another pad section in wet state revealed an inter-fibrillar distance of 4.93 ± 0.02 nm in the appendix and 4.73 ± 0.04 nm in the outer cuticle layers, respectively, revealing small variation between samples however within a similar trend.

6.3.4 Fibril orientation. The in-plane orientation of chitin-protein fibrils was determined from the anisotropic azimuthal distribution of the packing peak in the SAXS region (Fig. 6.5A). The out-of-plane angle of the fibrils on the other hand was extracted from the angular distribution of the (110) reflection of the chitin crystal in the WAXS region according to the method described in the literature.[265,266,267] The three-dimensional fibril orientation mapped in Fig. 6.6A shows strongly varying chitin-protein fibril orientation in different regions of the pad. The ventral side of the pad and the "appendix" are dominated by out-of plane chitin-protein fibril orientation (green-, yellow- and red- bars regions in Fig. 6.6A), while the dorsal and the distal parts of the pad are dominated by an in-plane organization of chitin-protein fibrils (blue-bars regions). This latter case may also arise from a plywood organization typical for spider cuticle.[130] In order to unequivocally determine the fibril orientation and microstructural arrangement, the same measurement and analysis were performed for two additional sections (assigned as transverse1 and transverse2 in Fig. 6.2B) cut orthogonally to the section described in Fig. 6.5. For a pure plywood organization, in-plane scattering patterns are obtained regardless of the incident beam orientation within the plywood plane, whereas a parallel fibril arrangement gives an in-plane orientation signal only when viewed perpendicular to the fibril long axis. In the transverse section in-plane fibril orientation dominates the entire sample, indicating that the blue-bars regions in Fig. 6.6A are characterized by a pure-plywood structure, while the

green-, yellow- and red-bars regions are dominated by a parallel fiber orientation in agreement with the observations from WAXS.

Figure 6.6B maps the distribution of diffuse scattering intensity at low q-values ($0.4\ nm^{-1} < q < 0.6\ nm^{-1}$). The signal at such low q-values arises from electron density contrast between nanometer-sized components in the sample. These may be pores, proteins, or other molecules (e.g. sclerotization agents) within the spider cuticle. There are two prominent regions exhibiting high diffuse SAXS signal intensity (cyan regions in Fig. 6.5B). One is close to the distal end where CLSM shows high sclerotization, the other in the center of the "appendix".

The slope of the integrated scattering intensity plotted in log-log units provides more details about the geometry of the scattering objects using the Guinier analysis.[268] For the wet sample a slope of -1 is found for measurements at the distal part of the pad and at the center of the "appendix". For the rest of the pad in the wet state the log-log slope equals to -2. Interestingly, in the pad's dry state the scattering intensity slope in the log-log plots equals to -2 for the entire sample.

For some regions of the pad the low-q SAXS signal discussed above shows pronounced anisotropy. In most of those cases, the anisotropy follows the same orientation as that of the chitin signal. However, in some regions it is miss-oriented with respect to chitin. The orientation of the low-q SAXS signal is shown in Fig. 6.6B together with the in-plane orientation of the chitin-protein fibrils. The region with the largest mis-orientation between the chitin signal and the low-q SAXS signal is in the distal part of the pad, the same region in which we find a slope of -1 in hydrated samples.

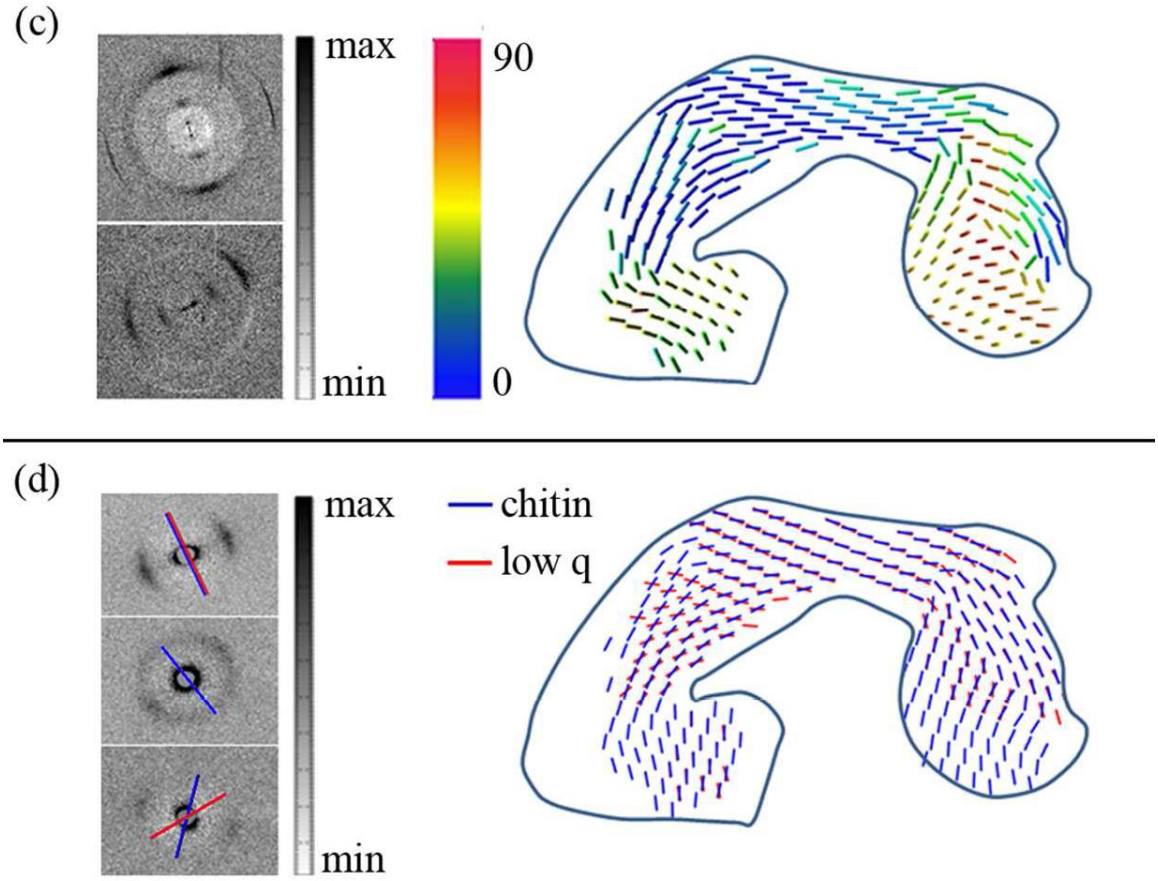

Figure 6.6: (A) Representation of 3D orientation of chitin fibrils in the pad. Data analysis was based on the non-symmetric azimuthal distribution of the (110) chitin crystal peak in the WAXS region. Bars show the mean orientation of the chitin fibrils in different parts of the pad. The color code indicates the chitin tilting angle out of the sample plane. Left: examples of the two-dimensional scattering pattern: in-plane fibers (upper), and out of plane (lower). (B) Orientation of the nanometer-sized objects extracted from the low-q signal and that of chitin fibrils extracted from the packing peak.

6.3.5 Interpretation of SAXS data. A SAXS slope of -2 in a log-log plot follows the Gaussian chain model of a randomly organized scattering object[269] which we attribute the scattering of the matrix proteins.[264] If there is no interference a slope of -1 indicates cylindrical scattering objects.[269] Applying the Guinier analysis[268] we determined an average cylinder diameter of 4.7 ± 0.1 nm. The size of these objects is similar to the size of the chitin-protein fibrils determined before using the packing peak position. We therefore assume that the scattering objects again are chitin-protein fibrils. Importantly, the analysis indicates that these chitin-protein fibrils are loosely packed and not arranged

in a lattice. Note, however, that in the same pad regions, we also detect the inter-fibrillar packing peak (albeit with different orientation), suggesting that two types of chitin-protein fibril arrangement occur in the same region of the pad.

This means that the "loose" fibrils are oriented almost perpendicular to the pad's distal surface while the tightly packed fibrils (i.e. in twisted plywood structure) follow the curvature of the pad surface. In the dorsal region and in the "appendix" the orientations of both components coincide.

6.3.6 Micro-channels and lamella organization at the distal and dorsal parts of the pad. Polarized light microscopy was used to further analyze the orientation of chitin-protein fibrils in different parts of the pad. The bright regions in Figure 6.4D arise from chitin-protein fibrils oriented within the plane of the sample (regions parallel to the polarization angle indicated by the white cross appear dark). In accordance with the results of X-ray scattering analysis, the dorsal and distal parts of the pad appear bright due to the contribution of the in-plane chitin-protein fibrils within the plywood structure. The "appendix" region and the ventral part of the pad, however, appears dark as this region is dominated by parallel chitin-protein fibrils oriented out of the sample plane, as previously obtained from the analysis of the WAXS signal. In the distal region of the pad we observe a striation pattern roughly perpendicular to the pad surface (in the same direction as the "loose" chitin signal obtained from the analysis of the SAXS signal above).

SEM and AFM images clearly show the lamellar arrangement in the pad cuticle (Fig. 6.7). The spacing between the lamellae, which is directly related to the rotation angle of the fibrils in the plywood structure, changes gradually from the surface towards the interior of the pad.

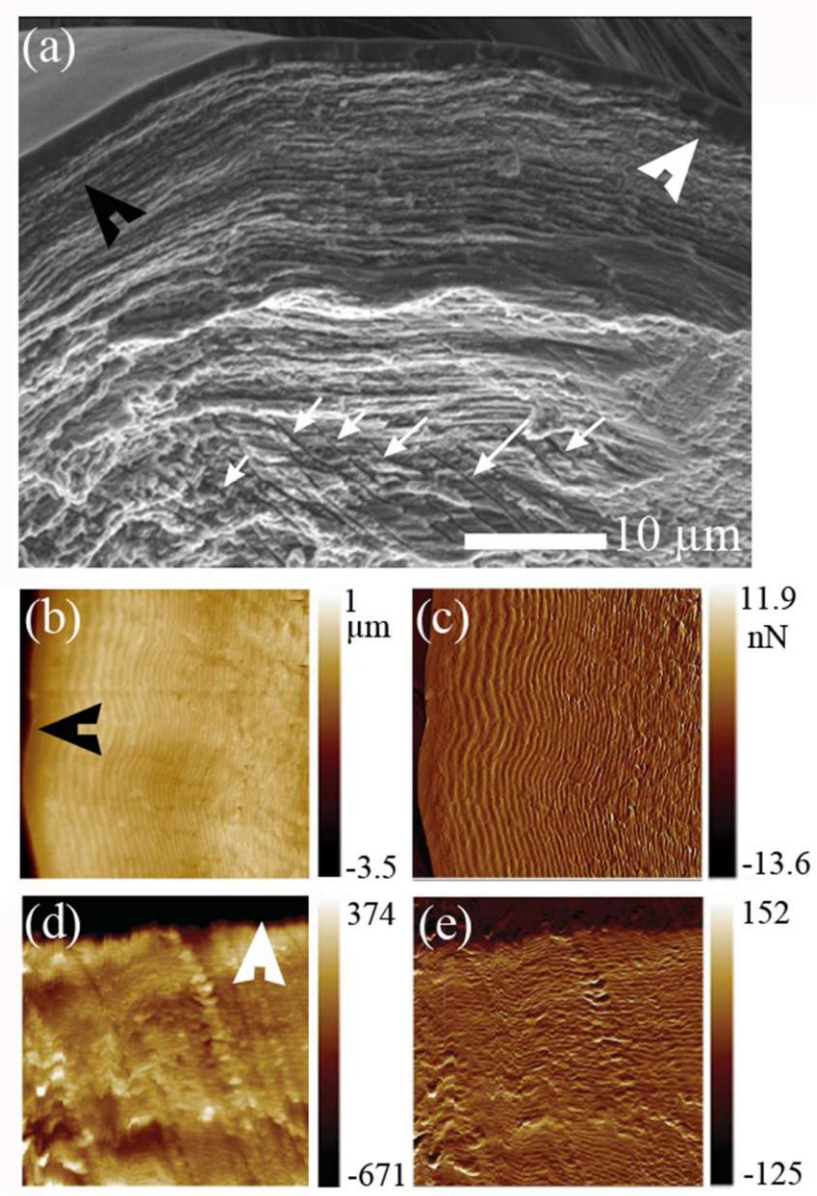

Figure 6.7: (A) SEM image of the dry fractured pad section (in sagittal plane). The distal and the dorsal directions are indicated by black and white arrowheads, respectively. The white arrows point to micro-channels within the chitin sub-structure of the pad. (B,C) Atomic force microscopy (AFM) images: topography (B); phase (C) of the distal surface of the pad. (D,E) AFM images: topography (D); phase (E) of the dorsal surface of the pad.

The direction of this gradient in lamella thickness changes in opposite directions distally and dorsally on the pad. Thus, on the dorsal side the spacing between two adjacent lamellae changes from ~250 nm at the surface to ~400 nm in the interior, as commonly observed in

arthropod cuticle. At the distal side the thicker lamellae are found close to the surface (~680 nm), and the lamellae become thinner (~300 nm) in the interior.

In addition, the SEM micrographs of the distal part of the pad show multiple channels a few micrometers in diameter, oriented perpendicular to the distal surface (Fig. 6.7A) which is in the same direction as the "loose" chitin-protein fibrils and the striation pattern in the polarized light microscope.

6.3.7 Micromechanical characterization. Scanning acoustic microscopy (SAM) quantifies the reflectivity, *R*, of focused acoustic waves from the surface of the sample with a spatial resolution of about 1 µm. The measured values for *R* depend on the sample stiffness and its mass density. SAM data obtained from embedded and polished pad sections, measured under water, show the spatial destribution of *R* along the pad (Fig. 6.4E). The previously observed variations in sclerotization degree and chitin-protein fibril orientation are highly correlated with the respective sound reflectivity values. The bright-coloured regions (high reflectivity) in Fig. 6.4E correspond to the dark reddish (highly sclerotized) regions in Fig. 6.4A. In addition, the "appendix" region shows a particularly high reflectivity. Since the stiffness is higher in the chitin-protein fibril direction, this correlates with the measured out-of-plane orientation of the fibrils in this region as determined from WAXS signal analysis. A noteworthy exception to this trend is a bright region in the center of pad. The bright line in the SAM image corresponds to the green-to-red transition region in the respective CLSM image. Note that in the absence of a measure of the sample mass density we cannot extract quantitative information regarding the elastic modulus.

For the quantitative determination of the elastic moduli, albeit at lower spatial resolution, we performed nanoindentation experiments under hydrated conditions on the same samples at four different regions. The regions examined are assigned as A-D in Fig. 6.4E. The

results show large differences of the reduced elastic modulus E_r between the regions studied. The highest value of 8.3 (± 1.1) GPa was found in region A, the "appendix" region, while in region B, the dorsal part of the pad, which shows a similar sclerotization level as the "appendix", we measured an average value of 2.8 (± 1.3) GPa. This result is consistent with SAM results and reflects the effect of fiber orientation. Note, that the elastic modulus of chitin is roughly 4 times higer along the *c*-direction (long axis) than along the *a/b* directions.[270]

The highly sclerotized internal region C of the pad, is characterized by E_r = 1.0 (± 0.3) GPa. And most strikingly, the distal part, region D, shows an extremely low reduced elastic modulus of E_r = 0.1 (± 0.07) GPa. Such low values are mostly known for wet and unsclerotized cuticles of insect larvae and puparia,[134] and are uncommon in adult cuticles.

6.4 Discussion on biological relevance

The cuticular pad at the distal end of the metatarsus of *Cupiennius salei* plays an important role in the mechanical transmittance and transformation of stimuli which deflect the tarsus and stimulate the metatarsal vibration receptor. The sources of the organ's adequate stimulation are manifold. Stimuli primarily include the vibrations of the plant, on which the spider sits and which are caused by the movements of predators or prey, as well as the vibrations actively used by the spiders to communicate during courtship. However, the metatarsal lyriform organ is also stimulated by low frequency tarsal deflections as they occur during the spider's own locomotion and other behavior such as prey capture and spinning behavior and as they are typical of the vibrational background noise caused by abiotic sources like wind.[84,271] Upon the deflection of the tarsus the proximal end of the tarsus pushes against the distal end of the metatarsus where the pad is located. High frequency stimuli beyond ca. 40 Hz are detected with high sensitivity regarding tarsal deflection amplitudes necessary to activate the sensory cells. The viscoelastic properties

of the unusually thick epicuticle of the pad represent a very effective mechanical high pass filter.[123] Low frequency stimuli (lower than about 40 Hz) require much larger tarsal deflections to be detected by the vibration receptor organ. Here we describe how the structural features of the pad allow for the transmittance of high amplitude low frequency stimuli and at the same time protect the sensory organ against over-compression and damage.

In their natural habitat spiders are also exposed to the lateral deflection of their tarsi (i.e. off the main long axis of the tarsus-metatarsus) and their vibration receptors respond to these. The crescent-like shape of the pad is well suited to allow such activations, as can be seen in Fig. 6.3C. Although other shapes might also be valid (for example a round pad), they might suffer from other drawbacks such as require more material at regions which are normally not activated. The elaborated morphology of the pad and, in particular, the sub-structure of the material of which it is made are discussed in more detail in the following.

6.4.1 The distal end of the pad. The distal end of the pad is extremely soft showing only 100 MPa for the reduced elastic modulus as measured in nanoindentation experiments under hydrated conditions. In agreement with this we have also found that this pad region is highly hydrated under natural conditions and the least sclerotized part of the pad. The lamella thickness in this region decreases from the surface inwards, which is uncommon in arthropod cuticle. Lamella thickness and chitin-protein fibril orientation were recently shown to affect water sorption capability of the cuticle where large lamella swell much more than thin ones. Thus, the occurrence of thick lamella at the distal end of the pad also contributes to the hydration properties of this region together with the low sclerotization.[262] SAXS results show that in addition to the plywood structure that forms the lamellae seen in Fig. 6.7B-C some chitin component occurs as loosely bound chitin-protein fibrils. Upon dehydration the signal from these fibrils disappears, indicating that the fibrils are suspended

in water or form gel-like material. This signal is highly anisotropic with directionality that follows the direction of multiple micro-channels observed in SEM (Figure 6.7A) and with polarized light microscopy (Fig. 6.4D). We therefore suggest that these channels are filled with chitin-based gel-like material, which might also account for the large swelling in this region. The micrometer-sized channels run in a direction perpendicular to the distal end surface (towards the contact region with the tarsus). Using AFM imaging Young et al.[123] reported droplets of epicuticular substance secreted from pores at the surface of the pad. We suggest that these are the openings of the micro-channels observed by us. The function of this secretion is unknown. On the other hand the secretion may serve to better couple tarsus and pad during stimulus transmission, similar to insect attachment pads,[272] however, if the secretion level is high it may act in the opposite way, i.e. as a lubricant. More study is needed in order to answer this question.

The softness (100 MPa) of the pad's distal contact region with the tarsus increases the contact area with the tarsus and allows the largest deformation upon tarsal deflection while comparatively only small displacement of the pad is observed at the contact region with the slits. In this way substrate displacements in the order of up to 200 µm, in accordance with Barth and Geethabali[88] are translated to small (non-destructive) slit compressions of only few micrometers (3.5 ± 0.7 µm at 9 ± 1° tarsal deflection), and over-stimulation, or slit damage is avoided. Thus the pad acts as a "bumper" damping the impact of large substrate displacements.

6.4.2 Internal layer of sclerotized cuticle. The interior part of the cuticle in the central region of the pad is highly sclerotized as judged from CLSM, which also endows it with a relatively high elastic modulus of 1 GPa. This specific distribution of cuticle sclerotization may imply a functional, probably mechanical role. From this region the pad is no longer deformed but displaced towards the slit region. This is most likely owed to the stiffening

in this region. In agreement with the present findings Schaber et al.[117] found that the force needed to deflect the tarsus against the metatarsus (ca. 1.5 mN at 4°) increases exponentially with the deflection angle. This increase of force from small deflection angles to higher ones may reflect the pad deformation behavior related to its structure, where at small angles the distal part of the pad is easily deformed and at higher angles, the internal sclerotized region might resist further deformation. The dorsal part of the pad is also highly sclerotized and is made up of dominantly twisted plywood structure with rather thin lamella. It thus provides bending stiffness to support pad displacement at higher loads and restrict the displacement.

6.4.3 The "appendix". The "appendix" region of the pad is characterized by a particularly high level of cuticle sclerotization as well as a high degree of parallel arrangement of chitin-protein fibrils. The parallel fibrils are oriented out of the plane of the sample sagittal sections. This also explains the measured values for the reduced elastic modulus (of about 8 GPa) in this region for sagittal sections. A similar structure of parallel fibril orientation was also found in the ventral side of the pad section. From μCT analysis we know that these two regions are connected (Fig. 6.2G,H) and could therefore form a stiff frame reinforcing the entire pad. This frame together with the unusually sclerotized internal cuticle is expected to resist further pad deformation instead allow small displacement of the pad towards the slits region.

Another interesting observation is that the "appendix" ridge runs parallel to the slits of the lyriform organ and extends underneath them (see for example Fig. 6.2C,D, 6.3C,D and E). We suggest that the ventral extension of the appendix helps to distribute the load to lower regions of the slits, ensuring an equal distribution of the compressive load along the long axis of the organ, perpendicular to long axis of leg and along the slit walls depth.

6.5 Conclusions

The pad was described as a high-pass filter transferring only high frequencies with high efficiency.[92] Most of this filtering occurs at the epicuticle whose viscoelastic mechanical properties were recently determined using AFM at various temperature and signal frequencies.[123] Low frequency stimuli are damped by the epicuticle and would not be transferred to the slits if applied with low amplitude. However, low frequencies below about 40 Hz and even down to 5 Hz applied with high amplitude are detected by the sensory cells of the slits.[88,124] Tarsal vertical displacements will then have to be as large as some hundreds of micrometers, corresponding to the tarsal angular tilt of ~10°. We propose a mechanism for the transmittance and filtering of the full frequency range of the biologically relevant stimuli via the pad to the metatarsal lyriform organ; our results suggest that during such substrate displacements, the tarsus pushes against the pad and deforms it by some tens of micrometers at its most distal, highly hydrated region. Beyond this region, the sclerotized region and the supporting frame (appendix and ventral pad region) resist the deformation and are displaced to push against the slits. Now, however, the displacement values are considerably scaled down to only few micrometers. In addition, the "appendix" running parallel and along the slits ensures a uniform compression roughly perpendicular to the long axes of the slits for stimuli deflecting the tarsus vertically or laterally.

Taken together with previous results on high-pass filtering properties of the pad, our results emphasize the multi-functionality of the pad allowing selective low frequency stimuli to be transferred thus allowing large relevant stimulus-frequency range. Unraveling the structural arrangement in such specialized organs may provide solutions for the design of sensory materials which are capable of detecting and filtering stimuli of signal wide range.

CHAPTER 7

A spider's biological vibration filter: Micromechanical characteristics of a biomaterial surface

A strain sensing lyriform organ (HS-10) on all legs of a Central American wandering spider (*Cupiennius salei*) detects courtship, prey, and predator vibrations transmitted by the plant on which it sits. It has been suggested that the viscoelastic properties of a cuticular pad directly adjacent to the sensory organ contribute to the organ's pronounced high-pass characteristics. Here, we investigate the micromechanical properties of the cuticular pad biomaterial in search of a deepened understanding of its impact on the vibration sensor´s function. These are considered to be an effective adaptation for the selective detection of signals for frequencies greater than 40 Hz. Using surface force spectroscopy mapping we determine the elastic modulus of the pad surface through a temperature range of 15-40 °C at various loading frequencies. In the glassy state, the elastic modulus was about 100 MPa, while in the rubbery state the elastic modulus decreased to 20 MPa. These data are analyzed according to the principle of time-temperature superposition to construct a master curve that relates mechanical properties, temperature, and stimulus frequencies. Estimation of loss and storage moduli versus temperature and frequency allowed for the direct comparison with electrophysiology experiments and revealed that the dissipation of energy occurs within a frequency window whose position is controlled by environmental temperatures.

7.1 Introduction

Biological sensory organs are indispensable for an organism to receive, interpret, and respond to environmental stimuli and serve as a popular source of inspiration for biomimetic engineering.[84,85,198,273,274,275,276,277] Spiders possess remarkably well developed

mechanosensory systems and heavily rely on their ability to detect biologically relevant vibratory signals when hunting and courting.[88,89,91,92,93,94,121] In the highlands of Central America[89,277] the nocturnal wandering spider *Cupiennius salei* sits on mechanically stiff plants (e.g. on a banana plant or a bromeliad) which transmit substrate vibrations caused by nearby prey, predators, or a potential sexual partner surprisingly well (Figure 7.1).[278]

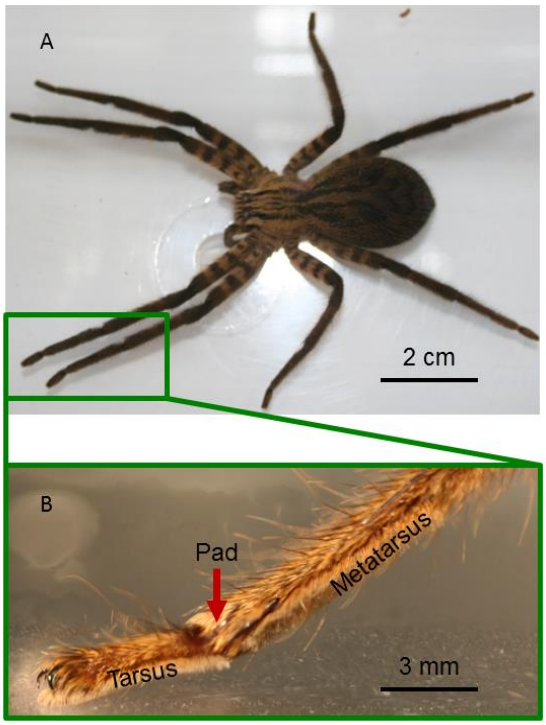

Figure 7.1: (A) Adult female *Cupiennius salei*. (B) The distal end of a leg of *Cupiennius* with an arrow-pointing to the joint between tarsus and metatarsus.

The sense organ responsible for the spider's highly developed vibration sensitivity is composed of 21 strain-sensitive innervated slits embedded in the cuticular exoskeleton.[84,100] Because of their similarity in their appearance with the ancient musical instrument such organs are referred to as lyriform organs.[84,88,279] Such lyriform organs are found in many species of spiders, and well as many other arachnids, such as scorpions.[84]

The vibration sensitive lyriform organ is found at the distal end of the metatarsus (the second last segment of the leg) in the middle of its dorsal surface on each leg (see Figure 7.2B).[84,92,100] The slits of the metatarsal lyriform organ are oriented perpendicular to the long axis of the leg, bridging a deep furrow in the metatarsus (Figure 7.2C), which increases the mechanical compliance at the site of the organ and thus its sensitivity to strains in the exoskeleton.[84] Strains due to external mechanical stimuli occur as the tarsus, resting on the plant, is deflected upwards and presses against the metatarsus as a result of substrate vibrations, ultimately compressing the slits.[84,88,92,117]

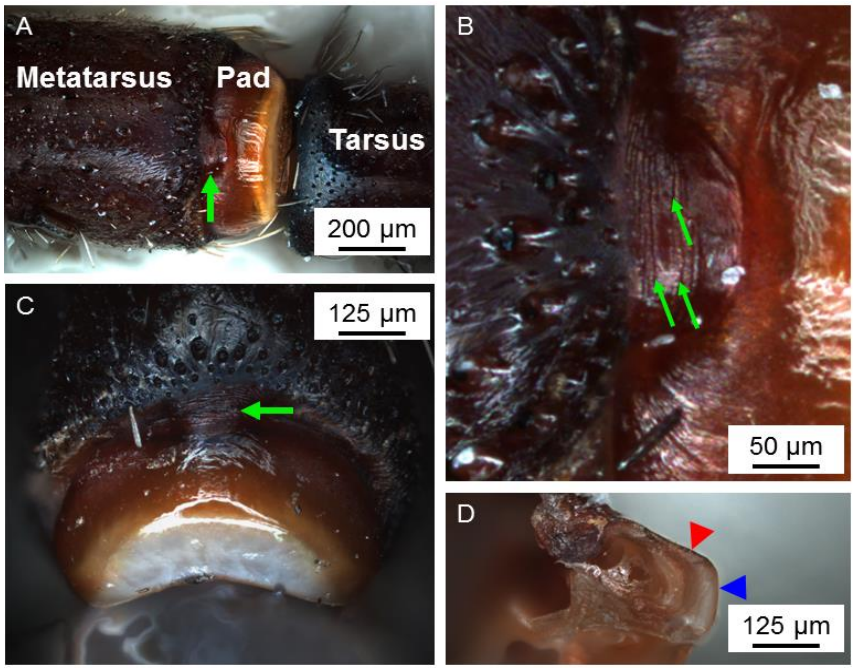

Figure 7.2: (A) Optical image of the pad with surrounding hairs removed for better viewing; arrow marks the location of the metatarsal lyriform organ. (B) Metatarsal lyriform organ with arrows pointing to several slits. (C) Distal view of the pad (point of contact) looking towards metatarsus. (D) Optical image of a pad sectioned longitudinally with arrowheads demarking its "dorsal" (red arrow) and "distal" (blue arrow) surfaces.

Along with its extreme sensitivity to substrate vibrations, the metatarsal lyriform organ is also known to effectively filter out low-frequency background noise, an ever present problem in sensory biology.[84,85] Electrophysiological experiments on *Cupiennius salei*

generated tuning (threshold) curves of the organ's slits which demonstrate their high-pass properties.[88] The threshold deflections of the tarsus required to elicit a nervous response from the sensory cells innervating the slits are on the order of 10^{-5} to 10^{-4} m for vibration frequencies ranging between 0.1 and about 40 Hz, while deflections as small as 10^{-9} to 10^{-8} m are sufficient to elicit action potentials for frequencies above 40 Hz.[84,88,124]

The processing of environmental stimuli, however, is not a function of sensory cells and the central nervous system alone. Rather, the pre-filtering of external stimuli for the fine tuning of sensory systems is also a function of the morphology, materials properties of the organs themselves and of the cuticle in which they are embedded.[85,137] In fact, McConney *et al*.[92] found that one mechanism responsible for the high-pass behavior of the metatarsal vibration receptor is the viscoelastic, time-dependent behavior of the cuticular pad adjacent to the organ which transmits the stimulus from the tarsus to the metatarsus with dramatic changes in mechanical properties depending on frequency and temperature.

As is well known, viscoelastic materials display pronounced time- and temperature-dependent mechanical properties.[5,6,125280,281,] McConney *et al*.[92] used atomic force microscopy (AFM) to determine the pad's elastic modulus at its surface as a function of probing rate. They found a sharp increase of the elastic modulus from around 10-20 MPa at probing rates ranging from 0.1 to 10 Hz to larger than 70 MPa at probing rates above 30 Hz. This finding mirrors the electrophysiologically determined tuning curves[84,88] with remarakable fidelity. By applying the principle of time-temperature superposition and by using the Williams-Landel-Ferry (WLF) equation,[7] the glass transition temperature was estimated to be 25 ± 2 °C.[92] A deeper understanding of the role which viscoelasticity plays for stimulus transmission in mechano-sensory organs needs direct measurements. This will also establish a basis for the design of highly selective and specific, biologically-inspired synthetic sensing systems.[85,86,105]

7.2 Experimental

7.2.1 Materials. For this study, live adult females of the spider *Cupiennius salei* (Ctenidae) were used, as described in Chapter 3 (Figure 7.1A).[84] In order to expose the pad for AFM measurements, the hairs surrounding the organ were removed by gently rubbing against the grain with a KimWipe, and by carefully removing the remaining hairs nearest the pad with tweezers. Freshly autotomized legs were also utilized for mechanical measurements, with all experiments taking place within 72 hours of the autotomization. In this way, the natural material properties of the spider were not significantly altered due to dehydration, allowing for a close estimate of the temperature-dependent mechanical properties of the pads in live spiders. The mechanical properties of freshly autotomized legs (still hydrated) were identical to those of live spiders. Additionally, the mechanical properties of dehydrated pad material are significantly different (e.g. compare 200-300 MPa elastic modulus for dehydrated pads, not presented here, to 20 MPa in live spider materials).

Pads were sectioned by slicing downward along the dorsal midline of the metatarsus (sagittal section) using a Bard-Parker #10 carbon steel surgical blade. A 1:1 weight mixture of beeswax (Sigma Aldrich) and rosin (colophony, Alpha Aesar) was used to secure individual spider legs and sections onto a glass substrate. A light microscope was employed to confirm that the sectioned surface was oriented parallel to the glass surface to avoid artifacts by scanning on a large angle. The glass substrate was then attached to a custom-made heating bath using Silver Conductive Paste 18DB70X (Electron Microscopy Sciences). The samples were then submerged in high-purity water (18.2 MΩ·cm, Synergy UV-R, Millipore) and the chosen temperature set by the user (typically starting at 40 °C and working to lower temperatures). After each temperature adjustment the system was allowed to thermally equilibrate for 30 minutes such that both the temperature readings and the cantilever deflection were constant. For each individual measurement constant temperature was maintained during the experiment using a thermocouple feedback loop

(ILX Lightwave LDT-5948 Precision Temperature Controller) which was attached next to the glass slide. The accuracy of the thermocouple (±0.01 °C) was independently verified using a volume expansion thermometer.

7.2.2 Atomic Force Microscopy. AFM experiments were undertaken according to procedures outlined in the experimental chapter of this dissertation. For the following AFM experiments, a combination of live spider legs and freshly autotomized legs were used to ensure that our experimental results apply to native pad materials of live spiders in their natural environment. The dorsal and distal surface of the pad were selected for detailed micromechanical probing, as indicated in Fig. 7.2D.

The cantilever's deflection sensitivity was determined by collecting force distance curves (FDCs) on a sapphire crystal. The cantilever spring constant, *K*, was measured using the thermal tune method.[215] Topography measurements were made in PeakForce QNM mode using the established procedure. Scan areas ranged from 500 nm x 500 nm to 20 µm x 20 µm using resolutions of either 512 x 512 pixels or 1024 x 1024 pixels. Scan rates were chosen within 0.5 - 1 Hz.

The detailed description of the SFS experiments needs a clarification of the terminology, similar to that discussed in § 4.1.3.3. An FDC taken on a sapphire crystal and presented in Fig. 7.3 illustrates this discussion. In a typical SFS measurement, the user selects a ramp size (the total size of the approach curve), a ramp rate (the inverse of the time it takes to make both the approach and retraction), and a deflection threshold (deflection at which the z-piezo stops extending and begins to retract). In SFS experiments, surface topography causes variations in the point at which the tip first contacts the sample surface. Furthermore, changes in surface stiffness from point to point cause the interaction time between the tip and sample to vary (e.g. a softer sample will deform more resulting in a

longer loading time to reach the deflection threshold). As a result, it is impossible for the AFM to reach the deflection threshold at the exact ramp rate and ramp size as defined by the user under different conditions. To compensate for this, AFM extension and retraction occur over a larger distance than set by the user, but at a velocity which would correspond to the user-defined size-rate pair and unnecessary data is truncated. Additional complexity can occur in the leathery regime (between glassy and rubbery behavior) in which the loading curves can become highly non-linear. Therefore, to avoid calculating each individual true loading rate and also the ambiguity of such calculations, which occurs when the true loading rate is non-linear, we group our experiments by "probing rate" (ramp rate).

In order to determine the viscoelastic properties of the pad surfaces, FDCs were taken at 0.05, 0.1, 0.5, 1, 2, 5, 10, and 20 Hz probing rates for each temperature within the range close to what the spiders might see in their natural environment (from 15 °C to 40 °C).[84,89] The manner in which force is applied to the pad by the tarsus is not physically similar to the manner in which the tip is applying forces to the pad surface. To ensure that we work only in the elastic regime, deformation levels were kept below 15 nm and the surface was routinely scanned after making FDCs to check for plastic deformation.

Capillary bridges, which form between the tip and the sample surface, are a common occurrence when scanning in ambient conditions (typically the relative humidity (RH) is ~40%). They produce significantly high snap-to-contact forces, distorting the information provided by the AFM. This distortion can be avoided by keeping the sample and probe completely immersed in water. Therefore, all probing experiments were performed in water. In our case, immersion in water also ensures that the pad material remained fully hydrated (RH > 80% in the spider's natural environment). A saline solution may be more appropriate to immerse our samples in to keep the properties as close to the properties of

the live spider. However, any exposure to solutions containing charged ions can cause severe corrosion in the electrical components of the scanner and thus should be avoided.

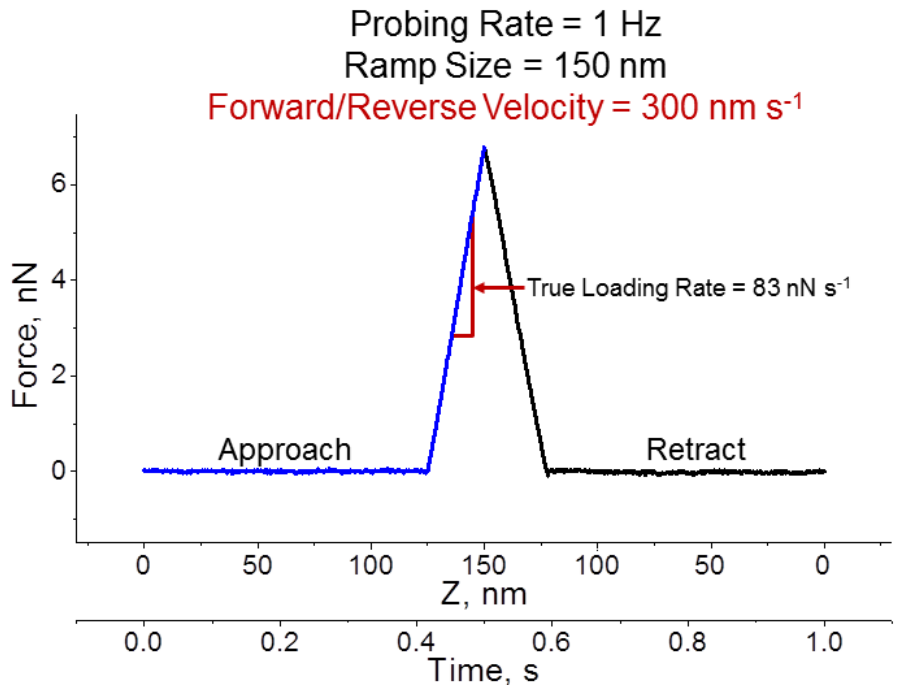

Figure 7.3: Sample loading curve taken on a sapphire crystal demonstrating the definition of probing rate, true loading rate, and probing velocity.

The analysis of the FDCs involved selecting curves from each frequency-temperature set which had low background noise and a clear contact point. Typically, more than 30 FDCs were collected at different locations and initially analyzed to determine the elastic modulus by fitting with the classical Sneddon equation for the purely elastic deformation of an elastic half space with a rigid paraboloidal punch:[28,169]

$$P = \left(\frac{4}{3}\frac{E}{1-\upsilon^2}R^{1/2}\right)\delta^{3/2} \tag{7.1}$$

where P is the applied force, R is the radius of curvature of the tip, δ is the penetration depth, ν is Poisson's ratio chosen to be 0.3 to be consistent with McConney *et al.*,[92] and

E is the elastic modulus of the outer-most surface layers. For fitting the FDCs we used unconstrained nonlinear optimization with MatLab software. The error bars presented with the data represent one standard deviation calculated from the elastic modulus fitted from each FDC. The values of modulus calculated for each temperature could then be plotted versus probing rate. They were shifted accordingly to construct a master curve at 19 °C according to the WLF principle of time-temperature superposition.[7]

7.2.3 Optical Microscopy. Optical and electron microscopy experiments were undertaken according to the procedures described in Chapter 3 of this dissertation.

7.3 Results and Discussion

7.3.1 Surface topography. AFM topographical imaging in high purity water revealed uniformly distributed pores on the dorsal surface of the pad (Fig. 7.4). Capping these pores is residual epicuticular fluid, seen as hemispheres with diameters ranging from 500-1000 nm. To directly measure nanomechanical properties of the pad material, only the surface areas not containing the pores or the epicuticular fluid were examined. The pad material surrounding the pores was very uniform and smooth, with a micro-roughness of 2-3 nm over an area of 1 µm x 1 µm. This micro-roughness is higher than previously reported[6] and attributed to the peak force tapping mode in fluid, in which force is applied directly to cause surface deformation. This is in contrast to standard soft tapping in air, in which the amplitude of a vibrating tip is damped by van der Waals forces.[19]

7.3.2 SFS mapping. The SFS version of AFM allows precise area mapping of tip-sample interactions.[19] SFS entails creating a two-dimensional array of FDCs, which is analyzed to simultaneously map the surface distribution of the elastic modulus and the surface topography (Figure 7.5).[19] 2D sets of such FDC data are produced by pressing an AFM probe against the sample surface, pixel-by-pixel, across the selected surface area (Fig. 7.5A, 7.5B). Vertical displacement of the probe results in small pad surface

deformations. Usually these are within 2-10 nm in the z-direction and are determined by the difference of the z movement of the piezo-element and cantilever deflection (Fig. 7.5C).

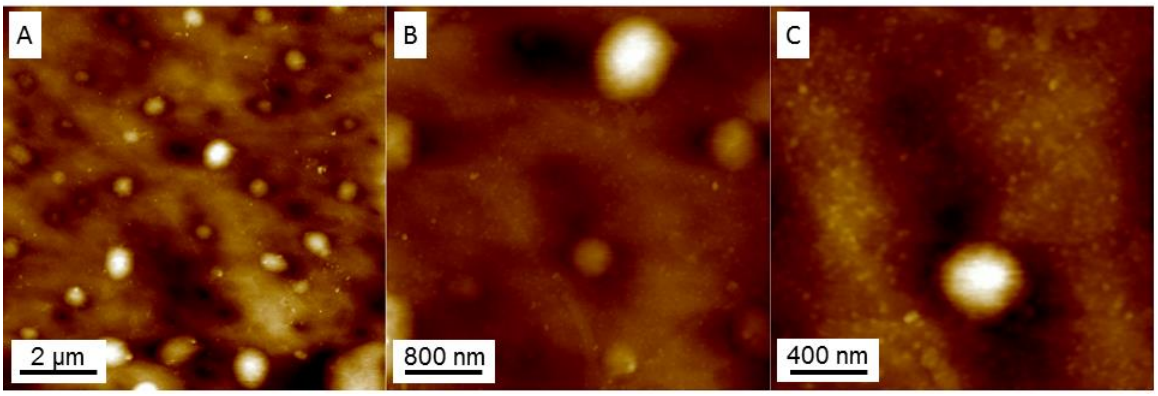

Figure 7.4: AFM topography images of the dorsal surface of the metatarsal lyriform organ, showing randomly distributed pore canals. Z-scales: (A) 155 nm, (B) 155 nm, (C) 55 nm.

Surface topography was evaluated from AFM images concurrently collected on the dorsal surface of the pad (Figure 7.5A). The surface was uniform and thus appropriated for SFS mapping. In the probing studies, in a number of surface areas between 1 μm^2 and 2 μm^2, 16x16 pixel (63-125 nm distance between each pixel) measurement fields were mapped (Figure 7.5B). At an average AFM tip radius of only 15-20 nm, each FDC collected in the elastic regime was unique and not affected by the strain fields of subsequent measurements.

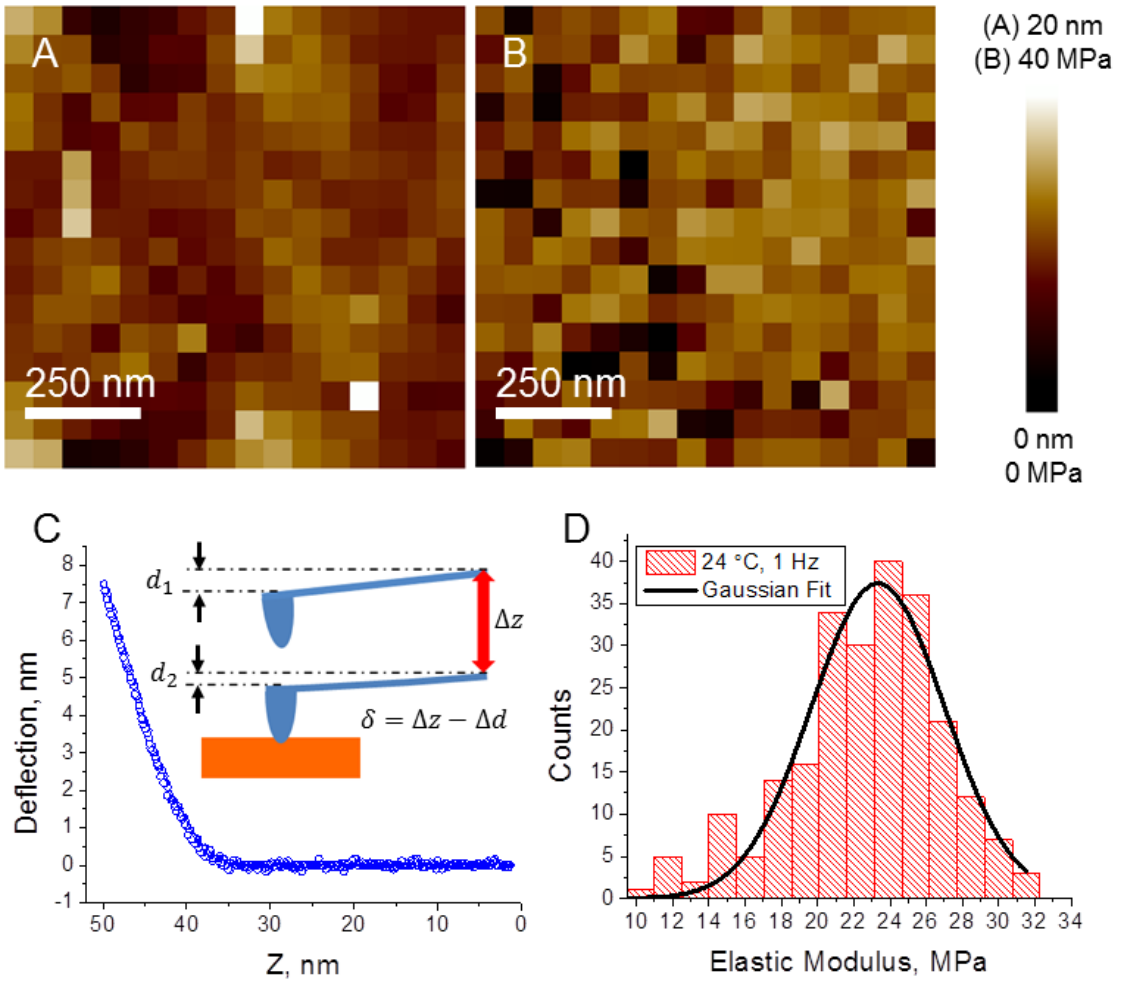

Figure 7.5: Topography (A) and modulus (B) maps taken concurrently using SFS on the dorsal surface of the pad. (C) Representative loading curve with an inset schematically showing indentation. (D) Modulus distribution of the pad taken at room temperature. Z-scales: 20 nm (A); 40 MPa (B).

After collecting these data sets, the FDCs were analyzed using Sneddon's contact model (Eqn. 7.1) to produce a map of elastic modulus values calculated under assumption of purely elastic deformation (Fig. 7.5B).[26,28,169] Based on the calculated elastic modulus for each pixel (Fig. 7.5B), the histogram of the surface distribution at a selected temperature and probing frequency was generated (Fig. 7.5D). The distribution was roughly symmetrical, with a longer low-value tail caused by the topographical distortions (elevated points and the edge of pores). Gaussian approximation of these histograms allowed for the

calculation of the average value and standard deviations, as demonstrated in Fig. 7.5D. In this selected example, calculated for 24 °C and a probing rate of 1 Hz, the average modulus value was 23 ± 4 MPa. This value corresponded very well with the values calculated by McConney *et al.*[92] for low loading rates at ambient conditions using 5 µm radius borosilicate colloidal probes.

7.3.3 Viscoelastic response.

7.3.3.1 Glassy-to-rubbery transition. Figure 7.6A presents loading curves taken at 1 Hz probing rate on the dorsal surface of the pad. The dramatic changes in deformational behavior related to the transition from glassy to rubbery behavior can be clearly seen. In general, the slope of the loading curve is a measure of the elastic modulus of the sample. This can be seen from Eqn. 7.1, where the applied force, P, is linearly related to $\delta^{3/2}$. For low temperatures, such as 17 °C a 9 nm piezo-element motion results in a cantilever deflection of roughly 7.3 nm, which corresponds to a surface deformation of 1.7 nm (Fig. 7.6A). At 25 °C, however, a similar tip deflection is only achieved after a z movement of 15 nm that results in an 8 nm surface deformation (Fig. 7.6A). Such changes imply a change from a high modulus in the glassy state to much more compliant properties in the rubbery state.

Using 1 Hz as a standard probing rate, SFS analysis on the dorsal surface through a range of biologically relevant temperatures with an interval of 1 °C revealed the dependence of the elastic modulus on temperature including the determination of T_g. Elastic moduli were calculated by averaging many (> 100) FDCs, which resulted in distributions similar to those shown in Fig. 7.7 for different temperatures. Fitting with a Gaussian function yielded an average modulus in the glassy regime of 105 ± 11 MPa for measurements taken at 16 °C with a probing rate of 1 Hz. For 30 °C and again using a probing rate of 1 Hz an average modulus of 20 ± 4 MPa was found in the rubbery state (Fig. 7.6B).

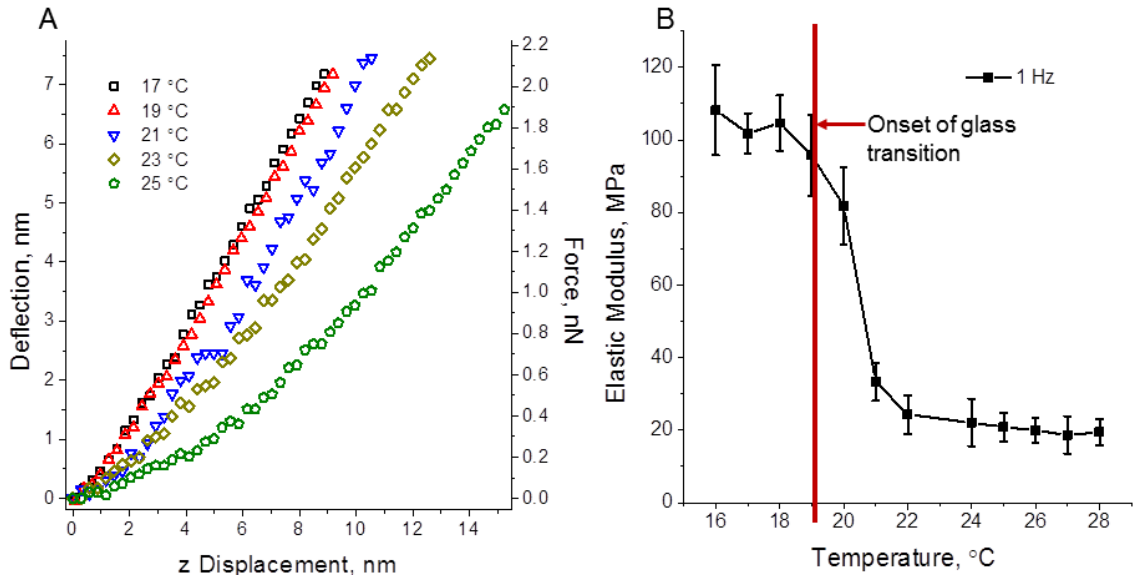

Figure 7.6: (A) Representative approach curves taken on the dorsal surface at 1 Hz for the temperatures indicated and showing a change in curve shape and slope through the glass transition temperature range. (B) Elastic modulus versus temperature of the dorsal surface of the pad using a 1 Hz loading rate.

According to this data the apparent onset of the glass transition occurs at approximately 19 °C, with the elastic modulus steeply decreasing above 22 °C. This result is close to that previously reported from colloidal force probing experiments with smaller surface deformations ($T_g = 25 \pm 2$ °C).[92]

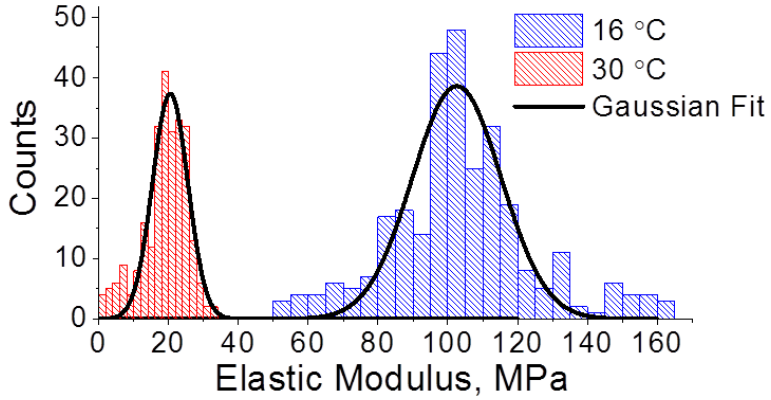

Figure 7.7: Elastic modulus distributions of the dorsal surface of the pad at 16°C and 30°C; both distributions were obtained using a 1 Hz probing rate.

7.3.3.2 Time-temperature analysis. It is worth noting that the experimental probing rate is limited by a number of factors including resonance properties and creep of the piezo-element, the rate at which the detector can collect data, and, at high enough rates, the viscosity of the fluid medium (all measurements were conducted in aqueous environment). Therefore, a complete characterization of the viscoelastic behavior was undertaken by allowing the pad material to thermally equilibrate at each temperature examined between 15 °C and 40 °C (in this case temperature intervals of 3 °C and 5 °C were used), and by producing FDCs using probing rates of 0.05, 0.1, 0.5, 1, 2, 5, 10, and 20 Hz at each temperature.

The elastic modulus as a function of probing rate and temperature is further plotted in Figure 7.8A. At temperatures sufficiently above or below the glass transition temperature, the rate-dependent behavior of the elastic modulus essentially disappears and its values remain largely constant. At temperatures of 27 °C and higher, the modulus does not change significantly with the probing frequency, with the average modulus of the 32 data points being 18.5 ± 3.9 MPa, which is well in line with the value (~20 MPa) obtained for the single point distribution (30 °C, 1 Hz) presented above. Similarly, at 15 °C, the lowest temperature probed, the modulus does not deviate significantly from ~106 MPa throughout most of the probing rates (Fig. 7.8A). However, a slight drop-off at 0.05 Hz most likely represents a rate-dependent effect, with some contributions from the greater instability of the measurements at extremely low probing rates with long-time piezo-element creep (generally the standard deviation for 0.1 and 0.05 Hz probing rates was greater than for all other probing rates at all temperatures). Close to room temperature, at 24 °C, a modest uptick in the measured elastic modulus to approximately 31 MPa is observed for the highest probing rates. However, the most dramatic temperature- and rate-dependent behavior is exhibited in the glassy-to-rubbery transition region at 18 °C and 21 °C (Fig. 7.8A).

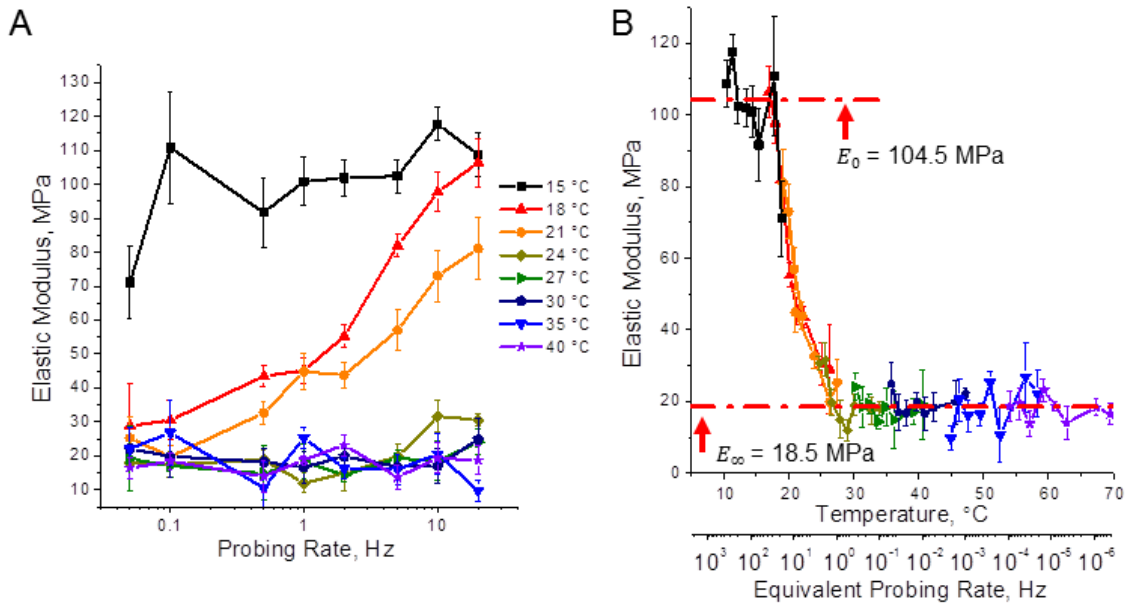

Figure 7.8: (A) Elastic modulus versus probing rate of the dorsal surface of the pad, grouped by measurement temperature. (B) Full time-temperature-modulus relationship of the dorsal surface of the pad obtained using the principle of time-temperature superposition via the WLF equation. Here the top x-axis corresponds to the expected elastic modulus of the pad at a given temperature using a 1 Hz probing rate, while the lower x-axis corresponds to the expected elastic modulus of the pad at a given probing frequency at a measurement temperature of 19 °C. The upper and lower bounds are averages taken from the extreme data points (i.e. the lowest temperatures and highest probing rates, and the highest temperatures and lowest probing rates).

We then applied the principle of time-temperature superposition to these probing data, whereby the modulus calculated for a certain apparent probing rate and temperature can be shifted with respect to a reference apparent probing rate and temperature. In this manner, a "universal" time-temperature-modulus relationship was created (as described in detail in Chapter 4). This analysis was accomplished using the WLF equation:[5,7]

$$log\left(\frac{f}{f_0}\right) = \frac{-c_1(T-T_0)}{c_2+(T-T_0)}\ , \tag{7.2}$$

where f is the shifted probing rate, f_0 is the reference probing rate, T is the temperature, T_0 is the reference temperature, and c_1 and c_2 are material-dependent constants. Because no values for these constants are available for the cuticular pad of *Cupiennius*, we used the

"universal" polymer constants of $c_1 = 17.44$ and $c_2 = 51.6$ for common amorphous rubbers. [7,92,280]

Because the onset of the glass transition was determined to be at approximately 19 °C (using 1 Hz apparent probing rate and a small temperature interval), this was chosen as the reference temperature (T_0). A universal time-modulus relationship was then obtained by solving Eqn. 7.2 for f, using the experimental probing rates as f_0. Similarly, the temperature-modulus relationship was then determined by using the calculated f values, choosing f_0 equal to 1 Hz, and solving Eqn. 7.2 for the equivalent temperatures, T (here T_0 was the experimental measurement temperatures). In this way the viscoelastic mechanical behavior of the pad material could be estimated for a much wider range of temperatures and probing rates (Fig. 7.8B). The resultant "master" curve for the elastic modulus of the dorsal surface of the pad displays the full time-temperature-elastic modulus relationship with two different variables. Here, the onset of the glassy-to-rubbery transition occurs at 18 °C, where the elastic modulus decreases sharply from an average of 105 MPa to 19 MPa at 26 °C. Similarly, when using the lower x-axis one can observe that at 19 °C, a temperature which the pad surface is likely to experience in its natural environment,[1] a sharp increase in elastic modulus occurs at approximately 1 Hz probing rate. From these results one can estimate how the pad should respond under a given temperature or probing rate. It should be noted that the present measurements were made at temperatures between 15 °C and 40 °C and projected to a wider range using the WLF equation. However, temperatures greater than 40 °C will hardly ever be experienced by *Cupiennius* and further decreases in the modulus of the pad may occur at such elevated temperatures.

7.3.4 Mechanical properties of the distal surface of the pad. The distal surface of the pad serves as the contact point with the tarsus (Fig. 7.2). Therefore, its mechanical properties are particularly important. In order to examine this area, a freshly autotomized leg was

clamped such that the pad's distal surface was facing upwards and reachable by the AFM tip. The tarsus was then deflected downwards and secured using a small amount of beeswax/rosin mixture. SFS of the distal surface was then performed using a probing rate of 1 Hz at two extreme temperatures, 16 °C and 30 °C (Fig. 7.9). The analysis of each data set gave similar modulus distributions, with an average value of 93 ± 14 MPa at 16 °C, and 18 ± 6 MPa at 30 °C. From this comparison we concluded that the viscoelastic mechanical properties of the distal and dorsal surfaces of the pad are the same. Since time and temperature are inter-related in viscoelastic systems, the elastic modulus at low/high temperatures at a given frequency correspond to the elastic modulus measured with high/low strain rates. Thus, the mechanical contact with the tarsus results in a higher effective modulus at high frequencies than at low frequencies. This implies a more effective mechanical energy transmission to the sensory slits and hence, high pass filtering properties as has been suggested earlier.[84,92]

Arthropod cuticle is a complex hierarchical, multilayered material with a wide range of properties serving a multitude of functions.[87,130,132,142,264] Specifically, the exoskeleton of *C. salei* contains a stiff exocuticle which is a laminated structure composed of sheets of parallel chitin fibrils embedded in a protein matrix which are rotated between each successive layer.[126,131] This exocuticle is covered by the outermost layer of the exoskeleton, the epicuticle. The composition of this layer is not characterized as well as other layers making up the exoskeleton of *Cupiennius*. It is thought to be made up of proteins and lipids which are not highly oriented like the chitin fibrils in the adjacent exocuticle. According to measurements on *C. salei*,[84,129] the thickness of the epicuticle on the metatarsal joint of the leg typically is less than 100 nm.

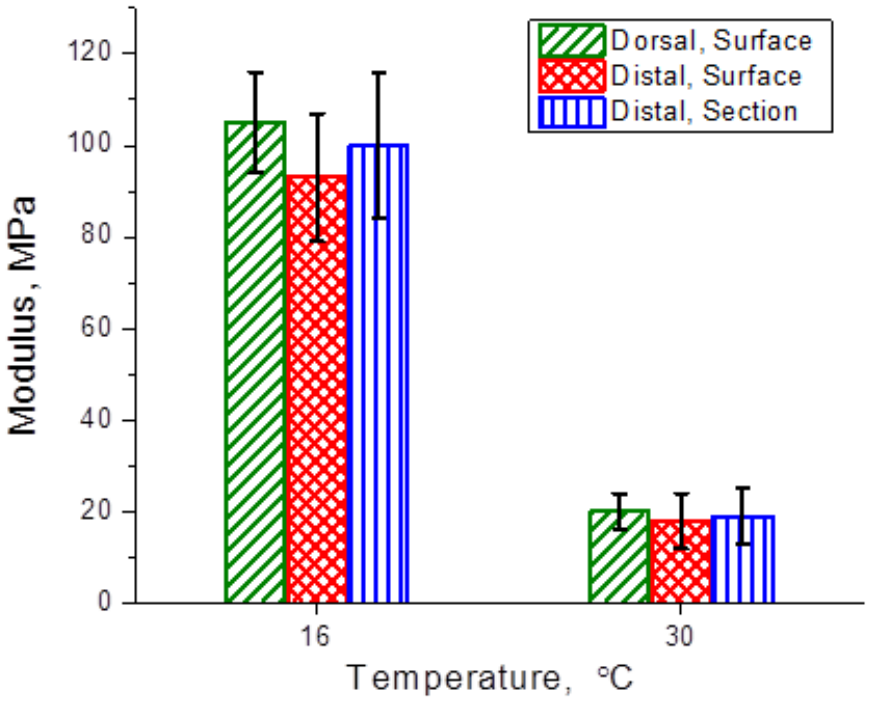

Figure 7.9: Summarized elastic modulus values for different locations of the pad measured below and above T_g.

In order to test whether the pad's mechanical properties measured here are characteristic of the topmost surface layer of the pads or are also affected by the supporting microstructure, we analyzed saggital sections of the pad and confirmed its layered morphology as suggested before for the exocuticle of *Cupiennius* (Fig. 7.10).[126,130] An outermost epicuticular region covers the entire pad. Its thickness of 1-2 µm is nearly an order of magnitude larger than that previously measured on the metatarsal joint.[84,129] AFM topographical measurements confirm the epicuticle's unusual thickness (Fig. 7.10C, D). According to high resolution images of the sections (Fig. 7.10E, 7.10F) the epicuticle shows a globular texture and, as expected from previous studies, lacks a chitin based laminated morphology. The thickness of the pad's epicuticle greatly reduces any contribution from the underlying substructure to the elastic modulus calculated from AFM probing. The detailed analysis of subsurface morphologies and their role in overall mechanical behavior will be discussed elsewhere.

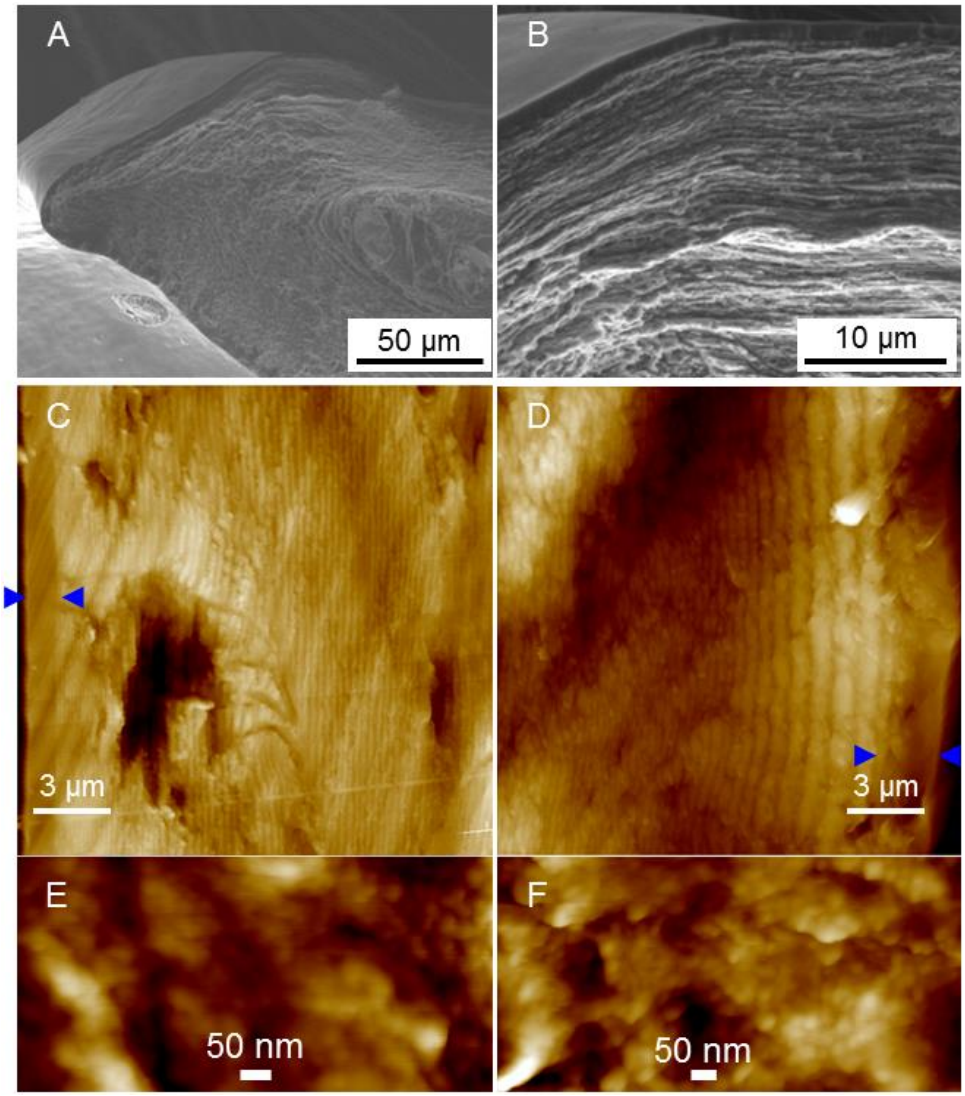

Figure 7.10: (A, B) SEM images of the pad showing a uniform coverage of an approximately 1-2 micrometer thick outer layer. AFM topography images of the pad section at the dorsal surface (C) and distal surface (D); blue arrows mark the outer layer. High resolution height images taken on the longitudinal section of the coating at the dorsal (E) and distal (F) locations. Z-scales (C) 240 nm, (D) 120 nm, (E) 20 nm, (F) 20 nm.

7.3.5 Relationship to natural stimuli. In the SFS measurements described above, the force was applied in a linear manner. However, in nature vibratory stimuli are transmitted to *Cupiennius* as a complex mixture of superimposed sinusoids of varying frequencies.[84,88] Therefore, it is important to relate the data we have obtained here to the expected response of the pad material to sinusoidal loading, which also allows for a direct comparison to the

electrophysiologically determined threshold curves.[88] In order to do so, we first analyzed time-temperature variation of SFS data to determine the relaxation times of the pad material.

7.3.5.1 Relaxation times of pad surfaces. Viscoelastic systems are usually modeled as an idealized combination of spring and dashpot elements in terms of Voight or Maxwell models.[6,169,280] Because the deformations levels throughout our measurements remained too low to cause plastic deformation, the pad was modeled using a standard linearly viscoelastic solid (SLS model) in order to simulate its complete time-temperature biomaterial properties (Fig. 7.11A). The application of load P to the linear viscoelastic solid results in an instantaneous elastic response characterized by the spring with an effective modulus E_0 (instantaneous modulus). At sufficiently long measurement time, the dashpot element relaxes and the material has an elastic response equivalent to the two springs in series, which corresponds to the so-called infinite elastic modulus E_∞. This effect is known as "delayed elasticity" and can be characterized by the creep compliance function:[26,169]

$$\varphi(t) = \frac{1-\upsilon^2}{E_\infty}\left(1 - \left(1 - \frac{E_\infty}{E_0}\right)e^{-t/\tau}\right) \tag{7.3}$$

where τ is the relaxation time of the material, which is a function of the dashpot's dynamic viscosity, η, and can be used to quantify the timescale of large-scale molecular motion at a given temperature, and t is a point in time after the application of load P. When the creep compliance function is plotted against $log(t)$, $log(\tau)$ represents the point of inflection of the sigmoidal curve (Fig. 7.11C).[6]

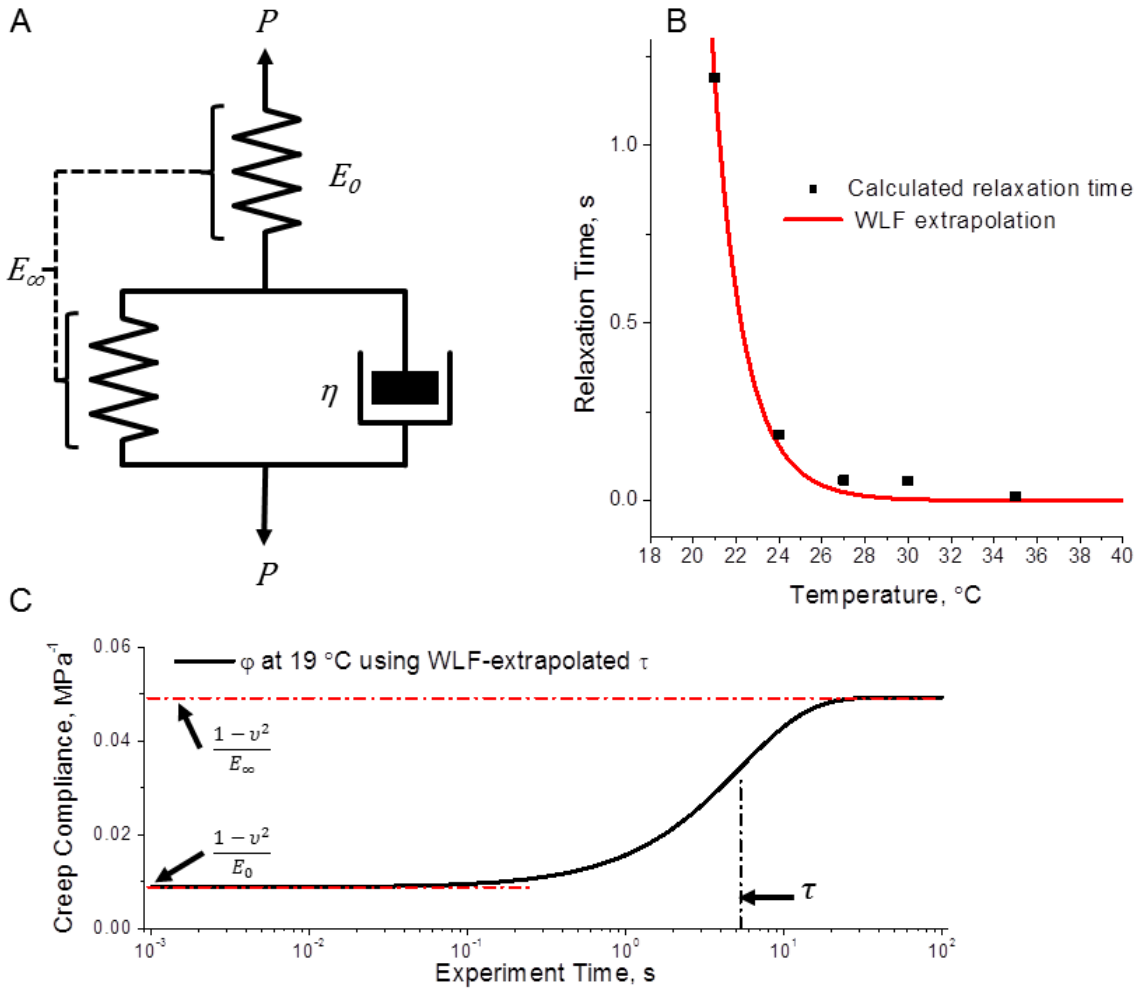

Figure 7.11: (A) Idealized spring and dashpot model of the standard linearly viscoelastic solid. (B) WLF fit for the relaxation time at the reference temperature of 19 °C (inset), and the extrapolation of all relaxation times for the entire temperature range measured. (C) Creep compliance function for the pad at 19 °C showing the location of the relaxation time along the curve and the upper and lower limits which were determined experimentally.

The temperature- and probing rate-dependent behavior observed on the pad surface (and viscoelastic materials in general) occurs when the thermal energy added to the system is sufficient to cause the rate for large-scale macromolecular rearrangements to be close to the timescale of the load application. In the glassy-to-rubbery transition regime, the stress strain relationship deviates from the classical Hookean behavior (spring-on-spring), due to the presence of the viscous dashpot, and the linear relationship between $\delta^{3/2}$ and the

applied force, P, is replaced by a time-dependent function.[26,169] We showed in Chapter 4 that the time-dependent penetration function suggested by Johnson[169] can be employed to determine τ as a function of temperature:

$$\delta^{3/2}(t) = \frac{3UL}{4\sqrt{R}}\frac{1-\upsilon^2}{E_\infty}\left(1-\left(1-\frac{E_\infty}{E_0}\right)e^{-t/\tau}\right) \tag{7.4}$$

where U is the loading rate (assumed to be constant), and L is the total time the tip is in contact with the surface during the approach fraction of the FDC. Here, we take the average of the extreme values of the calculated modulus shown in Fig. 7.8 to be E_∞ and E_0 (18.5 MPa and 104.5 MPa, respectively). Next, $\delta^{3/2}$ versus time curves were fitted according to Eqn. 4 to determine τ at 35 °C, 30 °C, 27 °C, 24 °C, and 21 °C (Fig. 7.11B). At the highest temperatures, the relaxation time of the pad material is short, ranging from 0.013 to 0.055 seconds. At 21 °C relaxation times are increased dramatically, up to 1.20 s suggesting very slow relaxation at this temperature range as is characteristic of highly viscous materials.[6,26]

Further fitting at lower temperatures is limited due to substantial errors resulting from a relaxation time exponentially increasing with temperature and becoming much longer than the actual contact portion of any FDC that we can produce with the AFM.[26] However, lower values of τ can be extrapolated using the WLF theory by fitting the previously determined relaxation times for τ_0 with:

$$\tau = \tau_0 10^{\frac{-c_1(T-T_0)}{c_2+T-T_0}} \tag{7.5}$$

where τ_0 is the relaxation time at the reference temperature, T_0 (19 °C) (solid line in Fig. 7.11B). From this analysis, it was determined that the relaxation time should increase

to 5.4 seconds for the pad surface at 19 °C, and further increase to as much as 156 seconds at 15 °C. Thus the pad material is made more resistive (i.e. the dashpot element becomes infinitely viscous) to mechanical deformation at low temperatures, increasing the effectiveness of stimuli transmission to the HS-10 organ (Fig. 7.11B).

7.3.5.2 Loss and storage moduli. A viscoelastic material's mechanical response to a sinusoidally applied stress is described by its storage and loss moduli, E' and E'' respectively.[6,280] During the application of periodic forces, the storage modulus represents the elastic response in which the deformation of the material is in phase with the force. Contrarily, the loss modulus is the out-of-phase, viscous response where mechanical energy is dissipated. E' and E'' can be related to the relaxation time and the previously calculated values of E_0 and E_∞ by:[26,212]

$$E' = E_\infty \frac{1+\omega^2\tau^2(E_\infty/E_0)}{1+\omega^2\tau^2(E_\infty/E_0)^2} \tag{7.6}$$

$$E'' = E_\infty \frac{\omega\tau\left(1-(E_\infty/E_0)\right)}{1+\omega^2\tau^2(E_\infty/E_0)^2} \tag{7.7}$$

where ω is the frequency of the sinusoidal force.

Plotted in Fig. 7.12 is E' and E'' for relaxation times corresponding to 19 °C, 24 °C, and 30 °C. From this, one can see that increases in temperature shift the rubbery to glassy transition and the peak of E" to higher frequencies. Examining the behavior of E' and E" at 24 °C allows us to compare with the tuning (threshold) curves produced at room temperature by Barth and Geethabali.[88] Here E' increases rapidly from 24 MPa to 99 MPa between 8 Hz and 115 Hz, with maximum energy dissipation (maximum E") occurring at 31 Hz, which is very close to the value of approximately 40 Hz beyond which the spider

becomes highly sensitive to substrate vibrations.[84,88] On the other hand, at 30 °C E' only begins increasing after 116 Hz, while the maximum of E" occurs at 435 Hz. Therefore mechanical energy applied at frequencies lower than 435 Hz at 30 °C is dissipated and not as easily transferred through the pad to the slits. At 19 °C the maximum energy dissipation occurs at 1 Hz, and E' quickly reaches its maximum (104.5 MPa) after ~10 Hz. This implies that at 19 °C temperature the spider is highly sensitive to substrate vibrations with frequencies greater than 5-10 Hz.

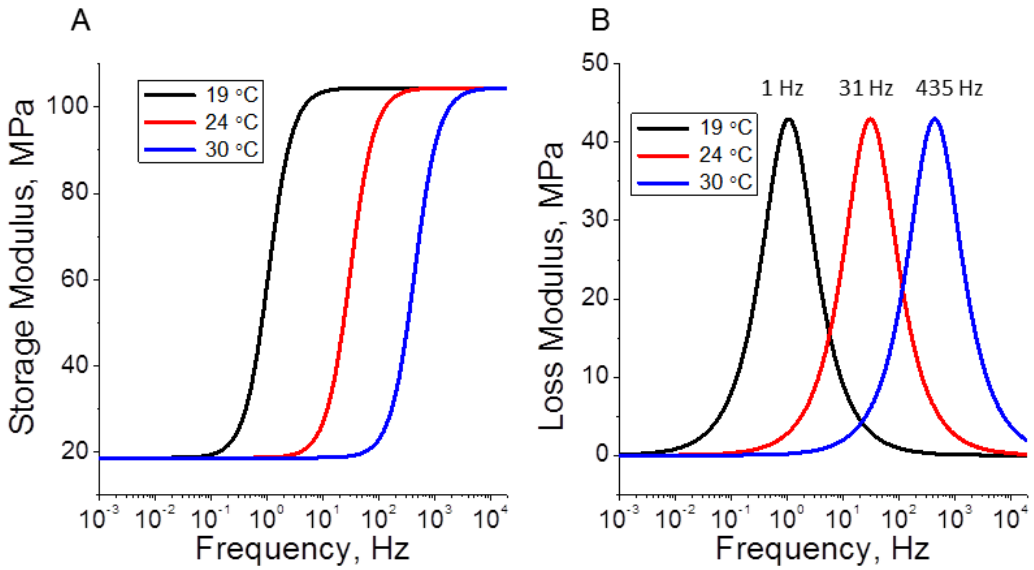

Figure 7.12: Storage (A) and loss (B) moduli calculated using Eqns. 5 and 6 demonstrating the dependence of the mechanical properties on the loading frequency (force applied sinusoidally) at 19 °C, 24 °C, and 30 °C.

7.4 Conclusions

We have shown here a non-destructive probing method can be applied to a natural biomaterial, allowing for a complete viscoelastic characterization of the pad surface materials not possible by any other means. Utilizing the standard linear viscoelastic solid model, we were able to describe universal time-temperature dependent mechanical behavior. By applying this approach, the dependence of the elastic modulus of the metatarsal pad of *Cupiennius salei* on both temperature and probing rate could be revealed.

The onset of the glassy-to-rubbery transition occurs at 19 °C, slightly below regular room temperature. In a narrow range from 18 °C to 24 °C the pad material exhibited highly time- and temperature-dependent mechanical behavior, with nominal elastic modulus values dropping from 105 MPa at the lowest temperatures to 19 MPa at the highest temperatures studied here. In contrast, the relaxation times increased dramatically at lowered temperatures from tens of milliseconds to seconds below 20 °C thus making the pad surface a highly damping viscous material at intermediate temperatures with maximum dissipation of mechanical energy. This range likely represents temperatures in which *Cupiennius* spends most of its active hours (night time when the mountainous area it is found in cools to around 20°C).[89] In the range where the pad is the most rate- and temperature-dependent, the most responsive time values ranged from ~0.1 s to 1 s. Such viscoelastic properties undoubtedly contribute to the high-pass behavior of the HS-10 organ and the spider's sensitivity to high frequency signals. Low frequency signals typical of environmental noise[84,88] are filtered out by the epicuticle and require larger tarsal deflections to elicit a neural response.[88]

The distal surface of the pad was directly measured here in comparison to the dorsal surface for the first time. Both showed similar mechanical properties. More research into the mechanical properties of all structures involved is needed to determine how substrate vibrations are transmitted to the slits proper of the spider's vibration receptor. Their physiological high pass characteristics to a large extent can now be explained by the viscoelastic mechanical properties of epicuticle. It should be borne in mind, however, that the metatarsal organ will respond to low frequency stimuli as well, provided these are strong enough. Under these circumstances in particular, which may also occur during locomotion, rapid escape and complex movements like those involved in spinning the eggsac or turning around in small crevices, the complex overall and sub-structure of the pad may not only allow effective stimulus transmission at low frequency but also help to

provide mechanical robustness and avoid damage. In addition, the mechanical properties of the overall structure (and substructure) of the pad might affect the transmittance and transformation of vibratory stimuli and be used to concentrate strains onto the metatarsal organ, as suggested earlier.[84]

CHAPTER 8

Micromechanical characterization of strain-sensitive lyriform organs of the wandering spider Cupiennius salei.

Highly sensitive lyriform organs located on the legs of the wandering spider, Cupiennius salei, allow the spider to detect nanometer-scale strains in the exoskeleton resulting from locomotion or substrate vibrations. Morphological features of the lyriform organs result in their specialization and sensitivity to specific mechanical stimuli, which makes them an ideal example for functionalized bioinspired strain sensors. However, there has been relatively few attempts to directly characterize the fundamental mechanical properties of the key components of the slit sensors themselves. Here we utilize atomic force microscopy (AFM)-based nanoindentation techniques to probe the nano-scale mechanical properties of two lyriform organs found on *Cupiennius salei*: the vibration sensitive metatarsal lyriform organ (HS10), and the proprioceptive tibial lyriform organ (HS8). Force distance curves (FDCs) obtained from AFM measurements displayed characteristic multi-layer structure behavior, with calculated elastic moduli ranging from 150 MPa to 500 MPa. In addition we also probed the lyriform organs with a large radius tip, which allowed for application of high forces and resulted in an apparent elastic modulus on the order of 2 GPa. Also apparent in the FDCs was time-dependent behavior indicative of viscoelastic behavior, which yielded relaxation times consistent with our previous measurements, and may suggest a critical role that viscoelastic mechanical behavior play in the time-dependent sensory adaption of the lyriform organs.

8.1 Introduction

In the life of a wandering spider (*Cupiennius salei*), perception is dominated by mechanosensory systems[84] which include tactile hairs,[86,101,102] air-flow sensing trichobothria,[91,93,94,136] and innervated slit sensilla embedded in the exoskeleton

(Fig. 8.1).[96,108,112,282,] Of the ~3300 slit sensilla, about half form 144 closely packed groups of parallel slits known as lyriform organs (a name derived from the ancient musical instrument which they resemble, examples shown in Fig. 8.1B,C), with most located on the legs of the spider near joints.[100] An interesting facet of the lyriform organs is their specialization in regard to their tuning to specific mechanical stimuli. Depending on many morphological factors including slit orientation within an organ (e.g. angles between slits, length gradients, and lateral shifts amongst the slits), orientation with respect to the axis of the leg, dendrite position, and surrounding structures (e.g. the cuticular pad), a single organ can be "tuned" to detect strain direction, a wide range of strain amplitudes, and also be more sensitive to specific frequency ranges.[88,92,108,110,111,116] Because of this, these slit sensory systems as well as their insect analogues, campaniform sensilla, have become particularly interesting as a form of biomimetic and bioinspired mechanosensing. In this regard there have been several recent proposed uses of such bioinspired devices as embeddable, tunable strain sensors for space exploration applications and for easily created strain sensing in flexible electronics.[283,284,285,286,287,288] However, to better understand how these organs can be applied to prospective problems, a fundamental understanding of their materials properties is required.

We have studied in detail the time- and temperature-dependent micromechanical properties of the epicuticular covering layer of the metatarsal pad which serves to enhance the response to high frequency vibrational stimuli.[92,123] Additionally, we have observed a variety of chitin fibril orientations and sclerotization levels resulting in a wide range of mechanical properties in the subsurface structures of the pad.[289] The pad was also observed to play key functional roles in HS10 compression including transformation of large deformations from the tarsus (on the order of 10s of μm) to smaller deformations (on the order of a 10s of nm) as well as maintaining parallel orientation of slit walls during compression, regardless of loading angle from the tarsus.[289] Despite the growing wealth

of knowledge on the biomechanical properties of surrounding cuticular structures such as the metatarsal pad, crack deformational behavior via modeling experiments,[108,110,111,116] and even sensory response through direct electrophysiological investigations,[88,124] there is very little direct micromechanical characterization of the lyriform organs themselves.

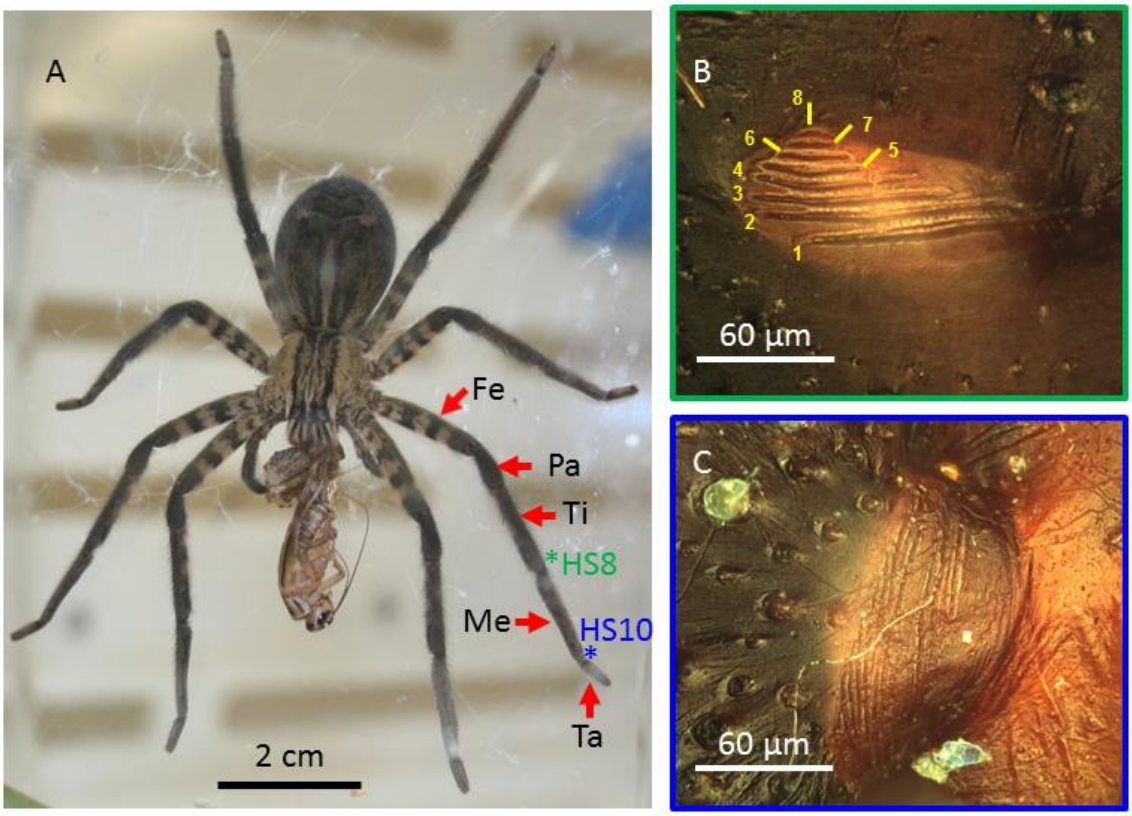

Figure 8.1: (A) Adult female *Cupiennius salei*. Arrows demark different leg segments: Ta = tarsus, Me = metatarsus, Ti = tibia, Pa = patella, Fe = femur. Colored asterisks demark approximate location of two lyriform organs measured in this study: green = HS8, located on posterior side of the leg; blue = HS10, located on the dorsal side of the leg. (B) Optical image of HS8 lyriform organ, slit numbering here is used for reference in later results. (C) Optical image of HS10 lyriform organ.

Each individual slit is a hole in the exocuticle which is generally 1-2 µm wide, and ranges from ~10-200 µm in length (sectional schematic presented in Fig. 8.2). Bridging the two slit walls at the outermost surface is an epicuticular outer membrane. Moving down within the slit (dorsal to ventral direction), one can find a viscous sodium-rich receptor lymph[107]

and an inner membrane which extends across the exocuticular layer and separates the bottom of the slit and the extracellular space where the neural cell body resides. Just below the inner membrane is the tip of a second, shorter dendrite. To date not much is known about the exact functional roles of the inner membrane or the second dendrite.[124] Attached to the outer membrane – typically centered in the middle of the width, but not necessarily in the middle of the length – via a coupling cylinder is a dendrite.

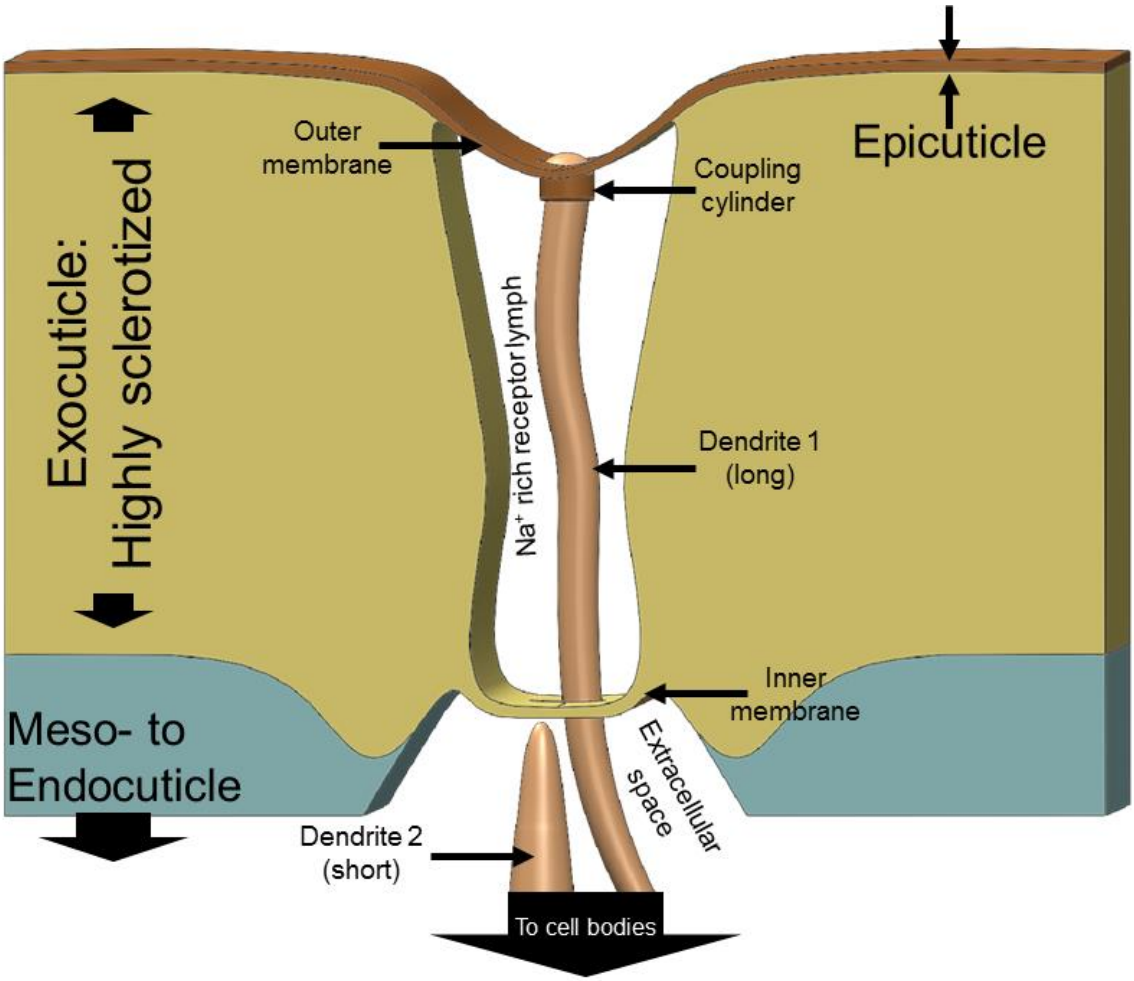

Figure 8.2: Schematic depicting a section through a single slit sensillum. Not shown here is a sheath which covers both dendrites, extending from the coupling cylinder down to the cell bodies. It should also be noted that sharp boundaries between cuticular layers may not necessarily be present.

As forces compress the slit, the outer membrane deflects downward causing deformation of the dendrite, resulting in the firing of action potentials. In this way, each slit is able to monitor strain in the exoskeleton of the spider caused by locomotion, changes in haemolymph pressure, and substrate vibrations caused by nearby prey and mates, with sensitivities on the order of 10^{-9} m. Therefore we suggest that the topographical and micromechanical properties of the outer membrane are critical in the functional performance and sensitivity of the lyriform organs, and as such merit careful investigation of their micromechanical properties.

Herein we present results of careful micromechanical characterization of the surface of two lyriform organs on *C. salei*: (i) the metatarsal lyriform organ, HS10, because of is unique sensitivity to vibrational stimuli, and (ii) a tibial lyriform organ, HS8, because the large width and shallow depth of several slits allow for easy access to measure the outer membrane. Additionally, there is a significant amount of literature existing on the HS8 organ, making facilitating comparison between the mechanical properties observed here and the electrophysiological response recorded earlier. We utilize atomic force microscopy (AFM) and surface force spectroscopy (SFS) to study the topographical and micromechanical properties of these organs with precise lateral control as well as in a controlled environment on living and rehydrated cuticle samples. Force distance curves (FDCs) were taken using as-received AFM tips as well as modified AFM tips with large radii of curvature in order to investigate the mechanical properties of the surface of epicuticular outer membrane (small radius tips) as well as membrane structural modulus (large radius tips) at different penetration depths. From this analysis we observed a multi-layered structure with a softer viscoelastic layer on top of a stiff supporting layer, with elastic modulus values calculated from FDCs ranging from approximately 150 MPa at the smallest penetration depths, to as high as 2 GPa for the highest applied forces obtained

using a modified AFM tip. Finally, we discuss how viscoelastic nature of the upper layers could potentially contribute to the functional response of the organ.

8.2 Materials and Methods

8.2.1 Materials. For measurements of the HS10 lyriform organ, live adult female wandering spiders were used, according to those descriptions presented throughout this thesis. Measurements were performed on a combination of living intact spiders, freshly autotomized legs, as well as stored rehydrated spider legs.

Rehydrated legs were inspected visually for signs of biofouling daily, with no visual or AFM evidence of biofouling being observed throughout the experiments. In order to ensure that the cuticle of these dissected legs was as close to its natural state as possible, prior to measurement spider saline solution was gently injected into the spider leg at the site of the dissection (with just enough pressure to slightly extend the metatarsal joint). The leg was placed back into the glass vial partially filled with saline solution and allowed to equilibrate to room temperature. Immediately before scanning the surface of the spider leg was rinsed with ultrapure water to protect the AFM scanner from the potentially corrosive saline solution.

8.2.2 Optical microscopy. Optical imaging was undertaken according to § 3.2.1.

8.2.3 Atomic force microscopy. All AFM measurements were made using a Bruker Icon AFM (Santa Barbara, CA, USA) equipped with a Nanoscope V controller (Chapter 3). For some experiments, we utilized probes with moderately-sized tip radii (~200-500 nm radius), which were created by annealing as received AFM tips at 1100 °C in air for 6-12 hours. The radius of curvature of each tip was determined prior to measurements by scanning a titanium roughness sample (Bruker), and utilizing the blind tip estimation

algorithm to create a height image of the reconstructed tip shape. This height image was sectioned and analyzed numerically, as described below. In the case of annealed AFM tips, the blind tip estimation method was used in combination with SEM in order to determine tip shape. Figure 8.3 shows topographical scans on the roughness sample with clear differences resulting from tip convolution after the tip was subject to annealing.

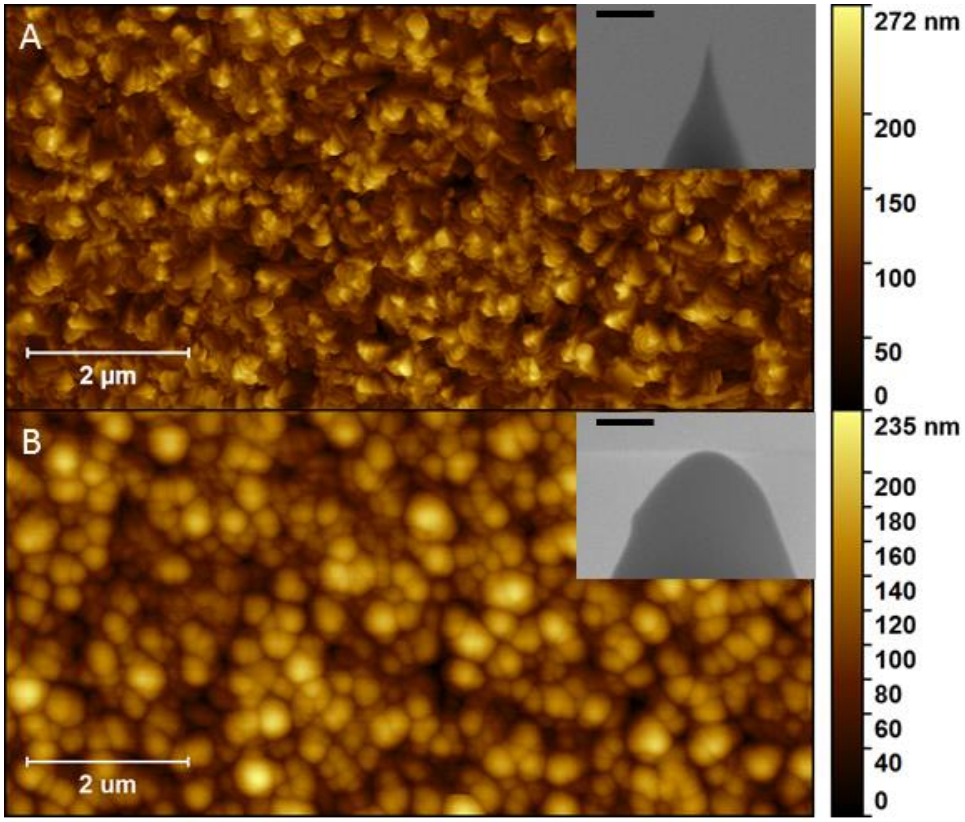

Figure 8.3: AFM height images of standard TiO_2 roughness samples used to determine tip shape by deconvolution before (A) and after oxidation at 1100 °C in air for 12 hours (B). Inset are SEM images of each tip used to take the AFM image, scale bar = 300 nm.

8.2.4 Electron microscopy. Scanning electron microscopy images were collected on a Hitachi S-3400N thermal emission SEM. AFM tips were placed in a spring loaded clamp and scanned under vacuum at magnifications of ~25k and ~100k with an accelerating voltage of 5 kV. Further modification of SEM images of AFM tips used in Fig. 8.10

consisted of background removal using Adobe Photoshop. In these cases some minor fine resolution features were lost near the very tip of the probe, but overall shape and size is preserved to give the reader an accurate feel for the size of the tip-surface interactions occurring in these studies.

8.3 Calculations

8.3.1 Determination of tip radius. The radius of curvature, R, of a simple polynomial curve can be determined by Eq. 8.1:

$$y = y(x) \rightarrow R = \frac{\left(1+\dot{y}^2\right)^{3/2}}{|\ddot{y}|} \tag{8.1}$$

where $\dot{y}$ and $\ddot{y}$ represent the first- and second-order differentiations of $y(x)$ with respect to x, respectively. For simplicity here we assume an axisymmetric tip shape with a parabolic cross section described by the equation $y = A + Bx + Cx^2$. Section profile data from reconstructed tip images were evaluated using a MatLab-based, in-house developed data analysis program (*MMA-SPM*) and fit with a parabola under non-linear optimization conditions, in order to determine the second order polynomial coefficients. These coefficients were then used to determine tip radius, according to Eqn. 8.2:

$$R_{tip} = \frac{\left(1+(B+2Cx)^2\right)^{3/2}}{|2C|} = \frac{1}{2C} \tag{8.2}$$

Prior to each measurement, a reference Ti roughness sample (obtained via Bruker) was scanned, and a blind-tip estimation algorithm was used in order to reconstruct a 3-dimesional estimation of tip shape. Several sectional profiles from this reconstruction were taken and this data was fitted according to Eqn. 8.1 and Eqn. 8.2 in order to determine the

radius of curvature for each tip apex (e.g. tip apex profile fit in Fig. 8.4). In the case of annealed tips, we also confirmed our estimation via SEM imaging (see Fig. 8.3).

8.3.2 Determination of elastic modulus. The elastic modulus of sample surface was determined by analyzing FDCs which had low background noise and a clear contact point. Generally, more than 30 FDCs were collected at different locations and the approach portion of each FDC was used to determine the elastic modulus by fitting with the classical Sneddon equation for the purely elastic deformation of an elastic half space with a rigid paraboloidal punch:[28,169]

$$P = \left(\frac{4}{3}\frac{E}{1-\upsilon^2}R_{eqv}{}^{1/2}\right)\delta^{3/2} \tag{8.3}$$

where P is the applied force, R_{eqv} is the equivalent contact radius, δ is the penetration depth, ν is Poisson's ratio (chosen to be 0.3 to be consistent with previous AFM-based mechanical measurements,[92,123] and E is the elastic modulus of the outer-most surface layers.

8.3.3 Effect of contact radius. In the vast majority of AFM-based micromechanical measurements found in the literature, a sharp AFM probe is pushed into surfaces which are flat with low surface roughness. In this case, the equivalent contact radius is taken to be the radius of curvature of the tip (i.e. sphere on sphere of infinite radius). However, in these experiments, the surface of the spider cuticle is rough with many ridges and valleys (see Fig. 8.4A). Therefore we also wanted to take into account the curvature of the surface to determine if the equivalent contact radius, and thus the calculated elastic modulus, has a significant effect on our results. Figure 8.4B shows section profiles taken corresponding to the dotted lines in the high-resolution height image presented in Fig. 8.4A. From these

we determined that we can treat our contact problem as a rigid parabolic punch on a cylindrical surface, resulting in an elliptical contact area with major and minor axes, A and B, respectively. As a result, the equivalent contact radius can be calculated by Eqn. 8.4:

$$R_{eqv} = \frac{1}{2}(AB)^{1/2} = \frac{1}{2}\left\{\frac{1}{4}\left(\frac{1}{(R_1{}')^2} + \frac{1}{R_1{}'R_2{}''}\right)\right\}^{-1/2} \tag{8.4}$$

where $R_1{}'$ is the major semi-axis of the indenter, and $R_2{}''$ is the minor semi-axis of the surface. Inclusion of the equivalent radius slightly changes the relationship between applied force and penetration depth to:

$$\delta = \left(\frac{9}{16}\frac{P^2}{R_{eqv}E^{*2}}\right)^{1/3} F_2\left(\frac{R'}{R''}\right) \tag{8.5}$$

where R' is the equivalent radius of the indenter, R'' is the equivalent radius of the surface, and $F_2\left(\frac{R'}{R''}\right)$ is a tabulated function which can be found in various literature[169] and more convenient electronic sources.[290]

In the case presented in Fig. 8.4 we found that taking into account the curvature of the ridges resulted in a calculated elastic modulus of 162 ± 34 MPa, while considering the surface a flat, semi-infinite half-space resulted in a calculated elastic modulus of 155 ± 27 MPa. Because these two numbers are in good agreement and within one standard deviation, we propose that with careful measurement (i.e. taking FDCs at the peak of ridges, and ensuring the entire sample is not significantly tilted) the elastic modulus of the surface of the spider legs can be reasonably determined without additional data treatment.

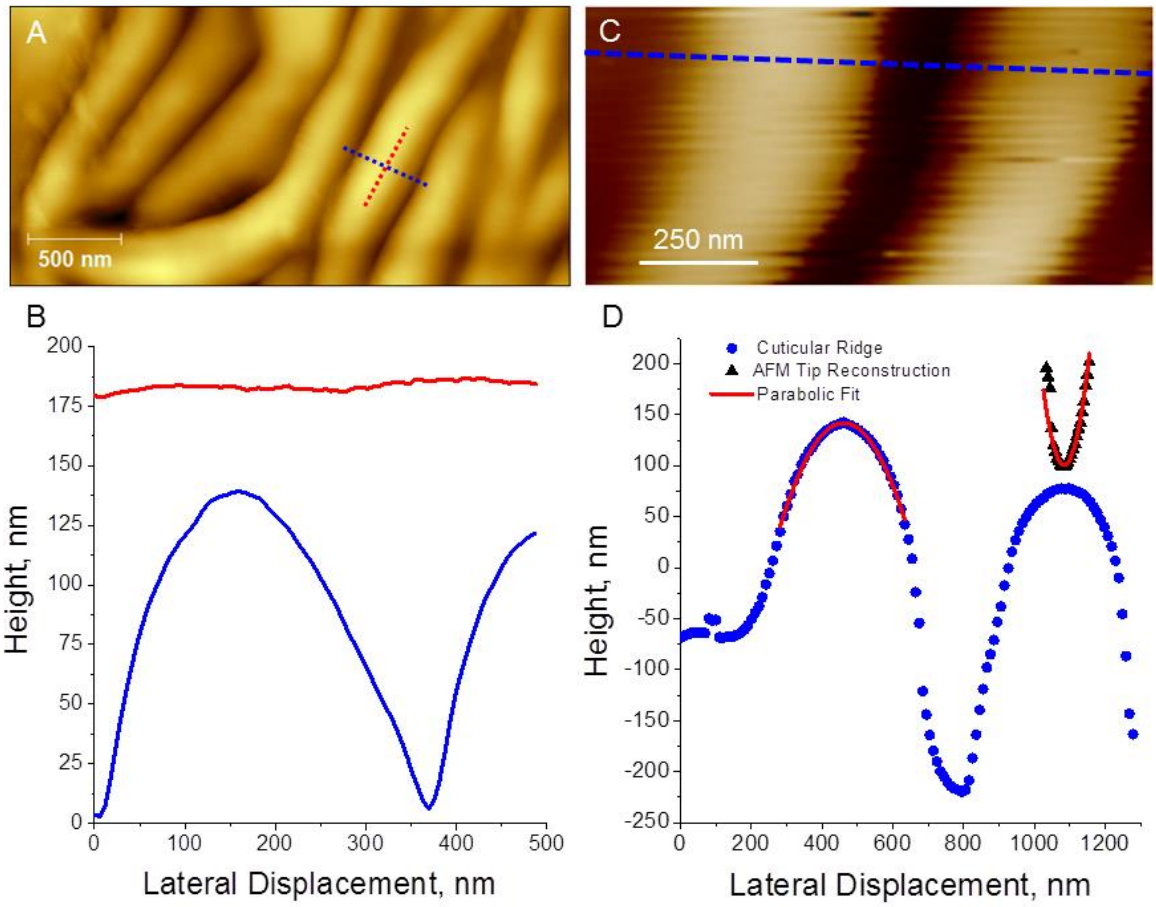

Figure 8.4: (A) High resolution (1024 pixels x 512 pixels) AFM topography image of cuticular ridges found just outside of a slit in HS10. (B) Sectional profiles corresponding to the colored dashed lines in A, showing that at the ridge peak one can assume the shape of a parabolic-cylinder. (C) Height image obtained from high-resolution SFS mapping (128 pixels x 64 pixels) of ridges on the cuticle surrounding HS10 slits. (D) Sectional profile obtained from (C), fit with a parabolic function to determine radius of curvature.

8.4 Results

8.4.1 AFM topographical imaging of lyriform organs. Figure 5 shows AFM topographical images of the metatarsal lyriform organ HS10 taken on a live female spider. Both height images show wavy morphology that we occurs naturally as the epicuticle is formed.[126,291] The cross-sectional profiles taken from the dashed lines superposed on the topographical data is presented in Fig. 8.5B and 8.5D. In each of these profiles the slits ends in sharp points, which are a result of tip shape rather than membrane topography. Therefore it was

determined that the slit sensilla in HS10 are too narrow and deep for the AFM tip to reliably reach the outer membrane for mechanical measurements. However, because this is the organ of interest for us, we found it informative to measure the cuticle surrounding the slit outer membrane (i.e. the areas in-between slits, referred to as "surrounding cuticle" or "SC" below, seen in Fig. 8.5A,B) and use for comparison with those organs in which the outer membrane is accessible via AFM. Consequently, it should also be emphasized here that measurements on HS10 were made on a live spider, thus in addition to organ to organ comparison, these measurements will serve as a control to compare against rehydrated HS8 organs.

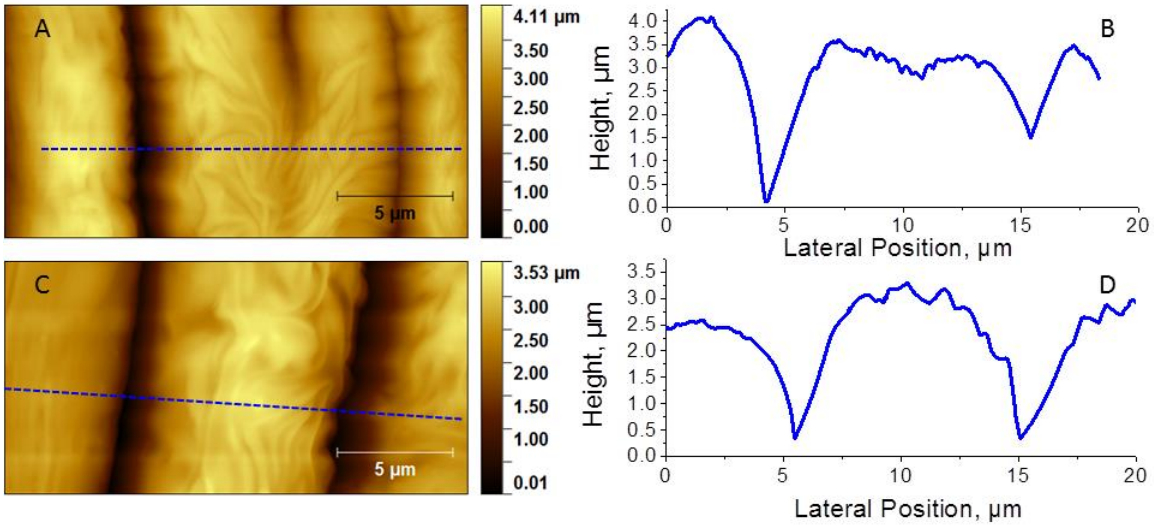

Figure 8.5: (A,C) AFM topography images of slits located in the metatarsal lyriform organ (HS10). (B,D) Section profiles corresponding to the blue dashed lines in A and C, respectively.

Figure 8.6 shows topographical AFM data of one of the tibial lyriform organs, HS8, taken from a freshly autotomized leg. In these images, slits 8 and 7 (see Figure 8.1B) are present, and it can be seen there is also a similar wavy morphology, with wider ridges occurring outside of the organ, thinner ridges appearing on the cuticle in between each slit, and low roughness (i.e. no ridges) on the surface of the outer membrane spanning the slit (see Fig. 8.2). The fact that we observe a different morphology on HS10 organs (Fig. 8.5) in

comparison to HS8 (Fig. 8.6), and furthermore morphology changes within HS8 (i.e. varying ridge size, to no ridges on the outer membrane) suggests that these ridges may serve some specific biological function. Also observable in Fig. 8.6 are the tips of the dendrites which are responsible for firing action potentials during compression of the slit under biologically-relevant loading. Here we operate under the assumption that the mechanical properties of slit sensilla are essentially equivalent from organ to organ, with the primary morphological factors (slit length, location of dendrite, lateral shift, etc.) affecting their functionality. Therefore we assume that the mechanical properties calculated from the measurements we perform on the HS8 organ (specifically the membrane and dendrite) are also applicable to the HS10 organ.

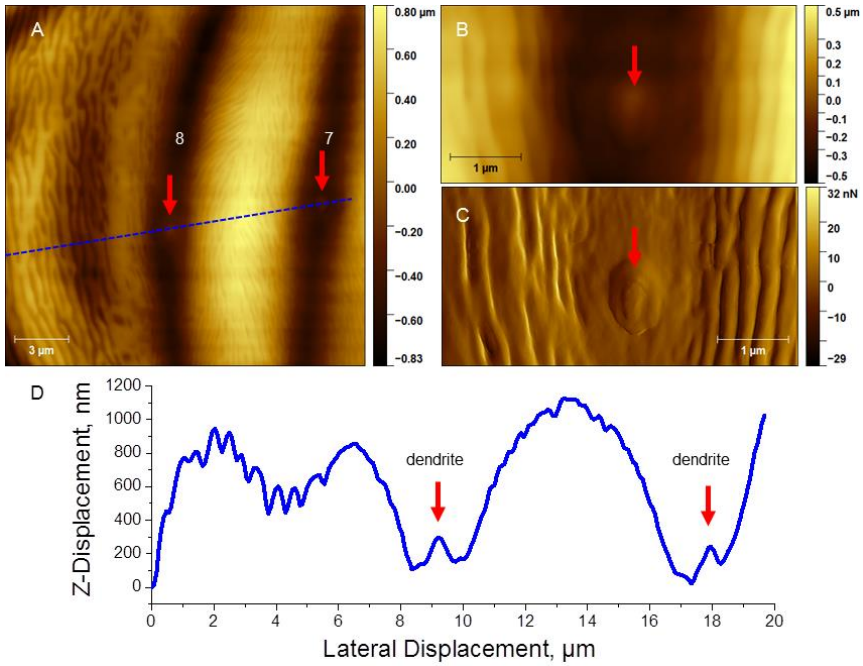

Figure 8.6: (A) AFM topography image containing a portion of slits 7 and 8 of the HS8 lyriform organ, in which the slit width and shallowness make it a viable organ to make measurements of the outer membrane as well as the dendrite region. A zoomed-in height image (B) and error image (C) of the dendrite region. The error image can be viewed as a type of differential height image, and as such is presented because it gives clear outlines in area where height changes significantly. Here the error image aids in visualizing the dendrite region. (D) Sectional profile taken from (A) as demarked by the blue dotted line. Red arrows indicate dendrite regions.

8.4.2 Micromechanical properties of lyriform organs. Careful FDC measurements were taken on slit 8 in the HS8 organ of a freshly autotomized leg using an as-received AFM tip (radius of curvature ~10-20 nm), and representative curves are presented in Fig. 8.7. It should be noted here that these measurements were taken with a very low spring constant tip, which results in probing of only the first few nm depth at the surface; greater probing depths yield different results (discussed below). In general the slope of the FDC is indicative of the elastic modulus of the material surface which is being measured.

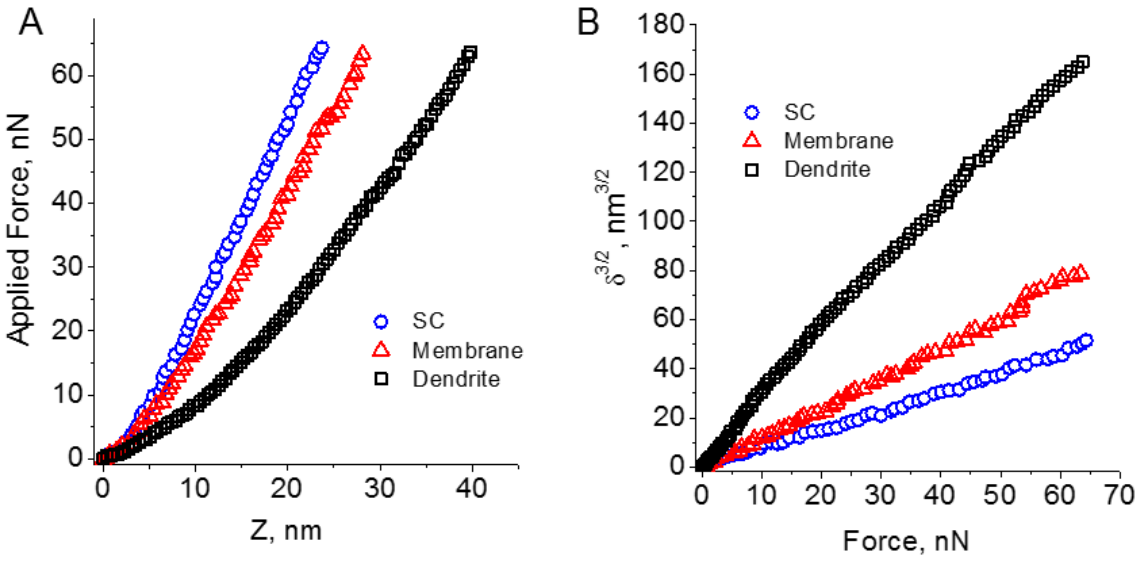

Figure 8.7: Example force versus displacement (A) and pentration depth versus force (B) plots from three distinct regions of HS8 lyriform organ from a freshly autotomized leg.

In Fig. 8.7B it can be seen that while the surface of the cuticle in between the slits and outer membrane surface have similar slopes, the slope at the site of the dendrite is noticeably different. Calculations on these curves revealed a general trend in which the elastic modulus of the surrounding cuticle is slightly larger than the calculated elastic modulus of the surface of the outer membrane (but still within one standard deviation), both of which are significantly larger than the calculated elastic modulus of the dendrite tip exposed at the surface. We also took FDCs on the accessible surface of the HS10 surrounding cuticle.

Due to the natural angle of HS10 organ with respect to the long axis of the leg (see section image in ref. [92]) careful attention was paid to the slope at which the AFM was scanning to ensure measurements were taken on surfaces with slopes < 5° (determined by unprocessed AFM data). The calculated elastic modulus of the surface of the surrounding cuticle of the HS10 surface was found to be similar to that of the HS8 organ. Therefore we assume that the fundamental materials properties of each set of organs are equivalent. Table 8.1 summarizes the values found from these measurements.

Table 8.1: Summary of elastic moduli calculated from force distance curves obtained on HS8 and HS10 lyriform organs of C. Salei. In each case > 30 curves were taken and the resulting calculation is presented as average ± one standard deviation.

HS8 – Surrounding Cuticle	HS8 – Membrane	HS8 – Dendrite	HS10 – Surrounding Cuticle
177 ± 37 MPa	125 ± 35 MPa	64 ± 14 MPa	165 ± 40 MPa

8.4.2.1 Micromechanical properties of the outer membrane at varying indentation depths. Because the outer membrane deflection under loading is ultimately responsible for the firing of action potentials, we focused on a careful characterization of the mechanical properties of the outer membrane. For these experiments measurements were taken primarily on slit 8 of HS8, within 1 µm of the dendrite tip. Measurements were also taken on slit 7 and slit 6 (to ensure no differences were observed slit-to-slit, data not presented) which corresponded well with those made on slit 8. The depth of the slit increased in slits 1-5 enough to make the outer membrane not easily accessible via AFM, therefore they were not measured here. However, as discussed in the literature[84,117] this highlights the potentially crucial effects that the depth of the outer membrane (and therefore the curvature) can have on the overall functioning of slit sensilla.

Figure 8.8 shows several examples of FDCs taken on the outer membrane with a sharp AFM probe, with lower (15-20 nm, Fig. 8A,B) and higher (25-40 nm, Fig. 8A,B; and 40-50 nm Fig. 8C,D) penetration depths (note that all curves presented here are shifted along the x-axis for better viewing). In general, the initial portion of the curves show similar shape and slopes. As mentioned, this is indicative of similar mechanical properties. However under increased loading (i.e. higher penetration depths) there is a noticeable kink in the $\delta^{3/2}$ versus force plots (Fig. 8.8B,D), which generally indicates a change in mechanical properties. The kink in this case is a decreasing positive slope, indicating a transition from a lower elastic modulus to a higher elastic modulus. Analysis of many whole curves yielded an average elastic modulus of 221 ± 76 MPa.

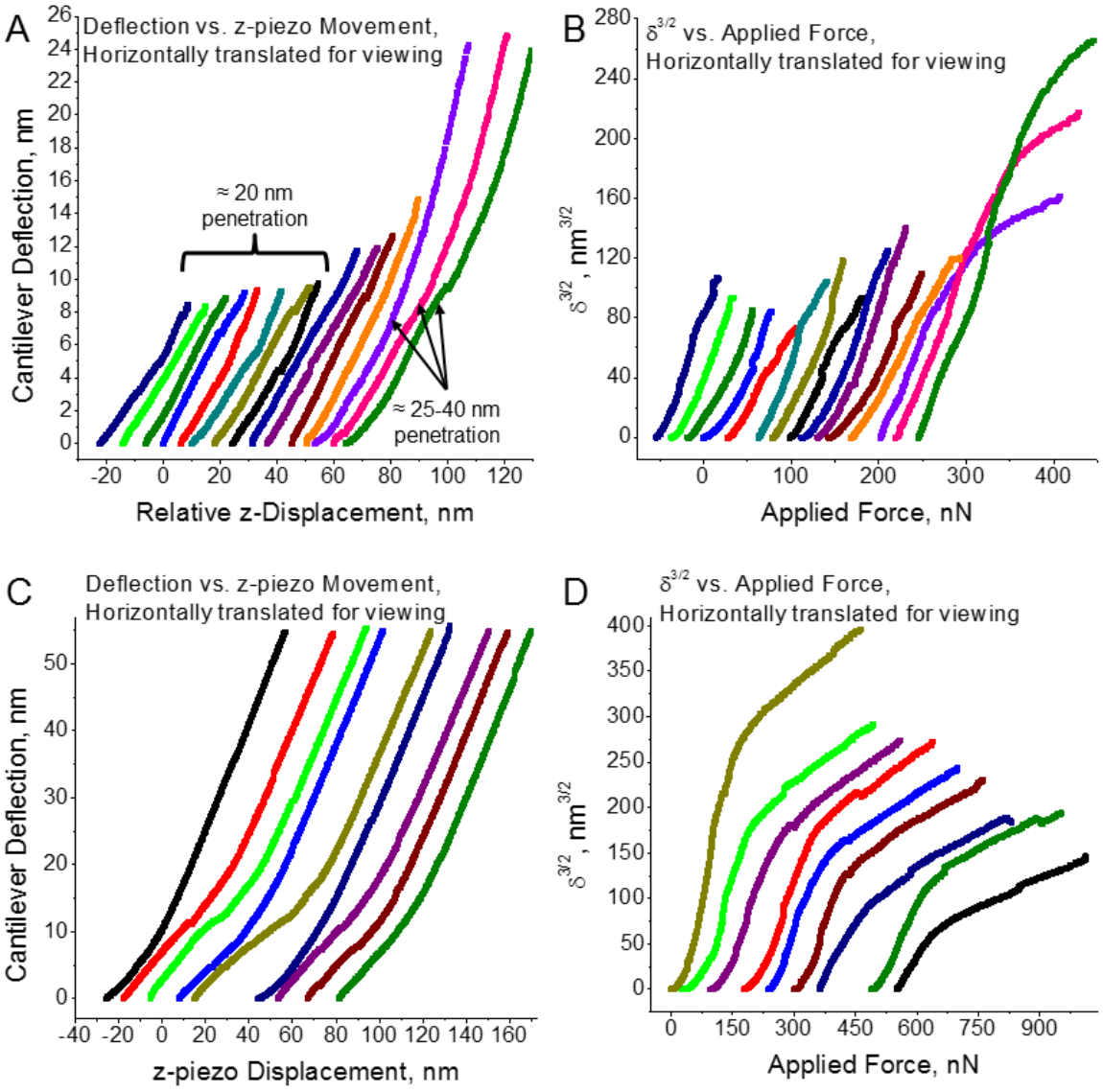

Figure 8.8: Example cantilever deflection versus displacement (A, C) and penetration depth versus force (B,D) plots obtained from loading curves taken on an HS8 lyriform organ from a rehydrated leg using low to moderate (A,B) and higher (C,D) deflections thresholds, resulting in applied forces ranging from ~64 nN to ~400 nN.

In order to quantify this change in modulus seen in the higher-penetration FDCs, we have fitted small portions of each curve corresponding to varying penetration depths (Fig. 8.9). In the case of Fig. 8.9A, we have used intervals of 4% of the maximum applied force; for example, for a maximum applied force of 100 nN, we fit with Eqn. 3 data ranging from 0-4 nN, 4-8 nN, 8-12 nN, and so forth. Typically fitting with Eqn. 3 assumes that the

penetration is zero at the starting point, therefore the fitting line in the penetration line goes through a point (0,0). However in the case of a sample with a soft surface layer above the studied material, penetration at the starting point could have a non-zero value. Therefore, when fitting the higher intervals in our FDCs (e.g. 12-16%, 16-20%, etc.) the fitting was also a straight line but did not necessarily pass through (0,0). When plotting the calculated values of modulus versus penetration depth there is clearly an observable "S-shaped" trend in which the calculated elastic modulus initially decreases, then increases and levels off (Fig. 8.9A,B). Because there is data scatter associated with both fitting FDCs as well as from taking FDCs in different locations, Fig. 8.9A shows the calculated modulus for each FDC which has been translated along the y-axis according to the average modulus of the entire curve (note: each data set in Fig. 8.9A represents calculations made from varying penetration depths for one FDC, color copy required and can be obtained online). All FDCs used in these calculations were then averaged to give the reader a sense of the overall shape of the curves (Fig. 8.9C). From Fig. 8.9C, it can be seen that there is a concave up portion located between 0-75 nN applied force, in which the modulus decreases from ~225 MPa to ~122 MPa. This concave up shape in the $\delta^{3/2}$ vs F curve is highly indicative of a viscoelastic material, and will be discussed further below. Finally, from the data the modulus appears to reach a limit at ~500 MPa, which is much greater than the values measured on the epicutical of the metatarsal pad measured previously.[92,123]

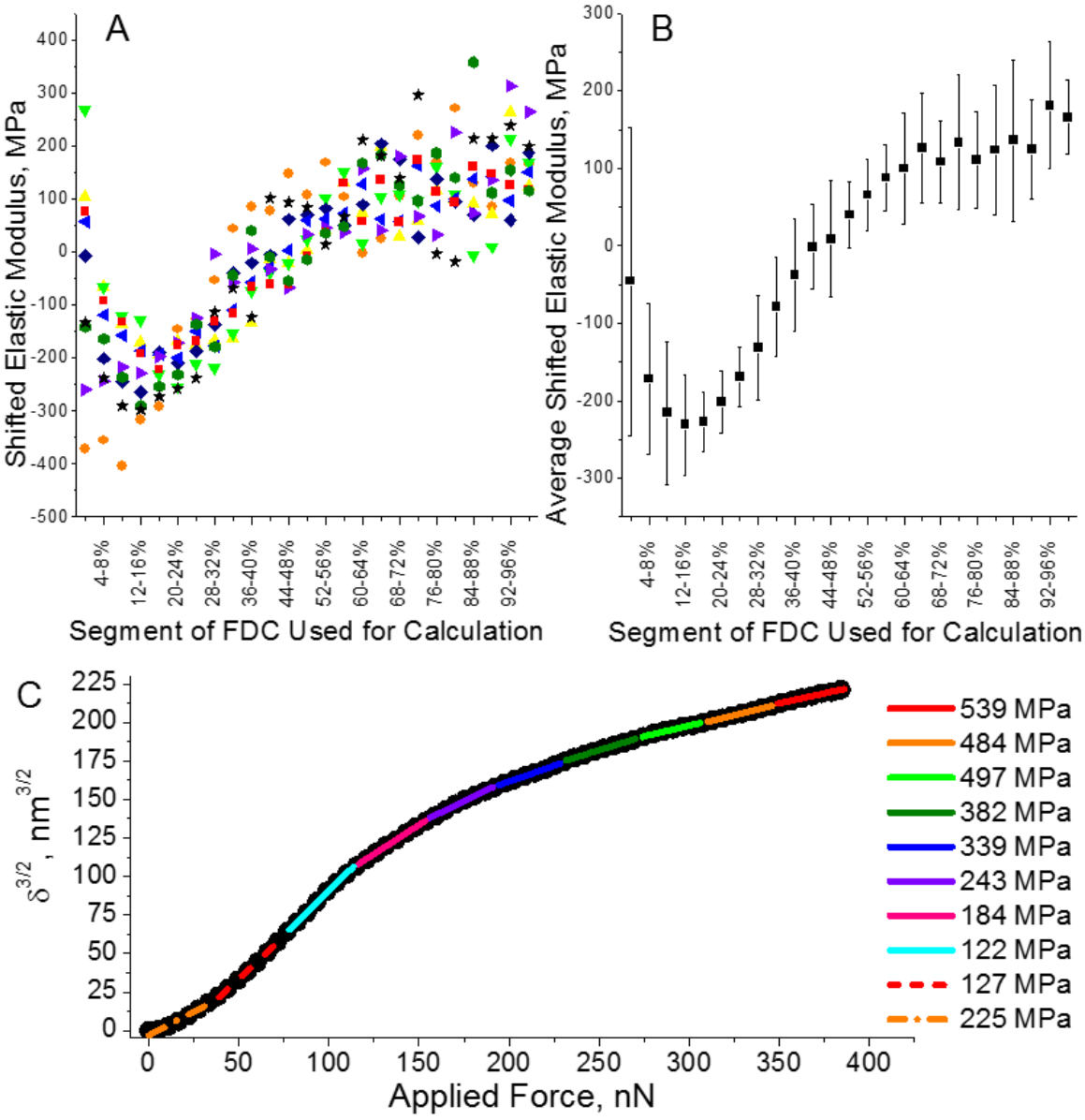

Figure 8.9: (A) Elastic modulus values calculated from different portions of 9 separate FDCs obtained with high (~400 nN) applied forces. Here each set of data represents a 4% interval of the total deflection. For example, when the total deflection is 50 nm, then each group of data represents the modulus calculated from 2 nm (~15 nN) segments of the FDC. (B) Average modulus values from all 9 curves, error bars represent one standard deviation. (C) Representative FDC formed from the average of all 9 deflection curves shown in Fig. 7C. Here each 10% interval was fit for modulus and overlaid on the plot to give the reader a sense of how the slope of the curve is changing with applied force (slope directly proportional to calculated elastic modulus). Legend indicates elastic modulus value calculated from each fit segments (color copy can be obtained online).

8.4.2.2 Membrane micromechanical properties using a large radius probe. We also explored the micromechanical properties of the outer membrane using a large radius probe.

In order to determine if such measurements could be taken without the AFM tip touching the sidewalls of the surrounding cuticle we overlaid SEM images onto sectional profiles taken from AFM height images (Fig. 8.10; scaled such that the scale bar from SEM images and axes from AFM images are equivalent). Here it is important to note that the sectional profiles should be taken from raw AFM topographical data (i.e. not flattened) to obtain a truer visualization of the tip-surface contact. From Fig. 8.10 it can be seen that probing is easily achievable with on the membrane with shallow contact angles and no contact with between the wider portions of the AFM tips and the sidewalls of the surrounding cuticle.

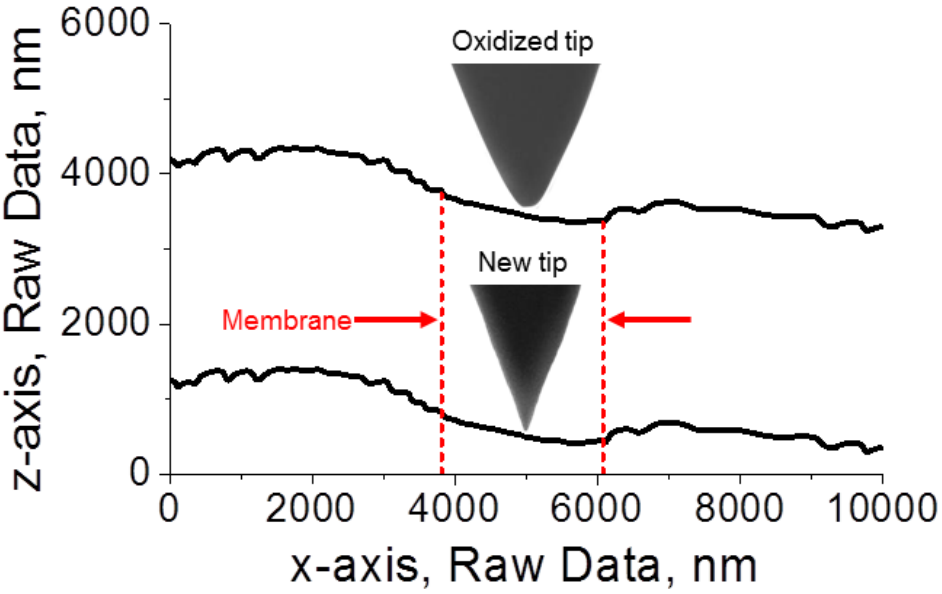

Figure 8.10: SEM images of a new AFM tip (lower part of graph) and an oxidized AFM tip (upper part of graph) superimposed on a line profile of unprocessed AFM height sensor data. Graph and SEM images have been sized such that the z-axis, x-axis, and SEM scale bars (cropped out) are all equal to give the reader an impression of the relative size of the slit-tip interaction. Here it can be seen that FDCs with indentation depths >100 nm can easily be performed on the slit membrane without the AFM tip contacting the slit walls (demarked in red dashed line and arrows).

Figure 8.11 shows randomly selected FDCs collected on slit 8 of the HS8 organ using a modified tip which had a radius of curvature of 408 nm. Analysis of many FDCs (>30) gives an average elastic modulus value of 1927 ± 592 MPa, an order of magnitude higher

than that obtained with a smaller radius tip. Examination of $\delta^{3/2}$ versus applied force (Fig. 8.11B) reveals very linear relationship without kinks or significant curvature in the early portions of the curves, indicative of elastic purely elastic behavior.

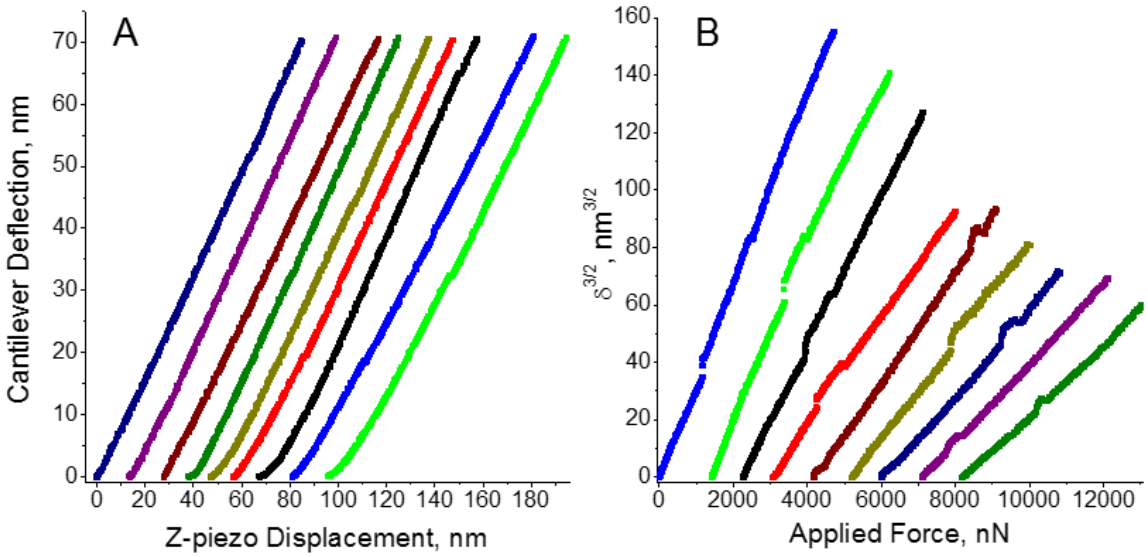

Figure 8.11: Example cantilever deflection versus displacement (A) and penetration depth versus force (B) plots obtained from loading curves taken on an HS8 lyriform organ using a modified tip with a radius of curvature of 408 nm. Similar to Fig. 8, these curves have been horizontally translated for better viewing.

The modulus of several curves were also calculated as a function of penetration depth (Fig. 8.12; same procedure as that discussed above for Fig. 8.9). In this case there is no clear trend in behavior, with average-shifted portions (Fig. 8.12B) all having very similar values, well within one standard deviation of each other. Creating an average FDC using the curves presented in Fig. 8.11A also results in a very linear FDC (Fig. 8.12C), without a clearly viscoelastic portion in the initial penetration region. With the exception of the first fitting region, all values of modulus calculated from this curve range from ~1700 MPa to ~1900 MPa.

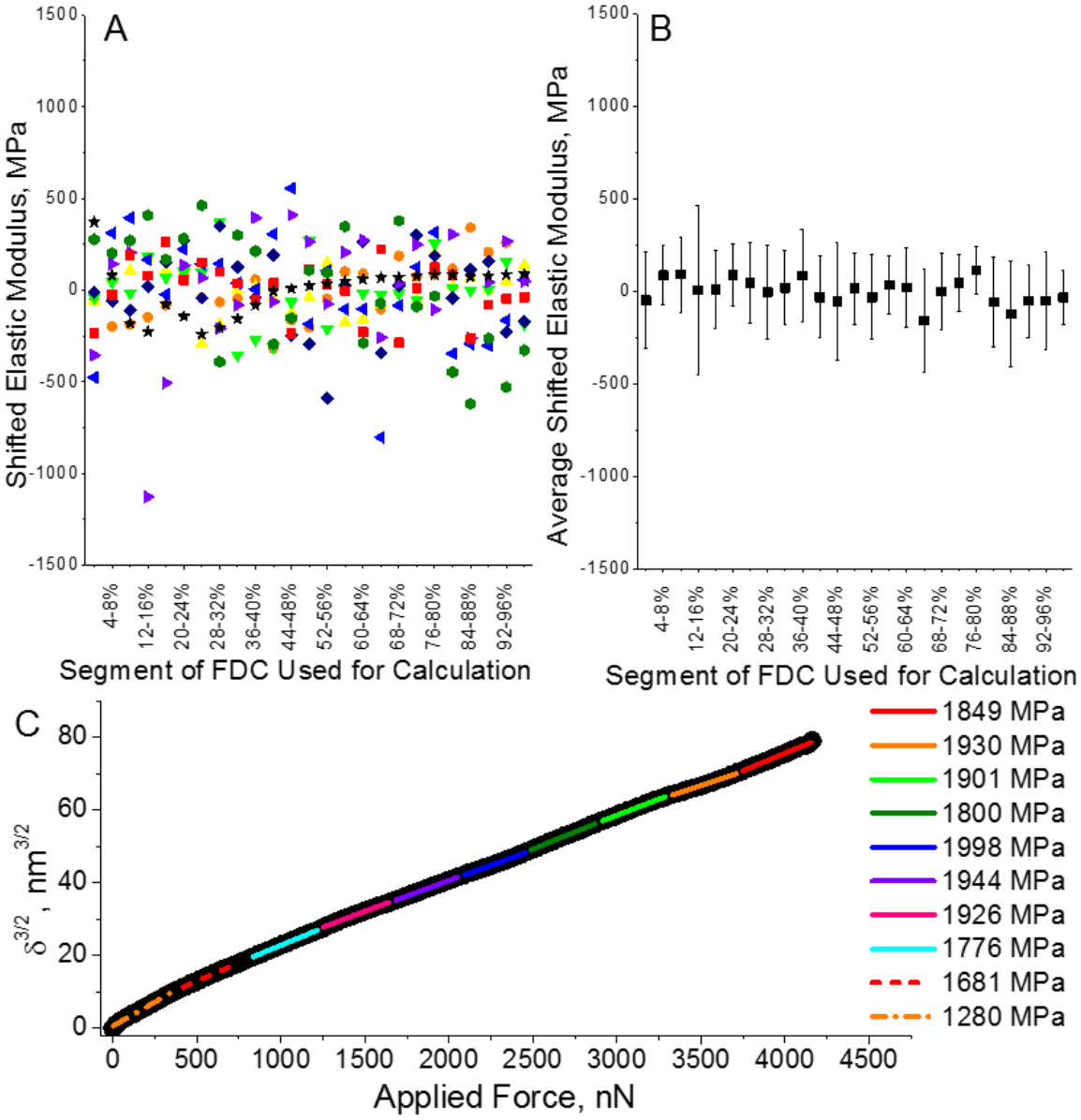

Figure 8.12: (A) Elastic modulus values calculated from different portions of 9 separate FDCs obtained with a modified AFM tip (408 nm radius of curvature). Here each set of data represents a 4% interval of the total deflection. (B) Average modulus values from all 9 curves, error bars represent one standard deviation. (C) Representative FDC formed from the average of all 9 deflection curves shown in Fig. 11A, with calculated modulus values from 10% interval regions (color copy can be obtained online).

8.5 Discussion

8.5.1 Outer membrane multi-layer structure. The outermost layer of arthropod cuticle, the epicuticle, is a very thin structure and serves as a protective barrier between the procuticle and the environment, for example by providing wear resistance and preventing

dessication.[292,293] The epicuticle is typically very thin and difficult to isolate from the procuticle, and as a result the mechanical properties of this layer are very rarely investigated.[292] Despite the epicuticle not being studied in-depth very frequently, it is known that it is a layered structure which includes cement, oriented lipid, and cuticulin layers.[84,129,291] The results we have presented here very much point to the layered nature of the epicuticle, with a few discernable layers (or regions of varying mechanical properties) observable in Fig. 8.7, Fig. 8.9 and Fig. 8.12. We see from using a very soft cantilever (spring constant ~0.2-0.4 N/m; Fig. 8.7, Table 8.1) with low indentation depths (~5 nm) a very compliant surface with a modulus of 125 MPa. As the indentation depth increases to 40 nm (Fig. 8.9), which corresponds to probing deeper into the subsurface, there is a clear increase in the apparent elastic modulus to ~500 MPa.

During nano-indentation experiments, given a constant penetration depth, the stress field directly beneath the probe increases with increasing tip radius. Therefore probing with a large radius tip such as that shown in Fig. 8.10 or Fig. 8.3B inset, results in interaction with materials much further into the sub-surface than can be achieved with a sharp probe. Here we obtain modulus values much higher than recorded in other measurements by using a large probe. What makes this an interesting result is that the outer membrane layer that spans the slit sensillum is very thin, on the order of ~200 nm thickness. It is unlikely that the viscous receptor lymph below the outer membrane is causing such a dramatic increase in modulus. However, electron micrographs (see Fig. 8.10 in ref. [115]) show random, residual nanoribbon-like structures which span the slit below the outer membrane. There also appears to be thin layer of greater electron density at the very bottom of the outer membrane. The tensile modulus of single chitin fibrils is estimated to be extraordinarily high (10s to 100s of GPa).[134,135] Our results here suggest that there is in fact a thin layer of chitin fibrillar structure or some other cross-linked protein that serves as a supporting layer of the outer membrane during the formation of the slit sensors, and perhaps the

observable nanoribbon structures are left over from the formation of the slit. A thin layer of stiff fibrils suggested here would not necessarily heavily affect the properties of the slit sensor because such fibrils are not resistant to deflections perpendicular to their long axis resulting from buckling under compressive loading (i.e. their high strength only applies to tensile loading).

We propose that the high modulus results we have calculated using larger penetration depths and large radius probes, are occurring as the stress field begins to interact with this fibril layer. For example in Fig. 8.9 as the indentation depth increases, we observe a modulus of ~500 MPa. However, the larger probe allows us to apply much larger forces without risking plastic deformation. Under large loads (~4 μN maximum load presented in Fig. 8.11), the deformational behavior of the tip-membrane contact interaction transitions from purely surface deformation to a combination of surface deformation with some tensile stretching of the membrane itself. We then are observing the dramatic increase in elastic modulus as a result of the large tensile modulus of cross-linked fibrils. While having a mechanically stiff layer to deposit epicuticle on during slit sensilla formation could be advantageous, there is no other apparent functions that this layer could serve. However the softer, viscoelastic upper layers could play a key functional role in the sensory output of slit sensilla.

8.5.2 Consequences of viscoelastic outer membrane layer. Mechanosensory organs in arthropods are known to have adaptive, time-dependent behavior.[294,295,296] The number of action potential impulses fired by the sensory organ as a function of time, $y(t)$, can be described by a simple power law:[84,99]

$$y(t) = a \cdot d \cdot t^{-k} \tag{8.6}$$

where a is an amplification constant, d is the stimulus amplitude, t is time, and k is a constant describing how quickly the receptor response declines under a constant stimulus. In the case of slit sensilla, as well as various mechanoreceptors across many species of arthropods, k ranges from 0, corresponding to a frequency-independent displacement detector, to 1, which is equivalent to a pure first-order velocity detector.[84,99] Recently we described the time- and temperature-dependent properties of the thick epicuticle layer on the metatarsal pad responsible for transferring mechanical stimuli to the HS10 lyriform organ, using the so-called creep compliance function.[26,123] The creep compliance function produces a sigmoidal curve which describes the mechanical response to a statically applied load in which the material transitions from the glassy regime (higher apparent elastic modulus) to the rubbery regime (lower apparent elastic modulus). According to this function, the apparent elastic modulus is proportional to $e^{-t/\tau}$, where t is time and τ is the relaxation time, which corresponds to the point of inflection on the sigmoidal curve. The relaxation time of a viscoelastic material is a function of its dynamic viscosity, and as a result is strongly dependent on the temperature. In our previous papers we observed materials relaxation times ranging from ~0.01 s at slightly elevated temperatures (35 °C) to ~5 s at lower temperatures (19 °C). Using our previously described fitting procedure,[26,123] we found that the initial viscoelastic portion of the curves shown in Fig. 8.8 exhibit average relaxation times of ~0.2-0.4 s, which is in good agreement with our previous calculations for the epicuticle measured at 22-24 °C (room temperature).

Inspection of HS8 electrophysiological response to loading reported in literature[99] reveals a sharp decrease in the impulse rate, $y(t)$, within the first few seconds of load application. To give the reader a sense of how the creep compliance function changes as a function of time, we have plotted $1 - e^{-t/\tau}$ versus time in Fig. 8.13 ("dimensionless creep compliance") for several τ, with the approximate temperature at which the epicuticle has that specific τ value also listed. It should be noted that the true creep compliance function

will scale differently along the y-axis, but the shape in the along the x-axis is preserved. From this one can see that the transition from higher modulus to lower modulus (upper limit) in response to a statically applied load occurs on the same order of time as the decrease in $y(t)$ for HS8 reported by Bohnenbuger,[99] As a result we suggest that the relaxation time is somehow related to the rate constant k. Furthermore, because τ varies with temperature, we also suggest that the time-dependent sensory response described by Eqn. 8.6 should also be dependent on measurement temperature, and may be better represented by including a temperature-dependent rate constant:

$$y(t,T) = a \cdot d \cdot t^{-k(T)} \tag{8.7}$$

For comparison we have also plotted t^{-k} versus time for several k, with each data set being normalized to 0.001^{-k}. The time required for a given percentage decrease in t^{-k} decreases as k decreases. On the other hand, the transitional time between upper and lower limits according to the creep compliance function decreases with decreasing τ. Perhaps then the rate constant k is inversely related to τ. It should be noted however, that this analysis is a bit over simplified in that it only considers the viscoelastic mechanical properties of the outer membrane. In reality several viscous components could also contribute to the time-dependent sensory adaptation of the HS8 organ, including the receptor lymph, dendrite, coupling cylinder, and dendritic sheath to name a few. Adding to this complexity are the signaling properties of the neuron itself.

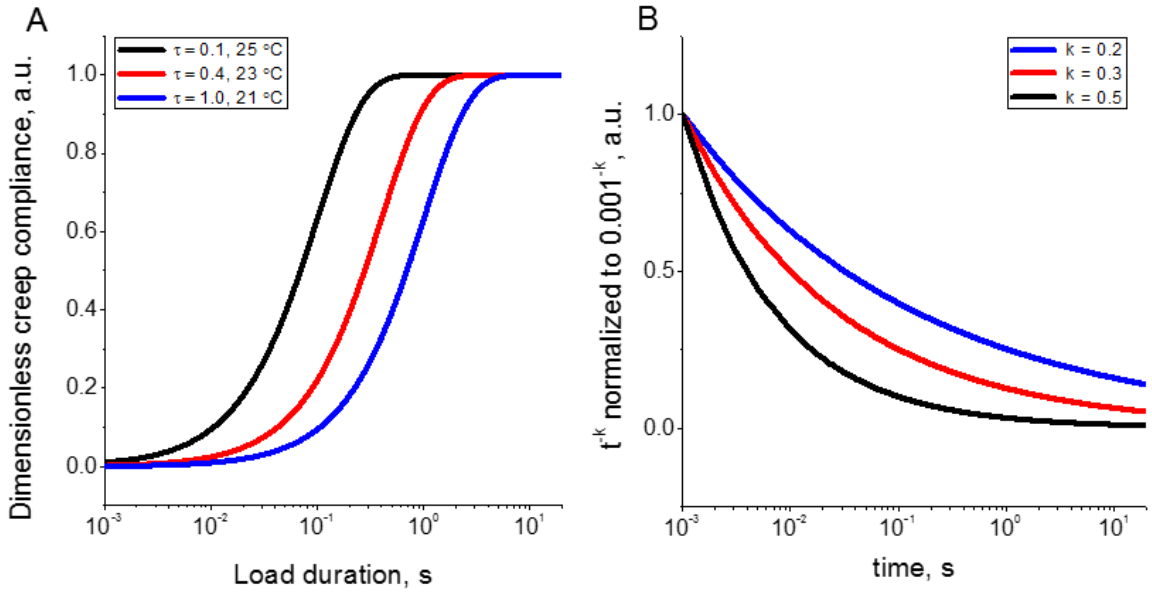

Figure 8.13: (A) "Dimensionless creep compliance function" (see text) for relaxation times of 0.1 s, 0.4 s, and 1.0 s. Approximate temperature in which the spider epicuticle would exhibit these relaxation times included in legend. (B) Plot of the exponential function $\boldsymbol{t^{-k}}$ for $\boldsymbol{k}$ = 0.2, 0.3, and 0.5 normalized to the maximum value of each set, which is $\boldsymbol{0.001^{-k}}$ in the range we have plotted here.

8.6 Conclusions

Here we have shown the direct characterization of the micromechanical properties of two strain-sensitive lyriform organs on the wandering spider, *Cupiennius salei*. Using AFM to perform nanoindenation curves we were able to quantify some differences in mechanical properties of the top-most surface layers of the cuticle surrounding the slits, the outer membrane, and the small exposed portion of the dendrite. A general trend was observed where the surrounding cuticle was only slightly stiffer than the outer membrane (but roughly equivalent), while the apparent elastic modulus of the dendrite was significantly lower than both the outer membrane and the surrounding cuticle. Furthermore, while the outer membrane of the HS10 organ is not readily accessible with the AFM probe, comparison between the surrounding cuticle of the HS8 and HS10 organs gave the same results. As a result, the fundamental materials properties we observe in the proprioceptive HS8 organ also apply for the vibration-sensitive HS10 organ.

Careful measurement of the tip-sample interactions at different indentation depths yielded mechanical properties of several different layers. At the shallowest depths we observed modulus values on the order of 100-200 MPa, which we have previously observed in the thick epicuticle of the metatarsal pad.[123] Increasing penetration depth resulted in calculated modulus values around 500 MPa. Finally, applying large forces with a blunted tip resulted in apparent modulus values on the order of 2 GPa. From this we proposed that a thin layer of chitin fibrils or some other cross-linked protein exists on the underside of the outer membrane.

We have also observed a viscoelastic response in the initial portions of the FDCs measured at moderate indentation depths. Because of the thin nature of the outer membrane and an underlying stiff layer which can convolute the force distance data, it is not clear if the viscoelastic layer is a discrete layer with a finite thickness or if there is a viscous component to each of the layers in the outer membrane. Nonetheless, simple analysis of just the viscoelastic portion of the penetration curves yielded calculated relaxation times on the order of 0.4 seconds, corresponding well to the careful time-temperature dependent measurements of the pad epicuticle made previously. These relaxation times are in the range of the time it takes to observe a drastic decrease in the rate at which impulses in the HS8 organ fire in response to a static load. Consequently we propose that the relaxation time that we are able to calculate via AFM-based nanoindentation experiments is somehow related to the rate constant used to describe sensory response to applied loads. However, the relaxation time of a material is strongly temperature-dependent. Therefore it is possible that the sensitivity of the organ as well as the functional response to certain stimuli also change with temperature, which could be significant as the spider would experience a moderate temperature decrease during the transition from day to night in its natural habitat.

CHAPTER 9

General conclusions and broader impact

9.1 General conclusions and discussion

The work presented throughout this dissertation focused on addressing two specific issues:

(1) Development of a practical, AFM-based surface force spectroscopy procedures and post-experimentation data processing routines to quantify nanoscale viscoelastic properties of soft polymeric and biological materials in terms of E_0, E_∞, E', E'', $\tan\delta$, and τ, under practical environmental conditions in a non-destructive manner.

(2) Testing this method to study such viscoelastic micromechanical properties for complex synthetic and biological materials in practical environments. Significant efforts were placed on quantification of time- and temperature-dependent mechanical properties of strain sensitive mechanosensory organs of live wandering spiders. These studies were conducted to gain a greater understanding of the fundamental materials properties of the sensing organ and how these properties can change the sensing properties of the organ as a function of temperature and stimuli frequency.

A detailed review of the currently available AFM-based techniques used to characterize viscoelastic mechanical properties revealed very few satisfactory methods which were readily available, simple (i.e. do not require cumbersome tip characterization or additional modeling experimentation to extract useful data), non-destructive, and quantitative while dealing with frequency and temperature ranges relevant to our studies. *Therefore we established experimental procedures and data analysis routines for quantitative characterization of viscoelastic properties of soft material surfaces using standard static force-distance data*. This procedure involved collection and analysis of multiple FDCs

with different applied forces at different loading rates as well as through a range of temperatures across glassy, leathery, and rubbery regimes, allowing for the calculation of a master curve which fully described the time-temperature-modulus relationship for viscoelastic material surfaces. These measurements were then analyzed using a combination of Johnson and Sneddon models for the quantitative analysis of indentation of a rigid axisymmetric indenter into a standard linearly viscoelastic solid. Our analysis allowed us to calculate several key viscoelastic mechanical parameters instantaneous modulus (E_0), infinite modulus (E_∞), storage modulus (E'), loss modulus (E''), the dissipation factor ($\tan\delta$), and characteristic relaxation time (τ).

Development of these experimental routines also included careful selection of appropriate measurement conditions, including selection of appropriate probes in order to accurately determine surface mechanics, environmental control procedures in order to minimize unnecessary artifacts such as capillary bridge formation or sample dehydration, and sample mounting procedures to ensure robust AFM measurements while scanning in fluid at varying temperatures with insignificant mechanical noise and reduced signal. In this regard, we illustrated using several example model materials the validity of our experimental and analysis routines.

First, we used a model viscoelastic polymer, PnBMA, which has a literature-reported glass transition temperature in the range from 25-35 °C. FDCs taken on the surface of a cast PnMBA film were measured through a wide range of temperature (10-55 °C) and loading rates (30-3000 nm/s), and analyzed according to the combination Johnson-Sneddon model. A large transition of elastic modulus values was reported within this temperature range, decreasing from ~1 GPa at the lowest temperatures/highest loading rates (i.e. the glassy state) down to ~30 MPa at the highest temperatures/lowest loading rates (i.e. the rubbery state).

Using these two limiting values and experimental conditions, we were able to determine the material relaxation times ranging from milliseconds to tens of seconds from penetration versus time curve fitting. *These three parameters could then be transformed into more commonly reported viscoelastic parameters, storage modulus, loss modulus, and tangent delta*. Comparison with literature-reported viscoelastic properties of PnBMA established through more traditional tensile and DMA techniques confirmed that our analysis routine produced quantitative values which corresponded well with those reported in the literature.

However, our analysis revealed that *in the vicinity of T_g elastic models under- and overestimate the modulus of the material significantly*. For example, at 40 °C (~10 °C higher than T_g) the modulus of the PnBMA surface considering only elastic behavior was 150 MPa, while the storage modulus was found to be only 50 MPa. These results highlight the critical impact that viscoelastic effects can have on the apparent mechanical properties of soft material surfaces. Such significant deviations in calculated elastic modulus *can have crucial downstream effects on the performance of nano- and microscale coatings, and can skew our understanding of fundamental mechanical properties of both synthetic and biological systems*.

Overall, the experimental methods and data analysis routines we demonstrate here are both practical and quantitative for a wide variety of material surfaces in varying environments and temperature ranges. However, our work here was conducted in a serial manner and both temperature and loading rates were changed manually. Thus, there can be much improvement on automation of these processes for better user experience and faster measurement times.

We also demonstrated the ability to measure complex, multiphase silicone-based contact lenses not only on their front curve surfaces, but also through a cross sectional area while submerged in a tear-like saline solution. Comparison of AFM-based mapping of mechanical properties with those reported in literature obtained via traditional methods revealed several key differences. First, traditional tensile testing methods can only probe the macro-scale bulk elastic properties. Because silicone is highly hydrophobic, all new generation lenses must undergo some surface treatment in order for lenses to remain comfortably on the patient's eye. Therefore we were able to map specifically the properties of these surface treatments, which bear much more significance on patient comfort, in contrast to measuring only the bulk hydrophobic silicone base. In addition to lack of component specificity, the traditional tensile testing procedures are highly dependent on measurement conditions which include sample damage during mounting as well biologically irrelevant strain modes and strain rates. *Our results indicate three times higher compressive modulus taken on the surface coatings of the lenses than manufacturer reported moduli obtain using tensile tests on bulk lenses*. We suggest that AFM-based measurements better represent deformational modes and loading rates experiences by the lens surface during patient use.

Integral to the survival of a living organism is the ability to interpret information about its surroundings in order to successfully capture prey and reproduce. Consequently, a rich diversity of biosensory systems can be found in nature which are highly tuned to specific stimuli. Spiders are known to possess a remarkably well developed mechanosensory systems, which are capable of detecting nanometer-scale strains. While these systems serve as model systems for engineered bio-inspired mechanosensors, much of the research to date has focused only on the nervous response of such sensing systems, with relatively little emphasis on the fundamental materials properties which contribute to sensor functionality and sensitivity.

Consequently, a major portion of this work was focused on *direct characterization of the* ***in-vivo*** *viscoelastic mechanical properties of slit sensory systems in wandering spiders* at a fundamental materials level in order to gain a deeper understanding of the interplay between structure, property, and overall functionality and sensitivity of these fascinating systems.

First, elaborate structural characterization of the metatarsal pad, which is responsible for transmitting vibrational stimuli from the substrate through the tarsus onto the vibration-sensitive metatarsal lyriform organ, revealed a myriad of chitin fibril packing densities and orientations, which result in a wide range of mechanical properties exhibited by the metatarsal pad/lyriform organ sensory system. Scanning acoustic microscopy mappings show significant changes in acoustic wave reflectivity, which corresponds to changes in a combination of mass density and material stiffness. The elastic modulus of several areas of the pad substructure, including the "appendix" structure, near the distal and dorsal surfaces, as well as near a largely unsclerotized region, were further investigated quantitatively using nanoindentation. These measurements yielded values of elastic modulus ranging from as much as 8 GPa on the appendix structure, down to 100 MPa neares the dorsal and distal surfaces. Furthermore, μCT imaging during tarsal deflection revealed several key functional aspects of the metatarsus pad structure and mechanical properties distributions that had not yet been realized.

Then, our newly developed AFM experimental methods and analysis routines were applied to the metatarsal pad of *Cupiennius*. ***Live adult female spiders*** were attached to the AFM chuck and used for measurement of FDCs through a biologically relevant temperature range (15-45 °C, in highly humid environment). From this, a full mapping of the time- and temperature-dependent mechanical properties were obtained, with limiting modulus values

of ~100 MPa and 20 MPa. The values established here however were obtained using triangular wave-form loading, which have no significant role in the natural occurring stimuli experienced by the wandering spider. Therefore transformation of our data to storage modulus, loss modulus, and tangent delta values, which correspond to sinusoidal loading, provided much a more biologically-relevant time-temperature-modulus relationship. Because the spider experiences a relatively constant temperature environment, we found it useful to explore the mechanical properties response to a range of frequencies for a specific temperature. As a result, it was seen that the peak of the loss modulus shifts with temperature, which could play a significant role in the sensory response of the spider in cooler, nighttime hours in which it is active, versus warmer daytime temperatures.

Finally, our studies focused on direct investigation of the micromechanical properties of the various accessible slit sensilla components including the slit walls, dendrite regions, and outer membrane. A general trend was observed in which the uppermost surface layers of the cuticle adjacent to the slit had an elastic modulus roughly equivalent to the surface of the outer membrane (~150-200 MPa). Measurements taken directly on the region of exposed dendrite yielded significantly lower values of elastic modulus of 60 MPa. By carefully probing the elastic modulus as a function of penetration depth, it was determined that the outer membrane was a layered structure with a softer, viscoelastic upper layer having a relaxation time of 0.4 sec. Probing to greater penetration depths revealed an increase in modulus to 500 MPa at the greatest depths using standard AFM tips. We also used annealed tips with large radius allowing for higher applied forces, which yielded modulus values on the order of 2 GPa. We suggest that this is the result of a residual layer of cross-linked proteins or residual fibrils.

It is unclear at this stage if this layer serves any functional role other than to maintain the mechanical integrity of the outer membrane during many the loading cycles experienced in the adult lifetime of the spider. Applying our data analysis routines, it was also found that the relaxation times of the upper viscoelastic layer were on the order of time in which the rate of impulse firing of the organ decrease dramatically. Because the relaxation time of a material is strongly dependent on measurement temperature, it was proposed that the functional sensitivity of the organ is finely tuned to lower temperatures that the spider would most like experience during nighttime activity.

9.2 Significance and broader impact

Viscoelastic behavior can strongly affect material performance, especially in operating environments near the glass transition temperature, where the apparent elastic modulus can easily span three orders of magnitude with only small changes in temperature. Measuring these properties using AFM-based methods often yields only qualitative data, damages the sample surface, or requires additional modeling and calibration procedures. *In this dissertation we lay out practical methodology for quantitatively measuring the viscoelastic mechanical properties of soft material surfaces in a non-damaging manner and in relevant environments and temperature ranges*. In fact, the method that we use comes as a standard package with all commercially available AFM systems, and only a simple Peltier stage was needed for heating/cooling. We found through this study that while far away from the glass transition temperature ($T_g \pm$ ~15 °C) a simple elastic model can be reasonably assumed. However, *we show that neglecting viscoelastic effects results in the under/overestimation of elastic modulus by greater than 50%.*

For example, at the frequency/temperature corresponding to the loss modulus peak, the calculated modulus of the PnBMA surface was ~150 MPa when considering the material as a simple elastic solid, while the storage modulus was determined to be ~50 MPa when

considering the material as a linearly viscoelastic solid. In this region the energy dissipation from viscous contributions is maximum, and emphasizes the need for careful measurement and a refined data analysis approach when measuring such materials. Ultimately this method is easily repeatable and applicable to a wide variety of interesting materials. *Furthermore, through the efforts of these studies a custom-built software (MMA-SPM) was created and licensed for analysis of force-distance curves.* This software enables elastic modulus calculations for a variety of tip geometries, adhesive behavior, and includes viscoelastic and tip radius of curvature modeling functionalities. *Micromechanical Analysis of Soft Polymeric Materials (MMA-SPM)* will be made available for academic as well as industry use upon request at the conclusion of licensing.

Within the context of understanding the fundamental materials properties that contribute to mechanosensing in the slit sensilla of the spider, the structural function of the metatarsal pad had not previously been documented or described in the literature. An interesting facet of this pad is its wide variety of mechanical properties which contribute heavily to its multi-functionality, as well as to the successful transmission of relevant vibrational stimuli to metatarsal lyriform organ as a whole. Mechanically stiff, highly sclerotized material was seen closest to the lyriform organ and as such serves as the final stage of transfer of stresses onto the lyriform organ. An area in the distal region of the pad remains largely unsclerotized, and comparison of hydrated versus dehydrated samples showed that this region experiences dramatic changes in volume, suggesting a large water content.

The location of this region is interesting in that it was found that during tarsal deflection the distal portion of the pad (i.e. the tarsus/metatarsus contact point) was easily deformed up to 30-50 μm. However, as a result of this deformation the slits themselves were only deformed by a distance on the order of 30-50 nm, a decrease of 3 orders of magnitude. Furthermore, a uniquely-shaped substructure ensured that the all slit deformations occurred

with the slit walls remaining exactly parallel, while the overall shape of the pad allows for slit compression through a wide range of tarsal loading angles. These together are key for the spider to successfully receive mechanical stimuli in a wide variety of environments. In fact, the spider is typically found in a vertical position with its cephalothorax facing downwards, resulting in a preloading of the metatarsal pad from some angle.

Our AFM investigation of the pad and lyriform organ highlighted the role that viscoelastic mechanical properties can play in these mechanosensory systems. Specifically, while some reports of the viscoelastic nature of these organs were found in the literature, discussion was limited only to changes in properties with respect to varying frequencies. For the first time we directly record measurements from the spider cuticle while varying temperature. This is vitally important in understanding slit sensory function as the spider not only experiences a range of vibrational frequencies, but it also experiences stimuli over the course of an entire day, in which the temperature can easily drop 10-15 °C. Our studies on the thick epicuticle covering the pad revealed a strongly temperature-dependent relaxation time, which were found to increase exponentially with decreases in temperature. At elevated temperatures the relaxation time was on the order of 10 msec (30 °C), while at lower temperatures the relaxation times surpassed 5 sec (15 °C).

We demonstrated that the relaxation time of the material is directly related to the frequency at which the loss modulus is at a maximum. As a result this peak frequency was investigated as a function of temperature. It was seen that with decreasing temperatures, the frequency corresponding to the loss modulus peak also decreased (e.g. ~30 Hz at 24 °C, down to ~1 Hz at 19 °C). By comparing with electrophysiological measurements taken at room temperature, we can see that this peak in loss modulus also corresponds well with the threshold for decreasing sensitivity (i.e. larger deflections were required to elicit an action potential for loading frequencies less than the threshold). Consequently, we can say that

the threshold frequency for decreasing sensitivity in the metatarsal lyriform organ decreases with temperature. In other words, the organ as a whole becomes more sensitive to vibrational stimuli with a wider range of frequencies. The temperature-dependence of the threshold frequency suggests that the nocturnal behavior of the spider may not be only a result of cooler temperatures reducing the amount of desiccation of fluids from the spider, but also because at the materials level, the spider is more sensitive to relevant vibrational stimuli than during the cooler nighttime temperatures.

The outer membrane, which directly transmits strains in the exoskeleton of the spider onto the dendrite, also exhibited distinctly viscoelastic behavior. It is known that these organs display adaptation to sustained loading, in which the rate of action potential impulses decreases exponentially. Interestingly, the relaxation time we calculated from our measurements are on the same order of time as the region of the most dramatic decrease in the impulse rate. Therefore we also suspect that these organs functional sensitivity are also changing as the viscoelastic response of the outer membrane changes with temperature. Ultimately the changing mechanical response with temperature is a well-known phenomenon, however it is not frequently discussed in sensory biology in the context of mechanosensing systems (certainly it is considered for thermal sensing), as measurements concerning the electrophysiological response to various strains are conducted at room temperature.

In conclusion, we have shown via direct experimentation, under relevant environmental conditions and at relevant temperatures, how the changes in mechanical behavior with temperature and loading rate can play a role in the behavior and sensing abilities of the spider. Furthermore we have reported on some of the fundamental biomechanical and structural features that contribute to the sensitivity and functionality of these fascinating slit sensory systems. In the grand scheme we believe that this work can serve as a

fundamental basis for the design of functional, tunable, and embeddable strain sensing devices. Such devices could easily find applications in the realm of flexible sensory electronics, for instance strain sensors embedded in a flexible display which detect the strain direction and amplitude could be used to compensate the image during flexion. Or another example could be functional strain sensors embedded into implantable medical devices in order to monitor stress-strain behavior in the device in order to understand failure modes and reduce failure rates.

The broader impact of the highly interdisciplinary work presented in this dissertation should not be understated. Such work often requires each discipline to learn a new set of principles as well as essentially a completely new language. As a result, each discipline also gets the chance to unlock a new "engineering toolbox" with different problem solving skills and ways of thinking than they previously had, which can be directly applicable to future endeavors, making for more well-rounded scientists and engineers with a greater appreciation for the work of their peers with different technical backgrounds.

As such, the dissemination of this work has brought together materials scientists, biologists and neurobiologists, as well as theoretical physicist working on AFM-based techniques, to name a few, who otherwise would have never been exposed nor interested in the area of mechanosensory systems in biology. The goal of interdisciplinary research is often to combine fundamental principles from various technical backgrounds to solve complex, multifaceted problems. Therefore we suggest that the work presented in this dissertation serves as an example of this process in work, and can ultimately serve as a basis for future generations to expand their knowledge base and background by participating in such cross-disciplinary work.

Indeed, the fundamental research presented within this dissertation can be a starting point for further, expansive interdisciplinary research projects. For example, while practical for quantitative analysis of viscoelastic mechanical properties, like most AFM-based techniques the experimental methods described above are still very time consuming. In this case, a major time commitment is spent by the user adjust sample temperatures, loading rates, as well as sampling position. To help remedy this, electrical and software engineers at instrumentation manufacturers could work towards a fully automated process in which a range of temperatures, loading rates, intervals, and X-Y step-sizes are input by a user, and then all FDCs are collected without further interaction. Such automation will not only decrease total data collection time, but also free up users to complete other duties while the measurement is ongoing.

As mentioned, a constant battle in scanning probe microscopy techniques is reduction in time consumption, where mapping one sample could take many hours, resulting in relatively low throughput and compromised resolution due to piezoelement creep. Current efforts in the industry are indeed focused on addressing this problem, with new state of the art AFM configurations having the ability to record a topographical image on the order of seconds already commercially available (e.g. Bruker FastScan). The next logical step in this development then will be to combine such fast topographical imaging with accurate mechanical properties characterization. In this regard, it would appear that the pulsed-force imaging mode is currently being underutilized as a means to characterize the viscoelastic mechanical properties of soft materials surfaces. Currently, to give real-time mechanical properties using this scanning mode, the scanning software uses *only two points* from all of the loading data to create a line from which to calculate the elastic modulus. By using only two points, valuable information which contains easily extractible tangent delta as well penetration depth as a function of time is completely lost. It is almost inevitable that computer processor speeds will continue to increase in the coming years,

which would certainly help in collecting and using all this data in real-time, which is currently impossible. Therefore, there needs to be a strong emphasis placed on the calculation algorithms used in this particular mode, in order to streamline the calculation times and open up the possibility of using more data for fitting FDCs in real time, which is subsequently deleted after the two points are selected.

To further expand our fundamental knowledge of the slit sensory systems in *Cupiennius salei*, experiments elucidating the geometrical changes in the outer membrane under applied loads should be undertaken. Here we have only studied the viscoelastic mechanical properties of this particular facet of the spider cuticle. While these properties will play a role in the bending modulus of the membrane, its complex layered structure and viscoelastic behavior could have unforeseen effects on how the membrane, which ultimately deforms the sensory dendrite, behaves under compressional loading. Therefore careful experiments with live spiders should be arranged such that the geometry of the membrane can be monitored via AFM topographical imaging while the spider leg is deflected in an appropriate manner. Measurements such as these would aid in our understanding of the mechanisms which elicit action potentials in the slit sensilla, but would require the development of specialized equipment which can simultaneously be used to deflect specific legs in certain directions while keeping the spider stable enough to be measured using extremely sensitive AFM equipment.

Furthermore, as discussed in Chapter 8 of this dissertation, while many experimental electrophysiological studies have been executed to study the sensory response to sustained loading in arthropod mechanical sensors, there has been markedly fewer experiments which address their behavior as a function of temperature. An interesting direction that these experiments could follow is a refinement of the simple power law describing sensory response to the application of a load (Eqn. 8.1). Such an endeavor would require significant

cross-collaboration between biologists, neurobiologists, and materials scientists. Complete time-temperature-modulus relationships could be built via our AFM-based experimental procedures and data analysis routines, while intricate electrophysiological testing could give a full time-temperature-impulse rate relationship.

Knowledge of (i) the fundamental time- and temperature-dependent viscoelastic mechanical properties of these mechanosensing organs, and specifically the outer membranes, (ii) bending behavior of the suspended outer membrane under compressional loading, and (iii) a more refined analysis of the rate of action potential impulses firing as a function of both time and temperature would then lead to the advancement of modeling experimentation which could be performed to study slit sensilla. Prior work has only considered crack compression under loading, and has considered the material as a homogeneous elastic solid. What we have discovered in this dissertation is that the modulus of the upper layers of the epicuticle and thus the outer membrane are completely different from the bulk, intact spider leg. New modeling experiments can be arranged to study the bending of a suspended, viscoelastic membrane to paint a broader picture of how the membrane deflects as a respond to compressional loading. This could potentially lead to the consideration of specific design features of the membrane itself. For instance, as discussed in Chapter 6, the large "appendix" structure underneath the vibration-sensitive HS10 organ ensured that all slits compressed in a specific manner. By using the structure and materials properties discussed in this dissertation a complete FE model of a strain sensing lyriform organ can be built, and this exercise can uncover some design features that have yet to be realized contributing to the sensitivity and functionality of the organ under dynamic loading at relevant temperatures.

Finally, many interesting design features of mechanosensory systems were learned from our work on the spider lyriform organs. However, specific to future materials scientist is

the role viscoelasticity has in strain sensing. The viscoelastic mechanical properties of synthetic polymers can easily be tuned, for example by changing side group chemistry, bulkiness, or length. This suggest that in future attempts to prototype imbeddable strain sensing devices mimicking the lyriform organs of wandering spider, specific filtering behavior can be imparted in the device by selection/synthesis of the appropriate polymeric material. In a broader sense, our studies on the spider mechanosensing organs demonstrate passive filtering achieved through viscoelastic materials properties. Rather than using sophisticated signal processing equipment, perhaps new materials scientists will take note of the sensitivity, functionality, and tunability that can be applied to a strain sensing device at a fundamental materials level, as exemplified by the strain sensing lyriform organs of a wandering spider.

Acknowledgements

Financial support from National Science Foundation, Division of Materials Research DMR-1002810 and Materials World Network Award DMR-1209332. We are grateful to the Department for Neurobiology of the University of Vienna for providing the spiders.

Dissemination of work

This work has been conveyed to the scientific community by the following publications and presentations.

Publications

1. **Young, S.L.**, Chyasnavichyus, M., Barth, F.G., Zlotnikov, I., Politi, Y., Tsukruk, V.V. Micromechanical properties of strain-sensing lyriform organs of a wandering spider (Cupiennius salei). *Acta Biomaterialia*, **2015**, Submitted

2. Chyasnavichyus, M., **Young, S.L.**, Geryak, R., Tsukruk, V.V. Measurements of elastic properties of soft materials with AFM: Exploring data analysis routines for several tip geometries. *Polymer*, **2015**, submitted.

3. Erko, M., Younus-Metzler, O.,Rack, A., Zaslansky, P., **Young, S.L.**, Milliron, G., Chyasnavichyus, M., Barth, F.G., Fratzl, P., Tsukruk, V.V., Zlotnikov, I., Politi, Y. Micro- and nanostructured details of the spider's mechanical vibration filter. Relevance for low frequency signal transmission. *Journal of the Royal Society Interface*, **2015**, *12* (104), 2014111.

4. Chyasnavichyus, M., **Young, S.L.**, Tsukruk, V.V. Recent advances in micromechanical characterization of polymer, biomaterial, and cell surfaces with atomic force microscopy. *Japanese Journal of Applied Physics*, **2015**, *54* (8 S2), 08LA02.

5. **Young, S.L.**, Chyasnavichyus, M., Erko, M., Barth, F.G., Fratzl, P., Zlotnikov, I., Politi, Y., Tsukruk, V.V. A spider's biological vibration filter: Micromechanical characteristics of a biomaterial surface. *Acta Biomaterialia*, **2014**, *10* (11), 4832-4842.

6. Chyasnavichyus, M., **Young, S.L.**, Tsukruk, V.V. Mapping micromechanical properties of soft contact lenses. *Polymer*, **2014**, *55* (23), 6091-6101.

7. Chyasnavichyus, M., **Young, S.L.**, Tsukruk, V.V. Probing of polymer surfaces in the viscoelastic regime. *Langmuir*, **2014**, *30* (35), 10566-10582. (Feature article, cover below).

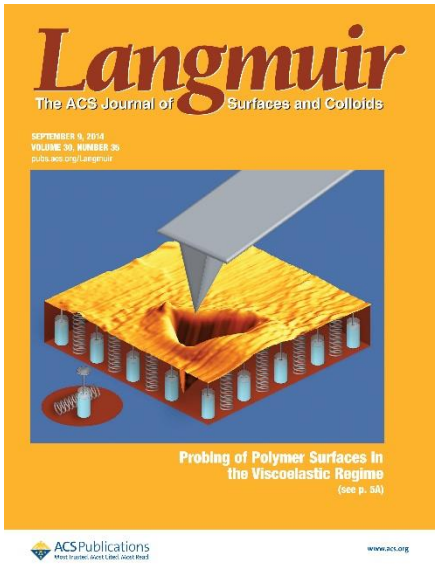

8. **Young, S.L.**, Gupta, M., Hanske, C., Fery, A., Scheibel, T., Tsukruk, V.V. Utilizing conformational changes for patterning thin films of recombinant spider silk proteins. *Biomacromolecules*, **2012**, *13* (10), 3189-3199.

The following publications are also related to the work in this dissertation:

9. Anderson, K.D., **Young, S.L.**, Jiang, H., Jakubiak, R., Bunning, T.J., Naik, R.R., Tsukruk, V.V. Plasma enhanced co-polymerization of amino acid and synthetic monomers. *Langmuir*, **2012**, *28* (3), 1833-1845.

10. Singamaneni, S., Bertoldi, K., Chang, S., Jang, J.-H., **Young, S.L.**, Thomas, E.L., Boyce, M.C., Tsukruk, V.V. Bifurcated mechanical behavior of deformed periodic porous solids. *Advanced Functional Materials*, **2009**, *19* (9), 1426-1436.

Presentations

1. Chyasnavichyus, M., **Young, S.L.**, Tsukruk, V.V. Mapping micromechanical properties of soft contact lenses. 2015 Fall ACS National Meeting, Boston, MA (Oral presentation)

2. **Young, S.L.**, et al.. A spider's biological vibration filter: Micromechanical characteristics of a biomaterial surface. 2014 SPM-on-SPM Conference, Toronto, Canada (Oral presentation)

3. Chyasnavichyus, M., **Young, S.L.**, Tsukruk, V.V. Mapping micromechanical properties of soft contact lenses. 2014 SPM-on-SPM Conference, Toronto, Canada (Poster presentation)

4. Chyasnavichyus, M., **Young, S.L.**, Tsukruk, V.V. Probing of polymer surfaces in the viscoelastic regime. 2014 SPM-on-SPM Conference, Toronto, Canada (Poster presentation)

5. **Young, S.L.**, et al. A spider's biological vibration filter: Micromechanical characterization (Cupiennius salei). 2014 Annual MSE at GT Graduate Poster Competition (Oral presentation)

6. **Young, S.L.**, et al. A spider's biological vibration filter: Micromechanical characterization (Cupiennius salei). 2013 MRS Fall meeting (Oral presentation)

7. **Young, S.L.**, et al. Using AFM to study the micromechanical properties of biological materials. 2013 MRS Fall meeting (Poster Presentation)

8. **Young, S.L.**, Previous relevant work and Tsukruk lab instrumentation capabilities. 2012 Meeting and NSF Project Kick-Off, MPIKG, Golm, Germany (Oral Presentation)

9. **Young, S.L.**, et al. Utilizing conformational changes for patterning thin films of recombinant spider silk proteins. 2012 SPM on-SPM Conference, Kerkrade, Netherlands (Oral Presentation)

References

1 Chyasnavichyus, M., Young, S.L., Tsukruk, V.V. Recent advances in micromechanical characterization of polymer, biomaterial, and cell surfaces with atomic force microscopy. *Japanese Journal of Applied Physics* **2015,** *54* (8S2), 08LA02

2 Müller, D.J., Dufrêne, Y.F. Atomic force microscopy: a nanoscopic window on the cell surface. *Trends in Cell Biology* **2011,** *21* (8), 461-469.

3 Iwamoto, S., Kai, W., Isogai, A., Iwata, T. Elastic Modulus of Single Cellulose Microfibrils from Tunicate Measured by Atomic Force Microscopy. *Biomacromolecules* **2009,** *10* (9), 2571-2576.

4 Young, T.J., Monclus, M.A., Burnett, T.L., Broughton, W.R., Ogin, S.L., Smith, P.A. The use of the PeakForce TM quantitative nanomechanical mapping AFM-based method for high-resolution Young's modulus measurement of polymers. *Measurement Science and Technology* **2011,** *22* (12), 125703.

5 Sperling LH. Introduction to Physical Polymer Science. 4th ed. Wiley: Hoboken, N.J.; 2006

6 Roylance, D. Engineering Viscoelasticity, October 2001. [online resource, accessed November 11, 2013]: <http://web.mit.edu/course/3/3.11/www/modules/visco.pdf>

7 Williams, M.L., Landel, R.F., Ferry, J.D. The temperature dependence of relaxation mechanisms in amorphous polymers and other glass-forming liquids. *Journal of the American Chemical Society*, **1955**, *77* (14), 3701-3707.

8 Hertzberg. R.W. Deformation and Fracture Mechanics of Engineering Materials. Wiley: Hoboken, N.J.; 1996

9 Schaffer, J.P., Saxena, A., Antolovich, S.D., Sanders, T.H., Warner, S.B. The Science and Design of Engineering Materials. McGraw Hill: Boston, Ma; 1999.

10 Stafford, C.M., Harrison, C., Beers, K.L., Karim, A., Amis, E.J., VanLandingham, M.R., Kim, H.-C., Volksen, W., Miller, R.D. and Simonyi, E.E. A buckling-based metrology for measuring the elastic moduli of polymeric thin films. *Nat Mater*, **2004**, *3* (8), 545-550.

11 Singamaneni, S. and Tsukruk, V.V. Buckling instabilities in periodic composite polymeric materials. *Soft Matter*, **2010**, *6* (22), 5681-5692.

12 Markutsya, S., Jiang, C., Pikus, Y. and Tsukruk, V.V. Freely Suspended Layer-by-Layer Nanomembranes: Testing Micromechanical Properties. *Advanced Functional Materials*, **2005**, *15* (5), 771-780.

13 Yin, Y., Hu, K., Grant, A.M., Zhang, Y. and Tsukruk, V.V. Biopolymeric Nanocomposites with Enhanced Interphases. *Langmuir*, **2015**, *31* (39), 10859-10870.

14 Kulkarni, D.D., Choi, I., Singamaneni, S.S. and Tsukruk, V.V. Graphene Oxide–Polyelectrolyte Nanomembranes. *ACS Nano*, **2010**, *4* (8), 4667-4676.

15 Fischer-Cripps, A.C. Critical review of analysis and interpretation of nanoindentation test data. *Surface and Coatings Technology*, **2006**, *200* (14–15), 4153-4165..

16 Tabor, D. *The hardness of metals*; Clarendon Press: Oxford, 1951.

17 Balasundaram, K., Raabe, D., Cao, Y. Identifying the limitation of Oliver and Pharr method in characterizing the viscoelasticplastic materials with respect to indenter geometry. *Mater. Res. Soc. Symp. Proc.* **2008,** 1137, 49-54.

18 VanLandingham, M.R., Chang, N.K., Drzal, P.L., White, C.C. and Chang, S.H. Viscoelastic characterization of polymers using instrumented indentation. I. Quasi-static testing*. *Journal of Polymer Science Part B: Polymer Physics*, **2005**, *43* (14), 1794-1811.

19 V. V. Tsukruk and S. Singamaneni, *Scanning Probe Microscopy of Soft Matter: Fundamentals and Practices* (Wiley, Weinheim, 2012) Chapter 2.

20 S. Magonov, J. Alexander, and S. Belikov, in *Nanoscale Applications for Information and Energy Systems*, ed. A. Korkin and D. J. Lockwood (Springer, New York, 2013) Chapter 7

21 T. Fukuma and M. J. Higgins, in *Atomic Force Microscopy in Liquid*, ed. A. M. Baró and R. G. Reifenberger (Wiley, Weinheim, 2012) Chapter 4

22 Ganser, C., Hirn, U., Rohm, S., Schennach, R. and Teichert, C. AFM nanoindentation of pulp fibers and thin cellulose films at varying relative humidity. *Holzforschung*, **2014**, *68* (1), 53-60.

23 Jimenez-Palomar, I., Shipov, A., Shahar, R. and Barber, A.H. Influence of SEM vacuum on bone micromechanics using in situ AFM. *Journal of the Mechanical Behavior of Biomedical Materials*, **2012**, *5* (1), 149-155.

24 Fischer, H., Stadler, H. and Erina, N. Quantitative temperature-depending mapping of mechanical properties of bitumen at the nanoscale using the AFM operated with PeakForce TappingTM mode. *Journal of Microscopy*, **2013**, *250* (3), 210-217.

25 Dufrene, Y.F., Martinez-Martin, D., Medalsy, I., Alsteens, D. and Muller, D.J. Multiparametric imaging of biological systems by force-distance curve-based AFM. *Nat Meth*, **2013**, *10* (9), 847-854.

26 Chyasnavichyus, M., Young, S.L. and Tsukruk, V.V. Probing of Polymer Surfaces in the Viscoelastic Regime. *Langmuir*, **2014**, *30* (35), 10566-10582.

27 Meyer, E., Heinzelmann, H., Grütter, P., Jung, T., Weisskopf, T., Hidber, H.R., Lapka, R., Rudin, H. and Güntherodt, H.J. Comparative study of lithium fluoride and graphite by atomic force microscopy (AFM). *Journal of Microscopy*, **1988**, *152* (1), 269-280.

28 Sneddon, I.N. The relation between load and penetration in the axisymmetric boussinesq problem for a punch of arbitrary profile. *International Journal of Engineering Science*, **1965**, *3* (1), 47-57.

29 Cappella, B. and Dietler, G. Force-distance curves by atomic force microscopy. *Surface Science Reports*, **1999**, *34* (1–3), 1-104.

30 Butt, H.-J., Cappella, B. and Kappl, M. Force measurements with the atomic force microscope: Technique, interpretation and applications. *Surface Science Reports*, **2005**, *59* (1–6), 1-152.

31 McConney, M.E., Singamaneni, S. and Tsukruk, V.V. Probing Soft Matter with the Atomic Force Microscopies: Imaging and Force Spectroscopy. *Polymer Reviews*, **2010**, *50* (3), 235-286.

32 Kovalev, A., Shulha, H., Lemieux, M., Myshkin, N. and Tsukruk, V.V. Nanomechanical probing of layered nanoscale polymer films with atomic force microscopy. *Journal of Materials Research*, **2004**, *19* (3), 716-728.

33 Tranchida, D., Pihan, S.A., Zhang, Y., Schönherr, H. and Berger, R. Nanomechanical Properties of Advanced Plasma Polymerized Coatings for Mechanical Data Storage. *The Journal of Physical Chemistry B*, **2011**, *115* (13), 3385-3391.

34 Silbernagl, D. and Cappella, B. Mechanical Properties of Thin Polymer Films on Stiff Substrates. *Scanning*, **2010**, *32* (5), 282-293.

35 Zhao, J., Chen, M., An, Y., Liu, J. and Yan, F. Preparation of polystyrene brush film by radical chain-transfer polymerization and micromechanical properties. *Applied Surface Science*, **2008**, *255* (5, Part 1), 2295-2302.

36 Liu, J., Yu, B., Ma, B., Song, X., Cao, X., Li, Z., Yang, W. and Zhou, F. Adhesion force spectroscopy of model surfaces with wettability gradient. *Colloids and Surfaces A: Physicochemical and Engineering Aspects*, **2011**, *380* (1–3), 175-181.

37 Dongmo, L.S., Villarrubia, J.S., Jones, S.N., Renegar, T.B., Postek, M.T. and Song, J.F. Experimental test of blind tip reconstruction for scanning probe microscopy. *Ultramicroscopy*, **2000**, *85* (3), 141-153.

38 Griepentrog, M., Krämer, G. and Cappella, B. Comparison of nanoindentation and AFM methods for the determination of mechanical properties of polymers. *Polymer Testing*, **2013**, *32* (3), 455-460.

39 R. Buzio, in *Scanning Probe Microscopy in Nanoscience and Nanotechnology 3*, ed. B. Bhushan (Springer Berlin Heidelberg, 2013) Chapter 3.

40 Tsukruk, V.V., Gorbunov, V.V., Huang, Z. and Chizhik, S.A. Dynamic microprobing of viscoelastic polymer properties. *Polymer International*, **2000**, *49* (5), 441-444.

41 van der Werf, K.O., Putman, C.A.J., de Grooth, B.G. and Greve, J. Adhesion force imaging in air and liquid by adhesion mode atomic force microscopy. *Applied Physics Letters*, **1994**, *65* (9), 1195-1197.

42 Zhong, Q., Inniss, D., Kjoller, K. and Elings, V.B. Fractured polymer/silica fiber surface studied by tapping mode atomic force microscopy. *Surface Science*, **1993**, *290* (1–2), L688-L692.

43 Raghavan, D., VanLandingham, M., Gu, X. and Nguyen, T. Characterization of Heterogeneous Regions in Polymer Systems Using Tapping Mode and Force Mode Atomic Force Microscopy. *Langmuir*, **2000**, *16* (24), 9448-9459.

44 Tsou, A.H., Lyon, M.K., Chapman, B.R. and Datta, S. Elastic properties of cast films from propylene elastomers. *Journal of Applied Polymer Science*, **2008**, *107* (2), 1362-1372.

45 Maivald, P., Butt, H.J., Gould, S.A.C., Prater, C.B., Drake, B., Gurley, J.A., Elings, V.B. and Hansma, P.K. Using force modulation to image surface elasticities with the atomic force microscope. *Nanotechnology*, **1991**, *2* (2), 103.

46 Zhang, J., Parlak, Z., Bowers, C.M., Oas, T. and Zauscher, S. Mapping mechanical properties of organic thin films by force-modulation microscopy in aqueous media. *Beilstein Journal of Nanotechnology*, **2012**, *3* 464-474.

47 Overney, R.M., Meyer, E., Frommer, J., Guentherodt, H.J., Fujihira, M., Takano, H. and Gotoh, Y. Force Microscopy Study of Friction and Elastic Compliance of Phase-Separated Organic Thin Films. *Langmuir*, **1994**, *10* (4), 1281-1286.

48 Xu, X., Koslowski, M. and Raman, A. Dynamics of surface-coupled microcantilevers in force modulation atomic force microscopy – magnetic vs. dither piezo excitation. *Journal of Applied Physics*, **2012**, *111* (5), 054303.

49 Mazeran, P.-E. and Loubet, J.-L. Force modulation with a scanning force microscope: an analysis. *Tribology Letters*, **1997**, *3* (1), 125-132.

50 Dinelli, F., Assender, H., Takeda, N., Briggs, G. and Kolosov, O. Elastic mapping of heterogeneous nanostructures with ultrasonic force microscopy (UFM). *Surface and interface analysis*, **1999**, *27* (5-6), 562-567.

51 Rosa-Zeiser, A., Weilandt, E., Hild, S. and Marti, O. The simultaneous measurement of elastic, electrostatic and adhesive properties by scanning force microscopy: pulsed-force mode operation. *Measurement Science and Technology*, **1997**, *8* (11), 1333.

52 Schön, P., Bagdi, K., Molnár, K., Markus, P., Pukánszky, B. and Julius Vancso, G. Quantitative mapping of elastic moduli at the nanoscale in phase separated polyurethanes by AFM. *European Polymer Journal*, **2011**, *47* (4), 692-698.

53 Choi, I., Kulkarni, D.D., Xu, W., Tsitsilianis, C. and Tsukruk, V.V. Star Polymer Unimicelles on Graphene Oxide Flakes. *Langmuir*, **2013**, *29* (31), 9761-9769.

54 Pakzad, A., Simonsen, J. and Yassar, R.S. Gradient of nanomechanical properties in the interphase of cellulose nanocrystal composites. *Composites Science and Technology*, **2012**, *72* (2), 314-319.

55 Martínez-Tong, D.E., Najar, A.S., Soccio, M., Nogales, A., Bitinis, N., López-Manchado, M.A. and Ezquerra, T.A. Quantitative mapping of mechanical properties in polylactic acid/natural rubber/organoclay bionanocomposites as revealed by nanoindentation with atomic force microscopy. *Composites Science and Technology*, **2014**, *104* 34-39.

56 Young, S.L., Gupta, M., Hanske, C., Fery, A., Scheibel, T. and Tsukruk, V.V. Utilizing Conformational Changes for Patterning Thin Films of Recombinant Spider Silk Proteins. *Biomacromolecules*, **2012**, *13* (10), 3189-3199.

57 Clifford, C.A. and Seah, M.P. Quantification issues in the identification of nanoscale regions of homopolymers using modulus measurement via AFM nanoindentation. *Applied Surface Science*, **2005**, *252* (5), 1915-1933.

58 Gheorghe, S. and Richard, S.G. Intermittent contact resonance atomic force microscopy. *Nanotechnology*, **2014**, *25* (24), 245702.

59 Schwarz, U.D. A generalized analytical model for the elastic deformation of an adhesive contact between a sphere and a flat surface. *Journal of Colloid and Interface Science*, **2003**, *261* (1), 99-106.

60 Moeller, G. AFM nanoindentation of viscoelastic materials with large end-radius probes. *Journal of Polymer Science Part B: Polymer Physics*, **2009**, *47* (16), 1573-1587.

61 Van Landingham, M.R., Chang, N.K., Drzal, P.L., White, C.C. and Chang, S.H. Viscoelastic characterization of polymers using instrumented indentation. I. Quasi-static testing*. *Journal of Polymer Science Part B: Polymer Physics*, **2005**, *43* (14), 1794-1811.

62 Ferry, J. D. *Viscoelastic properties of polymers*; Wiley: University of California, 1961.

63 Braunsmann, C., Proksch, R., Revenko, I. and Schäffer, T.E. Creep compliance mapping by atomic force microscopy. *Polymer*, **2014**, *55* (1), 219-225.

64 Fischer-Cripps, A.C. A simple phenomenological approach to nanoindentation creep. *Materials Science and Engineering: A*, **2004**, *385* (1–2), 74-82

65 Baro, A.; Reifenberger, R. *Atomic force microscopy in liquid: biological applications*; Wiley VCH: Weinheim, 2012.

66 Garcia, R. and Herruzo, E.T. The emergence of multifrequency force microscopy. *Nature Nano*, **2012**, *7* (4), 217-226.

67 Hurley, D. Contact Resonance Force Microscopy Techniques for Nanomechanical Measurements. In Applied Scanning Probe Methods XI; Springer: Berlin Heidelberg, 2009.

68 Zhou, X., Fu, J. and Li, F. Contact resonance force microscopy for nanomechanical characterization: Accuracy and sensitivity. *Journal of Applied Physics*, **2013**, *114* (6), 064301-1.

69 Yablon, D. G. S*canning probe microscopy for industrial applications: nanomechanical characterization*; Wiley: Hoboken, NJ, 2013.

70 Yuya, P.A., Hurley, D.C. and Turner, J.A. Contact-resonance atomic force microscopy for viscoelasticity. *Journal of Applied Physics*, **2008**, *104* (7), 074916-7.

71 Killgore, J.P., Yablon, D.G., Tsou, A.H., Gannepalli, A., Yuya, P.A., Turner, J.A., Proksch, R. and Hurley, D.C. Viscoelastic Property Mapping with Contact Resonance Force Microscopy. *Langmuir*, **2011**, *27* (23), 13983-13987.

72 Igarashi, T., Fujinami, S., Nishi, T., Asao, N., Nakajima and Ken. Nanorheological Mapping of Rubbers by Atomic Force Microscopy. *Macromolecules*, **2013**, *46* (5), 1916-1922.

73 Haugstad, G. *Atomic Force Microscopy: Understanding Basic Modes and Advanced Applications*; Wiley: Hoboken, NJ, 2012.

74 Cleveland, J.P., Anczykowski, B., Schmid, A.E. and Elings, V.B. Energy dissipation in tapping-mode atomic force microscopy. *Applied Physics Letters*, **1998**, *72* (20), 2613-2615.

75 Rodríguez, T.R. and García, R. Compositional mapping of surfaces in atomic force microscopy by excitation of the second normal mode of the microcantilever. *Applied Physics Letters*, **2004**, *84* (3), 449-451.

76 Garcia, R. and Proksch, R. Nanomechanical mapping of soft matter by bimodal force microscopy. *European Polymer Journal*, **2013**, *49* (8), 1897-1906.

77 Chawla, G. and Solares, S.D. Mapping of conservative and dissipative interactions in bimodal atomic force microscopy using open-loop and phase-locked-loop control of the higher eigenmode. *Applied Physics Letters*, **2011**, *99* (7), 074103.

78 Herruzo, E.T., Perrino, A.P. and Garcia, R. Fast nanomechanical spectroscopy of soft matter. *Nat Commun*, **2014**, *5*

79 Martinez-Martin, D., Herruzo, E.T., Dietz, C., Gomez-Herrero, J. and Garcia, R. Noninvasive Protein Structural Flexibility Mapping by Bimodal Dynamic Force Microscopy. *Physical Review Letters*, **2011**, *106* (19), 198101.

80 Ebeling, D., Eslami, B. and Solares, S.D.J. Visualizing the Subsurface of Soft Matter: Simultaneous Topographical Imaging, Depth Modulation, and Compositional Mapping with Triple Frequency Atomic Force Microscopy. *ACS Nano*, **2013**, *7* (11), 10387-10396.

81 Garcia, R. and Herruzo, E.T. The emergence of multifrequency force microscopy. *Nat Nano*, **2012**, *7* (4), 217-226.

82 Gorbunov, V., Fuchigami, N., Stone, M., Grace, M. and Tsukruk, V.V. Biological Thermal Detection: Micromechanical and Microthermal Properties of Biological Infrared Receptors. *Biomacromolecules*, **2002**, *3* (1), 106-115.

83 Peleshanko, S., Julian, M.D., Ornatska, M., McConney, M.E., LeMieux, M.C., Chen, N., Tucker, C., Yang, Y., Liu, C., Humphrey, J.A.C. and Tsukruk, V.V. Hydrogel-Encapsulated Microfabricated Haircells Mimicking Fish Cupula Neuromast. *Advanced Materials*, **2007**, *19* (19), 2903-2909.

84 Barth, F.G. *A spider's world: Senses and behavior*. **2002**, Springer-Verlag, Heidelberg.

85 Sane, S.P. and McHenry, M.J. The biomechanics of sensory organs. *Integrative and Comparative Biology*, **2009**, *49* (6), i8-i23.

86 Fratzl, P. and Barth, F.G. Biomaterial systems for mechanosensing and actuation. *Nature*, **2009**, *462* (7272), 442-8..

87 McConney, M.E., Anderson, K.D., Brott, L.L., Naik, R.R. and Tsukruk, V.V. Bioinspired Material Approaches to Sensing. *Advanced Functional Materials*, **2009**, *19* (16), 2527-2544.

88 Barth, F.G. and Geethabali. Spider vibration receptors: Threshold curves of individual slits in the metatarsal lyriform organ. *Journal of comparative physiology*, **1982**, *148* (2), 175-185.

89 Barth, F.G. and Seyfarth, E.A. Cupiennius-salei keys (araneae) in the highlands of central guatemala. *Journal of Arachnology*, **1979**, *7* (3), 255-263.

90 Barth, F.G., Bleckmann, H., Bohnenberger, J. and Seyfarth, E.-A. Spiders of the genus cupiennius simon 1891 (araneae, ctenidae). *Oecologia*, **1988**, *77* (2), 194-201.

91 Barth, F.G. How to catch the wind: Spider hairs specialized for sensing the movement of air. *Naturwissenschaften*, **2000**, *87* (2), 51-58.

92 McConney, M.E., Schaber, C.F., Julian, M.D., Barth, F.G. and Tsukruk, V.V. Viscoelastic nanoscale properties of cuticle contribute to the high-pass properties of spider vibration receptor (cupiennius salei keys). *Journal of the Royal Society Interface*, **2007**, *4* (17), 1135-1143.

93 McConney, M.E., Schaber, C.F., Julian, M.D., Eberhardt, W.C., Humphrey, J.A.C., Barth, F.G. and Tsukruk, V.V. Surface force spectroscopic point load measurements and viscoelastic modelling of the micromechanical properties of air flow sensitive hairs of a spider (cupiennius salei). *Journal of the Royal Society Interface*, **2009**, *6* (37), 681-694.

94 Klopsch, C., Kuhlmann, H.C. and Barth, F.G. Airflow elicits a spider's jump towards airborne prey. I. Airflow around a flying blowfly. *Journal of The Royal Society Interface*, **2012**, 9 (75), 2591-2602.

95 Klärner, D. and Barth, F.G. Vibratory signals and prey capture in orb-weaving spiders (zygiella x-notata, nephila clavipes; araneidae). *Journal of comparative physiology*, **1982**, *148* (4), 445-455.

96 Barth, F.G. Spider senses – technical perfection and biology. *Zoology*, **2002**, *105* (4), 271-285.

97 Barth, F.G. and Blickhan, R. Mechanoreception in *Biology of the Integument*. 1984. Springer-Berlin, Heidelberd

98 Barth, F.G. Spider mechanoreceptors. *Current Opinion in Neurobiology*, **2004**, *14* (4), 415-422.

99 Bohnenberger, J. Matched transfer characteristics of single units in a compound slit sense organ. *Journal of comparative physiology*, **1981**, *142* (3), 391-402.

100 Barth, F.G. and Libera, W. Ein atlas der spaltsinnesorgane von cupiennius salei keys. Chelicerata (araneae). *Zeitschrift für Morphologie der Tiere*, **1970**, *68* (4), 343-369.

101 Albert, J., Friedrich, O., Dechant, H.E. and Barth, F.G. Arthropod touch reception: Spider hair sensilla as rapid touch detectors. *Journal of comparative physiology*, **2001**, *187* (4), 303-312.

102 Dechant, H.E., Rammerstorfer, F. and Barth, F.G. Arthropod touch reception: Stimulus transformation and finite element model of spider tactile hairs. *Journal of comparative physiology*, **2001**, *187* (4), 313-322.

103 Humphrey, J.A.C., Devarakonda, R., Iglesias, I. and Barth, F.G. Dynamics of arthropod filiform hairs. I. Mathematical modelling of the hair and air motions. *Philosophical*

Transactions of the Royal Society of London. Series B: Biological Sciences, **1993**, *340* (1294), 423-444.

104 Barth, F.G., Wastl, U., Humphrey, J.A.C. and Devarakonda, R. Dynamics of arthropod filiform hairs. II. Mechanical properties of spider trichobothria (cupiennius salei keys.). *Philosophical Transactions of the Royal Society of London. Series B: Biological Sciences*, **1993**, *340* (1294), 445-461.

105 Humphrey, J.A.C., Barth, F.G., Reed, M. and Spak, A. The physics of arthropod medium-flow sensitive hairs: Biological models for artificial sensors in *Sensors and sensing in biology and engineering*. **2003**, Springer, Vienna.

106 Hößl, B. "Mechanical simulation of slit sensors of arachnids," Thesis, Institut für Leichtbau und Struktur-Biomechanik, Technischen Universität Wien, 2007.

107 Rick, R., Barth, F.G., Pawel, A. X-ray microanalysis of receptor lymph in a cuticular arthropod sensillum. *Journal of comparative physiology*, **1976**, *110* (1), 89-95.

108 Barth, F.G. and Pickelmann, P. Lyriform slit sense organs. *Journal of comparative physiology*, **1975**, *103* (1), 39-54.

109 Barth, F.G. Die physiologie der spaltsinnesorgane. II. Funktionelle Morphologie eines Mechanoreceptors. *Journal of comparative physiology*, **1972**, *81* (2), 159-186.

110 Hößl, B., Bohm, H.J., Rammerstorfer, F.G. and Barth, F.G. Finite element modeling of arachnid slit sensilla - I. The mechanical significance of different slit arrays. *Journal of Comparative Physiology a-Neuroethology Sensory Neural and Behavioral Physiology*, **2007**, *193* (4), 445-459.

111 Barth, F.G., Ficker, E., and Federle, H.-U. Model studies on the mechanical significance of grouping in compound spider slit sensilla (chelicerata, araneida). *Zoomorphology*, **1984**, *104* (4), 204-215.

112 Barth, F.G. and Stagl, J. The slit sense organs of arachnids. *Zoomorphologie*, **1976**, *86* (1), 1-23.

113 Barth, F.G. and Bohnenberger, J. Lyriform slit sense organ: Thresholds and stimulus amplitude ranges in a multi-unit mechanoreceptor. *Journal of comparative physiology*, **1978**, *125* (1), 37-43.

114 Hößl, B., Böhm, H.J., Rammerstorfer, F.G., Müllan, R. and Barth, F.G. Studying the deformation of arachnid slit sensilla by a fracture mechanical approach. *Journal of biomechanics*, **2006**, *39* (10), 1761-1768.

115 Barth, F.G. Die Physiologie der Spaltsinnesorgane. I. Modellversuche zur Rolle des cuticlaren Spaltes beim Reiztransport. *Journal of comparative physiology*, **1972**, *78* (3), 315-336.

116 Hößl, B., Bohm, H.J., Schaber, C.F., Rammerstorfer, F.G. and Barth, F.G. Finite element modeling of arachnid slit sensilla: II. Actual lyriform organs and the face deformations of the individual slits. *Journal of Comparative Physiology a-Neuroethology Sensory Neural and Behavioral Physiology*, **2009**, *195* (9), 881-894.

117 Schaber, C.F., Gorb, S.N. and Barth, F.G. Force transformation in spider strain sensors: White light interferometry. *Journal of The Royal Society Interface*, **2012**, *9* (71), 1254-1264.

118 Walcott, C. and van der Kloot, W.G. The physiology of the spider vibration receptor. *Journal of Experimental Zoology*, **1959**, *141* (2), 191-244.

119 Rovner, J.S. and Barth F.G. Vibratory communication through living plants by a tropical wandering spider. *Science*, **1981**, *214* (4519), 464-466.

120 Barth F.G. Neuroethology of spider vibration sense in *Neurobiology of arachnids*. **1985**. Springer, Berlin.

121 Barth, F.G., Bleckmann, H., Bohnenberger, J. and Seyfarth, E.A. Spiders of the genus cupiennius simon 1891 (araneae, ctenidae) .2. On the vibratory environment of a wandering spider. *Oecologia*, **1988**, 77 (2), 194-201.

122 Barth, 1998, the vibrational sense of spiders

123 Young, S.L., Chyasnavichyus, M., Erko, M., Barth, F.G., Fratzl, P., Zlotnikov, I., Politi, Y. and Tsukruk, V.V. A spider's biological vibration filter: Micromechanical characteristics of a biomaterial surface. *Acta Biomaterialia*, **2014**, *10* (11), 4832-4842.

124 Molina, J., Schaber, C.F. and Barth, F.G. In search of differences between the two types of sensory cells innervating spider slit sensilla (cupiennius salei keys.). *Journal of Comparative Physiology a-Neuroethology Sensory Neural and Behavioral Physiology*, **2009**, *195* (11), 1031-1041.

125 Williams, M.L., Landel, R.F., Ferry, J.D. The temperature dependence of relaxation mechanisms in amorphous polymers and other glass-forming liquids. *Journal of the American Chemical Society*, **1955**, *77* (14), 3701-3707.

126 Neville, A. *Biology of fibrous composites: Development beyond the cell membrane*. **1993**, Cambridge University Press, New York, USA.

127 Vincent, J.F.V. Arthropod cuticle: A natural composite shell system. *Composites Part A: Applied Science and Manufacturing*, **2002**, *33* (10), 1311-1315.

128 Vincent, J.F.V. *Structural biomaterials*. **2012**, Princeton, Princeton University Press.

129 Barth, F. Die Feinstruktur des Spinnenintegu ments. *Zeitschrift für Zellforschung und Mikroskopische Anatomie*, **1969**, *97* (1), 137-159.

130 Barth, F.G. Microfiber reinforcement of an arthropod cuticle - laminated composite-material in biology. *Zeitschrift Fur Zellforschung Und Mikroskopische Anatomie*, **1973**, *144* (3), 409-433.

131 Bouligand, Y. Twisted fibrous arrangements in biological materials and cholesteric mesophases. *Tissue and Cell*, **1972**, *4* (2), 189-217.

132 Bouligand, Y. Theory of microtomy artefacts in arthropod cuticle. *Tissue and Cell*, **1986**, *18* (4), 621-643.

133 Bonfante-Fasolo, P. and Vian, B. Wall texture in the spore of a vesicular-arbuscular mycorrhizal fungus. *Protoplasma*, **1984**, *120* (1-2), 51-60.

134 Vincent, J.F.V. and Wegst, U.G.K. Design and mechanical properties of insect cuticle. *Arthropod Structure & Development*, **2004**, *33* (3), 187-199.

135 Blickhan, R. Stiffness of an arthropod leg joint. *Journal of Biomechanics*, **1986**, 19 (5), 375-384.

136 Barth, F.G. Learning from animal sensors: the clever "design" of spider mechanoreceptors. *Proceedings of the SPIE* 8339: *Bioinspiration, Biomimetics, and Bioreplication*, **2012**, 833904.

137 Barth, F.G., *Spider strain detection.* Frontiers in Sensing: From Biology to Engineering, 2012: p. 251-273

138 Speck, J. and Barth, F.G.. Vibration Sensitivity of Pretarsal Slit Sensilla in the Spider Leg. *Journal of Comparative Physiology*. **1982**, *148* (2): p. 187-194.

139 Speck-Hergenroder, J. and Barth, F.G. Vibration Sensitive Hairs on the Spider Leg. *Experientia*, **1988**, *44* (1), 13-14.

140 Hergenroder, R. and Barth, F.G. The Release of Attack and Escape Behavior by Vibratory Stimuli in a Wandering Spider (Cupiennius Salei Keys). *Journal of Comparative Physiology*, **1983**, *152* (3), 347-358

141 Gingl, E., Burger, A.M. and Barth, F.G. Intracellular recording from a spider vibration receptor. *Journal of Comparative Physiology A*, **2006**, *192* (5), 551-558.

142 Politi, Y., Priewasser, M., Pippel, E., Zaslansky, P., Hartmann, J., Siegel, S., Li, C.H., Barth, F.G., Fratzl, P. A spider's fang: How to design an injection needle using chitin-based composite material. *Advanced Functional Materials*, **2012**, *22* (12), 2519-2528.

143 French, K. and Jones, L. A decade with silicone hydrogels part I. *Optometry Today*, **2008**, *48* (16), 42-46.

144 Gupta, M.K., Singamaneni, S., McConney, M., Drummy, L.F., Naik, R.R. and Tsukruk, V.V. A Facile Fabrication Strategy for Patterning Protein Chain Conformation in Silk Materials. *Advanced Materials*, **2010**, *22* (1), 115-119.

145 Serban, M.A. and Kaplan, D.L. pH-Sensitive Ionomeric Particles Obtained via Chemical Conjugation of Silk with Poly(amino acid)s. *Biomacromolecules*, **2010**, *11* (12), 3406-3412.

146 Zhou, C.-Z., Confalonieri, F., Jacquet, M., Perasso, R., Li, Z.-G. and Janin, J. Silk fibroin: Structural implications of a remarkable amino acid sequence. *Proteins: Structure, Function, and Bioinformatics*, **2001**, *44* (2), 119-122.

147 Asakura, T., Suita, K., Kameda, T., Afonin, S. and Ulrich, A.S. Structural role of tyrosine in Bombyx mori silk fibroin, studied by solid-state NMR and molecular mechanics on a model peptide prepared as silk I and II. *Magnetic Resonance in Chemistry*, **2004**, *42* (2), 258-266.

148 Maier, L., Root, T. and Seyfarth, E.-A. Heterogeneity of spider leg muscle: Histochemistry and electrophysiology of identified fibers in the claw levator. *Journal of Comparative Physiology B*, **1987**, *157* (3), 285-294.

149 Höger, U., Torkkeli, P.H., Seyfarth, E.-A. and French, A.S. Ionic Selectivity of Mechanically Activated Channels in Spider Mechanoreceptor Neurons. *Journal of Neurophysiology*, **1997**, *78* (4), 2079-2085.

150 Cappella, B., Kaliappan, S.K. and Sturm, H. Using AFM Force−Distance Curves To Study the Glass-to-Rubber Transition of Amorphous Polymers and Their Elastic−Plastic Properties as a Function of Temperature. *Macromolecules*, **2005**, *38* (5), 1874-1881.

151 Cappella, B. and Kaliappan, S.K. Determination of Thermomechanical Properties of a Model Polymer Blend. *Macromolecules*, **2006**, *39* (26), 9243-9252.

152 Tsui, O.K.C., Wang, X.P., Ho, J.Y.L., Ng, T.K. and Xiao, X. Studying Surface Glass-to-Rubber Transition Using Atomic Force Microscopic Adhesion Measurements. *Macromolecules*, **2000**, *33* (11), 4198-4204.

153 Friedenberg, M.C. and Mate, C.M. Dynamic viscoelastic properties of liquid polymer films studied by atomic force microscopy. *Langmuir*, **1996**, *12* (25), 6138-6142.

154 Hammerschmidt, J.A., Gladfelter, W.L. and Haugstad, G. Probing polymer viscoelastic relaxations with temperature-controlled friction force microscopy. *Macromolecules*, **1999**, *32* (10), 3360-3367.

155 Chizhik, S.A., Huang, Z., Gorbunov, V.V., Myshkin, N.K. and Tsukruk, V.V. Micromechanical properties of elastic polymeric materials as probed by scanning force microscopy. *Langmuir*, **1998**, *14* (10), 2606-2609.

156 Domke, J., and Radmacher, M. Measuring the elastic properties of thin polymer films with the atomic force microscope. *Langmuir* **1998,** *14*, 3320-3325.

157 Hertz, H. Ueber die Beruthrung fester elasticher Korper. *Journal für die reine und angewandte Mathematik*, **1882**, *92*, 156-171.

158 Johnson, K.L., Kendall, K., Roberts, A.D. Surface energy and the contact of elastic solids. *Proceedings of the Royal Society of London. A. Mathematical and Physical Sciences*, **1971**, 324 (1558), 301-313.

159 Michels, J. Confocal laser scanning microscopy: using cuticular autofluorescence for high resolution morphological imaging in small crustaceans. *Journal of Microscopy*, **2007**, *227* (1), 1-7.

160 Rasband, W., *ImageJ V 1.47* National Insitutes of Health, Bethesda MD, 1997-2013. http://imagej.nih.gov/ij/list.html.

161 Weitkamp, T., Tafforeau, P., Boller, E., Cloetens, P., Valade, J.P., Bernard, P., Peyrin, F., Ludwig, W., Helfen, L. and Baruchel, J. Status and evolution of the ESRF beamline ID19. *AIP Conference Proceedings*, **2010**, *1221* (1), 33-38.

162 Douissard, P.-A., Cecilia, A., Martin, T., Chevalier, V., Couchaud, M., Baumbach, T., Dupre, K., Kuhbacher, M. and Rack, A. A novel epitaxially grown LSO-based thin-film scintillator for micro-imaging using hard synchrotron radiation. *Journal of Synchrotron Radiation*, **2010**, *17* (5), 571-583.

163 Mirone, A., Brun, E., Gouillart, E., Tafforeau, P. and Kieffer, J. The PyHST2 hybrid distributed code for high speed tomographic reconstruction with iterative reconstruction and a priori knowledge capabilities. *Nuclear Instruments and Methods in Physics Research Section B: Beam Interactions with Materials and Atoms*, **2014**, *324* 41-48.

164 Weitkamp, T., Haas, D., Wegrzynek, D. and Rack, A. ANKAphase: software for single-distance phase retrieval from inline X-ray phase-contrast radiographs. *Journal of Synchrotron Radiation*, **2011**, *18* (4), 617-629.

165 Hammersley, A.P., Svensson, S.O., and Thompson, A. Calibration and Correction of Spatial Distortions in 2d Detector Systems. *Nuclear Instruments & Methods in Physics Research Section a-Accelerators Spectrometers Detectors and Associated Equipment*, **1994**, *346* (1-2), 312-321.

166 Oliver, W.C., Pharr, G.M. An Improved Technique for Determining Hardness and Elastic-Modulus Using Load and Displacement Sensing Indentation Experiments. *Journal of Materials Research*, **1992**, ***7*** (6), 1564-1583.

167 Häberle, W., Hörber, J.K.H., and Binnig, G., Force microscopy on living cells. *Journal of Vacuum Science & Technology B*, **1991,** *9* (2), 1210-1213.

168 Swallowe, G. M. *Mechanical properties and testing of polymers: an A-Z reference*; Kluwer Academic: Dordrecht, 1999.

169 Johnson, K. L. *Contact Mechanics*; Cambridge University Press: Cambridge, 1987.

170 Samori, P.; Cicoira, F. *STM and AFM Studies on (bio)molecular systems: unravelling the nanoworld*; Springer:Berlin, 2008.

171 Tsukruk, V. V.; Wahl, K. *Microstructure and microtribology of polymer surfaces*; ACS: Washington, DC, 2000.

172 Magonov, S.; Whangbo, M-H. *Surface analysis with STM and AFM: experimental and theoretical aspects of image analysis*, VCH, New York, 1996

173 Ratner, B. D; Tsukruk V.V. *Scanning probe microscopy of polymers*; ACS: Washington, DC, 1998.

174 Zhang, W. and Zhang, X. Single molecule mechanochemistry of macromolecules. *Progress in Polymer Science*, **2003**, *28* (8), 1271-1295..

175 Kühner, F. and Gaub, H.E. Modelling cantilever-based force spectroscopy with polymers. *Polymer*, **2006**, *47* (7), 2555-2563.

176 Shulha, H., Po Foo, C.W., Kaplan, D.L. and Tsukruk, V.V. Unfolding the multi-length scale domain structure of silk fibroin protein. *Polymer*, **2006**, *47* (16), 5821-5830.

177 Binnig, G., Quate, C.F. and Gerber, C. Atomic Force Microscope. *Physical Review Letters*, **1986**, *56* (9), 930-933.

178 Derjaguin, B.V., Muller, V.M. and Toporov, Y.P. Effect of contact deformations on the adhesion of particles. *Journal of Colloid and Interface Science*, **1975**, *53* (2), 314-326.

179 Maugis, D. Adhesion of spheres: The JKR-DMT transition using a dugdale model. *Journal of Colloid and Interface Science*, **1992**, *150* (1), 243-269.

180 Yang, G., Rao, N., Yin, Z. and Zhu, D.-M. Probing the viscoelastic response of glassy polymer films using atomic force microscopy. *Journal of Colloid and Interface Science*, **2006**, *297* (1), 104-111.

181 Weisenhorn, A.L., Hansma, P.K., Albrecht, T.R. and Quate, C.F. Forces in atomic force microscopy in air and water. *Applied Physics Letters*, **1989**, *54* (26), 2651-2653.

182 Rico, F., Roca-Cusachs, P., Gavara, N., Farré, R., Rotger, M. and Navajas, D. Probing mechanical properties of living cells by atomic force microscopy with blunted pyramidal cantilever tips. *Physical Review E*, **2005**, *72* (2), 021914.

183 Bradley, R.S. The cohesive force between solid surfaces and the surface energy of solids. *Philosophical Magazine Series 7*, **1932**, *13* (86), 853-862.

184 Drelich, J.; Mittal, K. L. *Atomic force microscopy in adhesion studies*; Taylor & Francis: Boston, 2005.

185 Johnson, K.L. and Greenwood, J.A. An Adhesion Map for the Contact of Elastic Spheres. *Journal of Colloid and Interface Science*, **1997**, *192* (2), 326-333.

186 Carpick, R.W., Ogletree, D.F. and Salmeron, M. A General Equation for Fitting Contact Area and Friction vs Load Measurements. *Journal of Colloid and Interface Science*, **1999**, *211* (2), 395-400.

187 Tsukruk, V.V. Scanning Probe Microscopy of Polymer Surfaces. *Rubber Chemistry and Technology*, **1997**, *70* (3), 430-467.

188 Hazel, J.L. and Tsukruk, V.V. Spring constants of composite ceramic/gold cantilevers for scanning probe microscopy. *Thin Solid Films*, **1999**, *339* (1–2), 249-257.

189 Tsukruk, V. V.; Huang, Z. Micro-thermomechanical properties of heterogeneous polymer films, *Polymer* **2000**, 41, 5541.

190 Tsukruk, V.V. and Huang, Z. Micro-thermomechanical properties of heterogeneous polymer films. *Polymer*, **2000**, *41* (14), 5541-5545.

191 Tsukruk, V.V., Sidorenko, A., Gorbunov, V.V. and Chizhik, S.A. Surface Nanomechanical Properties of Polymer Nanocomposite Layers. *Langmuir*, **2001**, *17* (21), 6715-6719.

192 Tsukruk, V.V. and Reneker, D.H. Scanning probe microscopy of organic and polymeric films: from self-assembled monolayers to composite multilayers. *Polymer*, **1995**, *36* (9), 1791-1808.

193 Sidorenko, A., Ahn, H.-S., Kim, D.-I., Yang, H. and Tsukruk, V.V. Wear stability of polymer nanocomposite coatings with trilayer architecture. *Wear*, **2002**, *252* (11–12), 946-955.

194 Julthongpiput, D., LeMieux, M. and Tsukruk, V.V. Micromechanical properties of glassy and rubbery polymer brush layers as probed by atomic force microscopy. *Polymer*, **2003**, *44* (16), 4557-4562.

195 LeMieux, M.C., Peleshanko, S., Anderson, K.D. and Tsukruk, V.V. Adaptive Nanomechanical Response of Stratified Polymer Brush Structures†. *Langmuir*, **2007**, *23* (1), 265-273.

196 Choi, T., Jang, J.H., Ullal, C.K., LeMieux, M.C., Tsukruk, V.V. and Thomas, E.L. The Elastic Properties and Plastic Behavior of Two-Dimensional Polymer Structures Fabricated by Laser Interference Lithography. *Advanced Functional Materials*, **2006**, *16* (10), 1324-1330.

197 Shulha, H., Zhai, X. and Tsukruk, V.V. Molecular Stiffness of Individual Hyperbranched Macromolecules at Solid Surfaces. *Macromolecules*, **2003**, *36* (8), 2825-2831.

198 Peleshanko, S., Julian, M.D., Ornatska, M., McConney, M.E., LeMieux, M.C., Chen, N., Tucker, C., Yang, Y., Liu, C., Humphrey, J.A.C. and Tsukruk, V.V. Hydrogel-Encapsulated Microfabricated Haircells Mimicking Fish Cupula Neuromast. *Advanced Materials*, **2007**, *19* (19), 2903-2909.

199 Ye, C., Drachuk, I., Calabrese, R., Dai, H., Kaplan, D.L. and Tsukruk, V.V. Permeability and Micromechanical Properties of Silk Ionomer Microcapsules. *Langmuir*, **2012**, *28* (33), 12235-12244.

200 Child Jr, W.C. and Ferry, J.D. Dynamic mechanical properties of poly-n-butyl methacrylate. *Journal of Colloid Science*, **1957**, *12* (3), 327-341.

201 Cook, S.M., Schäffer, T.E., Chynoweth, K.M., Wigton, M., Simmonds, R.W. and Lang, K.M. Practical implementation of dynamic methods for measuring atomic force microscope cantilever spring constants. *Nanotechnology*, **2006**, *17* (9), 2135.

202 Keller, D. Reconstruction of STM and AFM images distorted by finite-size tips. *Surface Science*, **1991**, *253* (1–3), 353-364.

203 Sedin, D.L. and Rowlen, K.L. Adhesion Forces Measured by Atomic Force Microscopy in Humid Air. *Analytical Chemistry*, **2000**, *72* (10), 2183-2189..

204 Lin, D.C., Dimitriadis, E.K. and Horkay, F. Robust Strategies for Automated AFM Force Curve Analysis—I. Non-adhesive Indentation of Soft, Inhomogeneous Materials. *Journal of Biomechanical Engineering*, **2006**, *129* (3), 430-440.

205 Tranchida, D., Piccarolo, S., Loos, J. and Alexeev, A. Mechanical Characterization of Polymers on a Nanometer Scale through Nanoindentation. A Study on Pile-up and Viscoelasticity. *Macromolecules*, **2007**, *40* (4), 1259-1267.

206 Shulha, H., Kovalev, A., Myshkin, N. and Tsukruk, V.V. Some aspects of AFM nanomechanical probing of surface polymer films. *European Polymer Journal*, **2004**, *40* (5), 949-956.

207 Tschoegl, N. W. *The phenomenological theory of linear viscoelastic behavior: an introduction* Springer-Verlag: Berlin; New York, 1989.

208 Johnson, K.L. Contact Mechanics and Adhesion of Viscoelastic Spheres. *ACS Symposium series*, **2000**, *741* (193), 24-41.

209 Chatterjee, S.; Hadi, A. S. *Regression analysis by example*; Wiley: Hoboken, NJ, 2013.

210 Teixeira, S.S., Dias, C.J., Dionisio, M. and Costa, L.C. New method to analyze dielectric relaxation processes: a study on polymethacrylate series. *Polymer International*, **2013**, *62* (12), 1744-1749.

211 Meier, G., Fytas, G. and Dorfmueller, T. Photon correlation study of the relaxation processes in bulk poly(n-butyl methacrylate). *Macromolecules*, **1984**, *17* (4), 957-961.

212 Tschoegl, N.W. and Emri, I. Generating line spectra from experimental responses. Part II: Storage and loss functions. *Rheologica Acta*, **1993**, *32* (3), 322-327.

213 Kaliappan, S. K. Characterization of physical properties of polymers using AFM force distance curves Ph.D. Dissertation, Siegen University, 2007

214 Lévy, R. and Maaloum, M. Measuring the spring constant of atomic force microscope cantilevers: thermal fluctuations and other methods. *Nanotechnology*, **2002**, *13* (1), 33.

215 Cook, S.M., Schäffer, T.E., Chynoweth, K.M., Wigton, M., Simmonds, R.W. and Lang, K.M. Practical implementation of dynamic methods for measuring atomic force microscope cantilever spring constants. *Nanotechnology*, **2006**, *17* (9), 2135.

216 Guz, N., Dokukin, M., Kalaparthi, V. and Sokolov, I. If Cell Mechanics Can Be Described by Elastic Modulus: Study of Different Models and Probes Used in Indentation Experiments. *Biophysical Journal*, **2014**, *107* (3), 564-575.

217 Lin, D.C. and Horkay, F. Nanomechanics of polymer gels and biological tissues: A critical review of analytical approaches in the Hertzian regime and beyond. *Soft Matter*, **2008**, *4* (4), 669-682.

218 Liu, C.-L., Fang, T.-H. and Lin, J.-F. Atomistic simulations of hard and soft films under nanoindentation. *Materials Science and Engineering: A*, **2007**, *452–453* 135-141..

219 Poon, B., Rittel, D. and Ravichandran, G. An analysis of nanoindentation in linearly elastic solids. *International Journal of Solids and Structures*, **2008**, *45* (24), 6018-6033.

220 Kopycinska-Müller, M., Geiss, R.H. and Hurley, D.C. Contact mechanics and tip shape in AFM-based nanomechanical measurements. *Ultramicroscopy*, **2006**, *106* (6), 466-474.

221 Flater, E.E., Zacharakis-Jutz, G.E., Dumba, B.G., White, I.A. and Clifford, C.A. Towards easy and reliable AFM tip shape determination using blind tip reconstruction. *Ultramicroscopy*, **2014**, *146* 130-143.

222 Berla, L.A., Allen, A.M., Han, S.M. and Nix, W.D. A physically based model for indenter tip shape calibration for nanoindentation. *Journal of Materials Research*, **2010**, *25* (04), 735-745.

223 Oliver, W.C. and Pharr, G.M. Measurement of hardness and elastic modulus by instrumented indentation: Advances in understanding and refinements to methodology. *Journal of Materials Research*, **2004**, *19* (01), 3-20.

224 Efron, N. Unravelling Contact Lens Specifications. *The Australian Journal of Optometry*, **1980**, *63* (6), 273-279.

225 Sorbara, L., Jones, L. and Williams-Lyn, D. Contact lens induced papillary conjunctivitis with silicone hydrogel lenses. *Contact Lens and Anterior Eye*, **2009**, *32* (2), 93-96.

226 González-Méijome, J.M., González-pérez, J., Cerviño, A., Yebra-pimentel, E. and Parafita, M.A. Changes in Corneal Structure with Continuous Wear of High-Dk Soft Contact Lenses: A Pilot Study. *Optometry & Vision Science*, **2003**, *80* (6), 440-446.

227 Nicolson, P.C. and Vogt, J. Soft contact lens polymers: an evolution. *Biomaterials*, **2001**, *22* (24), 3273-3283.

228 Fench, K. Contact Lens Material Properties. Part 2 - Mechanical behaviour and modulus. *Optician*, **2005**, *230* 29-34.

229 Stapleton, F., Stretton, S., Papas, E., Skotnitsky, C. and Sweeney, D.F. Silicone Hydrogel Contact Lenses and the Ocular Surface. *The Ocular Surface*, **2006**, *4* (1), 24-43.

230 French, K. and Jones, L. A decade with silicone hydrogels part I. *Optometry Today*, **2008**, *48* (16), 42-46.

231 Szczotka-Flynn, L. Looking at silicone hydrogels across generations. *Optom Manag*, **2008**, *43* 68-71.

232 Tranoudis, I. and Efron, N. Tensile properties of soft contact lens materials. *Contact Lens and Anterior Eye*, **2004**, *27* (4), 177-191.

233 Young, G., Garofalo, R., Harmer, O. and Peters, S. The effect of soft contact lens care products on lens modulus. *Contact Lens and Anterior Eye*, **2010**, *33* (5), 210-214.

234 Horst, C.R., Brodland, B., Jones, L.W. and Brodland, G.W. Measuring the Modulus of Silicone Hydrogel Contact Lenses. *Optometry & Vision Science*, **2012**, *89* (10), 1468-1476

235 Weikart, C.M., Matsuzawa, Y., Winterton, L. and Yasuda, H.K. Evaluation of plasma polymer-coated contact lenses by electrochemical impedance spectroscopy. *Journal of Biomedical Materials Research*, **2001**, *54* (4), 597-607.

236 Lisunova, M.O., Drachuk, I., Shchepelina, O.A., Anderson, K.D. and Tsukruk, V.V. Direct Probing of Micromechanical Properties of Hydrogen-Bonded Layer-by-Layer Microcapsule Shells with Different Chemical Compositions. *Langmuir*, **2011**, *27* (17), 11157-11165.

237 Last, J.A., Russell, P., Nealey, P.F. and Murphy, C.J. The applications of atomic force microscopy to vision science. *Investigative ophthalmology & visual science*, **2010**, *51* (12), 6083-6094..

238 Tsukruk, V., Huang, Z., Chizhik, S. and Gorbunov, V. Probing of micromechanical properties of compliant polymeric materials. *Journal of materials science*, **1998**, *33* (20), 4905-4909.

239 Tsukruk, V.V., Sidorenko, A. and Yang, H. Polymer nanocomposite coatings with non-linear elastic response. *Polymer*, **2002**, *43* (5), 1695-1699.

240 Lemieux, M., Minko, S., Usov, D., Stamm, M. and Tsukruk, V. Direct measurement of thermoelastic properties of glassy and rubbery polymer brush nanolayers grown by "grafting-from" approach. *Langmuir*, **2003**, *19* (15), 6126-6134.

241 Lemieux, M., Usov, D., Minko, S., Stamm, M., Shulha, H. and Tsukruk, V.V. Reorganization of binary polymer brushes: Reversible switching of surface microstructures and nanomechanical properties. *Macromolecules*, **2003**, *36* (19), 7244-7255.

242 Picart, C., Senger, B., Sengupta, K., Dubreuil, F. and Fery, A. Measuring mechanical properties of polyelectrolyte multilayer thin films: Novel methods based on AFM and optical techniques. *Colloids and Surfaces A: Physicochemical and Engineering Aspects*, **2007**, *303* (1), 30-36.

243 Cicoira F and Samorì P. STM and AFM Studies on (bio) molecular Systems: Unravelling the Nanoworld: Springer, 2008.

244 Guryča, V., Hobzová, R., Přádný, M., Širc, J. and Michálek, J. Surface morphology of contact lenses probed with microscopy techniques. *Contact Lens and Anterior Eye*, **2007**, *30* (4), 215-222.

245 Kim, S.H., Marmo, C. and Somorjai, G.A. Friction studies of hydrogel contact lenses using AFM: non-crosslinked polymers of low friction at the surface. *Biomaterials*, **2001**, *22* (24), 3285-3294.

246 Teichroeb, J.H., Forrest, J.A., Ngai, V., Martin, J.W., Jones, L. and Medley, J. Imaging protein deposits on contact lens materials. *Optometry & Vision Science*, **2008**, *85* (12), 1151-1164.

247 Anderson, M.S. and Gaimari, S.D. Raman-atomic force microscopy of the ommatidial surfaces of Dipteran compound eyes. *Journal of structural biology*, **2003**, *142* (3), 364-368.

248 Opdahl, A., Kim, S.H., Koffas, T.S., Marmo, C. and Somorjai, G.A. Surface mechanical properties of pHEMA contact lenses: viscoelastic and adhesive property changes on exposure to controlled humidity. *Journal of Biomedical Materials Research Part A*, **2003**, *67* (1), 350-356.

249 Kim, S.H., Opdahl, A., Marmo, C. and Somorjai, G.A. AFM and SFG studies of pHEMA-based hydrogel contact lens surfaces in saline solution: adhesion, friction, and the presence of non-crosslinked polymer chains at the surface. *Biomaterials*, **2002**, *23* (7), 1657-1666.

250 Adamcik, J., Berquand, A. and Mezzenga, R. Single-step direct measurement of amyloid fibrils stiffness by peak force quantitative nanomechanical atomic force microscopy. *Applied Physics Letters*, **2011**, *98* (19), 193701-193701-3.

251 Cappella, B. and Silbernagl, D. Nanomechanical Properties of Mechanical Double-Layers: A Novel Semiempirical Analysis. *Langmuir*, **2007**, *23* (21), 10779-10787.

252 Schneider, A., Francius, G., Obeid, R., Schwinté, P., Hemmerlé, J., Frisch, B., Schaaf, P., Voegel, J.-C., Senger, B. and Picart, C. Polyelectrolyte Multilayers with a Tunable Young's Modulus: Influence of Film Stiffness on Cell Adhesion. *Langmuir*, **2005**, *22* (3), 1193-1200.

253 Halperin, A. and Zhulina, E.B. Atomic Force Microscopy of Polymer Brushes: Colloidal versus Sharp Tips. *Langmuir*, **2010**, *26* (11), 8933-8940.

254 González-Méijome, J.M., López-Alemany, A., Almeida, J.B., Parafita, M.A. and Refojo, M.F. Microscopic observation of unworn siloxane–hydrogel soft contact lenses by atomic force microscopy. *Journal of Biomedical Materials Research Part B: Applied Biomaterials*, **2006**, *76B* (2), 412-418.

255 González-Méijome, J.M., López-Alemany, A., Almeida, J.B. and Parafita, M.A. Surface AFM microscopy of unworn and worn samples of silicone hydrogel contact lenses. *Journal of Biomedical Materials Research Part B: Applied Biomaterials*, **2009**, *88B* (1), 75-82.

256 Jones, L., Subbaraman, L., Rogers, R. and Dumbleton, K. Surface treatment, wetting and modulus of silicone hydrogels. *Optician*, **2006**, *232* (6067), 28-34.

257 Jones, L. Comfilcon A: a new silicone hydrogel material. *Contact Lens Spectrum*, **2007**, *22* (8), 15.

258 French, K. and Jones, L. A decade with silicone hydrogels: Part 2. *Optom Today*, **2008**, *48*, 38-43.

259 López-Alemany, A., Compañ, V. and Refojo, M.F. Porous structure of Purevision™ versus Focus® Night&Day™ and conventional hydrogel contact lenses. *Journal of Biomedical Materials Research*, **2002**, *63* (3), 319-325.

260 Le Rouzic, J., Delobelle, P., Vairac, P. and Cretin, B. Comparison of three different scales techniques for the dynamic mechanical characterization of two polymers (PDMS and SU8). *The European Physical Journal Applied Physics*, **2009**, *48* (01), 11201.

261 Bleuet, P., Roux, J.-P., Dabin, Y., and Boivin, G. In-situ microtomography study of human bones under strain with synchrotron radiation. *Proceedings of the SPIE 5535: Developments in X-Ray Tomography IV*, **2004**, 129-136.

262 Andersen, S.O. Insect cuticular sclerotization: A review. *Insect Biochemistry and Molecular Biology*, **2010**, *40* (3), 166-178.

263 Michels, J. and Gorb, S.N. Detailed three-dimensional visualization of resilin in the exoskeleton of arthropods using confocal laser scanning microscopy. *Journal of Microscopy*, **2012,** *245* (1), 1-16.

264 Erko, M., Hartmann, M.A., Zlotnikov, I., Valverde Serrano, C., Fratzl, P. and Politi, Y. Structural and mechanical properties of the arthropod cuticle: Comparison between the fang of the spider Cupiennius salei and the carapace of American lobster Homarus americanus. *Journal of Structural Biology*, **2013**, *183* (2), 172-179.

265 Lichtenegger, H., Muller, M., Paris, O., Riekel, C. and Fratzl, P. Imaging of the helical arrangement of cellulose fibrils in wood by synchrotron X-ray microdiffraction. *Journal of Applied Crystallography*, **1999**, *32* 1127-1133..

266 Seidel, R., Gourrier, A., Burghammer, M., Riekel, C., Jeronimidis, G. and Paris, O. Mapping fibre orientation in complex-shaped biological systems with micrometre resolution by scanning X-ray microdiffraction. *Micron*, **2008**, *39* (2), 198-205.

267 Paris, O. and Müller, M. Scanning X-ray microdiffraction of complex materials: Diffraction geometry considerations. *Nuclear Instruments and Methods in Physics Research Section B: Beam Interactions with Materials and Atoms*, **2003**, *200* 390-396..

268 Guinier, A. and G. Fournet, *Small-Angle Scattering of X-Rays*. 1955, London: Chapman & Hall, Ltd.

269 Pedersen, J.S. Analysis of small-angle scattering data from colloids and polymer solutions: modeling and least-squares fitting. *Advances in Colloid and Interface Science*, **1997**, *70* 171-210.

270 Nikolov, S., Petrov, M., Lymperakis, L., Friák, M., Sachs, C., Fabritius, H.-O., Raabe, D. and Neugebauer, J. Revealing the Design Principles of High-Performance Biological Composites Using Ab initio and Multiscale Simulations: The Example of Lobster Cuticle. *Advanced Materials*, **2010**, *22* (4), 519-526.

271 Friedel, T. and Barth, F.G. Wind-sensitive interneurones in the spider CNS (Cupiennius salei): Directional information processing of sensory inputs from trichobothria on the walking legs. *Journal of Comparative Physiology a-Sensory Neural and Behavioral Physiology*, **1997**, *180* (3), 223-233.

272 Dirks, J.-H. and Federle, W. Fluid-based adhesion in insects - principles and challenges. *Soft Matter*, **2011**, *7* (23), 11047-11053.

273 Gorb S. Attachment Devices of Insect Cuticle. Dordrecht: Kluwer Academic Publishers; 2001.

274 Bar-Cohen Y. (Eds). Biomimetics: biologically inspired technologies. CRC/Taylor & Francis: Boca Raton, FL; 2006.

275 Terashima S, Goris RC (Eds). Infrared Receptors and the Trigeminal Sensory System. Amsterdam: Harwood Academic Publishers; 1999.

276 Netten, S. Hydrodynamic detection by cupulae in a lateral line canal: functional relations between physics and physiology. *Biological Cybernetics*, **2006**, *94* (1), 67-85.

277 Barth FG. Sensory perception: Adaptation to lifestyle and habitat. In: Barth F, Giampieri-Deutsch P, Klein H-D, editors. Sensory Perception: Springer Vienna; 2012. p. 89-107.

278 Barth FG. Vibratory communication in spiders: Adaptation and compromise at many levels. In: Lehrer M, editor. Orientation and Communication in Arthropods: Birkhäuser Basel; 1997. p. 247-72.

279 Barth FG. Arthropod Strain Sensors. In: Bhushan B, editor. Encyclopedia of Nanotechnology: Springer Netherlands; 2012. p. 127-36.

280 Krevelen DWv. Properties of Polymers: Their Correlation with Chemical Structure, Their Numerical Estimation and Prediction from Additive Group Contributions. 3rd, completely rev. ed. Elsevier: Amsterdam ; 1990.

281 Tobolsky, A.V. Stress Relaxation Studies of the Viscoelastic Properties of Polymers. *Journal of Applied Physics*, **1956**, *27* (7), 673-685.

282 Barth F. Slit Sensilla and the Measurement of Cuticular Strains. In: Barth F, editor. Neurobiology of Arachnids: Springer Berlin Heidelberg; 1985. p. 162-88.

283 Skordos, A., Chan, P.H., Vincent, J.F.V. and Jeronimidis, G. A novel strain sensor based on the campaniform sensillum of insects. *Philosophical Transactions of the Royal Society of London A: Mathematical, Physical and Engineering Sciences*, **2002**, *360* (1791), 239-253.

284 Calvert P. Embedded mechanical sensors in artificial and biological systems. Vienna: Springer-Verlag Wien; 2003

285 Vincent, J.F.V., Clift, S.E. and Menon, C. Biomimetics of Campaniform Sensilla: Measuring Strain from the Deformation of Holes. *Journal of Bionic Engineering*, **2007**, *4* (2), 63-76.

286 Summerer, L. Thinking tomorrows' space - Research trends of the ESA advanced concepts team 2002-2012. *Acta Astronautica*, **2014**, *95* 242-259.

287 Kang, D., Pikhitsa, P.V., Choi, Y.W., Lee, C., Shin, S.S., Piao, L., Park, B., Suh, K.-Y., Kim, T.-i. and Choi, M. Ultrasensitive mechanical crack-based sensor inspired by the spider sensory system. *Nature*, **2014**, *516* (7530), 222-226.

288 Fratzl, P. Applied physics: The virtues of tiling. *Nature*, **2014**, *516* (7530), 178-179.

289 Erko, M., Younes-Metzler, O., Rack, A., Zaslansky, P., Young, S.L., Milliron, G., Chyasnavichyus, M., Barth, F.G., Fratzl, P., Tsukruk, V., Zlotnikov, I. and Politi, Y. Micro- and nano-structural details of a spider's filter for substrate vibrations: relevance for low-frequency signal transmission. *Journal of The Royal Society Interface*, **2015**, *12* (104), 20141111.

290 Boresi AP. Advanced mechanics of materials. 6th ed. ed. John Wiley & Sons: New York; 2003.

291 Dalingwater, JE. Chelicerate Cuticle Structure. In: Nentwig, W, editor. Ecophysiology of Spiders: Springer-Verlag Berlin Heidelberg; 1987. p. 3-15.

292 Hillerton, JE. Cuticle: Mechanical Properties. In: Bereiter-Hahn J, Matoltsy AG, Richards KS, editors. Biology of the Integument: Springer Berlin Heidelberg; 1984. p. 626-36.

293 Barbakadze, N., Enders, S., Gorb, S. and Arzt, E. Local mechanical properties of the head articulation cuticle in the beetle Pachnoda marginata (Coleoptera, Scarabaeidae). *Journal of Experimental Biology*, **2006**, *209* (4), 722-730.

294 Thorson, J. and Biederman-Thorson, M. Distributed Relaxation Processes in Sensory Adaptation. *Science*, **1974**, *183* (4121), 161-172.

295 Mann, D.W. and Chapman, K.M. Component mechanisms of sensitivity and adaptation in an insect mechanoreceptor. *Brain Research*, **1975**, *97* (2), 331-336.

296 Chapman, K., Mosinger, J. and Duckrow, R.B. The role of distributed viscoelastic coupling in sensory adaptation in an insect mechanoreceptor. *Journal of comparative physiology*, **1979**, *131* (1), 1-12.

VITA

Seth Lawton Young was born in Baton Rouge, Louisiana on November 14th, 1987 to Scott Young and Jo Sanders. He later moved with his mother to the metro Atlanta area where he attended Sims Elementary School, Edwards Middle School, and Heritage High School, graduating with honors in 2006. He earned his Bachelor of Science in Materials Science and Engineering from the Georgia Institute of Technology with high honors in Spring 2010. He pursued his Ph.D. in Materials Science and Engineering at the Georgia Institute of Technology under the advisement of Professor Valdimir V. Tsukruk. After graduating Seth will begin his professional career as a Development Chemist in the Core Growth Group at Georgia-Pacific Chemicals LLC, located in Decatur, Georgia.